ELECTRONIC PROPERTIES OF WELL-ORIENTED GRAPHITE AT LOW TEMPERATURES.

A thesis submitted to

THE UNIVERSITY OF LONDON

by

J. WOORE B.Sc., M.Sc., A.R.C.S.

Candidate for the Degree of
Doctor of Philosophy in the
Faculty of Science.

Department of Chemical Engineering and
Chemical Technology,
Imperial College of Science and Technology,
LONDON, S.W.7.

August, 1969.

ABSTRACT

Measurement and interpretation of galvanomagnetic effects in well-oriented pyrolytic graphite has been carried out over a temperature range from 300°K to 1°K in magnetic fields up to 17 k gauss.

A cryostat was designed and constructed to fit between the poles of a Newport electromagnet. The thin-walled stainless steel cryostat was thermally shielded by a silvered glass nitrogen dewar. Long tails were required on the dewar vessels because of the magnet shape. Pumping systems were built for lowering the temperature of the liquid helium bath and maintaining thermal isolation. A closed helium-3 system was incorporated in the cryostat design.

Graphite affords opportunity for studying the effects of extreme crystalline anisotropy and whilst much is known qualitatively about graphite, the present work makes a much-needed contribution to the quantitative knowledge of electronic conduction in graphite.

An analysis of the magnetoconductivity tensor components, following McClure's work on Soule's single crystal data, leads to values for carrier densities and mobilities over the above range of temperatures.

For the first time data are presented on the Shubnikov-de Haas oscillations in pyrolytic graphite. An analysis of these quantum oscillations at about 1°K was used to estimate carrier effective masses and Dingle temperatures. Oscillation periods were used to give estimates of the parameters Δ, γ_2, E_f which appear in the Slonczewski-Weiss band model of graphite and are not well determined by previous work.

It was necessary to present the band model with an algebraic clarity not evident in the literature before undertaking these calculations. Use was made of this to investigate the value of the Jones-Zener expansion of the low magnetic field magneto-conductivity tensor. Extensive use of the Imperial College IBM computer was made throughout the course of the work reported here.

Previous work on pyrolytic graphite has yielded general outlines only, though Spain's survey established that the electronic properties of the best pyrolytic graphite closely approaches that of single crystals. The present work affords a comparison between the two; we conclude that the electronic structure of both types are essentially comparable, differences lying partly in scattering introduced by the mosaic, micro-crystalline nature of pyrolytic graphite. Recent experimental results obtained by other workers have thrown new light on the interpretation of the Hall effect in particular: there are strong indications that carrier-carrier scattering is of outstanding importance in determining electronic conduction processes in graphite.

ACKNOWLEDGEMENTS

It is a pleasure to acknowledge the supervision and constant encouragement of Dr. D.A. Young, D.Sc.

Professor A.R. Ubbelohde, C.B.E., F.R.S., kindly provided laboratory facilities for this work and generously made available the means for a short extension to the S.R.C. studentship.

The author thanks M.L. Yeoman, Dr. B.J. Jackson and D. Cooper of this laboratory for helpful discussions and permission to quote results before publication where applicable.

Miss Nanette Kingan and Miss Linda Harding of Sussex University were patiently competent in the preparation of the manuscript and thanks are due to Mrs. Mary Lewis for help with xeroxing and diagram reproduction.

Finally, the author gratefully acknowledges the research studentship provided by the Science Research Council.

Στην Ελευθερίαν

CONTENTS

CHAPTER 1.

1.1 INTRODUCTION

The physical and electronic properties of graphite provide a unique opportunity for studying extreme crystalline anisotropy. Whilst a great deal is known qualitatively about graphite, there remains a great deal to be achieved in the quantitative description of electronic properties, particularly as they relate to the magneto conductivity tensor, Fermi surface metrication and carrier-lattice interactions.

The anisotropy of graphite stems from its crystal structure which (see Section 2.1) consists essentially of strongly bonded two-dimensional sheets weakly held together by van der Waals forces. Ratios of thermal and electrical conductivities in the basal planes to those perpendicular to the basal planes (along the c-axis direction) can exceed 200 and 5000 respectively, even at room temperature.

Unfortunately, very few single crystals of the required perfection exist. The best of these won from the calcite deposits of Essex County, New York included untwinned regions only 2 mm. in extent. The high melting point (about 3800°C at 100 atmospheres) and mechanical weakness in the direction of basal shear make the task of growing single crystals in the laboratory an unusually difficult one. Crystallisation from solution in iron or tantalum monocarbide yields

graphite crystals with untwinned regions of adequate size, but no such single crystal has a thickness in the c-direction sufficient for accurate characterisation of the c-axis properties of graphite.

The present work grew out of attempts in this laboratory to produce graphite by pyrolytic deposition which closely approached natural single crystal graphite in electrical and some physical properties. It is the first detailed analysis of the magnetoconductivity tensor components σ_{xx}, σ_{xy} and the periods and Dingle temperatures of the Shubuikow-de Haas oscillations in pyrolytic graphite. Previous publications have given general outlines only. In particular, Spain's (1967) survey of the electronic properties of the well-oriented material produced in this laboratory, though demonstrating convincingly the close approach of the best pyrolytic graphite to single crystal behaviour, did not extend to a detailed analysis of Hall-effect and conductivity data and he was unable to report any oscillatory behaviour observable under his experimental conditions. Some light is thrown on the striking low field behaviour of Soule's (1958) Hall-effect data which showed large excursions in the positive ($77^{\circ}K$) or negative ($298^{\circ}K$) direction at fields less than 1000 gauss. Soule suggested that these originated in the narrow regions connecting the hole and electron Fermi surfaces (see Figure 2.6). Ono and Sugihara (1968) disagreed, suggesting that on the simple model used by Soule the high mobility electrons near the tips of the electron Fermi

surfaces play the dominant part in displacing the calculated Hall coefficient in a negative direction. Only when this effect was reduced both by trigonal warping of the ellipsoidal energy surfaces and also by inclusion of carrier-carrier scattering between majority and minority carriers were they able to explain Soule's positive low temperature Hall coefficient. Later work by Yeoman has confirmed that carrier-carrier scattering is much more important in graphite than ever hitherto suggested.

1.2 Preparation of Pyrolytic Graphite.

Under suitable conditions very pure carbon can be deposited in highly-oriented layers by the pyrolysis of hydrocarbon vapours passed over a heated substrate. Subsequent manipulation of the deposit produces quite large slabs of substantially pure mosaic single crystals, with densities approaching 95% of the theoretical single crystal value.

Methane was used in this laboratory, but acetylene, cyclohexane, and other gases have been used elsewhere. Dilution with hydrogen, nitrogen or a rare gas serves to delay co-precipitation within the deposit of carbon particles nucleated in the gas phase as a fine black, and reduces the re-evaporation of the graphite crystallites which form with a finite distribution of c-axis directions centred about the normal to the substrate surface. Blackman et al. (1961) found that deposition temperatures around 2000°C led to deposits which were

highly ordered in this respect. Crystal orientation improved progressively with increase in deposition temperature up to 2200°C and was brought still closer to ideal graphite by annealing at around 2700°C.

Such a deposition texture leads to an increasing temperature gradient through the thickening deposit normal to the substrate surface if the former is resistance heated because of the low c-axis thermal conductivity. Temperature gradients ofup to 350°C/mm. perpendicular to the deposit surface can be sustained at these high temperatures so that a 2 mm. layer having an external temperature of say 2200°C may be close to 3000°C for the inner layers. Whilst clearly requiring less power for a given maximum temperature than a uniform heating configuration this methcd does lead to a marked radial inhomogeneity in the deposit. Further heat treatment at temperatures above 3000°C leads to increased crystallite size and improved properties but inhomogeneities remain. Samples from the best material of the inner layers are thin and curved. Deposits formed in this way are normally turbostratic and measure about 200 Å along the basal planes of the crystallites. The c-axis distribution at this stage is about 20° wide, but soot particles, 2 to 3μm across, falling on the surface act as nuclei for conical growths which can lead to misorientations of up to 80° for individual crystallites.

Fortunately it was discovered (Moore et al., 1964) that when the inner layers reached about 3700°C (corresponding to deposits about 4 to 5 mm. thick) they distorted parallel to the surface of the substrate and the resulting shear largely eliminated soot nuclei and ripples, leading to an orientation (plane-normal distribution) of less than 1° in width. Sample W3 used in the present work was cut from such highly-annealed inner-layer material.

Commercially produced pyrolytic graphite is usually made by cracking the hydrocarbon gas on to a former heated externally by radiation. Such homogeneous graphite is available in large sizes from High Temperature Materials Inc., and Le Carbone, but as it has not undergone basal shear nor has been treated at high temperatures, it is sooty, of small crystallite size, and not as well aligned as the inner-layer material described above. However, its homogeneity is an advantage as it offers the possibility of further heat treatment: Moore et al. (1964) cut pellets of commercial material, selected to be practically soot inclusion free, and subjected them to temperatures up to 2900°C. in a r.f. inductively-heated graphite die whilst under a unidirectional c-axis presure of 400 atmospheres. The die flowed plastically and allowed basal plane shear to occur. This increased the diameter of the pellets by 15 to 20% and produced samples within 0.1% of the theoretical density of pure graphite (2.266 gm/cm^3), compared with starting material densities as low as 2.04 gm/cm^3. Crystallite c-axes were oriented

within 0.4° on average, but crystallite size along the basal planes was only about 0.1 μm. Subsequent annealing at $3600^{\circ}C$ in a few atmospheres pressure of argon, under slight c-axis constraint to prevent exfoliation, led to no change in density but did reduce the half-width of the angular distribution of c-axes to 0.2°. Layer buckling over distances of the order of millimeters was much greater than this, say 1° depending on the starting material; score marks and other irregularities in the original substrate are not removed by the small shear which takes place on hot-pressing. X-ray work has shown that a slight radial inhomogeneity is present, presumably introduced by interaction of the pellet edges with the surrounding die. However, by this means, crystalline graphite of large c-axis dimensions and with crystallite basal planes some 2 to 3 μm wide has been produced with a spread of c-axis orientation angles small enough to make comparison of its properties with theoretical single crystal models rewarding, even though the basal plane vectors $\underline{a}_1$, $\underline{a}_2$ are still oriented planar-isotropically. Samples W1 and W2 reported here are both cut from pyrolytic graphite hot-pressed and then annealed as described above.

1.3 Texture of Pyrolytic Graphite

Klein (1962) reported in general terms that heating to greater than about $3500^{\circ}C$ was required to eliminate high angle grain boundaries in the as-deposited graphite, but in fact post-deposition heat

treatment has three main effects:

(1) The layer order is increased with increasing temperature;

A useful measure is the probability of stacking disorder p related to c-axis spacing, d, as given by the Bacon-Franklin equation (Franklin, 1951; Bacon, 1958). This drops rapidly towards zero (ideal graphite) for material deposited at successively higher temperatures above 1900°C (Blackman et al 1961).

$$d = 3.44 - 0.086(1-p) - 0.064(1-p)^2$$

A value of less than 0.07 is to be expected for good (not hot-pressed) material, implying less than one layer in 14 is disordered with respect to its neighbours. Spain et al (1967) suggest from electron microscopy that the crystallite dimensions in the c-axis direction were $L_c \sim 1000 \rightarrow 2000$ Å implying $p \sim 0.002$ for well-oriented hot pressed and annealed pyrolytic graphite.

(2) The distribution of preferred orientation decreases markedly in width. It has been pointed out that hot-pressing produces angular distribution half-widths of about 0.2° although layer-plane buckling sometimes leads to deviations of 1° or so over distances of mms.

(3) Crystallite growth occurs in both directions at high temperatures. This is reflected in the value of p, above, for the c-axis direction. In the basal planes Klein estimates from carrier mobility that crystallites have diameters $\gtrsim$ 1 μm after treatment above 3000°C. The approach of the low temperature thermal resistivity to the T^2 specific heat law was calculated by Hooker et al to yield values 2 → 5 μm for basal plane dimensions of the near-ideal material used by Spain et al in general agreement with Klein and the results of electron micrography.

Recrystallised soot nuclei, in orientations differing greatly from their surroundings (Moore et al, 1964) survived in some hot-pressed material. In such materials the differential thermal expansion which occurs on thermal cycling can lead to basal dislocation formation and the production of voids. Accordingly care was taken to select soot-free materials. Even so, sample W1 (Spain's SA22) used in the present work has a very narrow angular c-axis distribution despite the inclusion of some soot particles.

The density of ideal graphite is 2.2654 g/cm^3. With increasing deposition temperature above 1900°C (Blackman et al, 1961) the sample density quickly reaches values close to this. Hot-pressed graphites usually have densities greater than 2.263 ± 0.001 g/cm^3, implying a void concentration of less than 0.1%.

Since the covalent bond strength within basal planes of ~ 5 eV per atom (Kanter, 1957) is many times that between the planes

(~ 0.2 eV per atom) it is not surprising that glide takes place between layer planes and that non-basal glide has not been observed. The most common type of dislocation has its line and Burgers vector both lying within the basal plane. Because of the low stacking fault energy which causes basal glide, dislocations split into two partial dislocations with the region between the partials becoming effectively a ribbon some 600 to 1000 Å wide of rhombohedral material.

Screw dislocations with line and Burgers vectors both in non-basal directions have been observed, but are less common. Thus Hennig (1965) demonstrated 10^6 screws/cm^2 in pyrolytic graphite heated to 3600°C with the screw pitch equal to the layer spacing. Ticonderoga (New York) natural crystals show some screws and growth spirals with a pitch of 450 Å or more (for a review see Roscoe and Thomas, 1966).

Moiré patterns enabled Dawson and Follet (1959) to demonstrate the existence of crystallites of 3000 Å in diameterin material which X-ray line-broadening studies had led to mean estimates of ~ 800 Å. An interpretation of certain Moiré fringes in terms of a type of dislocation having its line in a non-basal direction and Burgers vector in the basal plane is not generally accepted, but the existence and importance of such dislocations in the graphitisation process seems indicated in experiments by Jenkins et al (1962)

on the crystallisation of carbon films at 3000°C.

From electron microscope studies Spain et al (1967) estimate a dislocation content of 10^4 cm per cm^2 basal plane area for the best of their stress-annealed material.

CHAPTER 2

2.1 BAND STRUCTURE

2.1.1 The Structure of Graphite and the Brillouin Zone

Graphite has a hexagonal close-packed structure with four atoms per unit cell (Bernal, 1924). Fig. 2.1 shows the stacking sequence abab.. and the interatomic separations. There are two inequivalent pairs of lattice sites, one (AA') having atoms immediately above and below in nearest planes and the other (BB') having atoms immediately above and below in next nearest planes.

A rhombohedral graphite modification with stacking sequence abc, obtainable by the passage of partial basal plane dislocations, can co-exist with the stable hexagonal form, but does not concern us here.

The first Brillouin-zone is a flat hexagonal cylinder, shown in Figure 2.3.

If we take the origin of the unit cell at an A site then the atomic positions within the unit cell are $\underline{t}_A = 0$, $\underline{t}_B = \frac{1}{3}(\underline{t}_1 - \underline{t}_2)$, $\underline{t}_{A'} = \underline{t}_4/2$, $t_{B'} = -(\underline{t}_1 - \underline{t}_2)/3 + \underline{t}_4/2$ where $\underline{t}_1$, $\underline{t}_2$, $\underline{t}_4$ are the primitive translations for a simple hexagonal Bravais lattice and $t_1 = t_2 = t_3 = 2.46$ Å (a_o) $t_4 = 6.74$ Å (c_o).

The reciprocal lattice vectors $\underline{K}_i$ are obtained from these primitive translation vectors through the definition $\underline{K}_i \cdot \underline{t}_j = 2\pi\delta_{ij}$ $(i,j = 1,2,4)$. This is most conveniently expressed in the form $\underline{\underline{K}} \cdot \underline{\underline{T}} = 2\pi \underline{\underline{I}}$ where the matrices $\underline{\underline{K}}$ and $\underline{\underline{T}}$ are composed of the rectangular cartesian components

of $\underline{K}_1, \underline{K}_2, \underline{K}_4$ and $\underline{t}_1, \underline{t}_2, \underline{t}_4$ and $\underline{\underline{I}}$ is the unit matrix.

$$\underline{\underline{K}} = \begin{bmatrix} K_{1x} & K_{1y} & K_{1z} \\ K_{2x} & K_{2y} & K_{2z} \\ K_{3x} & K_{3y} & K_{3z} \end{bmatrix} \quad \underline{\underline{T}} = \begin{bmatrix} t_{1x} & t_{2x} & t_{3x} \\ t_{1y} & t_{2y} & t_{3y} \\ t_{1z} & t_{2z} & t_{3z} \end{bmatrix} = \begin{bmatrix} \frac{\sqrt{3}ao}{2} & -\frac{\sqrt{3}ao}{2} & 0 \\ \frac{ao}{2} & \frac{ao}{2} & 0 \\ 0 & 0 & Co \end{bmatrix}$$

referred to axes in figure 2.2

For example, the equations for $\underline{K}_1$ are

$$K_{1x}\frac{\sqrt{3}ao}{2} + K_{1y}\frac{ao}{2} + K_{1z}.0 = 2\pi$$

$$-K_{1x}\frac{\sqrt{3}ao}{2} + K_{1y}\frac{ao}{2} + K_{1z}.0 = 0$$

$$K_{1x}.0 + K_{1y}.0 + K_{1z}.Co = 0$$

and these give $K_{1x} = {}^{2\pi}/_{\sqrt{3}ao}$, $K_{1y} = {}^{+2\pi}/_{ao}$, $K_{1z} = 0$

i.e. $\underline{K}_1 = (\frac{2\pi}{\sqrt{3}ao}, +\frac{2\pi}{ao}, 0)$

The power of this way of finding the reciprocal lattice vectors, due to Jones, is that we may now write down all the required components simply by inverting $\underline{\underline{T}}$, for $\underline{\underline{K}} = \underline{\underline{K}}.\underline{\underline{T}}.\underline{\underline{T}}.^{-1} = 2\pi\underline{\underline{I}}\underline{\underline{T}}^{-1} = 2\pi\underline{\underline{T}}.^{-1}$

We find

$$T^{-1} = \begin{bmatrix} \frac{1}{\sqrt{3}ao} & \frac{1}{ao} & 0 \\ -\frac{1}{\sqrt{3}ao} & \frac{1}{ao} & 0 \\ 0 & 0 & \frac{1}{Co} \end{bmatrix}$$

and so the required lattice vectors, referred to the cartesian axes shown in Figure 2.2. are

$$\underline{K}_1 = (\frac{2\pi}{\sqrt{3}ao}, \frac{2\pi}{ao}, 0)$$

$$\underline{K}_2 = (\frac{-2\pi}{\sqrt{3}ao}, \frac{2\pi}{ao}, 0)$$

$$\underline{K}_3 = (0, 0, \frac{2\pi}{Co})$$

FIGURE 2·1

HEXAGONAL LATTICE STRUCTURE OF GRAPHITE

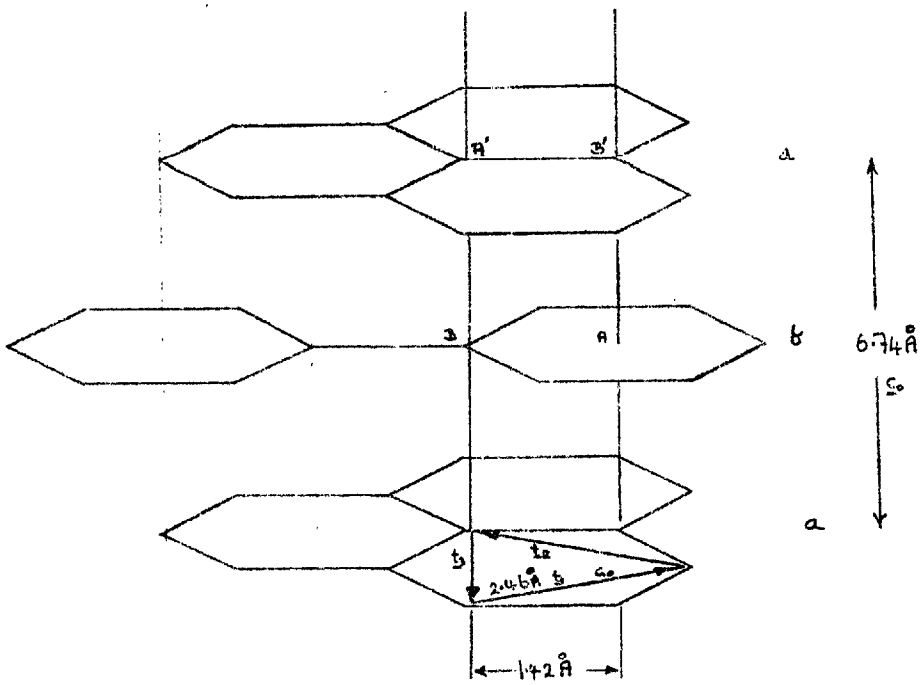

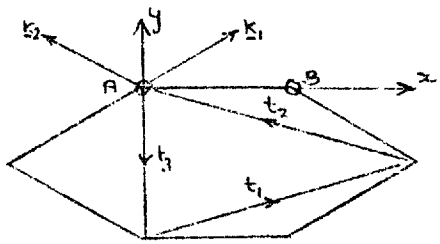

FIGURE 2·2

LATTICE VECTORS

FIGURE 2.3

THE FIRST BRILLOUIN ZONE OF GRAPHITE

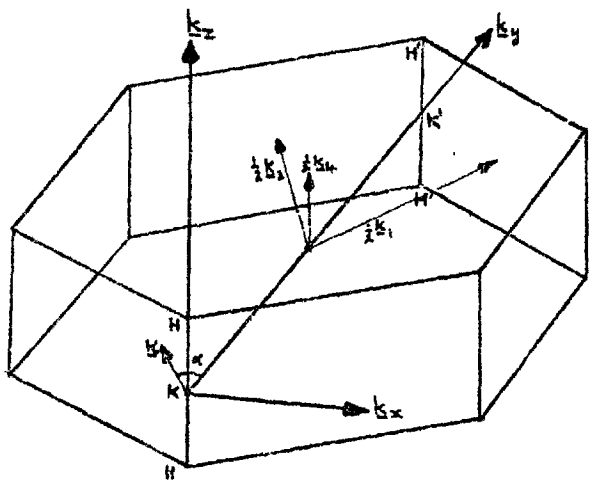

Reciprocal Lattice vectors are shown, together with McClure's notation for the coordinates of a point near a zone edge.

If we now construct planes to bisect the lines joining nearest neighbour reciprocal lattice points we see that all of reciprocal space can be filled by stacking together hexagonal prisms. We take the one arranged symmetrically about the origin to be the first Brillouin Zone, figure 2.3, where we have drawn the half vectors $\frac{\underline{K}_1}{2}$, $\frac{\underline{K}_2}{2}$, $\frac{\underline{K}_4}{2}$ and also included the co-ordinates (K,α) of a point near the vertical zone edge HKH in McClure's notation (which will be employed later).

2.1.2 The Band Structure of Graphite

Early calculations of the graphite band structure were based upon a two-dimensional approximation because the large spacing between layers compared with the atomic spacing within the layers suggested that interplanar interactions might be neglected in a first approximation. In such an approach each layer is, in effect, a covalently-bonded two-dimensional crystal held to the next layer by much weaker Van der Waals forces.

Wallace (1947) constructed trigonally hybridised covalent bonds (sp^2) from three of the valence electrons, forming two σ-bands; he considered the remaining one electron per atom to be in the $2p_z$ state with its symmetry axis perpendicular to the layer planes, forming two π-bands. Considering only nearest-neighbour interactions, he found that the highest occupied (valence) band and the lowest unoccupied (conduction) band were degenerate at the (two-dimensional)zone corners. Later tight-binding calculations by Coulson and Taylor (1952), Lomer (1955), Hove (1955), McClure (1956), Corbato (1956) using different

approximations, agreed qualitatively with Wallace and with each other. The calculations asserted that graphite behaves like a two-dimensional semiconductor with a zero energy gap. It was necessary to invoke surface electrons or impurities to account for electrical and magnetic properties (Haering and Wallace 1957). Also, the model did not allow differing hole and electron masses (Galt, Yager, Dail, 1956).

The $\sigma - \pi$ energy gap was found to be large (Lomer ~ 1ev, Corbato ~ 6ev) at the zone corners so that transport properties are determined by the π-bands only. Coupling between the σ and π bands, though weak (~ 0.01 eV), is important in that it helps determine the sign of one of the parameters (ν_2) in the Slonczewski-Weiss band model in three dimensions (to be described below).

In Wallace's calculations for the three-dimensional case, he considered only the nearest-neighbour interactions between different planes and neglected the difference between A and B atom sites. This led to two bands being degenerate along the vertical zone edge (HKH). All bands were degenerate at the zone corners. Johnston (1955,1956) took more distant neighbours into account which gave a band overlap and anisotropy of the constant energy surfaces in the K_x-K_y plane.

Group theoretical studies were then undertaken to establish which types of structure are possible. The single layer Brillouin zone was

investigated by Lomer (1955) and Slonczewski (1955) and the three-dimensional zone by Carter (1953), Slonczewski (1955), and Slonczewski and Weiss (1955). The latter combined group theory with perturbation theory: previous calculations, reported above, had shown that the interesting part of the Brillouin zone was near the zone edge (not more than 1% of the distance from the edge to the zone centre). Thus, S-W made a Taylor expansion of the Hamiltonian in terms of K_x and K_y. In the K_z direction, however, they made a Fourier expansion which, because of the large layer spacing, was rapidly convergent becoming essentially equivalent to the tight binding approach. They used the "K.P" perturbation method of B.S.W. (1936) to calculate the change in the Hamiltonian for points just off the zone edge. This approach leads to a band model containing six constants which S.W. proposed should be obtained from experiment.

Three later papers contained band calculations based on the 1955 S.W. proposal and in 1958 Sl-Weiss themselves published a full description of their group theoretical perturbation calculation.

McClure (1957) used the S.W. model to interpret the DHVA data of Shoenberg (1952), and Noziere (1958) interpreted the cyclotron resonance data of Galt, Yager and Dail (1956) using a modified form of the S.W. theory. He neglected the difference between A and B atom sites and replaced the hyperbolic bands by parabolic bands. Nozieres justified these approximations for interpretation of cyclotron

resonance data, but pointed out that they lead to a completely false picture of the bands near the hexagonal zone faces. This would be very important for the interpretation of other properties, e.g. diamagnetic susceptibility.

We now describe the Slonczewski-Weiss band model in some detail.

2.1.3 Slonczewski-Weiss Band Model.

The increasing complexity of early band models of graphite compelled an examination of the possible structures from a general point of view. The group theoretical study by Slonczewski and Weiss (SW, 1955, 1958) filled this need and has stood the test of experiment admirably.

The two-dimensional calculations located the carriers in graphite on the BZ corners and three-dimensional calculations all agreed that the Fermi surface must be close to the vertical edges of the zone. In summary, SW found from their symmetry calculations that the wave functions for points on the vertical zone edge can be written in terms of Bloch sums of the single-layer eigenfunctions. Points just off the edge were treated by perturbation theory. They found four bands coming from $2p_z$ orbitals, two of which are degenerate along the zone edge HKH and H'K'H' and on the hexagonal faces, the other two being degenerate only on the hexagonal faces in agreement with Haering's finding that the small representations on the

Conyers

hexagonal faces are 2-dimensional. Band 1 corresponds to the sum of Bloch waves made up from $2p_z$ orbitals on A and A' atoms and is generally the highest in energy. Band 2 corresponds to the difference between these same Bloch functions and is generally the lowest in energy. Bands 31 and 32 are degenerate along the zone edges and are made up from $2p_z$ orbitals based on B, B' atoms.

K.P. Perturbation Method

To explain the basis of this method we follow Callaway (p.173, 1964), but mention that a concise derivation is given by Jones, (p.40, 1960). We start with wave functions $\psi_n(\underline{K},\underline{r})$ for a state in the nth energy band with wave vector $\underline{K}$ and $\psi_j(\underline{K}_o,r)$ for a state in the jth band with wave vector $\underline{K}_o$, and assume there is no degeneracy. Define the functions $\Psi_j(\underline{K},\underline{r}) = e^{i(\underline{K}-\underline{K}_o)\cdot\underline{r}}\psi_j(\underline{K}_o,\underline{r}) = e^{i\underline{S}\cdot\underline{r}}\psi_j(\underline{K}_o,\underline{r})$ (where $\underline{S} = \underline{K} - \underline{K}_o$).

These are satisfactory functions for describing one-electron states since they still have the Bloch form:-

$$\Psi_j(\underline{K},\underline{r}) = e^{i\underline{S}\cdot\underline{r}}\psi_j(\underline{K}_o,\underline{r}) = e^{i\underline{S}\cdot\underline{r}}e^{i\underline{K}_o\cdot\underline{r}}U_j(\underline{K}_o,\underline{r}) = e^{i\underline{K}\cdot\underline{r}}U_j(\underline{K}_o,\underline{r})$$

where $U_j(\underline{K}_o,\underline{r})$ has the required lattice periodicity, since ψ_j is assumed to be in a Bloch form. Also, if the ψ_j form a complete orthonormal set then so do the Ψ_j and any wave function can be expanded

in a linear combination of the latter. In particular, we take;

$$\psi(\underline{K},\underline{r}) = \sum_j A_j(\underline{K})\,\Psi_j(\underline{K},\underline{r}) = e^{i\underline{S}\cdot\underline{r}} \sum_j A_j(\underline{K})\psi_j(\underline{K}_o,\underline{r})$$

Substituting into the Schrödinger equation for the required energy eigenvalues, $E : H\psi(\underline{K},\underline{r}) = E(\underline{K})\psi(\underline{K},\underline{r})$

- where $H = [\frac{1}{2m_o}(\frac{\hbar}{i}\nabla)^2 + V(r)]$

we obtain :- $H[e^{i\underline{S}\cdot\underline{r}} \sum_j A_j\,\psi_j] = E[e^{i\underline{S}\cdot\underline{r}} \sum_j A_j\,\psi_j]$

Now, the operator $(\frac{\hbar}{i}\nabla)^2$ acts on both parts of $e^{i\underline{S}\cdot\underline{r}}\psi_j$ so we have;

$$(\tfrac{\hbar}{i}\nabla)^2 e^{i\underline{S}\cdot\underline{r}}\psi_j = [\tfrac{\hbar}{i}\tfrac{\partial}{\partial x}(\tfrac{\hbar}{i}\tfrac{\partial}{\partial x} e^{i\underline{S}\cdot\underline{r}}\psi_j) + .. + ..]$$

$$= [\tfrac{\hbar}{i}\tfrac{\partial}{\partial x}(\tfrac{\hbar}{i} e^{i\underline{S}\cdot\underline{r}}\tfrac{\partial}{\partial x}\psi_j + \tfrac{\hbar}{i}iS_x e^{i\underline{S}\cdot\underline{r}}\psi_j) + .. + ..]$$

$$= (\tfrac{\hbar}{i})^2[e^{i\underline{S}\cdot\underline{r}}\nabla^2 + 2i\,e^{i\underline{S}\cdot\underline{r}}\,\underline{S}\cdot\nabla - e^{i\underline{S}\cdot\underline{r}}S^2]\psi_j$$

Thus, operating with H in the Schrödinger equation:-

$$e^{i\underline{S}\cdot\underline{r}}\sum_j E_j A_j\psi_j - i\tfrac{\hbar}{m_o}^2 e^{i\underline{S}\cdot\underline{r}}\,\underline{S}\cdot\nabla \sum_j A_j\psi_j + \tfrac{\hbar}{2m_o}^2 e^{i\underline{S}\cdot\underline{r}}S^2\Sigma A_j\psi_j = e^{i\underline{S}\cdot\underline{r}}E_n\sum_j A_j\psi_j$$

Multiplying by $e^{-i\underline{S}\cdot\underline{r}}\psi_i^*$ and integrating over the normalisation volume for the ψ_j :

$$E_iA_i - EA_i + \frac{\hbar^2S^2}{2m_o}A_i + \frac{\hbar}{m_o}\underline{S}\cdot\underline{\Sigma}_j P_{ij}A_j = 0 \quad \text{where } \underline{P}_{ij} = \int\psi_i^*(\tfrac{\hbar}{i}\nabla)\psi_j dt$$

Similarly, we may multiply by all other $e^{-i\underline{S}\cdot\underline{r}}\psi_i^*$ to generate further equations, obtaining a set of linear simultaneous equations for the coefficients A_i. For a non-trivial solution the determinant of the matrix of the coefficients of A_i must be zero, which leads to the usual polynomial in E :

The general element of this matrix is

$$M_{ij} = \frac{\hbar}{m_o}\underline{S}\cdot\underline{P}_{ij} + (E_i - E + \frac{\hbar^2S^2}{m_o})\delta_{ij}$$

which we write as $H_{ij} - E(K)\delta_{ij}$

where $H_{ij} = (E_i(\underline{K}_o) + \frac{\hbar^2S^2}{2m_o})\delta_{ij} + \frac{\hbar}{m_o}\underline{S}\cdot\underline{P}_{ij}$

Thus, we have the condition that $|H_{ij} - E\delta_{ij}| = 0$ and with this form of the equations we see that the required energy levels E at $\underline{K}$ (a distance $\underline{S}$ from $\underline{K}_o$) are given as the eigenvalues of the Hamiltonian H_{ij} in terms of the eigenvalues $E_i(\underline{K}_o)$ at K_o. Notice that if $\underline{S} = 0$ then $H_{ij} = E_i\delta_{ij}$ and the values of E are simply the $E_i(\underline{K}_o)$ at $\underline{K}_o$.

In the present case, we want to discover the effect on the energy levels of a very small change in ($\frac{|\underline{S}|}{|K_o|} \sim 1\%$) so we appeal to perturbation theory for a further simplification.

Second order perturbation theory gives an expression for the new energy levels in terms of the matrix elements of a perturbing Hamiltonian, H' (Schiff p.153).

$$E_n = E_n^o + H'_{nn} + \sum_{j \neq n} \frac{H'_{nj} H'_{jn}}{E_n^o - E_j}$$

- where E^o is an unperturbed level, belonging to the wave vector K_o in our case. Thus, we have finally :-

$$E_n(\underline{K}) = E_n(\underline{K}_o) + \frac{\hbar^2 S^2}{2m_o} + \frac{\hbar}{m_o} \underline{S}.\underline{P}_{nn} + \frac{\hbar^2}{m_o^2} \sum_{j \neq n} \frac{(\underline{S}.\underline{P}_{nj})(\underline{S}.\underline{P}_{jn})}{E_n(\underline{K}_o) - E_j(\underline{K}_o)}$$

- which is the required expansion of the energy in terms of $\underline{S}$.

The Hamiltonian Matrix

We shall now indicate how SW proceeded to derive their Hamiltonian for states near the vertical zone edges and relate this to McClure's Hamiltonian (1957) which is often used as a starting point for discussions relating to the SW band model. No attempt will be made to give a complete group-theoretical background to the derivation of the appropriate wave-funotions.

First of all Slonczewski and Weiss considered the single-layer wave functions, U, satisfying the Bloch condition (imposed by translational symmetry) and having the local symmetry of the zone edge. By applying the $\underline{K}.\underline{P}$ perturbation to the single-layer Hamiltonian they arrived at a secular equation giving energy values which varied linearly with $\underline{K}$, the distance from the zone edge HKH (see Figure 2.3).

The three-dimensional lattice has four atoms per unit cell, twice as many as in the single layer unit cell, so each layer state must give rise to two three-dimensional states. In particular, each of the layer π states, U_1, U_2 gives rise to two wave functions, ψ at $\underline{K}_S$ where S labels a general point on the vertical zone edge HKH. These ψ's can be constructed from single-layer functions but they must have the required symmetry at $\underline{K}_S$. The four wave functions are

$$\left.\begin{aligned} \psi_1 &= \tfrac{1}{\sqrt{2}}(a+a') \\ \psi_2 &= \tfrac{1}{\sqrt{2}}(a-a') \\ \psi_{31} &= b' \\ \psi_{32} &= b \end{aligned}\right\} \text{ where } \qquad \begin{aligned} a &= \sum_S e^{icK_zS}\{\varepsilon|S\underline{t}_4\}U_2 \\ b &= \sum_S e^{icK_zS}\{\varepsilon|S\underline{t}_4\}U_1 \\ a' &= \sum_S e^{icK_z(S+\frac{1}{2})}\{\rho_3|S+\tfrac{1}{2})\underline{t}_4\}U_2 \\ b' &= \sum_S e^{icK_z(S+\frac{1}{2})}\{\rho_3|(S+\tfrac{1}{2})\underline{t}_4\}U_1 \end{aligned}$$

This notation indicates the nature of the ψ's ; for example, if the function a were written as a linear combination of atomic orbitals, only those located on type A atoms would occur. Similarly for the a', b, b' functions and A', B, B'-type atoms respectively.

The symbols $\{\alpha|\underline{t}\}$ occurring in the above expressions are symmetry operators with the meaning $\{\alpha|\underline{t}\}f(\underline{r})=\alpha f(\underline{r}) + \underline{t}$ where $f(\underline{r})$ is a function of position $\underline{r}$, α is a point group operator (e.g. a rotation) and $\underline{t}$ is a translation vector. Thus, the $\{\varepsilon|S\underline{t}_4\}$ in ψ_{32} simply means

that U_1 is to be displaced through the translation $\underline{t}_4$ (on to the next-but-one layer) each time a new term is added to the sum over S. (ε stands for the identity operation, ρ_3 is a reflection in the $\underline{t}_4$-$\underline{t}_3$ plane). We note that the above wave functions are approximate in that overlap energies between layers and $\sigma - \pi$ band interaction energies have been neglected.

The way in which the energies $E_i(\underline{K}_z)$ of the above states vary with $\underline{K}_z$ is not given by group theory and appeal must be made to tight-binding approximations and experiment for this information. However, the change in energy levels as the wave vector $\underline{K}$ moves a short distance $\underline{K}$ away from the vertical zone edge at $\underline{K}_S$ can be obtained using the $\underline{K}.\underline{P}$ perturbation method; the new set of energy levels is obtained by diagonalising the matrix of the perturbed Hamiltonian $H = H_o + H'$, where $H' = \frac{\hbar}{m}\underline{K}.\underline{P} + \frac{\hbar^2K^2}{2m}$ and H_o has the eigenfunctions $\phi_1, \phi_2, \phi_{31}, \phi_{32}$ with corresponding eigenvalues E_1^o, E_2^o, E_3^o. Group theory gave the momentum matrix elements $\underline{P}_{ij}$ apart from a constant factor.

SW obtained a Hamiltonian matrix given below with respect to the orthogonal set of wave functions b, a, a', b' . The element H_{aa} in the matrix below, for instance is given by $H_{aa} = \int a(H_o+H')a\,d\tau$ which quickly reduces to

$$H_{aa} = \int a H_o a\,d\tau + \int a \frac{\hbar^2 K^2}{2m} a\,d\tau + \int a \frac{\hbar}{m} \underline{K}\cdot\underline{P}\, a\,d\tau$$

$$= \tfrac{1}{2}(E_1^o + E_2^o) + \frac{\hbar^2 K^2}{2m} + \int a \frac{\hbar \underline{K}\cdot\underline{P}}{m} a\,d\tau$$

---

	b	a	a'	b'
b	E_3^o+F	$-D(1+r)$	PD	qD^*
a*	$-D^*(1+r^*)$	$\frac{1}{2}(E_1^o+E_2^o)+F$	$\frac{1}{2}(E_1^o-E_2^o)$	P^*D
a'	P^*D^*	$\frac{1}{2}(E_1^o-E_2^o)$	$\frac{1}{2}(E_1^o+E_2^o)+F$	$-D(1+r^*)$
b'	qD	PD^*	$-D^*(1+r)$	E_3^o+F

In the above, $F = \hbar^2K^2/2m$ and $D = (\hbar P_o/m)Ke^{i\alpha}$ - this comes from the momentum matrix $\underline{P}$. The P, q, r are functions of $\underline{K}_z$. One could diagonalise this matrix to obtain the required energy levels, but we prefer to switch to McClure's notation in order to pursue our investigation of the band structure. Unfortunately, McClure quotes but does not derive a Hamiltonian matrix (see below) which is different

in form from the one given above. It is evident, in fact, that he has used a different set of basis functions to generate his matrix. To give the same eigenvalues, his matrix must be related through a unitary transformation to the SW matrix above and this implies that his basis functions are linear combinations of the a, a', b, b' . In fact, it is fairly obvious that he has used the actual ψ's above (ψ_1, ψ_2, ψ_{31}, ψ_{32}) as his basis. We proceed to demonstrate this :

We have $\psi_1 = \frac{1}{\sqrt{2}}(a+a')$, $\psi_2 = \frac{1}{\sqrt{2}}(a-a')$, $\psi_{31} = b'$, $\psi_{32} = b$.

Now, if our assumption is correct, McClure's Hamiltonian matrix elements are given by

$$H_{ij}^{Mc} = \int \psi_i H \psi_j d\tau$$ where i, j stand for the labels on the ψ's ((1), (2), (31) etc.).

Substituting for the ψ's :-

$$H_{1,1}^{Mc} = \int \frac{1}{\sqrt{2}}(a+a')H\frac{1}{\sqrt{2}}(a+a')d\tau = \tfrac{1}{2}\int aHad\tau + \tfrac{1}{2}\int aHa'd\tau + \tfrac{1}{2}\int a' Had\tau + \tfrac{1}{2}\int a' Ha'd\tau$$

$$= \tfrac{1}{2}(H_{aa} + H_{aa'} + H_{a'a} + H_{a'a'})$$

where H_{ij} is the ijth element of the SW Hamiltonian matrix.

Thus we see that it is not necessary to recalculate the matrix elements; it is sufficient to take combinations of elements from the SW Hamiltonian to generate the matrix with respect to the new basis

functions. We now list the required combinations

$$H_{1,1} = \tfrac{1}{2}(H_{aa} + H_{aa'} + H_{a'a} + H_{a'a'}) = E_1^o + F$$

$$H_{1,2} = \tfrac{1}{2}(H_{aa} + H_{a'a} - H_{aa'} - H_{a'a'}) = 0$$

$$H_{1,31} = \frac{1}{\sqrt{2}}(H_{ab'} + H_{a'b'}) = P^*D - D(1+r^*)$$

$$H_{1,32} = \frac{1}{\sqrt{2}}(H_{ab} + H_{a'b}) = P^*D^* - D^*(1+r^*)$$

$$H_{2,1} = \tfrac{1}{2}(H_{aa} + H_{aa'} - H_{a'a} - H_{a'a'}) = 0$$

$$H_{2,2} = \tfrac{1}{2}(H_{aa} - H_{aa'} - H_{a'a} + H_{a'a'}) = E_2^o + F$$

$$H_{2,31} = \frac{1}{\sqrt{2}}(H_{ab'} - H_{a'b'}) = P^*D + D(1+r^*)$$

$$H_{2,32} = \frac{1}{\sqrt{2}}(H_{ab} - H_{a'b}) = -(P^*D^* + D^*(1+r^*))$$

$$H_{31,1} = \frac{1}{\sqrt{2}}(H_{b'a} + H_{b'a'}) = PD^* - D^*(1+r)$$

$$H_{31,2} = \frac{1}{\sqrt{2}}(H_{b'a} - H_{b'a'}) = PD^* + D^*(1+r)$$

$$H_{31,31} = H_{b'b'} = E_3^o + F$$

$$H_{31,32} = H_{b'b} = qD$$

$$H_{32,1} = \frac{1}{\sqrt{2}}(H_{ba} + H_{ba'}) = PD - D(1+r)$$

$$H_{32,2} = \frac{1}{\sqrt{2}}(H_{ba} - H_{ba'}) = -(PD + D(1+r))$$

$$H_{32,31} = H_{bb'} = qD^*$$

$$H_{32,32} = H_{bb} = E_3^o + F$$

This leads to the following matrix which can be directly compared, term by term, with McClure's (neglecting the second order in K term, F, and assuming r, P are real.

$$H = \begin{bmatrix} E_1^o & 0 & (PD-D(1+r) & (PD-D(1+r))^* \\ 0 & E_2^o & (PD+D(1+r)) & -(PD+D(1+r))^* \\ (PD-D(1+r))^* & (PD+D(1+r))^* & E_3^o & qD \\ (PD-D(1+r)) & -(PD+D(1+r)) & qD^* & E_3^o \end{bmatrix}$$

From this point on we use McClure's notation (Figure 2.3) and the set of dimensionless cylindrical variables defined by:

$$\alpha = \tan_{GM}^{-1}\left(\frac{-K_x}{K_y}\right), \quad \sigma = \tfrac{1}{2}\sqrt{3}\, a_o |K|, \quad \zeta = K_z C_o$$

where, as shown in the figure (2.3) K is the perpendicular distance of a point $\underline{K}$ in the B.Z. from a vertical zone edge.

The Hamiltonian matrix given by McClure is

$$H = \begin{bmatrix} E_1^o & 0 & H_{13} & H_{13}^* \\ 0 & E_2^o & H_{23} & -H_{23}^* \\ H_{13}^* & H_{23}^* & E_3^o & H_{33} \\ H_{13} & -H_{23} & H_{33}^* & E_3^o \end{bmatrix}$$

which, we have seen, follows directly from Slonczewski's work, where

$$E_1^o = \Delta + \gamma_1 \Gamma + \tfrac{1}{2}\nu_5 \Gamma^2$$

$$E_2^o = \Delta - \gamma_1 \Gamma + \tfrac{1}{2}\gamma_5 \Gamma^2$$

$$E_3^o = \tfrac{1}{2}\nu_2 \Gamma^2$$

$$H_{13} = 2^{-\frac{1}{2}}(-\gamma_o + \gamma_4 \Gamma)\, \sigma \exp(i\alpha) \quad \text{and} \quad \Gamma = 2\cos(\tfrac{1}{2}K_z C_o)$$

$$H_{23} = 2^{-\frac{1}{2}}(\gamma_o + \gamma_4 \Gamma)\, \sigma \exp(i\alpha)$$

$$H_{33} = \gamma_3 \Gamma \sigma \exp i\alpha$$

It is clear that to first order in σ (second order does not change the form of the Hamiltonian) and to second order in the Fourier expansion the band structure can be completely described by six

parameters. S.W. did not attempt to derive these parameters from theory but proposed they be obtained from experiment; some of them may be negligible in a given application. We have neglected spin orbit effects at this stage as these have beer shown to be very small (G. Dresselhaus and M.S. Dresselhaus 1965), but of course each of the four bands obtained from this Hamiltonian is two-fold spin degenerate.

The secular equation for the above Hamiltonian matrix leads to an unwieldy quartic equation in energy which it is uninstructive to examine. Certain restrictions, however, lead to factorisation into two quadratics.

Multiplying out the secular determinant $|H - EI| = 0$ where I is the unit matrix, leads to the expression

$$\varepsilon_1\varepsilon_2\varepsilon_3^2 - \varepsilon_1\varepsilon_2\gamma_3^2\Gamma^2\sigma^2 - \varepsilon_1\varepsilon_3(\gamma_o+\gamma_4\Gamma)^2\sigma^2 - \varepsilon_2\varepsilon_3(-\gamma_o+\gamma_4\Gamma)^2\sigma^2$$
$$+ (\gamma_o+\gamma_4\Gamma)^2(-\gamma_o+\gamma_4\Gamma)^2\sigma^4 - \varepsilon_1\sigma^3\gamma_3\Gamma(\gamma_o+\gamma_4\Gamma)^2\cos 3\alpha$$
$$+ \varepsilon_2\sigma^3\gamma_3\Gamma(-\gamma_o+\gamma_4\Gamma)^2\cos 3\alpha = 0$$

where $\varepsilon_1 = E_1^o - E$, $\varepsilon_2 = E_2^o - E$, $\varepsilon_3 = E_3^o - E$. This is the equation which must be solved for the energy, E. A numerical solution is possible, but more physical insight is gained by examining approximate solutions. For instance, neglecting γ_3 leads to :-

$$\varepsilon_1\varepsilon_2\varepsilon_3^2 - \varepsilon_1\varepsilon_3(\gamma_o+\gamma_4\Gamma)^2\sigma^2 - \varepsilon_2\varepsilon_3(-\gamma_o+\gamma_4\Gamma)^2\sigma^2 + (\gamma_o+\gamma_4\Gamma)^2(-\gamma_o+\gamma_4\Gamma)^2\sigma^4$$
$$= 0$$

Which factorises into

$$(\varepsilon_1\varepsilon_3 - (-\gamma_o+\gamma_4\Gamma)^2\sigma^2)(\varepsilon_2\varepsilon_3 - (\gamma_o+\gamma_4\Gamma)^2\sigma^2) = 0$$

Leading to solutions which are independent of angle α :

$$\begin{aligned} E_{1,31} &= \tfrac{1}{2}(E_1^o+E_3^o) \pm [\tfrac{1}{4}(E_1^o-E_3^o)^2 + (\gamma_o-\gamma_4\Gamma)^2\sigma^2]^{\frac{1}{2}} \\ E_{2,32} &= \tfrac{1}{2}(E_2^o+E_3^o) \pm [\tfrac{1}{4}(E_2^o-E_3^o)^2 + (\gamma_o+\gamma_4\Gamma)^2\sigma^2]^{\frac{1}{2}} \end{aligned} \qquad (2)$$

Now, the reciprocal effective mass tensor is defined by

$$R_{ij}^{*} = \frac{1}{\hbar^2}\frac{\partial^2 E}{\partial K_i \partial K_j}$$

Thus,

$$R_{xx}^{*} = \pm \frac{1}{\hbar^2}\frac{\partial}{\partial K_x}\left[(\tfrac{1}{2}\tfrac{3}{4}a_o^2)(\gamma_o-\gamma_4\Gamma)^2 2K_x\left(\left(\frac{\Delta E^o}{2}\right)^2 + (\gamma_o-\gamma_4\Gamma)^2\sigma^2\right)^{\frac{1}{2}}\right]$$

$$= \pm \frac{1}{\hbar^2}(\gamma_o-\gamma_4\Gamma)^2 \tfrac{3}{4}a_o^2\left[\left(\frac{\Delta E^o}{2}\right)^2 + (\gamma_o-\gamma_4\Gamma)^2 \tfrac{3}{4}a_o^2 K_y^2\right] / \left[\left(\frac{\Delta E^o}{2}\right)^2 + (\gamma_o-\gamma_4\Gamma)^2\sigma^2\right]^{\frac{3}{2}}$$

where $\Delta E^o = E_1^o - E_3^o$ or $E_2^o - E_3^o$ depending on which surface the mass tensor is evaluated. The upper sign refers to the upper of two conjugate hyperboloids. For R_{yy}^{*}, K_y^2 should be replaced by K_x^2. For R_{xy}^{*} the term ΔE^o does not appear in the numerator, K_y^2 is replaced by $K_x K_y$ and the signs are written $\mp$:

We see that the effective mass depends on K_z (through Γ and ΔE^o), and also on the distance σ from the zone edge. However, for small enough σ one obtains paraboloidal bands and constant effective mass for a given value of K_z :-

$$R^*_{xx} = R^*_{yy} \simeq \pm \frac{3(\gamma_o - \gamma_4 \Gamma)^2 a_o^2}{2\hbar^2 \Delta E^o}$$

$$R^*_{xy} = 0$$

Inverting this tensor to give the effective mass tensor ;

$$M^*_{ij} = (R^{*-1})_{ij} = \frac{(\text{adj } R)_{ij}}{|R|}$$

leads to $m^* = \begin{bmatrix} \frac{1}{R^*_{xx}} & 0 & 0 \\ 0 & \frac{1}{R^*_{xx}} & 0 \\ 0 & 0 & \frac{1}{R^*_{zz}} \end{bmatrix}$ where we have invoked crystal symmetry (6/mm) to give $R_{iz} = R_{zi} = 0$ (where i = x,y). [See Birss, 1964]. Finally, then, we have an effective mass for directions parallel to the basal plane :

$$1/m^*_a(K_z) = \pm \frac{3(\gamma_o - \gamma_4 \Gamma)^2 a_o^2}{2\hbar^2 \Delta E^o}$$

The energy-wave number relationships for these four bands are quite complicated surfaces which can be envisaged by examination of figure 2.4.

Here an attempt has been made to indicate the variation of the bands with small excursions from the K_z axis (HKH) because this is all-important in determining where electrons and holes can exist. However, before examining this question further, we shall list the parameters defining the energy surfaces shown, indicating their main effects and where they arise in the theory. The latest values assigned by Dresselhams and Maveroides (1964) are quoted here, but are not completely independent of the method by which they were measured so various earlier experimental determinations will be discussed later.

γ_0. This is the same as Wallace's γ_0 and is most important in determining the dependence of energy on σ (i.e. $|K|$). It is the only parameter in the single-layer case and represents overlap between wave functions centred on nearest neighbour A and B atoms. (2.8eV).

γ_1. Represents the main splitting of the singly-degenerate bands caused by the interlayer interaction between wave functions on nearest A atoms. (0.39eV).

γ_2. Determines the amplitude of the variation of the E_3 bands with K_z and so is responsible for the band overlap. It arises from both the next-nearest layer interaction between B atoms and from $\sigma - \pi$ coupling, but these two effects almost cancel. It is now thought that γ_2 is + ve. (+ 0.016eV).

γ_3. Arising from nearest layer interactions, this gives rise to anisotropy in the xy plane and to extra degeneracies found by Johnston (see below). Wallace neglected this term although it appeared in his Hamiltonian. (0.15eV).

γ_4. Although this does not have a qualitative effect on the band structure, it could give rise to appreciable (10% or so) quantitative effects. It would be the same as γ_3 if the orbitals on A and B atoms were identical and was assumed to be $\simeq \gamma_3$ in the absence of experimental evidence. However, Dress. and Mavr. estimate $\gamma_4 = -0.20$eV.

γ_5. This is essentially the coefficient of the second term in the Fourier expansion along K_z and is often neglected. In the absence of an experimental value, it is assumed to be $\simeq \gamma_2$ (0.016eV).

Δ Reflects the fact that A and B atomic sites are situated in different crystalline fields and also involves next-nearest layer overlap integrals. It causes a separation in the two sets of levels at $K_z = \pm \pi/c_o$. (-0.02eV).

In practice, one cannot assume that the sample is entirely free from impurities so the Fermi level (somewhere between 0 and $2\gamma_2$) must be regarded as another unknown parameter. However, on the assumption of pure graphite (equal numbers of electrons and holes) Dresselhans and Mavroides have calculated $E_f \simeq 0.019eV$.

One must now decide where in the Brillouin Zone the holes and electrons must lie with these values of the band parameters. We still neglect γ_3. By writing equations 2.1.3(2) for small values of σ it is easy to see that the variations of the energy levels with σ are as indicated in figure 2.3. For instance, the E_1 level increases in energy with a small excursion from the zone edge (a small increase in σ) at constant K_z near $K_z \simeq$ zero but decreases in energy for a similar excursion made near $K_z = \pm \pi/c_o$. It is not so obvious at first sight where the change-over in behaviour takes place. We examine E_1 first and then ε_3 :

From 2.1.3(2) for small σ :

$$E_{1'} \simeq \tfrac{1}{2}(E_1^o+E_3^o) + \frac{(E_1^o-E_3^o)}{2}\left[1 + \tfrac{1}{2}\,4\frac{(\gamma_o-\gamma_4\Gamma)^2}{(E_1^o-E_3^o)}\sigma^2\right]$$

$$= E_1^o\left[1 + \frac{(\gamma_o-\gamma_4\Gamma)^2\,\sigma^2}{E_1^o(E_1^o-E_3^o)}\right]$$

Now, the σ-variation changes its nature (towards or away from the K_z-axis) when the slope of this linear relation between E_1 and σ^2

. . .

changes sign. Notice the constant inside the bracket has been made independent of K_z. Thus, the σ-variation changes its nature when $E_1^o(E_1^o - E_3^o) = 0$ i.e. $E_1^o = 0$ or $E_1^o = E_3^o$. So, as K_z is increased from zero, where E_1 increases positively away from the K_z-axis with a small σ-excursion, towards π/c_o, the E_1 behaviour will change where E_1^o crosses E_3^o and so beyond here E_1 will decrease (towards the K_z-axis) with increase in σ. At $E_1^o = 0$ the nature again changes so E_1 will once more increase away from the axis with small increase in σ, but its sign also changes here so this represents a continuation of previous behaviour, viz. a downward change in E_1 with σ. Thus, E_1 changes its σ-variation from an increase in E with σ to a decrease in E with σ as K_z is increased through the value where E_1^o and E_3^o intersect.

Similarly for E_3 :

$$E_{31} \simeq E_3^o - \frac{\frac{1}{4}(\gamma_o - \gamma_4\Gamma)^2\sigma^2}{(E_1^o - E_3)^2}$$

$$= E_3^o\left[1 - \frac{1}{4}\left(\frac{\gamma_o - \gamma_4\Gamma)^2\sigma^2}{E_3^o(E_1^o - E_3^o)^2}\right]\right.$$

So we see E_{31} changes its nature from E - increasing at $K_z = 0$ (easily verified) to E - decreasing with small excusions of σ as K_z makes $E_1^o - E_3^o$ change sign, i.e. as K_z increases through the point of intersection of E_1^o and E_3^o.

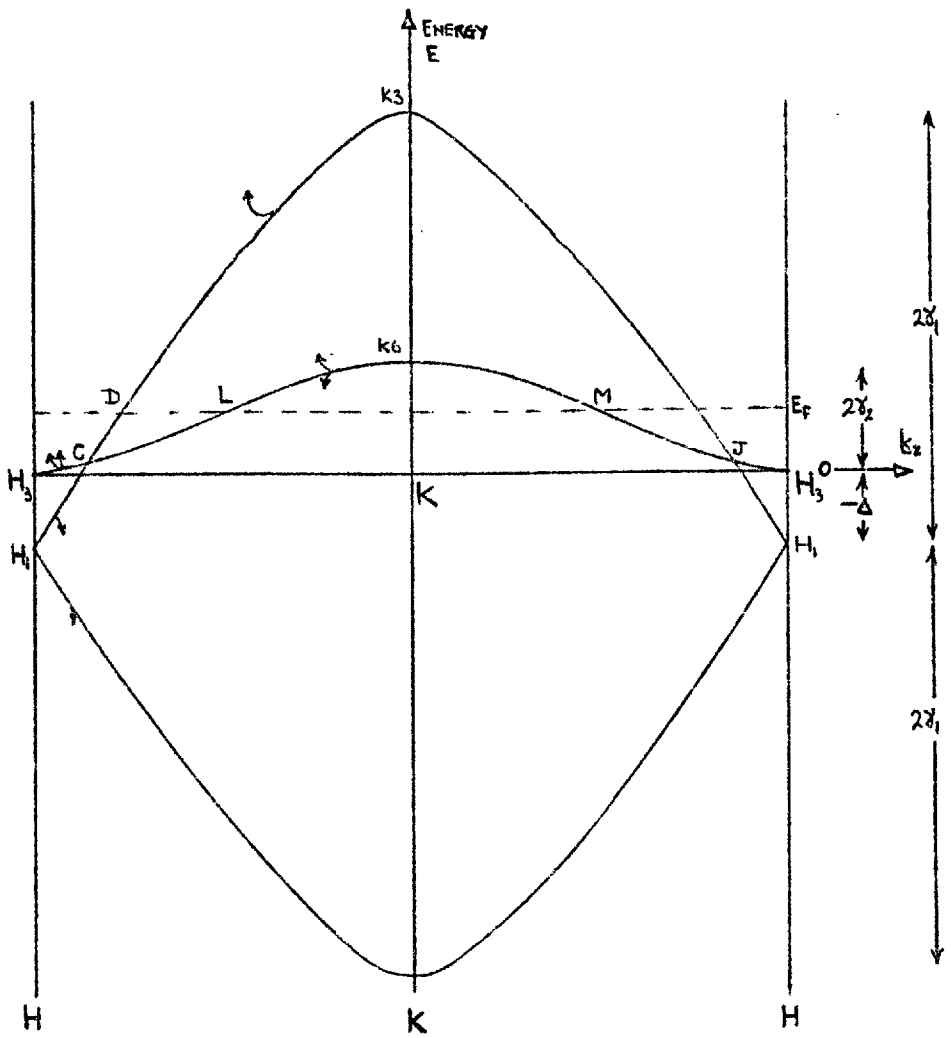

FIGURE 2.4

ENERGY BANDS ALONG A ZONE EDGE HKH. Energy increases and decreases a short distance from the edge are indicated by arrows.

E_{32} remains E-decreasing over the whole range $-\pi/c_o \leq K_z \leq \pi/c_o$.

We can now see that the curve $H_3CK_6JH_3$ represents the bottom of the conduction band and $H_1CK_6JH_1$ the top of the valence band. With the Fermi level as shown we have holes in the central region below LK_6M and electrons above the two end curves H_3CL, MJH_3 :

This is clear if we note the following properties of the bands. The effective mass tensor has only diagonal components m^*_{ii} for small enough σ and these have the same sign as the corresponding reciprocal mass tensor components R^*_{ii}. Now, by differentiating the expressions for the energy levels, E_i, twice with respect to the components of $\underline{K}$ (as we have demonstrated above in the case of $\frac{\partial^2}{\partial K_x \partial K_x}$) and also differentiating once with respect to σ, we can see that the sign of $\frac{\partial E}{\partial \sigma}$ is the same as that of R^*_{xx} $(=R^*_{yy})$. Thus, we have finally that the sign of $\frac{\partial E}{\partial \sigma}$ is the same as the sign of m^*_{xx} $(= m^*_{yy})$ and so the σ-variation of a particular band indicates the electron or hole nature of the band; + ve means the band is electronic in nature at the given value of $\underline{K}_z$. This arises from the particular form of the bands near to the vertical zone edge. We see immediately that holes are located on the E_3 surface below the line LK_6M, which is the cross-section taken where the band reaches its highest point. A complication arises near the point C, however, where the bands E_1 and E_3 are degenerate. Group theory does not require more than the two-fold E_{31}-E_{32} degeneracy at

this point on the zone edge so we have a case of so-called "accidental" degeneracy. To examine the probable consequences, it is convenient first to lift the degeneracy of the E_3 band by means of spin-orbit coupling. This effect is small, but enables one to draw E_{31}, E_{32} separately and thus see what is happening. We now have the situation shown in Figure 2.5A.

However, the interaction between these bands at this point will cause the wave-functions to mix and prevent their crossing (see Slater, Vol. II, p.270, 1967), leading to a situation shown in Figure 2.5B.

Putting in the σ-variation of energy in the usual way enables us to see immediately that there are two energy surfaces which can give rise to electron behaviour near the Fermi energy, LCH_3 and the new one DCH_3 which gives rise to a pocket of electrons. Indeed, in the presence of spin-orbit coupling, when the H_3 band splits all the way to the hexagonal zone face, the pocket is completely isolated. The Fermi surface is illustrated in Figure 2.6 for the case with no spin-orbit coupling where the pockets may be translated by the reciprocal lattice vector $\underline{K}_4$ to join on to the ends of the electron surfaces. This join is perfectly smooth because of time reversal degeneracy on the horizontal zone faces (McClure, IBM, 8, 258, 1964).

The inclusion of the γ_3 in the Hamiltonian leads to the additional structure shown in Figures 2.6 and 2.7), destroying the rotational symmetry of the energy bands so far considered. Although it is

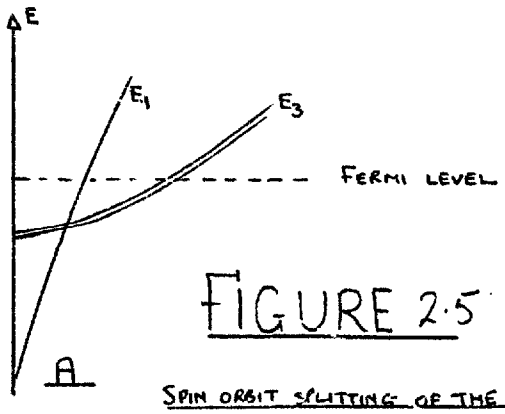

FIGURE 2·5

SPIN ORBIT SPLITTING OF THE BANDS NEAR A ZONE FACE

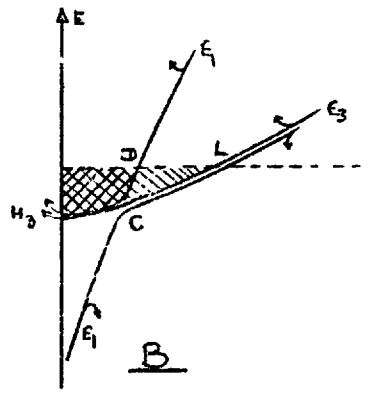

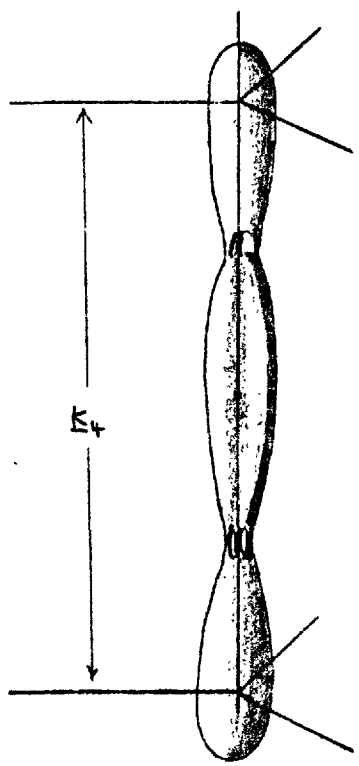

FIGURE 2·6

FERMI SURFACE WITH NO SPIN-ORBIT COUPLING

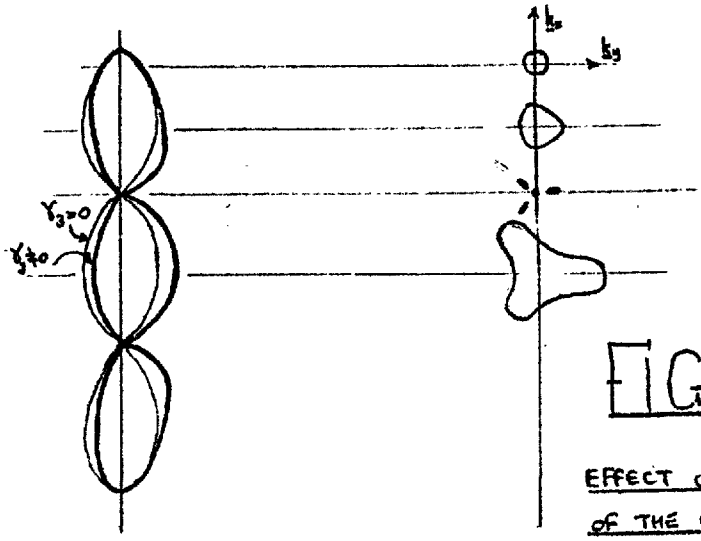

FIGURE 2.7

EFFECT OF γ_3 ON THE SHAPE OF THE FERMI SURFACE.

no longer possible to factor the secular equation for general values of α, σ, this is possible for special values of α ($=\frac{1}{3}n\pi$).

Equation 2.1.3(1) reduces to that expression with $\cos 3\alpha = (-1)^n$ which immediately factorises into two quadratics;

$$(\varepsilon_1\varepsilon_3+\varepsilon_1\nu_3\Gamma\sigma(-1)^n - (-\nu_0+\nu_4\Gamma)^2\sigma^2)(\varepsilon_2\varepsilon_3-\varepsilon_2\nu_3\Gamma\sigma(-1)^n - (\nu_0+\gamma_4\Gamma)^2\sigma^2) = 0$$

Substituting for ε_1, ε_2, ε_3 gives two quadratics in E which can be solved, leading finally to the solutions:

$$E_{1,31} = \tfrac{1}{2}(E_1^o+E_3^o+\gamma_3\Gamma\sigma\cos 3\alpha)\pm[\tfrac{1}{4}(E_1^o-E_3^o-\gamma_3\Gamma\sigma\cos 3\alpha)^2+(\gamma_o-\gamma_4\Gamma)^2\sigma^2]^{\frac{1}{2}} \qquad (3)$$

$$E_{2,32} = \tfrac{1}{2}(E_2^o+E_3^o-\gamma_3\Gamma\sigma\cos 3\alpha)\pm[\tfrac{1}{4}(E_2^o-E_3^o+\nu_3\Gamma\sigma\cos 3\alpha)^2+(\nu_o+\gamma_4\Gamma)^2\sigma^2]^{\frac{1}{2}}$$

$(\alpha = \frac{1}{3}n\pi)$

These equations can be used to obtain the cross-section of the Fermi-Surface in the K_z–K_y plane ($\alpha = 0$) for, putting $\alpha = 0$, $E = E_f$ we have, for example:

$$(\nu_o-\nu_4\Gamma)^2 = E_f^2 + E_1^oE_3^o - E_f(E_1^o + E_3^o + \nu_3\Gamma\sigma) + E_1^o\gamma_3\Gamma\sigma$$

– which gives σ in terms of K_z (contained in Γ). Putting $\alpha = 3x\frac{\pi}{3}$ leads to the same equation with the sign attached to γ_3 changed, so we can find the cross section of the Fermi-Surface in both halves of the K_z–K_y plane. The Figure 2.7 (after McClure) shows the cross sections

for the cases $\gamma_3 = 0$ and $\gamma_3 \neq 0$ superimposed to emphasize the asymmetry introduced by this parameter.

Obtaining the K_x-K_y cross sections is difficult because the secular equation has to be solved for general α and with γ_3 included. This can be done (in the case E_1, E_2 are well separated from E_3) but note that this will still leave the exact structure in the region near C (Figure 2.4) in some doubt.

Specifically, we aasume $\varepsilon_1\varepsilon_2 >> \varepsilon_3, E$, which reduces equation 2.1.3(1) to

$$E_1^o E_2^o \varepsilon_3^2 - E_1^o E_2^o \gamma_3^2 \Gamma^2 \sigma^2 - E_1^o \varepsilon_3 (\gamma_o + \gamma_4 \Gamma)^2 \sigma^2 - E_2^o \varepsilon_3 (-\gamma_o + \gamma_4 \Gamma)^2 \sigma^2$$

$$- E_1^o (\gamma_o + \gamma_4 \Gamma)^2 \sigma^3 \gamma_3 \Gamma \cos 3\alpha + E_2^o (-\gamma_o + \gamma_4 \Gamma)^2 \sigma^3 \gamma_3 \Gamma \cos 3\alpha$$

$$+ (\gamma_o + \gamma_4 \Gamma)^2 (-\gamma_o + \gamma_4 \Gamma)^2 \sigma^4 = 0$$

Substituting for $\varepsilon_3 = E_3^o - E$ leads to a quadratic in E :-

$$E^2 E_1^o E_2^o + E[-2E_1^o E_2^o E_3^o + E_1^o (\gamma_o + \gamma_4 \Gamma)^2 \sigma^2 + E_2^o (-\gamma_o + \gamma_4 \Gamma)^2 \sigma^2]$$

$$E_1^o E_2^o E_3^2 - E_1^o E_2^o \gamma_3^2 \Gamma^2 \sigma^2 - E_1^o E_3^o (\gamma_o + \gamma_4 \Gamma)^2 \sigma^2 - E_2^o E_3^o (-\gamma_o + \gamma_4 \Gamma)^2 \sigma^2$$

+

$$-E_1^o (\gamma_o + \gamma_4 \Gamma)^2 \sigma^3 \gamma_3 \Gamma \cos 3\alpha + E_2^o (-\gamma_o + \gamma_4 \Gamma)^2 \sigma^3 \Gamma \cos 3\alpha$$

$$+ (\gamma_o + \gamma_4 \Gamma)^2 (-\gamma_o + \gamma_4 \Gamma)^2 \sigma^4 = 0$$

This can be solved and simplified to give

$$E = E_3^o - \frac{1}{2E_2^o}(\gamma_o+\gamma_4\Gamma)^2\sigma^2 - \frac{1}{2E_1^o}(-\gamma_o+\gamma_4\Gamma)^2\sigma^2$$

$$\pm \Big\{ \frac{1}{4}\frac{(\gamma_o+\gamma_4\Gamma)^4}{E_2^{o2}}\sigma^4 + \frac{1}{4}\frac{(-\gamma_o+\gamma_4\Gamma)^4}{E_1^{o2}}\sigma^4 - \tfrac{1}{2}\frac{1}{E_1^oE_2^o}(\gamma_o+\gamma_4\Gamma)^2(-\gamma_o+\gamma_4\Gamma)^2\sigma^4 + \gamma_3^2\Gamma^2\sigma^2 + \Big(\frac{-1}{E_1^o}(-\gamma_o+\gamma_4\Gamma)^2 + \frac{1}{E_2^o}(\gamma_o+\gamma_4\Gamma)^2\Big)\gamma_3\sigma^3\Gamma\cos 3\alpha\Big\}^{\frac{1}{2}}$$

Finally, this can be written :

$$E = E_3^o + A\sigma^2 \pm \{B^2\sigma^4 - 2\gamma_3\Gamma\sigma^3 B\cos 3\alpha + \gamma_3^2\Gamma^2\sigma^2\}^{\frac{1}{2}} \qquad (4)$$

where $$A = \tfrac{1}{2}\Big\{\frac{(-\gamma_o+\gamma_4\Gamma)^2}{-E_1^o} + \frac{(\gamma_o+\gamma_4\Gamma)^2}{-E_2^o}\Big\}$$

$$B = \tfrac{1}{2}\Big\{-\frac{(-\gamma_o+\gamma_4\Gamma)^2}{-E_1^o} + \frac{(\gamma_o+\gamma_4\Gamma)^2}{-E_2^o}\Big\}$$

Apart from the terms $-E_1^o$, $-E_2^o$ in the denominators of A and B (McClure has $E_3^o-E_1^o$, $E_3^o-E_2^o$ respectively) this result is identical to that obtained by McClure (IBM, 1964) for levels near E_3 using a "perturbation treatment" under the restriction "E_1 and E_2 are well

separated from E_3". We note here that the definition of A and B is wrong by factors of σ in the 1964 paper, but is given correctly in McClure's 1957 paper. The latter gives the wrong sign to the cos 3α term, however.

2.1.4 CROSS-SECTIONAL AREAS OF THE FERMI-SURFACE

It is now fairly straightforward to derive estimates of cross-sectional areas of the Fermi surface in the x-y plane, for if we put $\gamma_3 = \gamma_4 = \gamma_5 = 0$ then equation 2.1.3(4) reduces to

$$\sigma^4(A^2-B^2) - 2\sigma^2(E_f-E_3^o)A + (E_f-E_3^o)^2 = 0$$

- which can be solved for σ^2 to give the result below.

$$2\sigma^2\gamma_o^2 = (E_f-E_3^o)\,[2E_f-(E_1^o+E_2^o) \pm (E_1^o-E_2^o)]$$

Since the LHS is always +ve we must take the positive sign for electrons and the negative sign for holes, so:

$$\sigma_e^2 = \frac{1}{2\gamma_o}(E_f-E_3^o)(E_f-E_2^o)$$

$$\sigma_h^2 = \frac{1}{2\gamma_o}(E_f-E_3^o)(E_f-E_1^o)$$

These give :

$$\sigma_e^2 = \frac{1}{\gamma_o^2}\left\{E_f^2 - E_f(\Delta-(\gamma_1-\tfrac{1}{2}\gamma_2\Gamma_e)\Gamma_e) + (\Delta-\gamma_1\Gamma_e)(\tfrac{1}{2}\gamma_2\Gamma_e^2)\right\} \quad \text{for electrons}$$

and $$\sigma_h^2 = \frac{1}{\gamma_o^2}\left\{E_f^2 - E_f(\Delta+2(\gamma_1+\gamma_2)) + (\Delta+2\gamma_1)(2\gamma_2)\right\} \quad \text{for holes.}$$

Γ_e is the value of Γ which maximises the electron cross-sectional area A_e and hence σ_e^2 :

$$\Gamma_e = \frac{1}{3\gamma_1}(\Delta - E_f + [(\Delta-E_f)^2 + 6\gamma_1^2/\gamma_2\ E_f]^{\frac{1}{2}})$$

Finally, we note that on the hexagonal zone faces ($\Gamma = 0$) the cross-sectional area is given by

$$\sigma_m^2 = \frac{1}{\gamma_o^2}\ E_f(E_f-\Delta)$$

Actual areas in K-space A are obtained from the above σ^2 by using

$$A = \pi K^2 = \pi\left(\frac{2}{\sqrt{3}a_o}\right)^2\sigma^2, \text{ where } a_o = 2.46\ \text{Å}.$$

The above results are quoted in Anderson et al (1968) but they give no indication of the derivation. They also state formulae for F. S. volumes in the same approximation.

For the more interesting case $\gamma_3 \neq 0$ a numerical solution of 2.1.3(4) is necessary but we can obtain a useful result by assuming that γ_3 merely introduces a trigonal perturbation in σ. Assume $\sigma=\sigma_o(1+\eta)$

where $\eta = \varepsilon \cos 3\alpha$, η, ε are to be found and σ_o is the solution found above for the case $\gamma_3=0$. Substituting back into 2.1.3(4) and using the fact that σ_o satisfies this for $\gamma_3=0$, we obtain a linear expression in η :

$$\eta = -\gamma_3\Gamma \cos 3\alpha \left[\frac{(\gamma_o+\gamma_4\Gamma)^2}{E_3-E_2} - \frac{(\gamma_o-\gamma_4\Gamma)^2}{E_3-E_1} \right] \sigma_o \; / D$$

where

$$D = 4\frac{(\gamma_o+\gamma_4\Gamma)^2(\gamma_o-\gamma_4\Gamma)^2}{(E_3-E_2)\;(E_3-E_1)}\,\sigma_o^2 + 3\gamma_3\Gamma \cos 3\alpha \left[\frac{(\gamma_o+\gamma_4\Gamma)^2}{E_3-E_2} - \frac{(\gamma_o-\gamma_4\Gamma)^2}{E_3-E_1} \right] \sigma_o$$

$$+ 2(E_f+E_3) \left[\frac{(\gamma_o-\gamma_4\Gamma)^2}{E_3-E_1} + \frac{(\gamma_o+\gamma_4\Gamma)^2}{E_3-E_2} \right] - 2\gamma_3\Gamma^2$$

Recall here that the above equation 2.1.3(4) is not valid when $E_{1,2}$ are close to E_3 so there are no critical points to examine. Putting in typical values for the parameters, we find the first and third terms dominate D making D practically independent of α so we have finally :

$$\sigma = \sigma_o(1+\varepsilon \cos 3\alpha) \text{ where } \varepsilon = -\gamma_3\Gamma\sigma_o \left[\frac{(\gamma_o+\gamma_4\Gamma)^2}{E_3-E_2} - \frac{(\gamma_o-\gamma_4\Gamma)^2}{E_3-E_1} \right] / D \approx 0.01$$

A simple calculation now demonstrates the effect that γ_3 has on the cross-sectional area of the Fermi surface normal to the c-axis

for this area (in σ-units) is

$$A = \tfrac{1}{2}\int_0^{2\pi} \sigma^2 d\alpha = \tfrac{3}{2}\sigma_0^2 \int_0^{2\pi/3} (1+\varepsilon \cos 3\alpha)^2 d\alpha$$

$$= A_0(1+\tfrac{1}{2}\varepsilon^2) \qquad \text{where } A_0 \text{ is the cross sectional area}$$

when $\gamma_3 = 0$.

Therefore γ_3 produces a negligible change in the cross-sectional area of the Fermi surface and will not measurably influence DHVA-type oscillation periods. Alternatively, measurement of periods will not give a reliable estimate of γ_3.

2.1.5. Values of Band Parameters

Finally, values quoted in the literature for the band parameters appearing in the Sloncewski-Weiss model will be collected together.

The review by Haering and Mrowski (1960) on the Band Structure of Graphite Crystals contains details of earlier determinations. At that time there were two schools of thought concerning the magnitude of γ_1. Haering and Wallace proposed a small ($\lesssim 0.005$ eV) value of γ_1 on the basis of constant susceptibility results. The analysis yields $\gamma_0 \simeq 2.6$ eV and gives roughly the correct specific heat. However, the small γ_1 model can account for the presence of holes only at high temperatures, whereas Hall effect and cyclotron resonance experiments

indicate the simultaneous presence of electrons and holes, the latter strongly suggesting equal concentrations of each (Nozieres, 1958). In the overlap model, γ_0 is determined by the susceptibility to be $\simeq$ 2.6 eV, which is in good agreement with theoretical predictions (Lomer, Johnston; 3eV) but γ_1 is calculated from the ratio $\frac{\gamma_0^2}{\gamma_1}$ whose value of 25 eV is given by DHVA, by cyclotron resonance and by electronic specific heat measurements. This gives $\gamma_1 \simeq 0.36$ eV, much larger than the value indicated by the susceptibility experiments. Independent estimates of γ_1 give 0.32 eV (electron energy loss, Ichikawa, 1958), 0.14 eV (infra-red absorption, Boyle and Nozieres, 1958). Later confirmation that γ_1 must be large came from the work of Soule, McClure and Smith (1964) in which they showed that both electron and hole Fermi surfaces are closed sheets. This is consistent with the overlap model whereas the small γ_1 model leads to an extended Fermi surface.

The DHVA effect yields a value of 0.016 eV for γ_2 the magnitude of which agrees with that given by Boyle and Nozieres (0.02 eV). Nozieres' analysis of cyclotron resonance data confirms the positive sign and a rough check is afforded by identifying the knee of the resistivity-temperature curve at 120°K with a carrier degeneracy temperature. Early determinations of Δ were uncertain in sign. Carter and Krumhanslestimate 0.01 eV while McClure's DHVA analysis indicated 0.02 eV and Dresselhaus and Mavroides obtain -0.02 eV. However, later experiments seem to agree on a larger negative value; Soule, McClure and Smith calculate -0.12 eV and McClure and Yafet obtain -0.1 eV.

Johnston estimated γ_3 to be 0.13 eV and γ_4 was assumed equal to γ_3 until the g-shift in electron spin resonance (McClure and Yafet, 1962) gave $|\gamma_4|$ ~0.28 eV and the 1964 magnetoreflection experiments of Dresselhaus and Mavroides (on pyrolytic graphite) led to γ_3=0.145 eV and γ_4=-0.2 eV. So far no experiment has yielded a value of γ_5 and it is assumed $\gamma_5=\gamma_2$ (McClure, 1960, Inoue, 1962).

2.2 GALVANOMAGNETIC PROPERTIES.

Introduction.

In this section we shall be concerned with understanding the galvanomagnetic effects in graphite, notably the magnetic-field and temperature-variation of the magnetoconductivity tensor $\sigma(\underline{H})$ and its inverse $\rho(\underline{H})$ with a view to correlating these experimental data with the SW band model. Broadly speaking, the phenomena can be divided between low field, high temperature effects; the classical effects, and quantum effects occurring at high magnetic fields and low temperatures. The weak field phenomena are strongly influenced by interactions between charge carriers and the lattice, e.g. the nature of the scattering process, whereas in strong magnetic fields certain transport processes become dependent upon charge carrier characteristics alone, such as density and Fermi energy. Section 2.3 will be devoted to the quantum effects.

2.2.1 Phenomenological Treatment.

One can write a relation between electric and thermal fields and fluxes in the following form:

$$J_i = \sigma_{ij}(\underline{H})\varepsilon_j^* + B_{ij}(\underline{H})\frac{\partial}{\partial x_j}\left(\frac{1}{T}\right)$$

$$Q_i = P_{ij}(\underline{H})\varepsilon_j^* + K_{ij}(\underline{H})\frac{\partial}{\partial x_j}\left(\frac{1}{T}\right) \qquad (1)$$

where $\underline{J}$ and $\underline{Q}$ are the electric and thermal currents, T is the temperature and $\underline{\varepsilon}^*$ is the electrothermal field which is essentially the gradient of the electrochemical potential, μ; $\underline{\varepsilon}^* = \frac{-1}{q}\nabla\mu$. The externally applied electrostatic field, $\underline{\varepsilon}$, is related to the electrothermal field by $\underline{\varepsilon}^* = \underline{\varepsilon} - \frac{\nabla\mu_c}{q}$ - where q is the charge of the carriers and μ_c is the chemical potential of the charge carriers.

Now experimentally it is more usual to define the current flows than the electric and thermal force-fields, so we invert these relations to give:

$$\varepsilon^*_m = \rho_{mn}(\underline{H})J_n + \alpha_{mn}(\underline{H})\frac{\partial}{\partial x_n}T$$

$$Q_m = \Pi_{mn}(\underline{H})J_n - K_{mn}(\underline{H})\frac{\partial}{\partial x_n}T \qquad (2)$$

- where the arrays ρ, α, Π, K are known as the resistivity, the thermoelectric power, the Peltier coefficient, and the thermal conductivity respectively.

For an isothermal, uniform conductor these reduce to $\underline{\varepsilon}^* = \underline{\varepsilon}$, $Q_i = \Pi_{ij}J_j$, $E_i = \rho_{ij}J_j$, where $\rho = \sigma^{-1}$ and $\Pi = P\sigma^{-1}$.

The general thermodynamic relations of Onsager apply to these tensors :

$$\sigma_{ij}(\underline{H}) = \sigma_{ji}(-\underline{H}) \quad \rho_{ij}(\underline{H}) = \rho_{ji}(-\underline{H}), \text{ etc.}$$

At first sight, one is still left with a large number of independent tensor elements to be obtained experimentally, but the requirements of crystal symmetry help to reduce this number. By Neumann's principle, the above tensors must be invariant under the symmetry operations of the point group of the crystal structure.

Graphite has the point group 6/mmm which consists of the symmetry elements 1, six of $2\underline{1}$, 2_z, $\pm 3_z$, $\pm 6_z$, together with all of these multiplied by the inversion operation $\bar{1}$, making 24 in all. It is easily seen that second order tensor effects are isotropic in the basal plane for zero magnetic field and this leads immediately to drastic restrictions on the components.

Thus: $\sigma_{xx} = \sigma_{yy}$

Also, $\sigma_{xy} = \sigma_{yx} = \sigma_{xz} = \sigma_{zx} = \sigma_{yz} = \sigma_{zy} = 0$

Now, when a magnetic field is applied, the symmetry of the system (crystal plus magnetic field) is considerably reduced and in general $\sigma(\underline{H})$ will have nine non-zero components. For small magnetic fields the tensor components can be expanded in terms of magnetic field components, H_i, with field-independent coefficients a :

$$\sigma_{ij}(\underline{H}) = a_{ij} + a_{kij}H_k + a_{klij}H_kH_l + a_{klmij}H_kH_lH_m + \cdots \qquad (3)$$

(see Kao and Katz and Birss). The coefficients must allow σ to obey the Onsager relations and are further restricted by crystal symmetry

From the former we have $a_{ij} = a_{ji}$, $a_{kij} = -a_{kji}$, $a_{klij} = a_{klji}$.

Following the method of Birss (1964) we find for the point group 6/mmm:

$$\begin{aligned}
\sigma_{11} &= a_{11} + (a_{1122}+a_{1221}+a_{1212})H_1^2 + a_{1122}H_2^2 + a_{3311}H_3^2 \\
\sigma_{22} &= a_{11} + a_{1122}H_1^2 + (a_{1122}+a_{1221}+a_{1212})H_2^2 + a_{3311}H_3^2 \\
\sigma_{33} &= a_{33} + a_{1133}H_1^2 + a_{1133}H_2^2 + a_{3333}H_3^2 \\
\sigma_{12} &= a_{312}H_3 + (a_{1212}+a_{1221})H_1H_2 \\
\sigma_{23} &= a_{123}H_1 + (a_{1313}+a_{3113})H_2H_3 \\
\sigma_{31} &= -a_{132}H_2 + (a_{1331}+a_{3131})H_1H_3 \\
\sigma_{13} &= -a_{123}H_2 + (a_{1313}+a_{3113})H_1H_3 \\
\sigma_{32} &= a_{132}H_1 + (a_{1331}+a_{3131})H_2H_3 \\
\sigma_{21} &= -a_{312}H_3 + (a_{1221}+a_{1212})H_1H_2
\end{aligned} \tag{4}$$

Now, obviously $a_{klij} = a_{lkij}$, and Onsager's relations give $a_{1212} = a_{1221}$, $a_{1313} = a_{1331}$, $a_{3113} = a_{3131}$ $a_{123} = -a_{132}$ so there are 10 independent coefficients to second order in magnetic field, 4 to first order, and only 2 in zero field as was mentioned above.

It is interesting to consider the case when the magnetic field is confined to the c-axis direction; $\underline{H} = (0,0,H)$. The conductivity tensor now reduces to

$$\sigma_{ij}(H) = \begin{pmatrix} (a_{11}+a_{3311}H^2) & (a_{312}H) & 0 \\ (-a_{312}H) & (a_{11}+a_{3311}H^2) & 0 \\ 0 & 0 & (a_{33}+a_{3333}H^2) \end{pmatrix} \qquad (5)$$

To obtain the resistivity tensor we use the fact that ρ is the inverse of σ; the above expressions for σ_{ij} apply to any second rank polar tensor property of graphite but to relate the coefficients a of the resistivity tensor ρ to those of its inverse, the conductivity tensor σ, we use the relation $\sigma_{ik}\rho_{kj} = \delta_{ij}$. These nine equations can be solved for a general (small) field but we restrict ourselves to the case $\underline{H} = (0,0,H)$ which leads to

$$\rho_{11} = \rho_{22} = \frac{\sigma_{11}}{\sigma_{11}^2 + \sigma_{12}^2}, \quad \rho_{33} = \frac{1}{\sigma_{33}}, \quad \rho_{31} = \rho_{32} = \rho_{13} = \rho_{23} = 0$$
$$\rho_{21} = -\rho_{12} = \frac{\sigma_{12}}{\sigma_{11}^2+\sigma_{12}^2} \qquad (6)$$

- giving to second order in magnetic field:

$$\rho_{ij}(H) = \begin{pmatrix} [\frac{1}{a_{11}} - (\frac{a_{3311}}{a_{11}^2} + \frac{a_{312}^2}{a_{11}^3})H^2] & (-\frac{a_{312}}{a_{11}^2}H) & 0 \\ (-\rho_{12}) & (\rho_{11}) & 0 \\ 0 & 0 & (\frac{1}{a_{33}} - (\frac{a_{3333}}{a_{33}^2})H^2) \end{pmatrix} \quad (7)$$

- which is of the same form as $\sigma_{ij}(H)$.

We can now see that the Hall coefficient is given by $-(\frac{a_{312}}{a_{11}^2})$ and the transverse magnetoresistance, $M_T^a = \frac{\rho_{xx}(H)-\rho_{xx}(0)}{\rho_{xx}(0)}$, by

$$M_T^a = -(\frac{a_{3311}}{a_{11}} + \frac{a_{312}^2}{a_{11}^2})H^2$$

The longitudinal c-axis magnetoresistance, $M_L^c = \frac{\rho_{zz}(H)-\rho_{zz}(0)}{\rho_{zz}(0)}$ is given by a similar expression:

$$M_L^c = -(\frac{a_{3333}}{a_{33}})H^2$$

2.2.2 Relation between single crystal and pyrolytic graphite.

The above tensors afford a description of the galvanomagnetic effects for single crystal graphite but it is not immediately obvious that they may be employed for the polycrystalline structure of pyrolytic graphite; although pyrolytic graphite is well aligned in the c-axis direction the a-axes of its individual crystallites are randomly orientated. To obtain rigorous expressions for the polycrystalline material would entail complex averaging calculations which are not at all well developed but it might be expected that the behaviour of such a material lies close to that of a hypothetical solid with perfect cylindrical symmetry about the c-axis. Calculation shows that none of the non-zero elements in the above tensors are reduced to zero by the increased symmetry of this solid so one expects the above tensors to hold for pyrolytic graphite for all effects which are not dependent too strongly upon crystallite shape and size.

Although the exact solution of this problem appears to be intractable at present (perhaps computer simulation studies would yield useful information as they do in the field of radiation damage) the above considerations provide reassurance. The following arguments, based on H.J. Juretschke's note in Appl. Phys. Letters, 12,213,1968, concerning the 'third order elastic constants of polycrystalline media', elucidate a little more clearly the restrictions under which one might reasonably expect an equivalence between the tensors for single crystal and

pyrolytic graphite. We start by writing the relation between current density $\underline{J}$, electric field $\underline{E}$, and conductivity tensor $\underline{\underline{\sigma}}$: $J_i = \sigma_{ij} E_j$. For a polycrystalline specimen, we are interested in a spatial average, giving $\langle J_i \rangle = \langle \sigma_{ij} E_j \rangle$ which reduces to $\langle J_i \rangle = \langle \sigma_{ij} \rangle E_j$ when we make the (extreme) assumption of uniform electric field throughout the polycrystalline mass. The problem has now been reduced to an averaging of the single crystal tensor $\underline{\underline{\sigma}}$ over all the orientations which occur. Pyrolytic graphite is composed of crystallites with randomly-orientated a-axes so one has to average over all possible rotations θ about the c-axis. For a rotation θ of the crystal about the z-axis (which is coincident with the crystal's c-axis) the tensor components are transformed in the following way: $\sigma'_{ij} = \alpha_{ip}\alpha_{jq}\sigma_{pq}$ where repeated indices are summed in the usual manner. σ'_{ij} denotes the new tensor components and $\underline{\alpha}$ is the rotation matrix describing θ ;

$$[\alpha_{ij}] = \begin{bmatrix} C & S & 0 \\ -S & C & 0 \\ 0 & 0 & 1 \end{bmatrix} \quad \text{where} \quad C \equiv \cos\theta, \quad S \equiv \sin\theta$$

The average value of σ_{ij} is thus

$$\langle \sigma_{ij} \rangle_{\theta} = \frac{1}{2\pi} \int_0^{2\pi} \sigma'_{ij}(\theta)d\theta = \frac{1}{2\pi} \int_0^{2\pi} \alpha_{ip}(\theta)\alpha_{jq}(\theta)\sigma_{pq}d\theta$$

As an example, we take

$$\langle\sigma_{12}\rangle_E = \frac{1}{2\pi}\int_0^{2\pi}(\alpha_{11}\alpha_{21}\sigma_{11}+\alpha_{11}\alpha_{22}\sigma_{12}+\alpha_{12}\alpha_{21}\sigma_{21}+\alpha_{12}\alpha_{22}\sigma_{22})d\theta$$

$$= \frac{1}{2\pi}\int_0^{2\pi}(-\sigma_{11}S.C + \sigma_{12}C^2 - \sigma_{21}S^2 + \sigma_{22}S.C)d\theta = (\sigma_{12}-\sigma_{21})\frac{1}{2}$$

Similarly, we find

$$\langle\sigma_{11}\rangle_E = \langle\sigma_{22}\rangle_E = \frac{1}{2}(\sigma_{11}+\sigma_{22})$$

$$\langle\sigma_{12}\rangle_E = -\langle\sigma_{21}\rangle_E = \frac{1}{2}(\sigma_{12}-\sigma_{21}) \qquad \langle\sigma_{13}\rangle = \langle\sigma_{31}\rangle = \langle\sigma_{23}\rangle = \langle\sigma_{32}\rangle = 0$$

$$\langle\sigma_{33}\rangle_E = \sigma_{33}$$

The corresponding resistivity tensor is found by inverting $\langle\sigma\rangle$:

$$\langle\rho_{11}\rangle_E = \langle\rho_{22}\rangle_E = \frac{\langle\sigma_{11}\rangle_E}{\langle\sigma_{11}\rangle_E^2+\langle\sigma_{12}\rangle_E^2} = \frac{\frac{1}{2}(\sigma_{11}+\sigma_{22})}{\frac{1}{4}(\sigma_{11}+\sigma_{22})^2+\frac{1}{4}(\sigma_{12}-\sigma_{21})^2}$$

All others zero

$$\langle\rho_{33}\rangle_E = \frac{1}{\langle\sigma_{33}\rangle_E} = \frac{1}{\sigma_{33}}$$

$$\langle\rho_{21}\rangle_E = -\langle\rho_{12}\rangle_E = \frac{\langle\sigma_{12}\rangle_E}{\langle\sigma_{11}\rangle_E^2+\langle\sigma_{12}\rangle_E^2} = \frac{\frac{1}{2}(\sigma_{12}-\sigma_{21})}{\frac{1}{4}(\sigma_{11}+\sigma_{22})^2+\frac{1}{4}(\sigma_{12}-\sigma_{21})^2}$$

Referring to equation (5) for the single-crystal conductivity tensor under a magnetic field $\underline{H} = (0,0,H)$, we see that the average resistivity tensor reduces to :

$$\left.\begin{aligned} \langle\rho_{11}\rangle_E = \langle\rho_{22}\rangle_E &= \frac{\sigma_{11}}{\sigma_{11}^2+\sigma_{12}^2} \\ \langle\rho_{33}\rangle_E &= \frac{1}{\sigma_{33}} \\ \langle\rho_{21}\rangle_E = -\langle\rho_{12}\rangle_E &= \frac{\sigma_{21}}{\sigma_{11}^2+\sigma_{12}^2} \end{aligned}\right\} \text{all others zero} \qquad (8)$$

- under the assumptions of c-axis directed magnetic field and uniform electric field.

Now, we may carry through the same analysis under the assumption of uniform current density; $\langle E_i \rangle = \langle \rho_{ij} J_j \rangle = \langle \rho_{ij} \rangle J_j$. This leads to an average resistivity tensor expressed in terms of the single-crystal components:

$$\langle\rho_{11}\rangle_J = \langle\rho_{22}\rangle_J = \frac{\rho_{11}+\rho_{22}}{2}$$

$$\langle\rho_{33}\rangle_J = \rho_{33}$$

$$\langle\rho_{12}\rangle_J = -\langle\rho_{21}\rangle_J = \tfrac{1}{2}(\rho_{12}-\rho_{21})$$

Finally, these may be expressed in terms of the single-crystal conductivity tensor components under the assumption of $\underline{H} = (0,0,H)$:

$$\left.\begin{aligned} \langle\rho_{11}\rangle_J = \langle\rho_{22}\rangle_J &= \frac{\sigma_{11}}{\sigma_{11}^2+\sigma_{12}^2} \\ \langle\rho_{33}\rangle_J &= \frac{1}{\sigma_{33}} \\ \langle\rho_{21}\rangle_J = -\langle\rho_{12}\rangle_J &= \frac{\sigma_{12}}{\sigma_{11}^2+\sigma_{12}^2} \end{aligned}\right\} \text{ all others zero} \qquad (9)$$

Comparing (8) and (9) we see the average tensor components are the same under both extreme assumptions with the additional one that the magnetic field is along the c-axis in each case.

In short, provided one does not destroy the high symmetry of this material about the c-axis by H_1, H_2 field components, the tensors describing the polycrystalline material have exactly the same components as the single crystal tensors under each of the assumptions; uniform current density and uniform electric field distribution. This does not prove the identity between the macroscopic descriptions of the two types of graphite, but it certainly makes a common assumption more plausible and indicates that one should be even more wary when the magnetic field has components in the basal plane.

2.2.3 The Boltzmann Transport Equation.

It was shown in Appendix 1 that for some purposes electrons in a crystal can be treated as fictitious particles with mass given by $(\frac{1}{m})_{ij} = \frac{1}{\hbar^2}\frac{\partial^2 E}{\partial k_i \partial k_j}$ moving classically under the influence of the

external electric and magnetic fields. We now consider the average effect of the whole assembly of electrons on the transport processes; a statistical approach is necessary to condense the vast amount of information required for a complete description of the microscopic behaviour of the system. We define a distribution function $\underline{f}(\underline{K},\underline{r},t)dV_K d^3r$ giving the probability of finding a particle with position $\underline{r}$ and momentum $\underline{K}$ lying within d^3r, dV_k. The fundamental equation determining this distribution function is the Boltzmann equation, derived for instance in Wilson p.4.

$$\frac{\partial f}{\partial t} + \underline{V}.\nabla_r f + \dot{\underline{K}} .\nabla_K f = \frac{\partial f}{\partial t}) \text{ collisions}$$

The term on the right-hand-side of the Boltzmann equation represents the effect of certain terms in the crystal Hamiltonian (which have so far been neglected) leading to transitions between electron states. Whenever the principle of detailed balance applies, such transitions do not influence the equilibrium distribution function (the Fermi function) but they do establish it in the first place, and in the presence of disturbing external fields they have the effect of limiting the response of the system so that in the steady state there is a balance between the external fields and the effects of scattering.

The change in f due to collisions can be written more explicitly in terms of the probability per unit time $W(\underline{K},\underline{K}')$ that an electron will make the transition $\underline{K} \rightarrow \underline{K}'$ induced by an aperiodic term in the crystal

Hamiltonian resulting from an irregularity in the lattice. Such irregularities can be lattice vibrations (phonons), leading to temperature-dependent scattering, isolated impurities, electron-electron scattering due to the screened Coulomb repulsion between electrons remaining after the usual one-electron treatment has taken care of the average potential, and other lattice disturbances such as vacancies, grain boundaries and dislocations.

As an example, consider the scattering by a fixed impurity or grain boundary which are both massive compared to an electron. The energy change of such an irregularity is tiny because of the disparity in masses and we may regard the process as being one in which the electron energy is conserved; $W(\underline{K},\underline{K}')$ is proportional to $\delta(E_K - E_{K'})$. The probability of a transition occurring from state $\underline{K}$ into any other state in time dt depends on the occupancy of the initial and final states and is given by

$$dt \int_{BZ} W(\underline{K},\underline{K}') f_K (1-f_{K'}) dV_{K'}$$

Similarly, the probability of a transition into state $\underline{K}$ is

$$dt \int_{BZ} W(\underline{K}',\underline{K}) f_{K'} (1-f_K) dV_{K'}$$

Thus, the net increase in f_K due to collisions of this kind per unit time is

$$\left.\frac{\partial f}{\partial t}\right)_{coll} = \int_{BZ} [W(\underline{K}',\underline{K}) f_{K'}(1-f_K) - W(K,K') f_K(1-f_{K'})] dV_{K'} \qquad (1)$$

A formally similar equation is obtained for processes which do change the electron energy with $\Omega(\underline{K},\underline{K}')$ in place of $W(\underline{K},\underline{K}')$, where Ω is no longer proportional to $\delta(E_K - E_{K'})$. Because of the additivity of independent-event probabilities, the total expression for $\left.\frac{\partial f}{\partial t}\right)_{coll}$ will be the sum of the appropriate integrals for the independent scattering processes.

In uniform equilibrium, the left hand side of the Boltzmann equation is zero which implies that $\left.\frac{\partial f}{\partial t}\right)_{coll}$ must be zero for all scattering processes. This forces the intergrand in (1) to be zero, leading to

$$W(K',K)\ f_o(E_{K'})\ (1-f_o(E_K)) = W(K,K')\ f_o(E_K)\ (1-f_o(E_{K'}))$$

This is a consequence of the 'principle of detailed balancing'; every process and its inverse must occur with equal frequency in equilibrium.

The equilibrium solution is the Fermi distribution function

$$f_o = \frac{1}{e^{(E-\mu)KT} + 1}$$

where E is the total electron energy and μ is the electrochemical potential per electron or 'Fermi energy'.

Now the electric current density $\underline{J}$ is given by

$$\underline{J} = \frac{-e}{4\pi^3} \int \underline{V} f \, dV_K$$

so our task is to solve the Boltzmann equation in the presence of electric and magnetic fields and then substitute in the above equation to obtain the conductivity. We note immediately that, since graphite obeys Ohms' law, we are only interested in functions f which lead to an integral proportional to electric field.

2.2.4 The Relaxation Time Approximation.

The solution of the Boltzmann equation is greatly simplified if it is assumed that disturbances die out with time with a time constant $\tau(\underline{K})$;

$$\left.\frac{\partial f}{\partial t}\right)_{coll} = - \frac{f_K - f_K^o}{\tau_K}$$

This is not always a valid assumption (e.g. for lattice scattering at low temperatures) but is a commonly used starting point for transport calculations. S. Ono and K. Sugihara (1966) show that it is a reasonable assumption for graphite at least in the region 25°K to 400°K, where lattice scattering is dominant. When the approximation fails, it is necessary to solve the full integral equation for the distribution function as has been carried out by E.H. Sondheimer (1950) for some special cases.

Substituting in, and using the effective mass approximation, the Boltzmann equation in the steady state becomes

$$-\frac{e}{\hbar}\left(\underline{\varepsilon}+\frac{1}{C}\underline{V}\wedge\underline{H}\right)\nabla_K f+\underline{V}\cdot\nabla_r f=-\frac{f-f_o}{\tau}$$

where $\tau(\underline{K})$ must have the same symmetry as the crystal.

For an isothermal, uniform conductor;

$$\left(\frac{e}{\hbar}\right)\left[\underline{\varepsilon}+\underline{V}\wedge\underline{H}/_C\right]\cdot\nabla_K f+(f_o-f)/_\tau=0$$

This is the starting point for our discussion of McClure's method of solution for a general band structure in section 2.4., but we note here that Chambers (1952) has given a formal solution which is of use in high magnetic fields and can be expanded in low fields. However, the same low-field expansion can be obtained more simply by an iterative procedure presented by Jones and Zener (1934).

2.2.5 The Jones-Zener Solution.

In the above-mentioned paper, Jones and Zener obtained a solution by simple iteration. Let us define a vector operator

$$\underline{\mathbb{C}}=\frac{e}{C\hbar^2}\nabla_K E\wedge\nabla_K$$

and assume a solution of the form $f=f_o-\phi\frac{\partial f_o}{\partial E}$. Then the Boltzmann equation can be written

$$\frac{e}{\hbar}\underline{\varepsilon}\cdot\nabla_K f_o-\frac{\partial f_o}{\partial E}\frac{e}{\hbar C}\underline{V}\wedge\underline{H}\cdot\nabla_K\phi+\frac{\phi}{\tau}\frac{\partial f_o}{\partial E}+\frac{e}{\hbar C}\underline{V}\wedge\underline{H}\cdot\nabla_K f_o-\phi\frac{e}{\hbar}\underline{\varepsilon}\cdot\nabla_K\frac{\partial f_o}{\partial E}$$

$$-\frac{\partial f_o}{\partial E}\frac{e}{\hbar}\underline{\varepsilon}\cdot\nabla_K\phi-\phi\frac{e}{\hbar C}\underline{V}\wedge\underline{H}\cdot\nabla_K\frac{\partial f_o}{\partial E}=0$$

This reduoes to the following equation when we neglect all powers of $\underline{\varepsilon}$ higher than the first (to impose Ohm's law) and note that

$$\underline{V}\wedge\underline{H}\cdot\nabla_K f_o = \frac{\partial f_o}{\partial E}\ \underline{V}\wedge\underline{H}\cdot\nabla_K E \equiv 0 \quad \text{since } \nabla_K E = \hbar\underline{V}$$

$$\frac{e}{\hbar}\,\underline{\varepsilon}\cdot\nabla_K E + \underline{H}\cdot\underline{\Omega}\,\phi + \frac{\phi}{\tau} = 0$$

Putting $\underline{H} = 0$ one obtains the zero-order solution

$$\phi_o = -\frac{\tau e}{\hbar}\,\underline{\varepsilon}\cdot\nabla_K E$$

Higher-order solutions are obtained by substituting back successively into

$$\phi_r = -\frac{\tau e}{\hbar}\,\underline{\varepsilon}\cdot\nabla_K E - \underline{H}\cdot\underline{\Omega}\,\phi_{r-1},\ r = 1,2,3\ \ldots\ldots$$

Obviously, there is some critical value of magnetic field, $\underline{H}$, above which the series no longer converges for a given band structure. The critical value is best found by actual computation as no general expression is available. Jones and Zener themselves point out that the Boltzmann equation is only meaningful for values of H such that $\frac{eH\tau}{mc} \ll 1$ - this restricts the magnetic field to values below the quantum-effect region so that electrons never have time to complete more than a small fraction of an orbit in the field before being scattered. We shall mean by a 'small magnetic field' a value which satisfies the above condition and which is also small enough to ensure convergence of the Jones-Zener expansion.

The development of this series solution is undertaken in Appendix 2 where the conductivity tensor $\sigma_{ij}(\underline{H})$ is calculated from $J_i = \sigma_{ij}E_j$ and $\underline{J} = \int \frac{e}{4\pi^3} \underline{v} \frac{\partial f}{\partial E} dV_K$. The Jones-Zener terms are compared with the terms in the phenomenological expansion;

$$\sigma_{ij}(\underline{H}) = \sigma_{ij}(0) + \sigma_{kij}H_K + \sigma_{klij}H_K H_l + \cdots\cdots$$

and integral expressions applicable to graphite are developed for the coefficients σ_{ij}, σ_{kij}, σ_{klij}. These final expressions involve integrations over the Fermi surface and have been derived under certain conditions: Degeneracy of the carriers, magnetic field parallel to the c-axis, and $\gamma_3 = 0$. The final expressions are:-

$$\sigma_{ij} = \begin{pmatrix} \pi & 0 \\ 0 & \pi \end{pmatrix} \frac{e^2}{4\pi^3\hbar} \int \tau \left(\frac{\partial E}{\partial K}\right)_K dK_z$$

$$\sigma_{3ij} = \begin{pmatrix} 0 & \pi \\ -\pi & 0 \end{pmatrix} \frac{-e^3}{4\pi^3 c\hbar^4} \int \tau^2 \left(\frac{\partial E}{\partial K}\right)^2 dK_z$$

$$\sigma_{33ij} = \begin{pmatrix} \pi & 0 \\ 0 & \pi \end{pmatrix} \frac{-e^4}{4\pi^3 c^2\hbar^6} \int \tau^3 \left(\frac{\partial E}{\partial K}\right)^2 \frac{1}{K} dK_z$$

It is interesting to note, in passing, that the analysis in Appendix 2 yields as a condition for a non-zero c-axis longitudinal magneto-resistance or conductivity that the expression $\left(\tau(K_z) \frac{\partial E}{\partial K_z}\right)$ must have some K or α-dependence; a K_z-dependence alone is insufficient.

We are using here the cylindrical co-ordinate system introduced in Section 2.1.3 ; K is the distance from the zone edge. The angle α has gone out of our expressions because the neglect of γ_3 leads to circular symmetry about a zone edge.

To proceed, one needs to know $\tau(K_z)$, $\frac{\partial E}{\partial K_z}$, $K(K_z)$. The latter two functions can be obtained in a straightforward manner from the Sloncewski-Weiss band model with $\gamma_3 = 0$, but τ is a very doubtful quantity. Perhaps the best one can do at present is to regard τ as a parameter (varying with K_z and temperature). K. Sugihara and H. Sato (1963) have calculated the relaxation time for two temperatures, 25°K and 50°K, where lattice scattering is dominant, but it could differ considerably at lower temperatures. In a later paper, S. Ono and K. Sugihara (1968) show that the inclusion of γ_3 causes τ to vary with position on the hodograph (with α), though the magnitudes at the two temperatures are maintained roughly at the same values of 1.3×10^{-12} sec (50°K) and $3 \rightarrow 3.5 \times 10^{-12}$ sec (25°K).

A computer programme has been written to evaluate the above integrals for a given set of band parameters (γ_0, γ_1, γ_2, γ_4, Δ, E_f). These parameters yield, through the equations of Sections 2.1.3, 2.1.4, expressions for the factors K (from the cross-sectional areas in Section 2.1.4) and $\frac{\partial E}{\partial K}$ in terms of the integration variable K_z. The range of K_z was split into three, corresponding to values of K_z between K and M, M and H, and J and H of Figure 2.4 which parts of

the Fermi surface describe holes, electrons and minority electrons, respectively.

It was found that to prevent computational difficulties the region of the electron surface near M had to be excluded from the range of integration. We recall that the expressions developed in Sections 2.1 are not valid for this difficult region in any case. The lower limit on K_z for this integration was increased away from the K_z value of M by some 0.5 to 1%. No such automatic adjustment occurred for the other two types of carrier although this was allowed by the programme.

No absolute values are available for the magnetoconductivity tensor components at the present time, but using the Dresselhaus and Mavroides (1964) set of parameters (2.88, 0.39, 0.016, -0.2, 0.012), the following ratios m_i = (minority electron/majority electron),

h_i = (hole /majority electron),

for the contributions to the zero field conductivity (i = 1), Hall effect (i = 2) and magnetoconductivity (i = 3) were obtained;

$m_1 = 0.06$, $m_2 = 0.3$, $m_3 = 0.96$

$h_i = 4.8$ $h_2 = 1.4$, $h_3 = 0.2$

showing the important influence of holes on the low field Hall effect and that of the minority electrons on the magnetoconductivity.

Changing the Fermi level from 0.012 to 0.019 resulted in:

$m_1 = 0.03$, $m_2 = 0.13$, $m_3 = 0.41$

$h_1 = 0.59$, $h_2 = 0.22$, $h_3 = 0.57$

showing how sensitive electrical conduction is to changes in Fermi level, for the majority electrons now dominate completely.

The band parameter set (2.85, 0.3, 0.021, -0.2, -0.006, 0.029) yields:

$m_1 = 0.14$, $m_2 = 0.05$, $m_3 = 0.11$

$h_1 = 0.67$, $h_2 = 0.30$, $h_3 = 0.11$

The above calculations were performed with a constant relaxation time τ but the programme can accept any K_z-dependence one wishes to attribute to τ.

2.3 Quantum Oscillations.

In degenerate conductors it is possible under certain conditions to observe quantum effects in the electrical conductivity. The application of a magnetic field to an electronic system causes a quantisation of electron energy levels for motion perpendicular to the magnetic fields, such that the energy level spacing becomes $\hbar\omega$ where the cyclotron frequency $\omega = \frac{eH}{m^*c}$ At sufficiently low temperatures, where $KT \leq \hbar\omega$, the thermal broadening of the levels is less than the level spacing and the effects of this quantisation can be observed provided other level broadening mechanisms are not dominant. For graphite, the above condition requires liquid helium temperatures and magnetic fields above about 6kgauss.

This section illustrates the effect of magnetic condensation of energy levels in 2.3.1 by means of a semiclassical model, and goes on in 2.3.2 to present the 'generalised Landau' formula which is used for data analysis in Section 4.2.3. Literature cited below should be consulted for details.

2.3.1 Motion of Wave Packets in a Magnetic Field.

It was shown in Appendix 1 that, under conditions stated there, electrons in crystals may be regarded as classical particles with an effective mass m^* and with $\hbar\underline{K}$ replacing the classical momentum. In particular, under the influence of a magnetic field $\underline{H}$ the representative point in $\underline{K}$- space, $\underline{K}$, is given by $\dot{\underline{K}} = \frac{e}{c\hbar}\,\underline{V} \wedge \underline{H}$ where $\underline{V}$ is the velocity of the electron. Thus $\underline{K}$ is normal to both

$\underline{H}$ and $\underline{V}$. The latter is normal to the Fermi surface, being given by $\underline{V} = \frac{1}{\hbar}$ grad $\underline{K}E$. Thus $\underline{K}$ is confined to an orbit defined by the intersection of a plane normal to the magnetic field with the Fermi surface. The electron makes one revolution in a period

$$\frac{2\pi}{\omega} = \frac{c\hbar}{eH} \oint \frac{dK}{V_{\perp}} \qquad (1)$$

where $d\underline{K}$ is an element of the orbit and $V_{\perp}$ is the electron velocity perpendicular to $\underline{H}$ in the plane of the orbit. For free electrons $E = \frac{\hbar^2 \underline{K}^2}{2m}$, $V = \frac{\hbar K}{m}$ so that $\omega = \frac{eH}{mc}$. It is convenient to define a 'cyclotron effective mass' for other band shapes $m^* = \frac{eH}{\omega c}$ (2) From (1) above this obviously varies from orbit to orbit in general.

We point out here that equation (1) leads usefully to the definition of a 'phase variable' $\phi = \omega \frac{c\hbar}{eH} \frac{dK}{V_{\perp}}$ which is equal to 2π for a complete circuit. This is used in Section 2.4.1. to solve the Boltzmann transport equation.

The periodic motion of an electron in a magnetic field leads, as one might expect by analogy with a simple harmonic oscillator, to a quantisation of the electron energy levels in units of $\hbar\omega$ to motion perpendicular to the magnetic field. (See for instance Ziman, 1965).

It can be shown that (2) is equivalent to $m^* = \frac{\hbar^2}{2\pi} \frac{\partial A}{\partial E}$ where A is the area of an orbit in K-space. Thus if $\delta E = \hbar\omega$, we have

$\delta A = \frac{2\pi m^*(\omega)}{\hbar}$ which indicates that the areas of orbits in $\underline{K}$-space are themselves quantised. In a crystal the area of an orbit on the nth energy level is $A_n = \frac{2\pi eH}{c\hbar}(n+\gamma)$ where γ is $\simeq \frac{1}{2}$.

As the magnetic field is increased the areas of occupied cylindrical energy surfaces increase, but these cylinders depopulate as they pass through the Fermi surface. Consequently, the density of states jumps (discontinuously at $0^{\circ}K$) every time a magnetic energy level passes through the Fermi surface of area A_F. This happens as n changes by unity in intervals of reciprocal magnetic field of

$$\Delta\left(\frac{1}{H}\right) = \frac{2\pi e}{c\hbar} \quad \frac{(n+1+\gamma)-(n+\gamma)}{A_F} \qquad (3)$$

For a more complicated Fermi surface the energy cylinders may cut the Fermi surface in several places and cannot be said to be 'passing through' the Fermi surface at any given value of magnetic field; many values of A_F are involved. However, a more thorough analysis shows that the effects of all but the extremal cross sectional areas of the Fermi surface average out and the density of states changes periodically in $\left(\frac{1}{H}\right)$ with (possibly superimposed) periods determined by the extremal cross sections. Electronic properties such as the electrical conductivity or Hall effect which depend directly on the density of states reflect the above changes in the form of oscillations superimposed on the classical background. The semiclassical model is presented in an interesting manner by Pippard (1965).

2.3.2 The Generalised Landau Formula.

Equation (3) of the last section gives the relation of Onsager (1952) and Lifshitz (1957) for the period P (gauss^{-1}) of oscillations in resistivity, known as the Shubnikov - de Haas effect (1930), and Hall effect. All theories of the SDH effect agree on this period behaviour and also on the thermal damping factor D (Landau, 1939) which describes the temperature dependence of the oscillation amplitude, $D = {}^{u}/\sinh u$, where $u = \frac{2\pi^2 KT}{\hbar\omega}$. T is the temperature, $\omega = \frac{eH}{m^* c}$ and m^* is an orbital effective mass. This factor is seen to reflect the condition mentioned in Section 2.3 above.

Extensive references to the literature on theories of susceptibility-type oscillations are given in the paper by Soule et al (1964). This presents data on a graphite single crystal which proves that the electron and hole Fermi surfaces of graphite are closed and effectively resolves the controversy mentioned in Section 2.1.5 in favour of the overlap model. Roth and Argyres (1966) give a review of magnetic quantum effects with an extensive bibliography of direct interest in the present case.

Imperfections affect the motion of the electrons in a variety of ways. Scattering is all-important for transport phenomena but another effect, the broadening of the unperturbed energy levels through collisions with imperfections, proves to be important in determining the amplitude of the oscillations. Dingle (1952) was the first to

derive the effect of a finite level width ($\sim \Gamma$) on the oscillations; the amplitude of the rth term is diminished by the factor $\exp(\frac{-2\pi\Gamma_r}{\hbar\omega})$ This goes quickly to zero as the broadening becomes comparable with the level separation. It is sometimes useful to express Γ as an equivalent temperature ΔT, the 'Dingle temperature' $\Delta T = \hbar/\pi K\tau$ where τ is the collision time. In the relatively low field region where an exponential approximation can be made to the hyperbolic sine term mentioned above the collision damping term amounts to a simple additive correction to the measured temperature.

Soule, McClure and Smith (1964) give a formula which can approximately reproduce most of the results of the various theories of the SDH effect. This gives for the oscillatory term due to one carrier:

$$G = H^n \sum_{K=1}^{\infty} W_K \frac{KU}{\sinh KU} \exp\left(-\frac{KU\Delta T}{T}\right) \cos\left(\frac{2\pi K}{PH} - \psi_K\right)$$

where $U = \frac{2\pi^2 KTm^*c}{\hbar e} \frac{1}{H}$ and ΔT is the effective temperature change due to collision broadening $\Delta T = \hbar/\pi K\tau$ where τ is the collision time. Another similar term is added for the other carrier.

The results of various theories can be represented by choosing specific values of n, w, ψ. The generalisation comes in allowing these to have arbitrary values. In Section 4.2.3 this expression is used to fit experimental data in order to derive values for m^* and P the effective mass and period, respectively.

2.4 MAGNETO-CONDUCTIVITY TENSOR ANALYSIS

We follow McClure, 1956, in deriving the form of the magneto-resistance effect and Hall effect as functions of magnetic field strength. However, we shall not carry it through to the end with the generality of McClure's paper as this would be unjustified in view of our subsequent application of the theory.

2.4.1 General Theory

Wilson p.196, gives the Boltzmann equation in the presence of uniform electric and magnetic fields, assuming a relaxation time τ (see section 2.2.4):

$$(e/\hbar)[\underline{\varepsilon} + \underline{v} \wedge \underline{H}/c].\nabla_k f + (f_o - f)/\tau = 0 \qquad (1)$$

Writing the distribution function as

$$f = f_o - \Phi \, \partial f_o/\partial E \qquad (2)$$

Where Φ is proportional to electric field strength (leading to a solution satisfying Ohm's law) we find the Boltzmann equation reduces to:

$$e/\hbar \; \underline{\varepsilon}.\nabla_k f_o - e/\hbar c \, \frac{\partial f_o}{\partial E} \; \underline{v} \wedge \underline{H}.\nabla_k + \Phi/\tau \; \frac{\partial f_o}{\partial E} = 0$$

i.e. $$- (e/\hbar c) \; \underline{v} \wedge \underline{H}.\nabla_k \Phi + \Phi/\tau + e \; \underline{\varepsilon}.\underline{v} = 0 \qquad (3)$$

This is to first order in ε.

The first term represents the derivative of Φ along a curve called the hodograph, formed by the intersection of a plane perpendicular to H with a constant energy surface.

To describe the position of the representative wave vector of the electron on the hodograph we define a new variable S such that $\frac{\partial \underline{k}}{\partial S} = -(e/\hbar c)\, \underline{v} \wedge \underline{H}$. Thus S represents the time at which the representative point, moving in a magnetic field only, reaches the point $\underline{k}$. Equation (3) now becomes:

$$\frac{\partial \phi}{\partial S} + \phi/\tau + e\, \underline{\varepsilon}.\underline{v} = 0 \qquad (4)$$

This is easily solved, to give:

$$\Phi = -\int_r^S dS' e\underline{\varepsilon}.\underline{v}(S') \exp\left[-\int_{S'}^S dS''(S'')\right] \qquad (5)$$

where r is to be determined by the boundary condition that ϕ must be a periodic function of S and turns out to be $-\infty$.

If we now assume that τ is constant on a given hodograph and use the periodicity of the velocity to write it as a Fourier expansion:

$$\underline{v} = \sum_{-\infty}^{\infty} \underline{v}(m) \exp(im\omega s) \qquad (6)$$

where ω is the cyclotron frequency for the hodograph, given by $\frac{2\pi}{\omega} = \oint \frac{\hbar c}{eH} \frac{dk}{v\rho}$; $v\rho$ is the velocity component perpendicular to H, our

solution now becomes:

$$\phi = -\tau \sum_{-\infty}^{\infty} \frac{e\underline{\varepsilon}.\underline{v}(m)\ \exp(im\omega s)}{(1 + im\omega\tau)} \tag{7}$$

To find the conductivity tensor we must first write down the current. For a single band this is:

$$\underline{j} = -e/(2\pi)^3 \int d^3k\underline{v}f = \frac{-e}{(2\pi)^3} \int_{BZ} d^3k\underline{v}\phi(\frac{-\partial f_o}{\partial E}) \tag{8}$$

Now, since for a given band, the energy is a continuous function of $\underline{k}$ within the Brillouin zone, we may replace the integrand at any point $\underline{k}$ by the average over the hodograph through $\underline{k}$. This does not change the value of the integral over the BZ.

Thus,
$$\underline{j} = e^2/(2\pi)^3 \int_{BZ} d^3\underline{k}(-\partial f_o/\partial E)\underline{M} \tag{9}$$

Where the vector
$$\underline{M} = -(\frac{\omega}{2\pi e\tau})\oint dS\ \phi\underline{v} \tag{10}$$

Substituting for ϕ from 7 we find

$$\underline{M} = \frac{\omega}{2\pi e\tau} \sum_{m} \frac{1}{1 + im\tau} \oint dS \left[\sum_{n} \underline{v}(n)e^{in\omega s}\right]\underline{\varepsilon}.\underline{v}(m)e^{im\omega s} \tag{11}$$

i.e.
$$\underline{M} = \sum_{-\infty}^{\infty} [\underline{\varepsilon}.\underline{v}(m)]\underline{v}(-m)/(1 + im\omega\tau)$$

We now define a tensor $\underline{\underline{S}}$ by $\underline{M} = \underline{\underline{S}}.\underline{\varepsilon}$, and choose $\underline{H}$ to be parallel to the z-axis. The components of $\underline{\underline{S}}$ give rise to the components of the magnetoconductivity tensor. Using the fact that $S_{xx} = \left.\frac{M_x}{\varepsilon_x}\right\} \varepsilon_y = \varepsilon_z = 0$ etc., it is easily shown that the components of $\underline{\underline{S}}$ are:

$$S_{xx} = v_x^2(0) + \sum_{m=1}^{\infty} \frac{|v_x(m)|^2}{1 + (m\omega\tau)^2} \tag{12}$$

$$S_{xy} = \sum_{m=1}^{\infty} \left[(v_x(m)v_y(-m) + v_x(-m)v_y(m)) + im\omega\tau\,(v_x(-m)v_y(m) - v_x(m)v_y(-m)) \right] / (1 + (m\omega\tau)^2) \tag{13}$$

$$S_{zz} = v_2^2(0) + \sum_{m=1}^{\infty} \frac{|v_z(m)|^2}{1 + (m\omega\tau)^2} \tag{14}$$

Similar expressions hold for the other components. In general, $S_{ij}(\underline{H}) = S_{ji}(-\underline{H})$. McClure shows that $v_x(0) = v_y(0) = 0$, but this is imposed by our more severe symmetry restrictions in any case. Thus, S_{zz} is the only component which approaches a finite limit as $H \to \infty$.

The conductivity follows:

$$\underline{\sigma} = e^2/(2\pi)^3 \int_{BZ} d^3k\, (-\partial f_o/\partial E)\tau\, \underline{\underline{S}} \tag{15}$$

If degenerate statistics apply, $\partial f_o/\partial E$ is only appreciable for energies near the Fermi energy so the integral can be transformed to one over the FS. If, in addition, τ is constant over the FS the form of $\underline{\underline{\sigma}}$ would be the same as that of $\underline{\underline{S}}$.

So far we have been dealing with one band only and we note here that summing the contributions from several bands would lead to additive contributions to $\underline{\underline{\sigma}}$ from the different bands, each of the form derived above.

It is now necessary to find the Fourier components of velocity for use in 12, 13, 14. The energy can be expressed in cylindrical coordinates, $E = E(\rho, \theta, k_z)$. A given hodograph can be described by $k_z = \text{const.}$, $\rho = \rho(\theta)$. Since the energy is a single-valued function of $\underline{k}$ for a given band, it must be periodic in θ:

We can write,
$$E = \sum_{-\infty}^{\infty} E_n(\rho, k_z) \exp(in\theta) \qquad (16)$$

The velocity is obtained by taking the gradients of E. e.g. $v_x = \frac{1}{\hbar} \frac{\partial E}{\partial k_x}$.

It is easy to show that the gradient operators required are:

$$\frac{\partial}{\partial k_x} = \cos\theta \frac{\partial}{\partial \rho} - \frac{1}{\rho} \sin\theta \frac{\partial}{\partial \theta}$$

$$\frac{\partial}{\partial k_y} = \sin\theta \frac{\partial}{\partial \rho} + \frac{1}{\rho} \cos\theta \frac{\partial}{\partial \theta}$$

Thus

$$v_x = 1/\hbar \sum [\partial E_n/\partial \rho \cos \theta - i(n/\rho)E_n \sin \theta] \exp [in \theta]$$

$$v_y = 1/\hbar \sum [\partial E_n/\partial \rho \sin \theta + i(n/\rho)E_n \cos \theta] \exp [in \theta]$$

These can be written:

$$v_x = 1/\sqrt{2} \ (g + g^*) \tag{17}$$

$$v_y = i/\sqrt{2} \ (g - g^*) \tag{18}$$

where $$g = \sum_{n=-\infty}^{\infty} 1/\sqrt{2}\hbar \ [\partial E_n/\partial \rho - (n/\rho)E_n] \exp(i(n + 1)\theta) \tag{19}$$

Now we shall restrict ourselves to a band structure with rotational symmetry about the k_z axis. This implies that E is independent of θ and so all Fourier coefficients, E_n, except E_o (ρ, k_z) are zero. McClure considers less severe symmetry restrictions but as we intend to apply the Kramers-Kronig relations to our conductivity at a later stage, it is more convenient to impose one of the conditions for their validity, viz. cylindrical symmetry, at this point. (19) now becomes

$$g = \frac{1}{\sqrt{2}\hbar} \ \frac{\partial E_o}{\partial \rho} \exp(i\theta) \tag{20}$$

But this must be expressed in terms of the time variable, S. In general, ρ is a function of θ and θ is a function of S ($\theta = \omega S +$ periodic function of S). For our symmetry, ρ is independent of θ and $\theta = \omega S$ so we have:

$$g = \left[\frac{1}{\sqrt{2\hbar}} \frac{\partial E_o}{\partial \rho}\right] \exp(i\omega S) = B \exp(i\omega S), \text{ say.} \tag{21}$$

Thus, the velocity components are

$$v_x = \frac{1}{\sqrt{2}} (B \exp(i\omega S) + B^* \exp(-i\omega S))$$

$$v_y = \frac{i}{\sqrt{2}} (B \exp(i\omega S) - B^* \exp(-i\omega S))$$

Comparing this with (6), we see that

$$v_x(1) = B/\sqrt{2}, \qquad v_y(1) = iB/\sqrt{2}$$

all other v(m)'s are zero.

$$v_x(-1) = B^*/\sqrt{2}, \qquad v_y(-1) = -i B^*/\sqrt{2}$$

Hence we have for the tensor $\underline{\underline{S}}$

$$S_{xx} = S_{yy} = \frac{B^2}{1 + (\omega\tau)^2}$$

$$S_{xy} = -S_{yx} = \frac{B^2 \omega\tau}{1 + (\omega\tau)^2} \tag{22}$$

The conductivity follows from (15):

$$\sigma_{xx} = \sigma_{yy} = \sum_b \frac{e^2}{(2\pi)^3} \int_{BZ} \tau \left(\frac{-\partial f_o}{\partial E}\right) \frac{B^2}{1 + (\omega\tau)^2} \, d^3K$$

$$\sigma_{xy} = -\sigma_{yx} = \sum_b \frac{e^2}{(2\pi)^3} \int_{BZ} \tau \left(\frac{-\partial f_o}{\partial E}\right) \frac{B^2 \, \omega\tau}{1 + (\omega\tau)^2} \, d^3K \qquad (23)$$

where summation b is over the bands.

Now, for graphite, which is highly degenerate below 200°K, $\partial f_o/\partial E$ localises the integrand to the neighbourhood of the FS. We have thus reduced the number of independent variables to one, since the integration is over a surface with circular symmetry. Fixing any one of the functions τ, B, H (proportional to ω), k_x, k_y, or k_z immediately fixes the values of the others (with the reservation that some functions may be multi-valued with respect to a given variable) and thus the value of the integrand.

McClure 1958, chooses a variable $S \equiv (\frac{\omega\tau}{H})$ which is proportional to relaxation time. The fact that τ has been taken to be constant on a given hodograph in the above analysis is of no consequence, nor is the possibility that parts of the integrand may be multi-valued in the new variable, as this is easily absorbed into the function g(S) with which we now replace all explicit references to τ, $\underline{k}$, B or E. Bearing this last remark in mind, we can see that the integration is merely

being taken over all complete nodographs lying on the FS, each one being labelled by its relaxation time and that the appropriate limits of integration are from 0 to ∞ .

Thus, we have finally:

$$\sigma_{xx} = \sum_b \int_0^\infty \frac{g(S)\, dS}{1 + (SH)^2}$$

$$\sigma_{xy} = \sum_b \int_0^\infty \frac{SH\, g(S) dS}{1 + (SH)^2} \qquad (24)$$

Where the summation b is over the bands.

2.4.2 Application to Graphite

We shall now employ the expressions obtained in the last section to show how the carriers in graphite can be separated and their properties found from measurements of the conductivity and Hall effect.

Dividing the carriers in graphite into positive and negative carriers, we can write:

$$\sigma_{xx} = \sigma^p_{xx} + \sigma^n_{xx} = \int_0^\infty \frac{dS\, gp\,(S)}{1 + (SH)^2} + \int_0^\infty \frac{dS\, gn\,(S)}{1 + (SH)^2} \qquad (1)$$

$$\sigma_{xy} = \sigma^p_{xy} + \sigma^n_{xy} = \int_0^\infty \frac{dS(SH)g^p(S)}{1 + (SH)^2} + \int_0^\infty \frac{dS(SH)gn(S)}{1 + (SH)^2}$$

where σ^p, σ^n could each possibly contain additive contributions from several carriers of differing mass, etc. We recall, too, that these

expressions are based on circular orbits and a constant relaxation time on a given orbit.

Kramers-Kronig Relations

It can be shown, by contour integration, that

$$\frac{1}{i\pi} \; P \int_{-\infty}^{\infty} f(x)/(x - X)\, dx = f(X)$$

where P means that the Cauchy principal part of the integral is to be taken. Now suppose f(X) is complex: $f(X) = f'(X) + if''(X)$. Then we find:

$$f'(X) = \frac{1}{\pi} P \int_{-\infty}^{\infty} \frac{f''(x)\, dx}{(X - x)}$$

$$f''(X) = \frac{1}{\pi} P \int_{-\infty}^{\infty} \frac{f'(x)\, dx}{(X - x)} \qquad (2)$$

By applying these to two functions of magnetic field

$$f(H) = \sigma_{xx}^{P}(H) + i\sigma_{xy}^{P}(H)$$

and

$$f(H) = \sigma_{xy}^{n} + i\sigma_{xx}^{n} \; ,$$

we obtain relations between the diagonal and off-diagonal partial conductivities:

$$\sigma_{xx}^{P} = \frac{-1}{\pi} P \int \frac{\sigma_{xy}^{P}\, dx}{H - x} \qquad \sigma_{xy}^{P} = \frac{1}{\pi} P \int \frac{\sigma_{xx}^{P}\, dx}{H - x}$$

$$\sigma_{xx}^{n} = \frac{1}{\pi} P \int \frac{\sigma_{xy}^{n}\, dx}{H - x} \qquad \sigma_{xy}^{n} = \frac{1}{\pi} P \int \frac{\sigma_{xx}^{n}\, dx}{H - x}$$

These can be reassembled to relate the partial conductivities to the total conductivities:

$$\sigma_{xy}^{P} - \sigma_{xy}^{n} = \frac{P}{\pi} \int_{-\infty}^{\infty} \frac{dH'}{H - H'} \sigma_{xx}(H') \qquad (3)$$

$$-\sigma_{xx}^{P} + \sigma_{xx}^{n} = \frac{P}{\pi} \int_{-\infty}^{\infty} \frac{dH'}{H - H'} \sigma_{xy}(H')$$

It can now be seen that by simple addition and subtraction between 1 and 3 the four partial conductivities can be obtained. We assume, of course, that σ_{xx} and σ_{xy} can be written in the form of the integral expressions in (1); this point is taken up later.

Total Number of Electrons and of Holes

Swanson (1955), and Lifshitz et al (1957), show that the number of carriers of a given kind is given by $pec = \int_{o}^{\infty} \frac{ds\, \rho_0(S)}{S}$, where p is the number of holes per unit volume (n for electrons), e is the electronic charge and c is the velocity of light. Thus we can obtain p and n from high-field Hall data for obviously $pec = (H\sigma_{xy}^{P})_{H \to \infty}$ and $nec = (H\sigma_{xy}^{n})_{H \to \infty}$. (4)

Average mobilities of electrons and holes

For a given carrier, we have the relation between conductivity and mobility μ : $\sigma = ne\mu$. Thus, using the zero-field partial conductivities:

$$\mu_n = \frac{\sigma^n(0)_{xx}}{ne}, \quad \mu_p = \frac{\sigma^p(0)_{xx}}{pe} \tag{7}$$

Where p and n are known from the above section. The mobilities so derived are obviously 'averaged' in the sense that they have been calculated from a combination of high and low-field data.

Finally, the difference in the zero-field conductivities can be shown to be given by:

$$\sigma^p_{xx}(0) - \sigma^n_{xx}(0) = \frac{2}{\pi} \int_0^\infty \frac{dH}{H} \sigma_{xy} \tag{8}$$

For

$$[\sigma^p_{xx} - \sigma^n_{xx}]_{H=0} = -\frac{1}{\pi} \int_{-\infty}^{\infty} \frac{dH'}{-H'} \sigma_{xy}(H')$$

Now, $\sigma_{xy}(H) = -\sigma_{yx}(-H)$ since $\sigma_{xy} = -\sigma_{yx}$ for graphite.

Hence, $$\text{LHS} = +\frac{1}{\pi} \int_{-\infty}^{0} \frac{dH'}{+H'} \sigma_{xy}(H') + \frac{1}{\pi} \int_0^\infty \frac{dH'}{+H'} \sigma_{xy}(H')$$

$$= -\frac{1}{\pi} \int_0^{-\infty} \frac{+dH'}{+H'} \sigma_{xy}(+H') + \frac{1}{\pi} \int_0^\infty \frac{dH'}{H'} \sigma_{xy}(H')$$

QED $$= \frac{2}{\pi} \int_0^\infty \frac{dH'}{H'} \sigma_{xy}(H')$$

Total number of carriers

As a check on 4 and a useful result in itself, we shall show that the total number of carriers, $(n + p)$, is given by

$$(n + p)ec = \frac{2}{\pi} \int_0^\infty dH\, \sigma_{xx}(H) \tag{5}$$

The RHS is, from 1,

$$= \frac{2}{\pi} \int_0^\infty dH \left[\int_0^\infty \frac{(g_p + g_n)\, dS}{1 + (SH)^2} \right]$$

Hence, as there are no discontinuities in the plane of integration, we may reverse the order of integration, to obtain:

$$\frac{2}{\pi} \int_0^\infty dS \left[\frac{1}{S} \tan^{-1} \frac{H}{S} \right]_0^\infty = \frac{2}{\pi} \int_0^\infty \frac{dS}{S} (g_p + g_n) \frac{\pi}{2}$$

which is the LHS by the relations $pec = \int_0^\infty \frac{dS\, gp(S)}{S}$ etc.

In analogy to equations (4), a further expression for the total number of carriers is:

$$(n + p)ec = (H\sigma_{xy})_{H \to \infty} \tag{6}$$

Representation of data as a function of magnetic field

Our problem at this stage is to obtain the integrals in (1) which describe the experimental variations of the conductivity with field. We follow McClure in using a sum of Lorentzians of the form

$$\sigma_{xx},\ \sigma_{xy}/H = \sum_n \left\{A_n/(1 + (H/H_n)^2)\right\} \qquad (9)$$

where the A_n and H_n are constants to be used in fitting the experimental points. The justification for this is that very good fits can be obtained with two or three terms and that these expressions make it easy to apply the Kramers-Kronig relations. We regard this as a convenient way of representing the data and do not at first make any identification between the individual terms and the various carriers, though such might be justified if the carriers turned out to have very different characteristics. The procedure used in fitting data to these expressions is described elsewhere (4.1.3).

Let us now apply the K-K relations to these Lorentzians as required by (3). To evaluate the integrals (3) we use partial fractions

$$\int_{-\infty}^{\infty} \frac{dH'}{H - H'}\sigma_{xy}(H') = \sum_i \int_{-\infty}^{\infty} \left(\frac{H}{H_i'^2 + H^2}\ \frac{dx}{H - x} + \frac{H}{H_i'^2 + H^2}\ \frac{xdx}{H_i'^2 + x^2}\right.$$

$$\left. - \frac{H_i'^2}{H_i'^2 + H^2}\ \frac{dx}{H_i'^2 + x^2}\right)$$

$$= \sum_i \frac{H}{H'^2_i + H^2} \frac{1}{2}\left[\log \frac{H'^2_i + x^2}{H^2 - 2Hx + x^2}\right]_{-\infty}^{\infty}$$

$$- \sum_i \frac{H'^2_i}{H'^2_i + H^2} \frac{1}{H'^2_i}\left[\tan^{-1} \frac{x}{H'_i}\right]_{-\infty}^{\infty}$$

$$= - \sum_i \frac{H'_i \pi}{H'^2_i + H^2}$$

Similarly,

$$\int_{-\infty}^{\infty} \frac{dH'}{H - H'} \sigma_{xx}(H') = \sum_i \frac{\pi}{H_i} \frac{H}{H_i^2 + H^2}$$

Tnis equations (3) become:

$$\begin{aligned} - \sigma^p_{xx} + \sigma^n_{xx} &= - \sum_i \frac{A'_i H'^3_i}{H'^2_i + H^2} \\ \sigma^p_{xy} - \sigma^n_{xy} &= H \sum_i \frac{A_i H_i}{H_i^2 + H^2} \end{aligned} \qquad (10)$$

In accordance witn tne view that tne A_i, H_i, A'_i, H'_i are merely fitting parameters, we do not expect tne H_i and H'_i to be tne same in general.

By combining (1) and (10) we obtain the four partial conductivities.

Summary of formulae

We now collect some of the above formulae for future convenience, using the fitting parameters to describe the magnetoconductivity tensor components.

Carrier densities

$$\left(\begin{matrix}p\\n\end{matrix}\right) ec = \left(H\sigma^{\begin{matrix}p\\n\end{matrix}}_{xy}\right)_{H\to\infty} = \tfrac{1}{2}\left[\sum_j A'_j H'^2_j \pm \sum_i A_i H_i\right] \tag{11}$$

$$(n + p)\, ec = \frac{2}{\pi}\int_0^\infty dH\sigma_{xx}(H) = \sum_i A_i H_i \tag{12}$$

Partial conductivities

$$\begin{aligned}
\sigma^{\begin{matrix}p\\n\end{matrix}}_{xx} &= \tfrac{1}{2}\left[\sum_i \frac{A_i H_i^2}{H_i^2 + H^2} \pm \sum_j \frac{A'_j H'^3_j}{H'^2_j + H^2}\right] \\
\sigma^{\begin{matrix}p\\n\end{matrix}}_{xy} &= \tfrac{1}{2}\left[H\sum_j \frac{A'_j H'^2_j}{H'^2_j + H^2} \pm H\sum_i \frac{A_i H_i}{H_i^2 + H^2}\right]
\end{aligned} \tag{13}$$

$$\sigma^P_{xx}(0) - \sigma^n_{xx}(0) = \frac{2}{\pi}\int_0^\infty \frac{dH}{H}\,\sigma_{xy} = \sum A'_j H'_j \tag{14}$$

Mobilities

$$\bar{\mu}_{n}^{p} = \frac{\overset{p}{\underset{n}{\sigma(0)_{xx}}}}{(\overset{p}{n})_{e}} = \frac{(\Sigma A_i \pm \Sigma A'_j H'_j)}{(\Sigma A'_j H'^{2}_j \pm \Sigma A_i H_i)} \, c \qquad (15)$$

CHAPTER 3

EXPERIMENTAL

3.1 MATERIALS - PREPARATION OF SAMPLES

Sample Shape

With materials which are known to be highly anisotropic, it is essential to ensure that the current flow in principal directions is homogeneous. This makes the adoption of suitable sample shapes, electrode positions and application techniques more important than is perhaps the case with homogeneous isotropic media. Thus it is desirable to minimise the shorting effects of the current electrodes on the hall voltage and the perturbation of the potential probes on the uniform current distribution down the sample. Spain (1967) used paper coated with a nearly uniform conductive layer to form a two-dimensional analogue of the proposed sample configuration and verified that corrections were negligible provided that the ratio of sample length to width was greater than about four. The samples used in the present investigation were cut with this finding in mind and a similar analogue technique was used to observe the actual current flow in the samples as fabricated. A photograph was taken of each sample and the outline traced onto the conductive paper from an enlarged print. Silver dag was then painted along the outlines of the plated contact areas and a current of about 10 mA was passed through the current electrodes from an accumulator. An ordinary pencil connected to a high impedance electronic voltmeter was used to plot the course of

the equipotential lines across the analogue. In particular, the positions of the three equipotential lines leaving the silver paint on the three potential arms were noted, and it was found that a slight correction was necessary to give the actual distance between these equipotentials (electrical separation). The correction was usually less than 1%. The three analogues obtained for the samples reported here are shown in Figure 3.1.

Previous measurements of c-axis properties have depended upon having samples from 5 to 10 mm. thick in the c-axis direction. However, analogue experiments by M.L. Yeoman (unpublished) have shown that it is possible to perform useful measurements upon samples only 2 or 3 mms. thick. The technique is to cut a rectangular piece out of a cleaved disc of the required thickness and to copper-plate all of the top and bottom faces except for small islands near the centre of each face. These regions are plated separately, leaving a narrow annulus of untouched graphite between the two areas on each face. Current is fed into the large areas and potential leads attached with silver dag in the usual manner to the central areas. It is doubtful whether accurate absolute values of resistivity can be obtained by this means because of the difficulty in measuring the thickness of the slab and in making the side faces perfectly parallel to the c-axis. Additionally, corrections to the measured resistance of the order of a few % must be applied. Probably an analogue investigation of samples as-

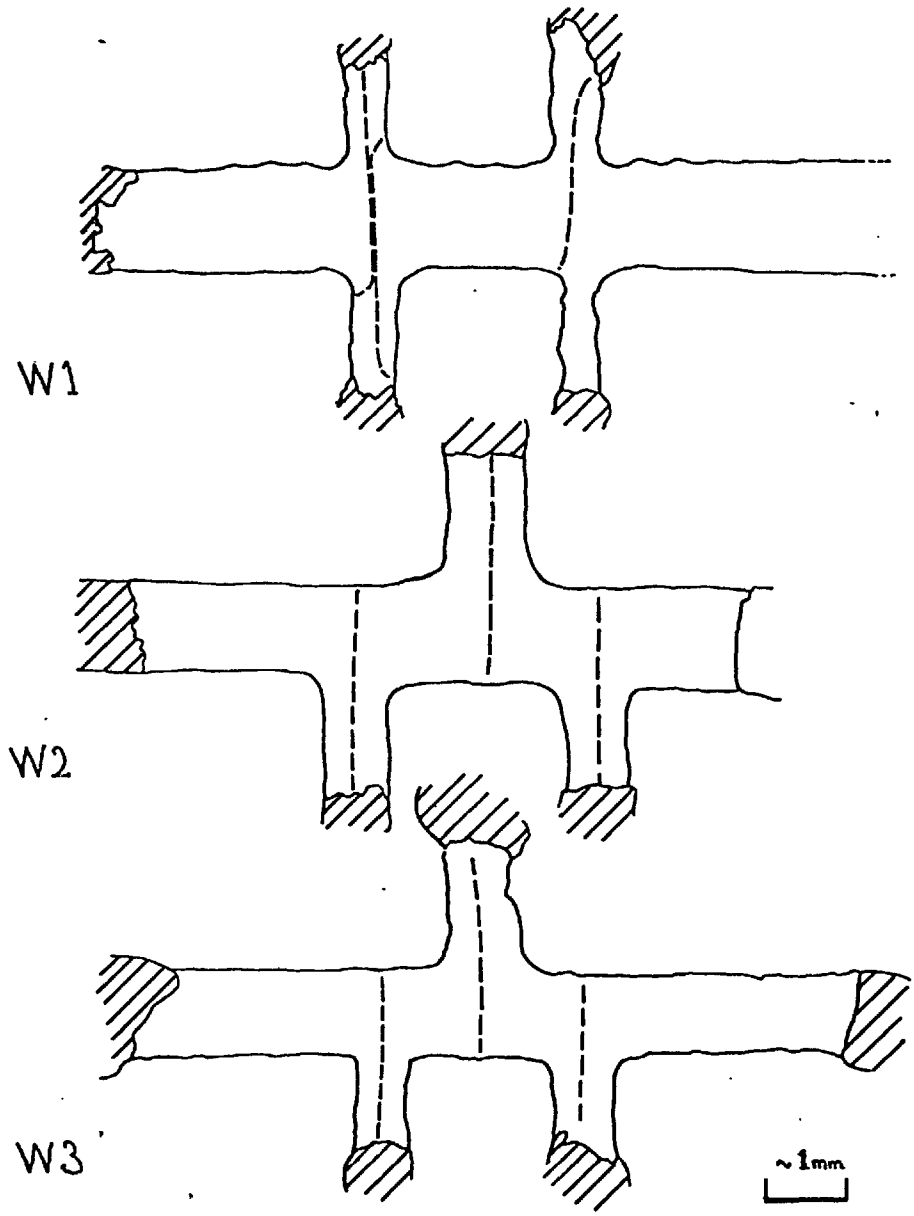

FIGURE 3·1

PYROLYTIC GRAPHITE SAMPLES, SHOWING THE EQUIPOTENTIAL LINES FROM EACH OF THE THREE POTENTIAL PROBE ARMS.

made rather than as-desired would enable the correction to be estimated with sufficient accuracy, as is the case with basal plane samples. Extra care must be exercised during plating to prevent the formation of copper globules on the edge of the sample since these would have a disatrous effect on the current distribution.

Cutting the samples

The samples reported here were cut from ~~four~~ three different preparations of pyrolytic graphite. Their properties are listed in the table following. W1 had been prepared previously by Spain(1967) with four potential arms, only three of which were in good enough condition to be used. Unfortunately, these were wrongly disposed relative to each other for simple Hall measurements and it was necessary to reverse the magnetic field and subtract two sets of readings before a meaningful Hall voltage could be obtained. This considerably complicated the analysis of chart recordings for this sample. The other two basal plane samples were cut in the usual bridge pattern: starting with a cleaved disc in the case of W2 and a cleaved piece of inner-layer material in the case of W3 (the current path was parallel to the cylinder axis so this sample ended up with slightly curved potential probes), the pyrolytic graphite was fixed to a layer of tissue paper stretched over a hole in a brass plate. A suitable shaped mask, cut and filed from thin brass, was similarly fixed with a flexible red cement onto the upper face of the graphite and an air-carried jet of abrasive dust (alumina) was directed at the unprotected parts of the graphite. After a little practice it was possible to cut samples with

straight edges, at right angles to the front face, in about 20 minutes. A pencil brush was used to remove mask, tissue, and backing plate from the sample with the assembly immersed in acetone.

Before plating, the contact areas were slightly abraded with the dust jet. A simple mask was employed to shield the main body of the sample and one or two quick passes with the jet were all that was required. The coloured cement was used to shield all areas of the sample except the tips which were to be plated, particular care being taken with the edges of the graphite where plating occurs very readily. A plating lead was attached with silver dag cement and the sample left to plate in a slightly acid 10% solution of copper sulphate with a current density of about $1mA/cm^2$. Once a continuous copper sheath sufficient to short all the graphite layers together had formed, the plating wire was removed with acetone and wires were attached to all other contact areas of the sample with the conducting silver paint. This final contact was then completed in a similar manner. The initial copper plating was considered to be essential to the success of this technique because analogue experiments have shown the extreme importance of electrically tying all the high conductance basal planes together. Finally, all contact areas were given another plating to form copper caps over the dried

silver cement. Great care was needed to prevent shorting the current and potential areas of c-axis samples, and for both types of sample there was a tendency for copper to be plated in globules along the "masked" edge of the graphite. Several carefully applied cement layers were needed to prevent this. The 40 swg copper wires used to make connection to the samples could be bent without fear of damaging the graphite but they were easily broken off at the sharp edges of the silver paint. Any short length of wire inadvertently sheathed in silver paint could not be safely bent at all. Contact resistances achieved by the above techniques were quite insignificant compared with the several ohms resistance of the wires leading out of the cryostat.

Mounting of samples - alignment

Basal-plane samples were stuck to tufnol frames for ease of manipulation, the current leads being soldered to electrically insulated heat posts attached by "Araldite" to the copper sample block. By gently bending these wires until a travelling microscope indicated that the basal-planes were parallel to the axis of the copper block, the normal to the basal-planes was brought to within 0.2° of a position perpendicular to this axis. Once the copper block was screwed into position on the cryostat, the sample c-axis was within 0.2° of the horizontal plane. Because of the effective planar isotropy within the layer planes it was

SAMPLES USED IN THIS STUDY

W1 Starting material IFP53 (Spain et al. 1967). Hot-pressed at 2970°C, annealed at 3500°C. Density 2.266 gms/cm^3.

W2 Starting material IFP64T. Hot-pressed at 2850°C, annealed at 3500°C. Density 2.26gms/cm^3.

W3 Selected inner layer material (Section 1.2); annealed at $\geq$ 3700°C.

not necessary to align the current axis accurately to the vertical so this was done by eye. A simple rotation of the magnet about its vertical axis now brought the magnetic field vector (B) parallel to the c-axis (position T1), or normal to it (position T2) see Figure 3.2. Coloured cement was used to fix the sample into position and to hold the wires firmly in contact with the copper block. Forces of the order of fractions of a gram-wt were expected on the wires when the magnetic field was near its maximum value so they were coated with the cement to stiffen them sufficiently to prevent movement. Tissue paper was used where electrical insulation was required. C-axis samples were aligned in a similar way and fixed with the cement. The thermocouple bead was attached to the sample face with a thin layer of tissue paper to isolate it electrically but not thermally. Care was taken to prevent any wire from touching the outer copper cap which was slipped over the whole assembly to form the exchange gas space.

3.2 FORM OF THE RESULTS - TAKING THE MEASUREMENTS

Sample voltages were of the order from μV to hundreds of μV for the Hall effect and from μV up to mV for magnetoresistance. A Pye three-dial Vernier potentiometer, measuring to 1 μV on the last dial, was employed with a Tinsley galvanometer amplifier to enable voltages to be estimated to within 0.1 μV. By means

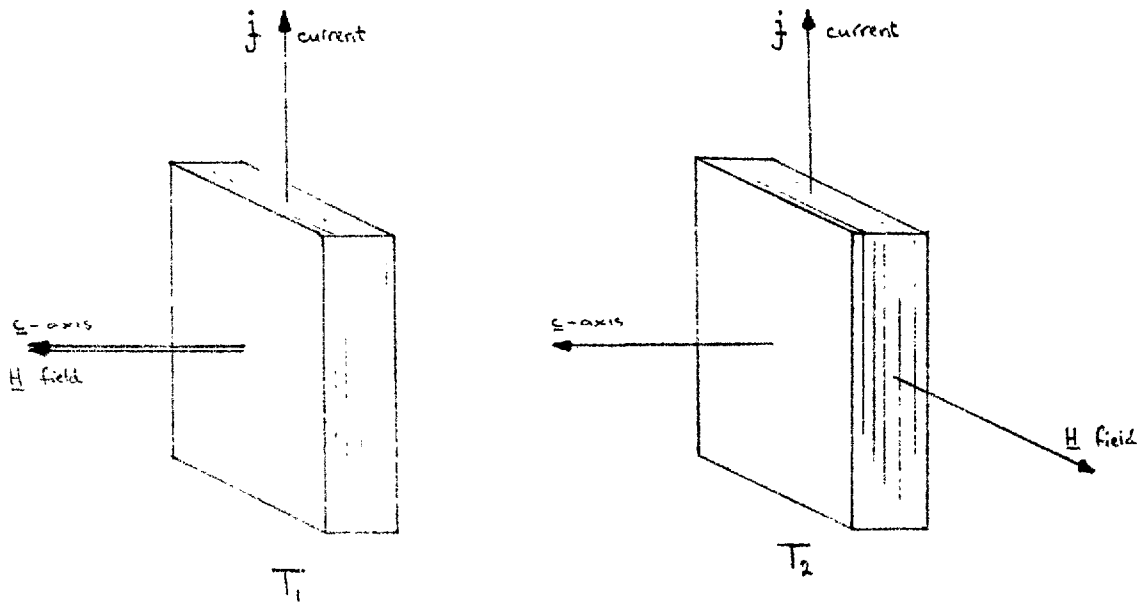

FIGURE 3.2 SAMPLE ORIENTATIONS

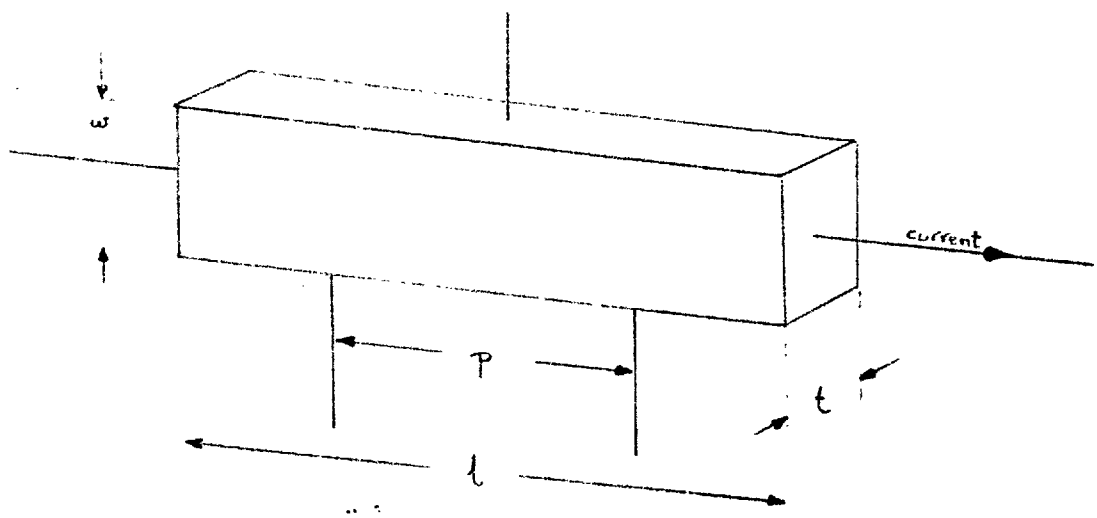

FIGURE 3.3 ILLUSTRATING SAMPLE DIMENSIONS

of a switchbox described below this potentiometer was used for measuring sample resistive and Hall voltages, sample current as measured by the voltage developed across a standard 0.1 Ω and the current supplying a Hall probe placed in the magnet pole gap. The Hall probe output could be switched to the potentiometer when required. Free inputs on the potentiometer itself were used for measuring the thermocouple output with respect to a liquid oxygen standard maintained in a dewar vessel. The Hall probe output and sample voltage were usually switched into the two axes of an X-Y chart recorder to produce a trace which was approximately a plot of sample voltage against magnetic field - approximately because, although the electronic system was verified to be linear in response to about 1/10th percent, the Hall probe output was quadratic in field. A slow-sweep unit was used to change the magnetic field at a low rate, generating a trace on the chart recorder. It was usual to generate two sets of charts for each temperature - one set over the whole field range available (up to nearly 18 kgauss) and the other, using expanded recorder scales, up to about 6 kgauss. Calibration points were put onto charts by stopping the field sweep as was convenient and measuring relevant voltages with the potentiometer.

Consider now a sample with the dimensions shown in the diagram, Figure 3.3 of width ω, thickness t and with a uniform current flow down its length.

The Hall coefficient R_H and resistivity $\rho(H)$ in transverse magnetic field H are related to the Hall voltage V_H across the width of the sample and the voltage V_S down the length of the sample (between probes spaced a distance p apart) by

$$R_H = \frac{V_H/\omega}{HI/\omega t} = \frac{V_H t}{HI}$$

$$\rho = \left(\frac{V_S}{I}\right)\left(\frac{\omega t}{p}\right)$$

Now suppose we make a series of measurements of Hall voltage, reversing magnetic field and current to give four measured voltages:

$$V_1 = V_H + RI + \Delta V + f(I)g(H)$$
$$V_2 = -V_H - RI + \Delta V + f(-I)g(H)$$
$$V_3 = -V_H + RI + \Delta V + f(I)g(-H)$$
$$V_4 = +V_H - RI + \Delta V + f(-I)g(-H)$$

where RI represents a resistive drop due to misalignment of the two effective Hall potential probes, ΔV represents spurious current-independent thermal emf's in the copper leads, and

$f(I)g(H)$ is a function of current I and field H representing magnetothermal effects. We see that the usual practice of taking the combination $(V_1 - V_2 - V_3 + V_4)/4$ gives $V_H + \frac{1}{4}(f(I)g(H) + f(-I)g(-H) - f(-I)g(H) - f(I)g(-H))$ which is just equal to the Hall voltage V_H if the second term is zero.

The second term is zero provided only that $f(I)g(H)$ is not odd in both of the variables I or H. Now if we examine the consequences of the sample not being completely isothermal we see that there are three main sources of transverse voltage, stemming from combinations of magnetothermal and thermoelectric effects. Diagrammatically, we have

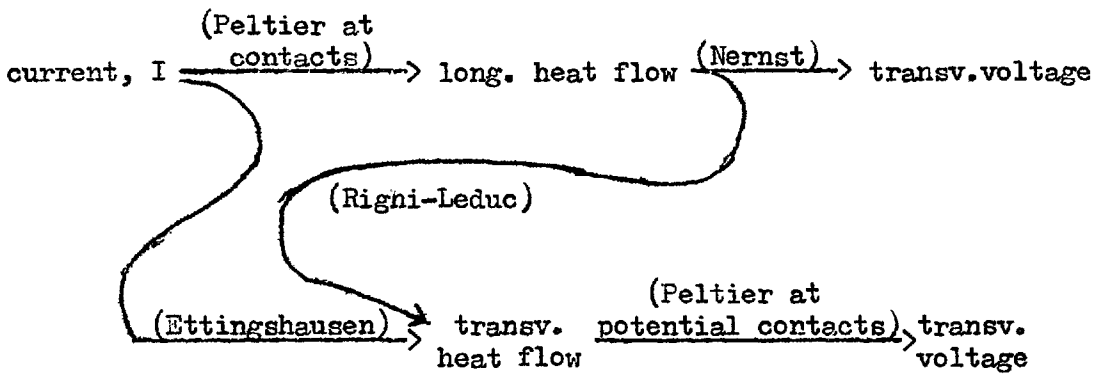

The final effects, the transverse voltages, depend on heat flows and so take time to decay and re-establish themselves if the current is reversed. Measurements taken so quickly that thermal gradients do not have time to change appreciably are termed 'fast'. 'Slow' measurements enable the thermal gradients to reverse completely. The effect of fast and slow reversals of I and H on

TABLE 3.1

			'FAST'	'SLOW'
REVERSAL of CURRENT	N	$f(-I)\,g(H) =$	$f(I)\ g(H)$	$-f(I)\,g(H)$
	RLP	$f(-I)\,g(H) =$	$f(I)\ g(H)$	$-f(I)\,g(H)$
	EP	$f(-I)\,g(H) =$	$f(I)\,g(H)$	$-f(I)\,g(H)$
REVERSAL of MAGNETIC FIELD	N	$f(I)\ g(-H) =$	$-f(I)\,g(H)$	$-f(I)\,g(H)$
	RLP	$f(I)\ g(-H) =$	$f(I)\,g(H)$	$-f(I)\,g(H)$
	EP	$f(I)\ g(-H) =$	$f(I)\ g(H)$	$-f(I)\,g(H)$

EFFECT OF CURRENT AND MAGNETIC FIELD REVERSAL ON THE MAGNETOTHERMAL EFFECTS REPRESENTED BY $f(I)g(H)$.

for example: The magnetothermal voltages change sign on reversal of current ('slow') unless measurements are made before thermal gradients have time to change appreciably ('fast').

the transverse voltages produced by the Nernst (N), Righi-Leduc-Peltier (RLP), and the Ettingshausen-Peltier (EP) combinations are shown in the following table 3.7.

We see that either of the two combinations formed by slow or by fast magnetic field reversal with fast current reversal leads to elimination of all these spurious effects but that the other two combinations, with slow current reversal, fail to eliminate either the Nernst (N) effect of any effect at all.

Hall measurements on sample W1 were performed by reversing both current and field at leisure, since there was no hope of being able to take 'fast' current-reversed measurements because of the high layer-plane thermal conductivity. This procedure eliminated the appreciable misalignment voltage inevitable with this particular sample and also thermal voltages in the leads but it left in the above effects. However, c.f. Putley (1960) P. 86, estimates give about 0.1 μV at 5000 gauss for the dominant effect (Nernst) and orders of magnitude less for the others. Observation of these spurious voltages is possible with bismuth using an oscilloscope triggered by the current or field reversing switch but a high gain d.c. amplifier with sufficiently short response time was not available for checking in the present case. The other basal plane samples were measured by reversing the current. The field was not reversed partly because of the practically impossible task of

rotating the water-cooled magnet through 180° in the confined space around the cryostat without endangering the long-tailed glass dewar which rested, with little lateral movement, in the pole gap. The alternative procedure of slowly decreasing the field to zero, shutting down the generator, reversing the magnet leads and then re-setting the field to its original value took too long to be practicable for the time-limited low temperature runs and introduced the risk of inducing temperature changes through eddy-current heating. 'Slow' current reversal alone eliminated the (not negligible) thermal voltages in the sample leads but accurate zero field balancing was necessary to ensure that no resistive term (RI) appeared in the measured voltage. Two resistance boxes gave a total of about 30 ohms connected across the sample potential arms and the Hall voltage was measured between the junction of the boxes and the third potential arm on the sample. In zero field, the measured voltage was set to zero by adjusting the box resistances to within 0.1 ohm. Thus, at worst, one third of one percent of the resistive voltage drop across the first two potential arms appeared added to or subtracted from the actual Hall voltage. This is most critical at magnetic fields near 3 kgauss where the Hall effect sometimes changes sign. Below this field the magnetoresistance voltage dropped rapidly to zero as H^2 whilst the Hall voltage increased in magnitude before dropping to zero. Above 3 kgauss

the Hall voltage increased more rapidly than the magnetoresistance voltage (though it was always of smaller magnitude) so the fractional error decreased once more. We see that, except for a slight shift in the position of zero Hall coefficient on the field axis, this effect is less than the error involved in measuring sample thickness which appears explicitly in the calculation of the Hall coefficient.

We define magnetoresistance by $M = \frac{\rho(H) - \rho(0)}{\rho(0)}$. In practice this reduced to $M = \frac{V_s(H) - V_s(0)}{V_s(0)}$, since negligible current change occurred during a run. Once more, spurious thermomagnetic potentials could have arisen to perturb the potential difference due to the sample resistance. No current was drawn through the contacts in the potentiometer balance position so only Seebeck emfs due to longitudinal temperature gradients down the sample were likely to have an effect. 'Slow' current reversal does not eliminate these but the temperature gradient which can be established down the sample is held to low values by the high layer-plane thermal conductivity.

3.3 APPARATUS

The apparatus used in the present investigations may be divided into three parts for the purposes of description: the magnet, the cryostat and its associated vacuum equipment, and the electrical measuring equipment.

3.3.1 MAGNET

This dictated the main dimensions of the cryostat. The magnet employed was a Newport Type D electromagnet fitted with high-power, water-cooled coils. Special conical pole-pieces made by Newport to increase the maximum attainable field-strength at the expense of pole-gap. The working pole-gap with these pole-pieces was 4.5 cms, giving a maximum field of about 18 kgauss.

The magnet yoke was mounted on a turn-table inscribed in degrees and fitted with a vernier device reading to tenths of a degree. A trolley enabled the whole magnet assembly to be moved into position on a pair of rails.

A Newport Type 905 C power supply was used in conjunction with the magnet. This consisted of a 25 kW motor-generator whose output was controlled and stabilised from a bench consol. A slow-sweep unit was used to vary the magnet current linearly with time, although this did not, of course, result in a linear variation of field-strength with time.

3.3.2 CRYOSTAT

It was required to maintain the samples at temperatures ranging from room temperature down to below $1^{\circ}K$. Because of the fairly narrow magnet pole-gap and the requirement that it should be possible to rotate the magnet about a vertical axis passing through the sample, the cryostat had to be quite long and thin.

This severely restricted pumping speeds for tubes of reasonable diameter extending down to the sample, and it was apparent that the higher-vapour pressure liquid helium-3 would have to be used to attain temperatures below $1^{\circ}K$.

A diagram of the cryostat appears in Figure 3.4.

The sample was mounted on a copper block screwed into the copper helium-3 chamber. This was kept evacuated at all but the lowest temperatures, when helium-3 was condensed into it. Stainless-steel tubes with thin walls were used to suspend the copper sample block in vacuum and to provide lines for the evacuation of the helium-3 chamber and connections to a vapour pressure manometer. The sample vacuum jacket, maintained within a removable copper cap, was produced by pumping through a further thin-walled stainless-steel tube. It was possible to fill the sample vacuum space with helium-4 gas during initial cooling operations to thermally short-circuit the stainless-steel tubes and ensure rapid cooling of the sample.

The above assembly was immersed in a bath of liquid helium-4 contained in a metal dewar extending upwards to the thick brass base-plate, keeping the steel pumping tubes at very low temperatures (and hence considerably reducing their thermal conductivity) for most of their lengths. In particular, the copper radiation trap was as low down in the dewar as possible to ensure that it

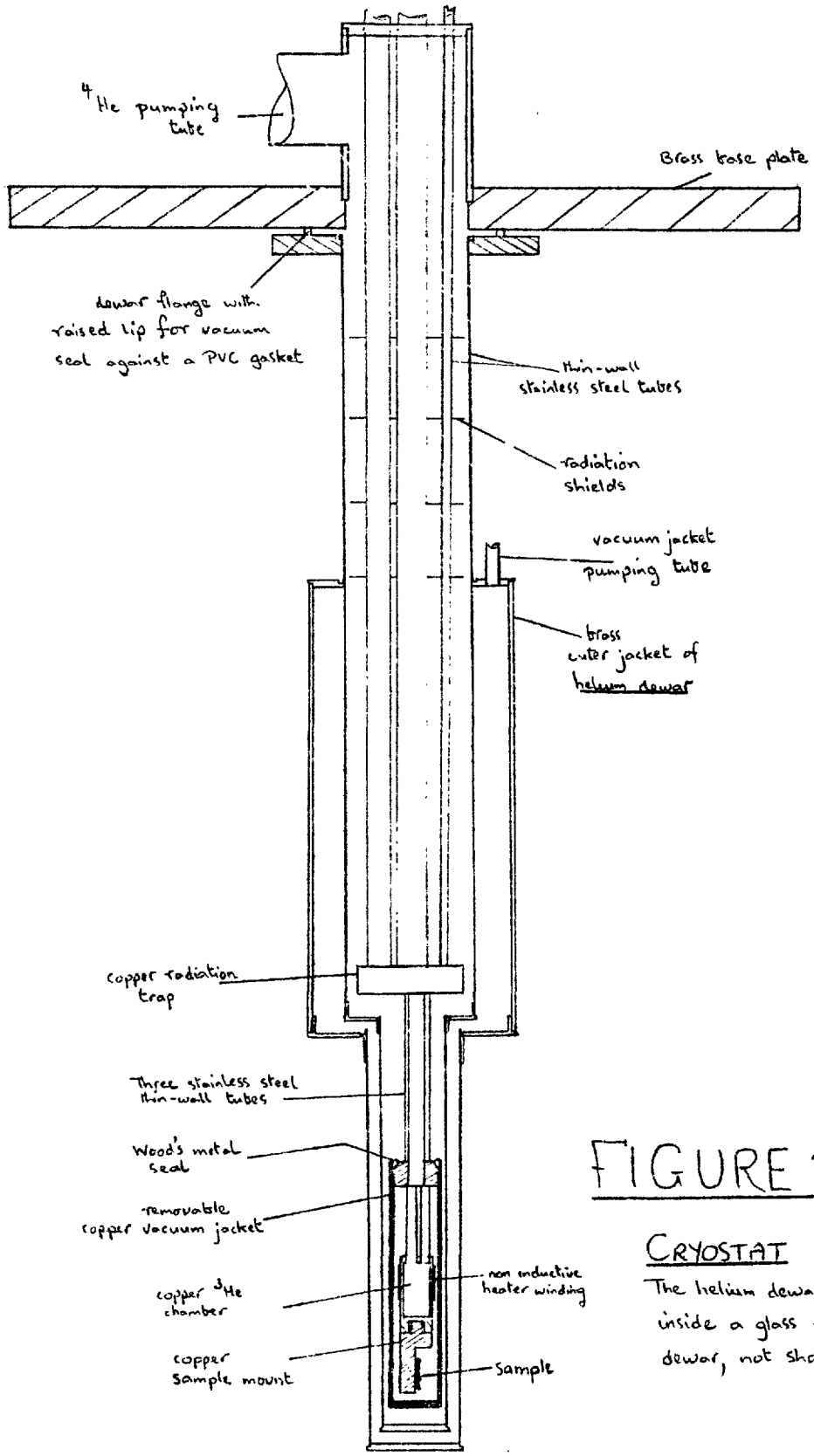

FIGURE 3.4

CRYOSTAT

The helium dewar is inside a glass nitrogen dewar, not shown

re-emitted energy at a low power to the sample block hanging immediately below it. Radiation shields consisting of foam plastic faced with aluminium foil were positioned at intervals along the pumping tubes. These helped to reduce room-temperature radiation reaching the liquid helium and so boiling off large volumes of cold helium gas; the shields acted as heat exchangers which caused the radiation to warm the helium gas already boiled-off by other thermal leakage currents. The helium dewar vacuum space was continuously pumped by means of an Edwards E02 oil diffusion pump - it was not sealed for fear that a leak of superfluid helium into this space might cause an explosion on warming up.

To reduce radiation across the helium dewar vacuum space the standard procedure was adopted of surrounding the dewar by a jacket of liquid nitrogen: a long-tailed glass dewar fitted over the metal helium dewar and was hung in a webbing harness from six stout springs attached to the base-plate.

Different parts and systems making up the cryostat will now be described in greater detail.

Sample Exchange-Gas Space

This was filled with helium-4 gas to speed the initial cooling down process and, in fact, whenever a thermal tie was required between the copper sample block and the liquid in the metal dewar. For temperatures differing from that in the metal dewar, and

especially for helium-3 work, the space was evacuated with an Edwards 102 oil diffusion pump backed by an ED 150 two-stage rotary pump. Exchange gas could be admitted from a small coiled copper tube reservoir (Figure 3.5), a Bourdon gauge enabling the pressure to be monitored up to 20 torr.

Helium-4 Dewar

Thin-walled stainless steel tubing was used for this dewar because of its low thermal conductivity and high mechanical strength. The limited width between the magnet pole-pieces precluded the use of a relatively thick-walled glass dewar. Flanges were machined from stainless steel plate and then the dewar was assembled and argon-arc welded commercially. Brass tubes were supplied to act as a thermal sink and spacing tube during the welding operations which were made more delicate by the thinness of the steel tubes. Six bolt-holes in the upper steel flange enable the dewar to be fixed to the brass base plate of the cryostat, using a plastic gasket to render the assembly vacuum-tight. The large outer tube of the vacuum jacket was constructed of 18 gauge brass for strength. It was hard-soldered into position.

A type E02 oil diffusion pump was used to evacuate the helium dewar vacuum jacket through a liquid nitrogen vapour trap. The pressure, monitored on a Penning gauge, was usually 2.0 or 3.10^{-5} torr near the diffusion pump. However, because of space limitations, a small ($\frac{1}{4}$" diameter) pipe had to be used near to the dewar and this

constriction undoubtedly allowed the inner wall of the vacuum jacket to cryopump this space to a much lower pressure when the dewar was being used with liquid helium.

It was necessary to lower the temperature of the main bath to below 1.5°K to enable helium-3 to be condensed into its chamber at a reasonably low pressure. This meant lowering the pressure above the liquid helium-4 to below 3.6 torr. A large rotary pump, an Edwards ED450, was used through a 4" diameter line to effect this. Metal bellows were placed strategically in the line to isolate pump vibrations. Temperatures close to 0.9°K were achieved using this system alone. This seems to indicate that esoteric devices for limiting the rate of flow of the superfluid film below the lambda-point (2.2°K), such as minute pinholes in an otherwise blocked pumping line, are unnecessary unless the lowest temperatures attainable with single-stage helium-4 cooling are desired.

In the event of a sudden energy input to the helium bath (through, for instance, failure of the vacuum jacket) considerable volumes of helium gas would have been boiled-off, because of the low latent heat of liquid helium. A flap valve was fitted on the pumping line at the top of the cryostat to prevent the internal pressure ever building up much above atmospheric pressure.

The dewar pumping system enabled temperatures down to about 50°K to be reached by pumping on liquid and solid nitrogen

contained in the metal dewar. A liquid nitrogen jacket in the glass outer dewar was not essential for this but did increase the length of runs at the lower temperatures.

By using a small (1SC35) rotary pump plugged into the helium transfer port it was possible to pump at the slow rates necessary at higher temperatures. A butterfly valve in the large 4" line and small valves in the transfer-port line made it possible to vary the pressure continuously over the whole range attainable.

Helium-3 System

This was designed to enable helium-3 gas to be condensed into the small copper chamber on which the sample was mounted and then to pump on the liquid to lower its temperature. As the gas is expensive a closed system was necessary, (Figure 3.6).

A mercury diffusion pump, type 2M4, was chosen to pump on the liquid helium-3 because it can work into backing pressures as high as 3.5 cms. Hg. This means that no rotary backing pump was required provided that the system was not filled to a pressure higher than 3.5 cms. Hg. In fact, a mercury Toepler pump was included for several reasons: it was not known (during the design stage) what temperature could be reached in the main helium dewar (mainly because of the uncertain effect of superfluid film-flow) and a value of 1.4^{o}K was assumed. It then appeared that the condensing pressure required was greater than 3.5 cms. Hg. which meant that either the system had to be filled to the higher pressure, implying

some form of backing pump for the 2M4, or it could be filled to below 3.5 cms. Hg., implying some form of condensing pump. A Toepler pump could be switched to fulfill either of these functions as needed. In addition, it is normal practice to return as much as possible of the helium-3 to the storage vessels to avoid loss by diffusion out through glass parts of the system or contamination with atmospheric helium-4 diffusing into the system.

From the diagram (Figure 3.6), it can be seen that suitable combinations of valve positions gave the following facilities:

1. The system could be evacuated through a connection to the EO2 diffusion pump prior to filling with helium-3 gas.
2. Filling was accomplished through valve 1 and the storage-cylinder valves.
3. Once the sample chamber was below 1.4^{o}K, condensation of helium-3 could be achieved by using the Toepler pump to force gas through the small-bore condensing line via valve 4. During this operation the large volume of the diffusion pump was isolated by means of valves 5, 6 and that of the vapour-pressure manometers by valve 7.
4. The liquid helium-3 could be pumped off rapidly through the diffusion pump and returned to storage via the path 6, 5, 3, 1. In this mode, the needle valve, 8, was effectively across the diffusion pump, controlling its pumping speed and hence the temperature of the sample.

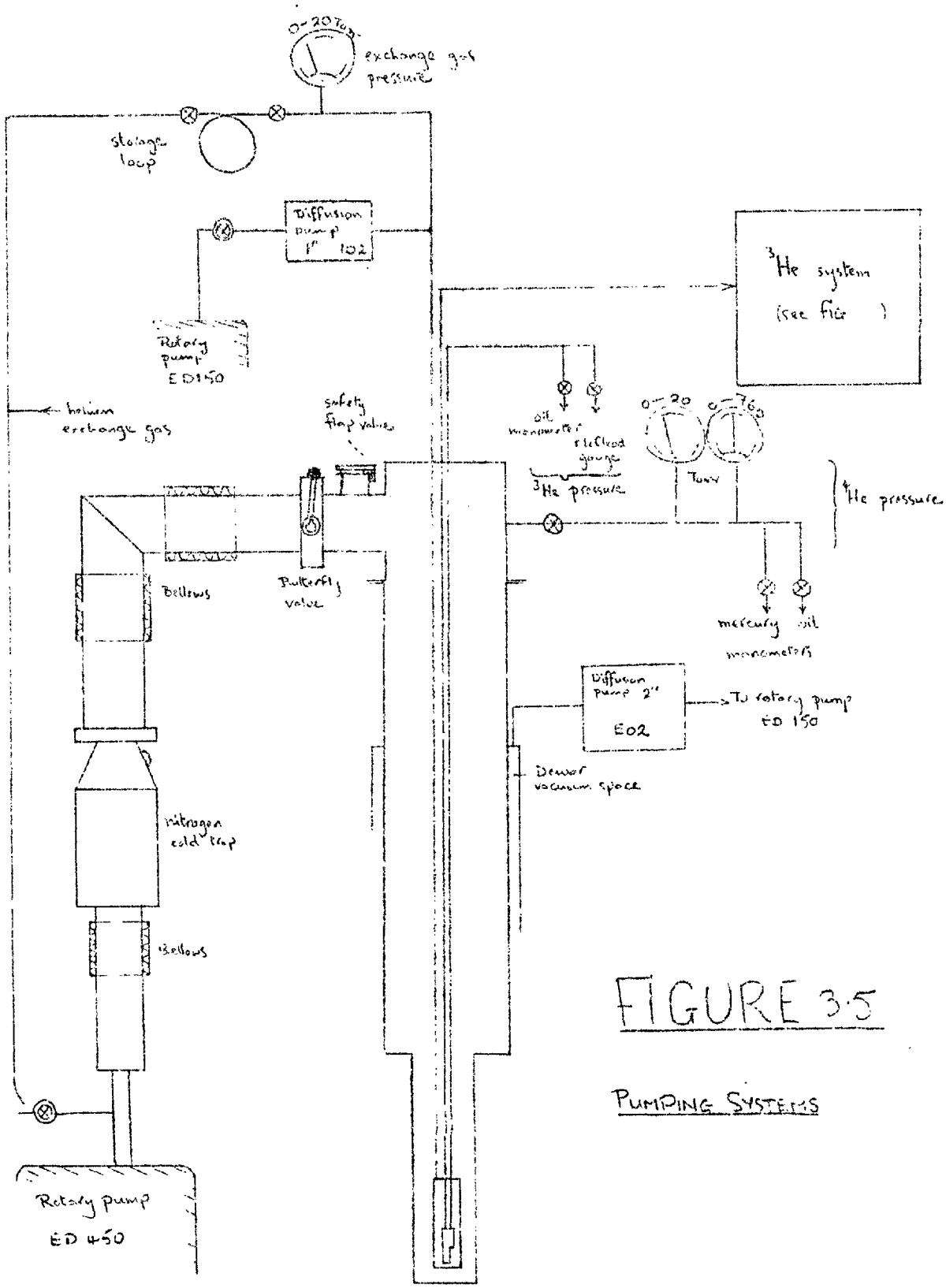

FIGURE 3.5

PUMPING SYSTEMS

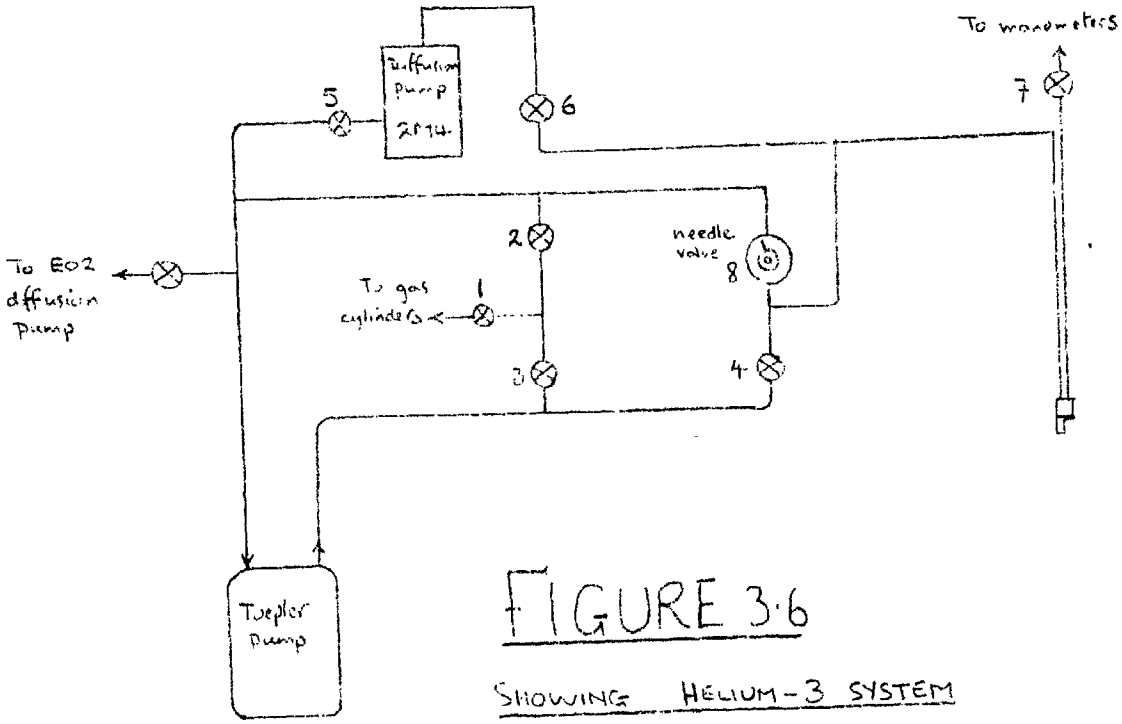

FIGURE 3.6

SHOWING HELIUM-3 SYSTEM

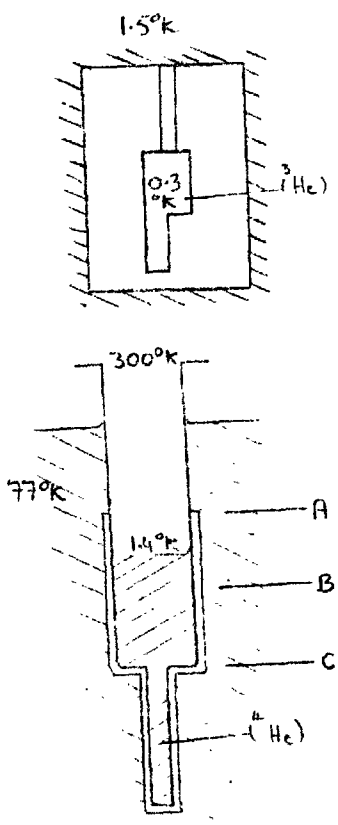

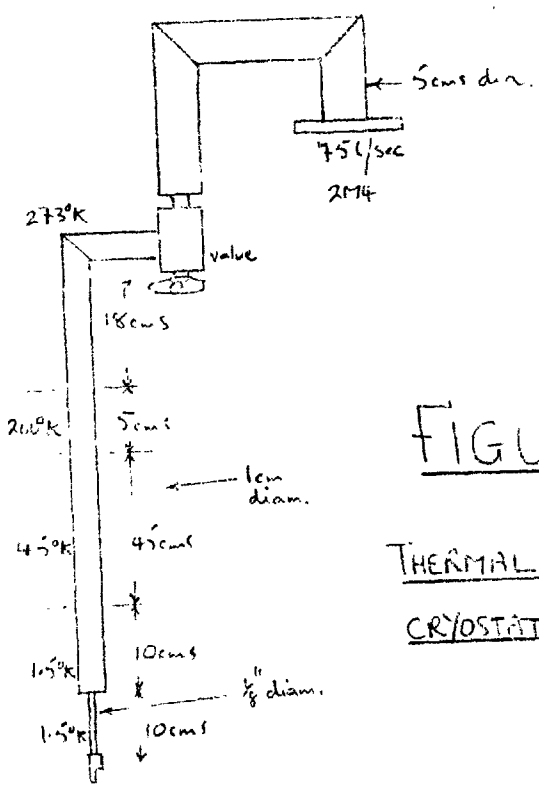

FIGURE 3.7

THERMAL DESIGN OF CRYOSTAT

Thermal Design of the Cryostat

The main dimensions of the cryostat were dictated by the magnet. Thus, the largest diameter of the outer, nitrogen, dewar was fixed by the distance between the magnet current coils and the diameter of the tail was fixed by the pole gap. This, in turn, decided the diameters of the stainless steel tubes used in the construction of the helium dewar - since there is a limited choice of diameters of thin-walled cryogenic-quality tubing.

It is proposed to examine the cryostat as constructed rather than report the design process which was affected by many outside influences.

Helium-3 System

The copper sample block was hung on two stainless steel tubes, 4 cms. long, $\frac{1}{8}$" diameter, and of 0.006" wall thickness, within a vacuum space. These provide the thermal isolation necessary to maintain a temperature difference between the sample and the main helium bath. We shall consider the extreme case of the helium bath at 1.5°K and the sample at (about) 0.3°K (due to pumping on the helium-3), see (Figure 3.7). The actual sample temperature depends on the balance between pumping speed at the surface of the liquid helium-3 and the total heat flux into the helium-3 bath.

Heat Leakage to the helium-3 Chamber

a) Down the two steel tubes. Taking a mean thermal conductivity of 0.7 mW $deg^{-1}cm^{-1}$ this is easily calculated to be approximately $\leq$ 0.007 mW.

b) Radiation from the copper cap at $1.5^{\circ}K$. Taking an area of 60 cms^2 and using the Stefan-Boltzmann constant ($5.67 \ 10^{-9}$ mW cm^{-2} deg^{-4}) this is $1.7 \ 10^{-6}$ mW -negligible. It is interesting to note here that if the radiation trap had been maintained at liquid nitrogen temperature then radiation down the two $\frac{1}{8}$" diameter tubes would have been 70,000 times this value.

c) Joule heating of sample. A typical sample would have dimensions 1 x 0.1 x 0.05 cms. and resistivity 0.3×10^{-5} ohm-cm at these temperatures. Joule heating for the fairly high sample current of 200 mA is then 0.012 mW.

d) Heat down copper leads. There were seven copper wires of 40 s.w.g. Using a mean thermal conductivity of 2 Watts $deg^{-1}cm^{-1}$ this gives 0.5 mW.

e) Joule heating of copper leads. Assuming all the heat generated flows into the helium-3 chamber, a resistivity of $\sim 10^{-9}$ ohm-cm and a sample current of 200 mA, the heat input from the two current wires is ~ 0.001 mW. Calculation yields 46 gauge as the size of wire which minimises the sum of contributions (d) and (e), giving a value of 0.02 mW. However, such thin wire would overheat with reasonable currents for room temperature measurements.

f) Heat down thermocouple wires. The gold wire had a diameter of 0.012" which gives a heat leak of 0.2 mW. We expect the chromel contribution to be negligible.

g) Conduction through residual gas in the vacuum space. Assuming the abnormally high pressure of 10^{-4} torr this was estimated at less than $\frac{1}{10}$th μW which is negligible.

h) Eddy current heating due to changing the magnetic field. This was observed during the flyback of the magnetic field scanning system but was negligible during the slow measuring scan.

Pumping Speed at the Surface of the helium-3

Figure 3.7 shows the layout of the helium-3 pumping line. Assuming the temperature distribution indicated, the conductance of the line was estimated to be 0.008 litres/sec. Now under equilibrium conditions, the gas flow rate through the line is equal to the rate of boil-off due to heat leaks into the helium-3 chamber. This, together with the above value for the line conductance, enables us to calculate the pressure drop across the line. Neglecting the pressure at the throat of the 2M4 diffusion pump then leads directly to an estimate of the vapour pressure in the helium-3 chamber. Calculation shows that the gas flow rate (throughput) is 7.84×10^{-4} W litre-torr/sec where W is the heat leak input in milliwatts, giving a pressure drop of 0.98×10^{-4} W torr. Thus we expect the lowest vapour pressure to be (W = 0.7 mW) 0.07 torr, corresponding to a temperature of 0.45°K. This is the worst value for the lowest attainable temperature because the greatest values for heat leaks have been used throughout the calculation and we might expect something a little better in practice. The run duration, assuming

2 cm^3 of liquid helium-3 and a heat leak of 0.7 mW, comes out at about 20 minutes.

Helium-4 System

The purpose of this system during a very low temperature run was to maintain the liquid helium-4 in the metal dewar at 1.4^{o}K or below for as long as possible. Figure 3.7 shows the essential features. The pumping system was shown in (Figure 3.5).

Helium-4 System - Heat leaks into the helium-4 bath

a) Down the wall of the dewar. Making the reasonable assumption that all heat from the top flange is dumped into the liquid nitrogen bath, we are left with a leak path from the nitrogen bath to the helium which grows longer as the helium level falls. With a full helium dewar (level at A Figure 3.7) this must completely dominate the situation and cause a rapid boil off of helium but as the level falls the low thermal conductivity of the wall quickly reduced the heat influx. With the level at B the heat leak is 0.076 watts. When the level has fallen to C the heat leak is reduced to 0.038 watts.

b) Down the pumping tubes leading to the radiation trap and the sample block. There were two tubes of $\frac{1}{2}$" diameter, 0.010" wall thickness and one of $\frac{1}{8}$" diameter, 0.006" wall thickness. They conduct heat directly from the room-temperature base-plate of the

cryostat into the helium bath. Once again the length of the conduction path varies with the helium level. Calculations taking into account the variation with temperature of the thermal conductivity (p. 57, Rose-Innes) give heat leaks of 0.20 watts for a helium level at B and 0.15 watts for the case C.

c) Conduction down electrical leads. This is estimated at $\lesssim 5$ mW.

d) Radiation. Shields were used in an attempt to stop direct room-temperature radiation. It was hoped that the cold helium gas would remove this heat from the shields and maintain the lower ones at least at nitrogen temperatures. We assume, then, that the lowest shield radiates at a temperature of 77°K, directly into the helium bath. This gives a heat influx of 6.3 mW. A surface maintained at room-temperature would radiate about 160 times as much power.

The above heat leaks into the helium bath, total about B: 0.29 and C: 0.20 watts, cause the helium to boil-off and limit the duration of a run. 0.3 watts correspond to 415 ccs of liquid helium per hour which is appreciable. However, the cold helium gas being driven off is capable of absorbing a lot of heat as it warms up to room-temperature. The enthalpy of the gas between a few degrees Kelvin and room-temperature is about 13 watts/mole. Thus, the gas boiled off by the above heat leaks is capable of

absorbing all and more of the unwanted heat influx, implying that if efficient heat transfer is arranged between the issuing gas and the leakage paths a very low nett boil off rate will results.

The situation is complicated by the fact that liquid helium is in the superfluid state at temperatures below 2.2°K. The superfluid film is extremely mobile and climbs up all surfaces kept below the transition temperature (lambda point), greatly increasing the surface area from which the liquid can evaporate. The upper limit of the film corresponds to the position of the 2.2°K isothermal in the cryostat, for above this the helium could only exist as ordinary helium - without any climbing abilities. A typical maximum film flow rate is 6×10^{-2}ccs liquid/sec for a one cm film-width but a dirty wall surface or an air-film can increase this by an order of magnitude. Provided the pumping system can take care of this evaporation rate then temperatures below the lambda-point can be reached; at higher pumping rates the more distant parts of the film will become depleted and the evaporation area will be reduced once more.

Considering conditions at the lambda point; the maximum evaporation rate is around $20 \times 6 \times 10^{-2}$ccs/sec, assuming the upper edge of the film to have a perimeter of about 20 cms. This is easily converted into the gas flow rate and corresponds to a throughput of 0.4 liter-torr/sec. A vapour pressure of 3 torr is assumed under

these conditions. Now, the ~~conductance~~ impedance of the pumping tube was made negligible and the main pressure drop will occur across the nitrogen trap in the line. This has a conductance of 60l/sec. Hence the pressure drop is throughput/conductance or approximately 0.01 torr. This means the pressure at the inlet of the rotary pump will be 3 torr and the pump speed required will be throughput/pressure or 0.4/3 liters/sec. A pump, then of some 10 liters per minute is required. Even if the film flow were much higher due to surface contamination 100 liters per minute would suffice. It appears that the pump actually used, an Edwards ED450, had an adequate reserve of pumping speed and its full 450 liters per minute could be used to take the system down to temperatures below the lambda point.

Estimates of durations of runs to be expected from one filling of the helium dewar are difficult to make because it is not known how much heat the cold gas takes up before reaching the top of the cryostat. However, assuming very poor heat exchange between the gas and the lower parts of the cryostat, the heat leaks calculated above lead to a boil off rate of 0.42 liters/hour for level B and 0.28 liters/hour for level C. These are maximum rates expected for these levels. Since the volume of the dewar between these levels is about 0.4 liters, a run duration of about 1.2 hours is to be expected and was in fact exceeded in practice.

At lower temperatures, a large fraction of the liquid helium is used to cool the body of the rest of the liquid; approximately $\frac{1}{3}$ of the liquid is required to cool the helium bath from $4.2^{\circ}K$ to the λ-point. However, the liquid-level will quickly approach B and less will have been boiled off uselessly by the heat leak from the nitrogen bath.

Procedure for Working at Chosen Temperatures up to Room Temperature

There are few easily-available refrigerant liquids: liquid nitrogen is by far the most convenient for higher temperatures and can be employed usefully in the solid form below $63^{\circ}K$ down to about $50^{\circ}K$. Liquid oxygen has a boiling point of $90^{\circ}K$ which is too close to that of nitrogen ($77^{\circ}K$) to make it of considerable use but its high latent heat is an advantage in that long runs are possible. Helium-4 boils normally at $4.2^{\circ}K$ and is convenient for temperatures down to about $1^{\circ}K$ but below this very high pumping speeds are required and it is easier to use the higher vapour-pressure isotope, helium-3, for the very low temperatures down to $0.3^{\circ}K$, say. The large temperature gap between helium and nitrogen can be reached by heating the sample block with a small heater wound onto the helium-3 chamber. However, the extra power input resulted in considerably shorter runs. There are refrigerants with normal boiling points in the gap but they are expensive and sometimes

are only supplied on condition that the gas be returned to the suppliers - implying the possession of a complete gas recovery unit.

Below $1^{o}K$

The nitrogen dewar was filled and about 2½ liters of liquid nitrogen poured into the metal dewar. Helium gas at about 20 torr was let into the exchange gas space to connect the sample thermally with the nitrogen in the metal dewar. The system was then allowed to cool to $77^{o}K$. When this temperature was reached, the metal dewar was evacuated and refilled with helium gas from a cylinder. Any remaining liquid nitrogen would cause a drop in sample temperature at this stage and pumping was continued until the temperature started to rise again. Solid nitrogen has a low thermal conductivity and would prevent successful cooling down to helium temperatures if allowed to remain. With the dewar and contents at $77^{o}K$ in an atmosphere of helium gas the system was ready for helium transfer.

Liquid helium was transferred through a vacuum-jacketed tube by squeezing on a rubber bladder attached to the supply dewar. It came over as gas until the transfer line had cooled to $4.2^{o}K$ when liquid started to issue from the tube, accompanied by a characteristic limpness in the rubber bladder. As liquid condensed in the metal-dewar tail the sample temperature decreased rapidly but it

took about half an hour for thermal gradients to die out. The transfer process was not hurried unduly to avoid wasting the liquid helium; gas issuing from the top of the cryostat should have absorbed heat from the cryostat interior in warming up to room temperature and not from the top of the cryostat. A gas rotameter plugged into the flap-valve port enabled the helium flow rate to be monitored. It was found that an average rate of about 1.3 liters/minute with occasional puffs of over 3 liters/minute gave a reasonably short cooling time with little wastage of the liquid helium. When the dewar was full, as indicated by a rapid increase in the rotameter reading, the transfer tube was removed and the transfer port was plugged. After closing the flap valve against its rubber sealing ring, pumping on the helium bath was started. Again, the cryostat top was not allowed to cool appreciably as this would have meant inefficient cooling of the cryostat interior.

When the sample temperature had reached 1.4°K or below, helium-3 was condensed into its chamber by means of the Toepler pump, as described earlier. Pumping on the liquid helium-3 with the 2M4 diffusion pump then resulted in a further lowering of temperature, after evacuating the exchange gas space thoroughly by means of the 102 diffusion pump.

Temperatures between the lowest attainable and 1°K could be maintained either by adjusting the 2M4 pumping speed or by using

the sample block heater. The former method was preferable the point of view of run length.

1.0°K to 4.2°K

Temperatures below the normal boiling point of helium-4 were reached by pumping on the helium in the metal dewar, using helium gas in the exchange gas space. This gas condensed at about $\lesssim 1.9^{\circ}K$ and its vapour-pressure provided a convenient indication of temperature at lower temperatures. Temperature control was effected by varying the pumping speed of a small rotary pump plugged into the helium transfer-port, leaving the butterfly valve to the large rotary pump cracked open a convenient amount. The small pump could be used alone down to the lambda point but it could make no impression on the large volumes of vapour produced by the evaporating superfluid film at lower temperatures.

4.2°K to 50°K

This was the most difficult region to work in as refrigerants with boiling points in the region were not available. The procedure used was to fill the metal dewar with helium-4, as described above, and with a suitable helium exchange gas pressure, to pass a current through the constantan heater winding on the sample block. Temperature was controlled by varying this current.

At low temperatures a fairly high exchange gas pressure was required (10 to 20 torr) to reduce the sensitivity to small changes

in current. At the higher temperatures a lower pressure (below 1 torr) enabled these temperatures to be reached with a reasonably small power dissipation.

$50^{o}K$ to $77^{o}K$

By filling the metal dewar with liquid nitrogen and pumping on this liquid, temperatures below the normal boiling point ($77^{o}K$) down to about $50^{o}K$ could be reached. The nitrogen solidified at $63^{o}K$ and this proved to be a convenient, stable, point provided it was approached from below to ensure that an appreciable volume of the solid had formed. Pumping on the solid nitrogen lowered the temperature further but, because of the low thermal conductivity of the solid, cooling of the sample was very slow in this range.

$77^{o}K$ to Room Temperature

A similar technique was employed in this range to that employed for working above the normal helium boiling point; a suitable exchange gas pressure was used and the sample block heater current was adjusted to maintain the desired temperature. The exchange gas pressure was reduced from about 10 torr to about 10 microns as the working temperature was increased to avoid an unmanageable sensitivity to current variation at low temperatures and to enable reasonably small power levels to be used at higher temperatures.

3.3.3 ELECTRICAL MEASUREMENTS

Voltages from the sample arms were presented to one axis of an X-Y chart recorder or, for calibration purposes, to a Pye 1 μV Vernier potentiometer with a Tinsley photocell galvanometer amplifier enabling voltages to be estimated to 0.1 μV. A Keithley Model 149 milli-microvoltmeter was used to amplify sample voltages up to the millivolt level before they were presented to the Y-axis of the chart recorder. By this means, a sensitivity of better than 0.1 μV per 1% chart width could be obtained but the maximum useable sensitivity was usually determined by noise-broadening of the trace. This originated mainly in the Keithley because of mains-frequency pickup but was kept to acceptable levels by the insertion of a low-pass filter in the input lead to this instrument. The main source of interference appeared to be from the mains transformers of the various electronic instruments since capacitive coupling to their chasses caused currents to flow between the chasses giving rise to potential differences between the ends of the signal wires carrying these currents. Thorough grounding with thick wire seemed to have a useful effect. The X-axis of the chart recorder was driven by a signal from a commercial hall probe AEI Mk III placed in the magnet pole gap and supplied with a constant current of about 10 mA from a 250 V supply through large dropping resistors.

The electrical measuring system was thus required to present either the sample hall voltage or the voltage across the sample potential probes to the chart recorder or to the potentiometer. In addition, the potentiometer was to be used to measure the sample and hall probe currents and it was necessary to ensure that the Keithley milli-microvoltmeter was never open-circuited for long because the ensuing drift of its output to the f.s.d. of 10 volts would have damaged the chart recorder. The fairly complicated switching arrangement dictated by these requirements is indicated in the block diagram, figure 3.8.

High quality (Cropico) stud switches were used to switch these low-level voltages, an aluminium box being used for screening. Screened cables were used for interconnecting the various instruments and the wires from the sample to this box were confined inside a rigidly-mounted copper pipe to prevent movement (noticeable voltages were induced by movement of wires in the laboratory stray magnetic field).

A 30 V Farnell constant voltage supply DSV 30/5 was available for the sample current. Two modes of operation were considered - the usual case where a large dropping resistor is used to convert voltage stability into current stability and the method actually employed: a 100 ohm constantan resistor was wound non-inductively on a long thin-walled stainless steel tube and was connected in series with the negative lead from the supply as shown (Figure 3.9).

The voltage developed across this stable resistor was taken back to the 'feedback' terminals of the supply which consequently varied the output voltage to keep this feedback voltage, and hence the sample current, constant. It is estimated that the current stability using this method was better than that given by the usual method by a factor of at least four. Sample current was varied by means of the feedback controls on the supply unit which did not carry any large currents and could be changed without fear of drifting whenever required. Previous trials using a switched set of resistors to vary the sample current led to long periods of drifting current values between measurements. In the interests of current stability, again, it was found necessary to employ the on-off switches available in an unusual manner because of their relatively unreliable operation. Had such a switch been connected in series with the sample, its varying contact resistance would have ruined any current stability achieved in the power supply so it was connected across the sample current leads as shown. The 6 ohm lead resistance between the sample and switching box ensured that the sample current fell to the tens of μA level whenever the switch was closed ('off').

Magnetic Field Measurement

A commercial AEI hall probe was used either to drive the X-axis of the chart recorder or to provide a magnetic field-dependent

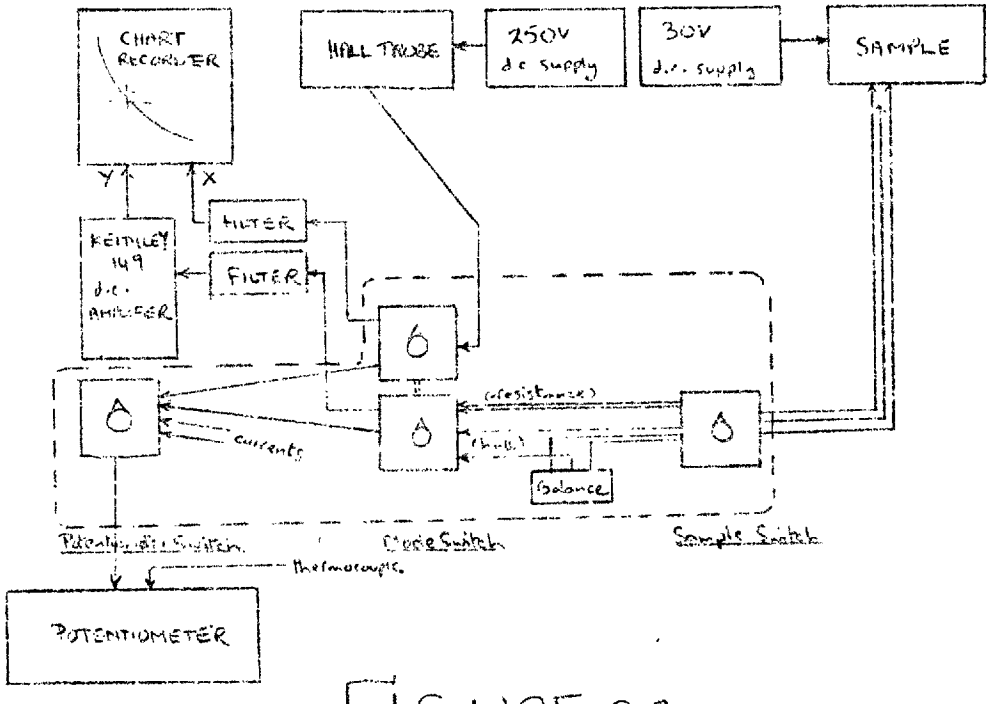

FIGURE 3.8

BLOCK DIAGRAM OF ELECTRICAL MEASURING SYSTEM

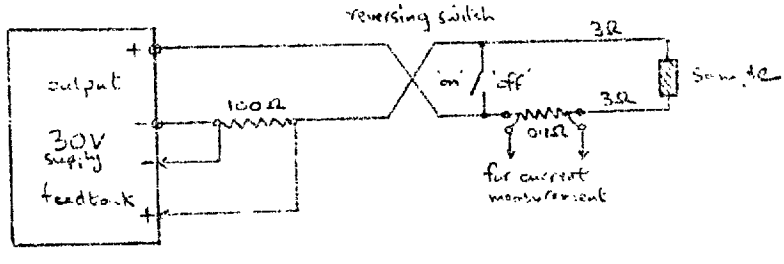

FIGURE 3.9

STABILISED SAMPLE CURRENT SUPPLY

voltage for the potentiometer as determined by the position of the mode switch, see Figure 3.8. Constant current of about 10 mA was provided by a 250 V stabilised Roband power supply through a 25 kohm resistor. Calibration to 1% of the probe was effected using a Norma ballistic fluxmeter. It was found that the output voltage was related to the magnetic field through the relation $V/I = 10^{-3}B\,[(0.2346 \pm 0.001) - (0.496 \pm 0.025)10^{-6}B]$ where V is the probe output (volts), I the probe current (amps) and B is the magnetic field (gauss). The current was measured by connecting the potentiometer across a 0.1 ohm Rivlin standard resistor. With the probe head used, it was necessary to draw current out of one of the potential leads in order to obtain a zero output in zero field - only two potential leads were provided on the hall plate. A simple variable resistor enabled the probe to be zeroed before each run, though this was only really necessary for low fields - it had very little effect on the high field readings. As with the Keithley voltmeter input, it was found necessary to use a low pass filter in the input circuit of the X-axis to prevent sluggish operation of the chart recorder induced by a.c.-mains pickup.

Temperature Measurement

A gold (plus 0.03% iron) alloy - Chromel P thermocouple was used for measuring temperatures against a liquid oxygen standard. The gold wire (0.012" diameter) was from the same Johnson-Mathey batch that Berman et al (1963-64) used in their thermoelectric power

measurements. Their emf - temperature data (private communication) was used for interpolation between calibration points, but it was first neoessary to reduce this data graphically to values against an oxygen reference. We employed this particular combination because it maintains a high thermoelectric power down to below $4^{\circ}K$ ($\sim 10\mu V/deg.$) whilst having a reasonable value over the higher temperature range up to $300^{\circ}K$.

It is convenient to mention here that oil and mercury manometers were connected to monitor pressures in the main helium-4 dewar and these provided a useful indication of temperature when pumping on the refrigerant in this dewar (whether helium or not). An aneroid-type manometer (0-20 mm Hg) connected to the exchange-gas space proved very useful at temperatures below $4^{\circ}K$ when it acted as a helium-4 vapour pressure thermometer, and an oil manometer and McLeod gauge were provided for the helium-3 system.

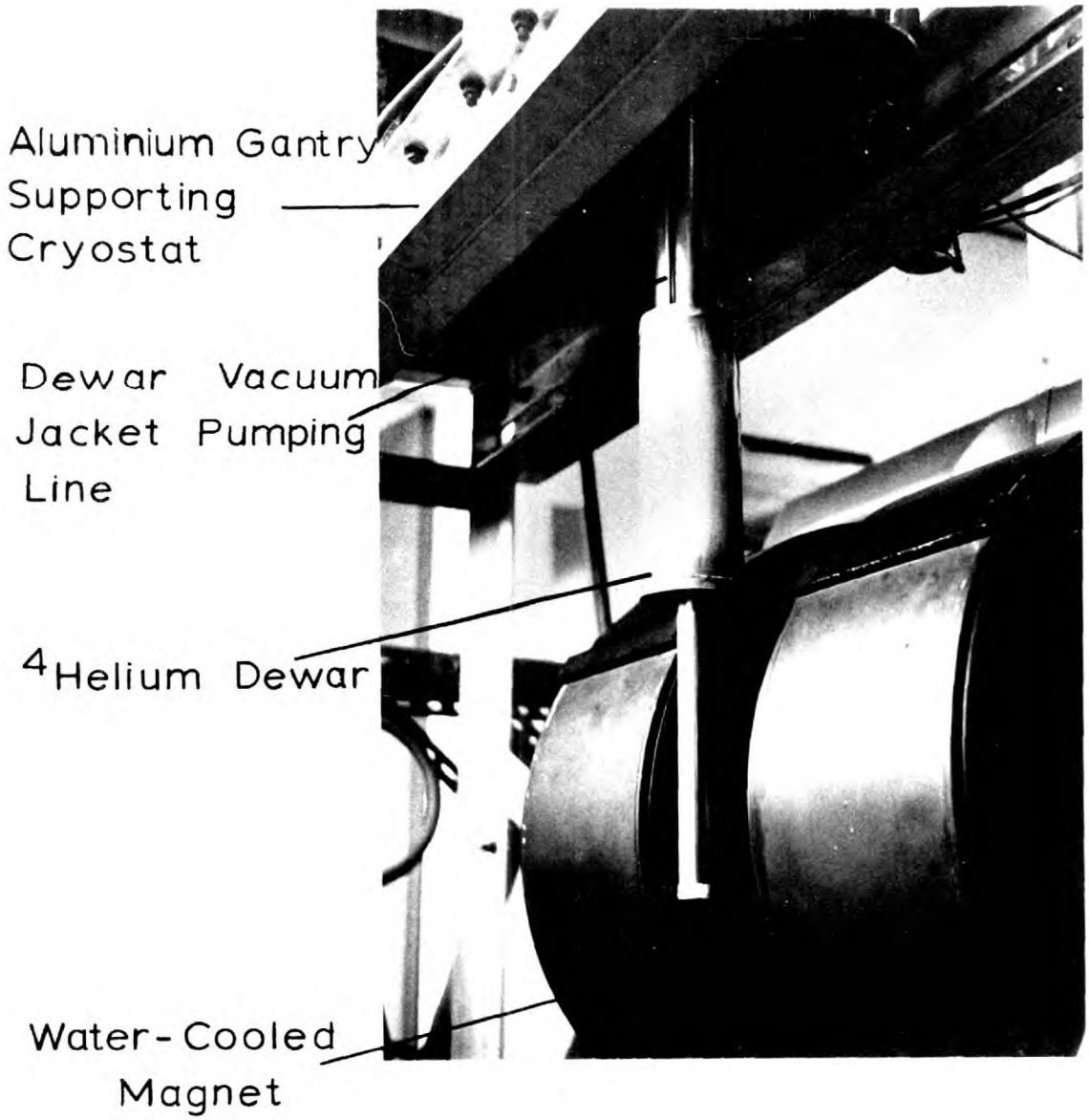

APPARATUS

Showing Helium Dewar in place

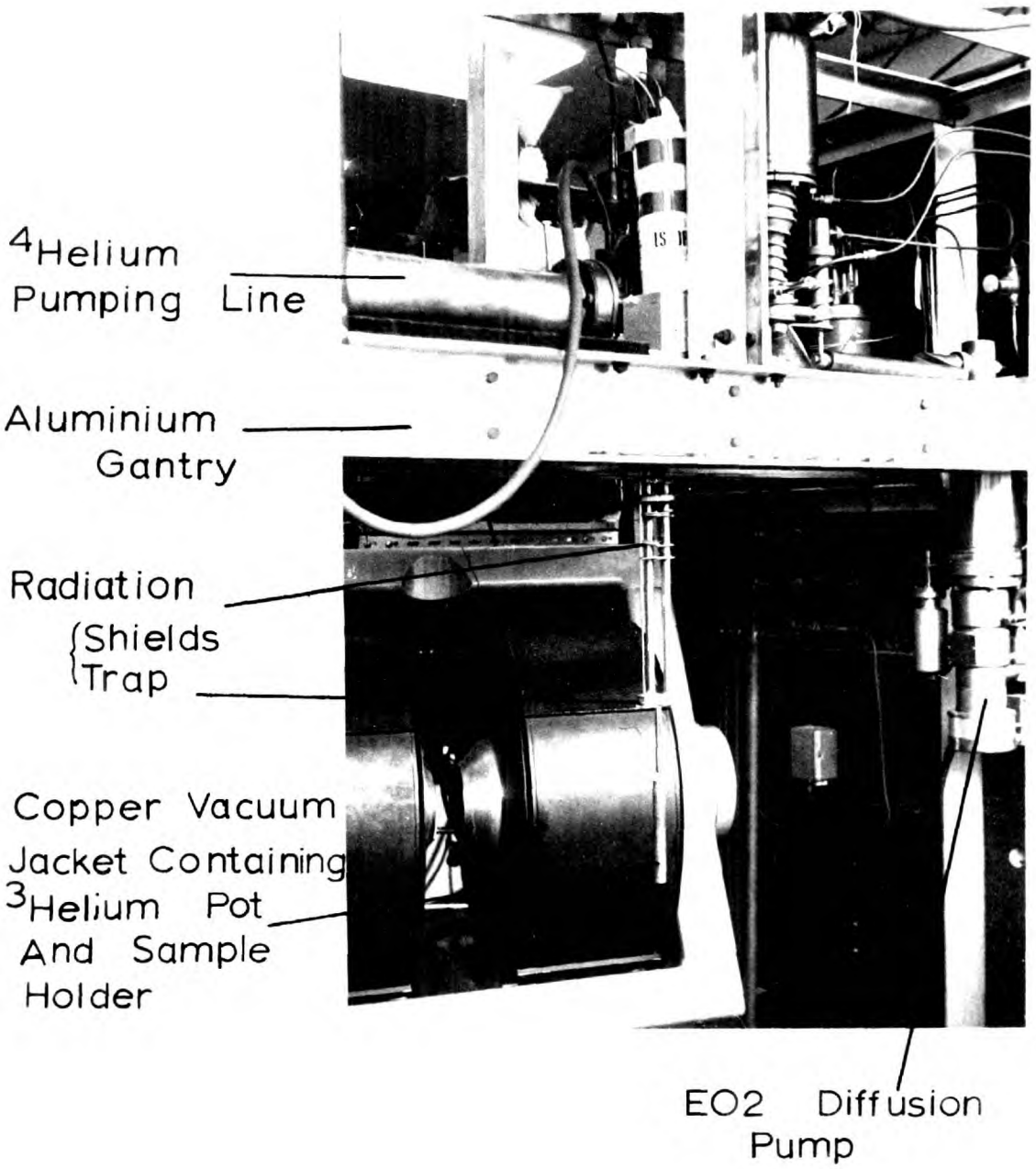

APPARATUS

Showing Cryostat Interior

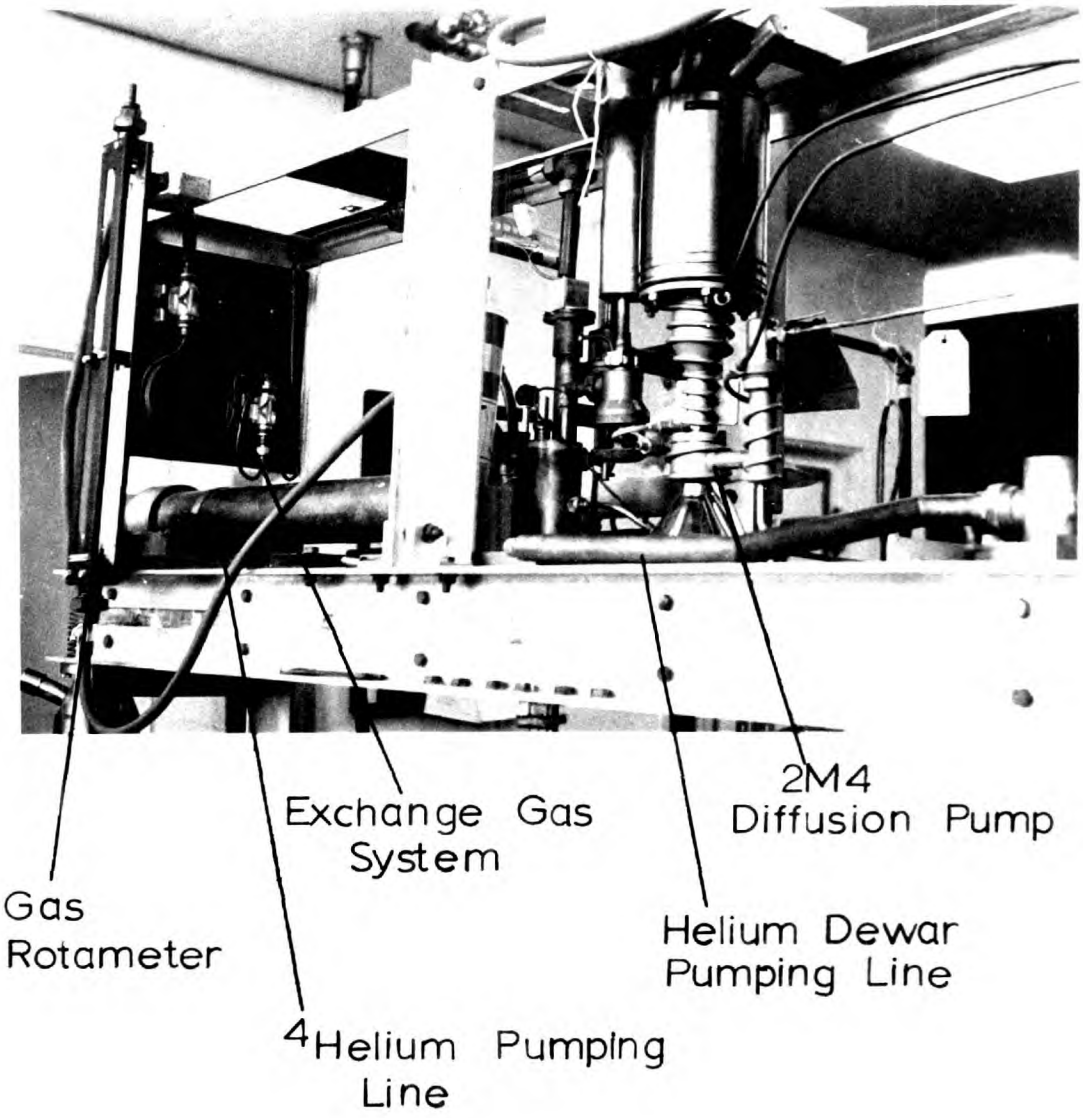

APPARATUS

Showing Pumping Systems

CHAPTER 4

RESULTS - DATA

The present chapter deals firstly with the nature and the preliminary analysis of the non-oscillatory Hall effect R(H) and magnetoconductivity $\sigma(H)$, and secondly with the treatment of data obtained on Shubnikov - de Haas oscillations, observed at magnetic fields above 5kgauss for temperatures of $4.2^{\circ}K$ or below. Procedures adopted for data fitting, described at the end of each of these sections, lead on to the derived results contained in the next chapter.

4.1 Non-Oscillatory Data.

4.1.1. Chart Reading.

It was described earlier ("experimental") how chart recordings were produced on which voltages proportional to the sample Hall or magnetoresistive voltage and the output of a Hall probe placed in the magnet pole gap were automatically plotted on an X-Y recorder by slowly scanning the magnetic field. Calibration points were inked on to the chart at intervals during each run, using the potentiometer to obtain voltage co-ordinates of each point.

The first stage in the chart reading process was to obtain the relationship between chart distances and voltage input for a particular channel (X or Y). This procedure was identical for both channels.

A pencil line ruled on the chart parallel to one axis served as a datum, and the distances of the calibration points from this line were measured using the printed lines on the chart as units. An engraved glass scale was used for interpolation between chart lines when necessary. Preliminary measurements of this sort produced straight line plots (within $\pm$ 0.2%) of voltage against chart distance for between ten and twenty calibration points, so later runs usually employed only three to six calibration points. To avoid tedious graphical work, a simple least-squares fitting programme was written for use with an IME86S electronic desk calculator. One writes for the Hall probe (P) axis (X) and the sample (S) axis (Y):-

$$\frac{V_P}{I_P} = Q_p + K_p d \ , \qquad \frac{V_S}{I_S} = Q_S + K_S d$$

where V and I are voltage and current respectively Q and K are the constants to be found and d is the chart distance. The programme reduced the problem of finding the best pair of coefficients in the linear law to a routine sequence of operations with the desk calculator on data for all samples and temperatures reduced to a common form in consistent units.

The actual reading of the chart then followed. Sixty or more lines were ruled at intervals along the Hall probe (magnetic field, X) axis and the corresponding distances of the trace along the other axis (Y) measured. Later analysis required that the data from both

Hall and magnetoresistance charts, taken under a given set of conditions, be tabulated in pairs as functions of magnetic field, so it was necessary to derive the chart intervals corresponding to a given set of magnetic field values for each chart before laying off the construction lines along the Hall probe axis. A computer programme was written to generate chart distances for a batch of charts, corresponding to a standard set of magnetic field values contained within the programme. For this purpose it was only necessary to read-in the coefficients of the linear law between Hall probe voltage and chart distance along that (X) axis for each chart, the (non-linear) Hall probe calibration being written into the programme in a suitable form.

Conversion of the Y-axis chart distances into sample (voltage/current) was performed either with the desk calculator or, later, as part of a larger computer programme. The latter went on to derive the actual values of Hall coefficient, $R(H)$, and conductivity, $\sigma(H)$, and also the magnetoconductivity tensor components, σ_{xx}, σ_{xy}. It required the input data to be in the form of pairs of chart distances (from the Y-axes of Hall and magnetoresistance charts) together with the corresponding values of magnetic field. A printed output was produced tabulating R, σ, σ_{xx}, σ_{xy} and some intermediate products against magnetic field. Punched cards were also obtained as part of the output with the values of field, σ_{xx}, σ_{xy} coded on to them in a

form suitable for later analysis.

The following Hall coefficient values, R(H), given in units of cm^3/coulomb, are calculated from the expression $R(H)=(V_H/I_S)(t/H)$ where V_H is in volts, I_S in amperes, t in cms, and H is in gauss/10^8.

4.1.2. Results, Hall coefficient and conductivity

We mention here that temperatures quoted on the following graphs should be regarded as labels; actual temperatures are given in the tables of Appendix 3 and in Table 5.1, which also contain data for temperatures other than the four selected for full presentation. The conductivity curves afford a close approximation to the desired σ_{xx} curves since the correction from the Hall effect usually amounts to less than 10% when deriving σ_{xx}.

Graphs 4.1, 4.2, 4.3 display conductivity against magnetic field for the three samples W1, W2, W3 at temperatures of 300°K and 77°K. Results for the three samples superimpose well at high magnetic fields but deviate markedly at low fields; successively higher zero-field values of σ are reached by W1, W2, W3 in that order. This high field behaviour provides a check on the reproducibility of our sample preparation technique, in particular the establishing of uniform current flow across the width of the samples. Similar superposition is evident at 63°K and 4°K (Graphs 4.4, 4.5, 4.6) with the same trend in the low-field deviations. Our extension of the range of measurement to magnetic fields above the 6kG used by Spain is fully

justified by the significant tail on the conductivity curve at higher fields. The present analysis is based on estimating the area beneath such curves and the tail obviously contributes greatly to this, at least above helium temperatures. The maximum available field of 18kG is reasonable for all temperatures except room temperature where at least double this value would have been desirable.

At low fields, room temperature behaviour for samples W1 and W2 closely mirrors that shown by Soule's (1958) samples EP-14 and EP-7 respectively, in that one shows a downward trend towards zero magnetic field whilst the other has a pronounced positive-going excursion which leads to a positive Hall coefficient below a few hundred gauss. W3 shows an intermediate type of behaviour with a less-pronounced rise starting at a lower field than W2. At higher fields W1 and W2 slowly converge but W3 shows a steeper, roughly linear, increase in the negative direction. Such characteristic behaviour (Graph 4.7) for sample W1 follows closely that reported for Spain's materials SA19/20/22/12/18 and places this sample outside the group of best materials used in their study.

The insistent positive excursion at low fields of some of these Hall curves down to 63°K has not been detected before in pyrolytic graphite. At 77°K in particular the trend is most interesting; the peak at roughly 2kgauss appears to move to lower fields and less negative values with samples W1, W2, W3 whilst the low field side

for the peak becomes more dominated by a positive-going tendency leading in the case of W3 to almost complete smoothing of the peak. It should be noted, however, that the exact details of the curves were markedly irreproducible at this temperature and appeared to change upon thermal cycling, an effect not present at other temperatures studied.

The general shape, viz. large negative values on either side of a peak rising towards zero at a few kilogauss, is a familiar picture for pyrolytic graphite (Spain at al., 1967). For material of high perfection the peak actually crosses the zero axis, having a range of positive Hall coefficient for a few kilogauss at around 77°K. We note that none of our samples crossed the axis in this region, although W2 practically touches the axis at 77°K (Graph 4.7) whilst all samples approach very closely at 63°K (Graph 4.10).

Graph 4.11 illustrates the result of fitting the magneto-conductivity tensor components, derived from the data presented above, to Lorentzian curves as described in Section 4.13. The fitting parameters for σ_{xx}, σ_{xy} have been used to regenerate Hall coefficient curves by means of the loop from raw data to tensor components to fitting parameters and thence back via regenerated tensor components to Hall curves. The fits obtained for the conductivity are usually so good that little is gained by showing them, but

we will illustrate here extreme examples of good and of disappointing results one obtains for the more complicated Hall curves. Thus, sample W2 at 300°K yields a very good fit provided four Lorentzians are used, whereas sample W3 at 63°K has not been satisfactorily fitted even by four terms. This is discussed further in Section 5.1.1.

4.1.3. Data Fitting.

We now come to the fitting of the magnetoconductivity tensor components. It has been shown in Section 2.2.1 that only two independent components σ_{xx}, σ_{xy} need to be considered in the basal plane configuration and that these are given by

$$\sigma_{xx}(H) = \frac{\sigma(H)}{1 + (R\sigma H)^2}, \quad \sigma_{xy}(H) = R\sigma H \times \sigma_{xx}(H)$$

- where R, σ are the (field-dependent) Hall coefficient and conductivity, respectively. Gaussian units are used throughout, various useful relationships being:

$$R(\text{gaussian}) = R(\text{cm}^3/\text{coulomb}) \times {}^1/(9\times10^{19})$$

$$\sigma(\text{gaussian}) = \sigma(\text{ohm-cm})^{-1} \times (9\times10^{11})$$

where the value 9 comes from the velocity of light squared and is more accurately 8.988.

Calculated tensor components $\sigma_{xx}(H)$, $\sigma_{xy}(H)$ and the results of this fitting process are presented in chapter 5.

As indicated elsewhere, (Section 2.4.2) representation of the experimental data in the form

$$\sigma_{xx} = \sum_i \frac{A_i}{1 + (H/H_i)^2}, \quad \sigma_{xy}/H = \sum_i \frac{A'_i}{1 + (H/H'_i)^2}$$

is necessary before the partial conductivities due to electrons and holes can be found. The present section deals with the methods employed to fit data to the expressions; we use σ_{xx} as an example, but all remarks apply equally to σ_{xy}/H.

Were the data free from errors, it would be sufficient to take 2i (i=1, 2, 3 ...) data points and solve the resulting equations for the A_i, H_i. This is not the case in practice, where random errors are superimposed on data. The calculated values of $\sigma_{xx}(H)$ would not pass through all the experimental values unless the number of fitting parameters (2i) were equal to the number of data points, but our object is to represent the data to sufficient accuracy with as few terms as possible, preferably less than four, so some statistical criterion is necessary to decide upon the goodness of fit. We use the sum of the squares of residuals (the differences between experimental and calculated values) and employ the standard theory of linear least squares fitting where possible.

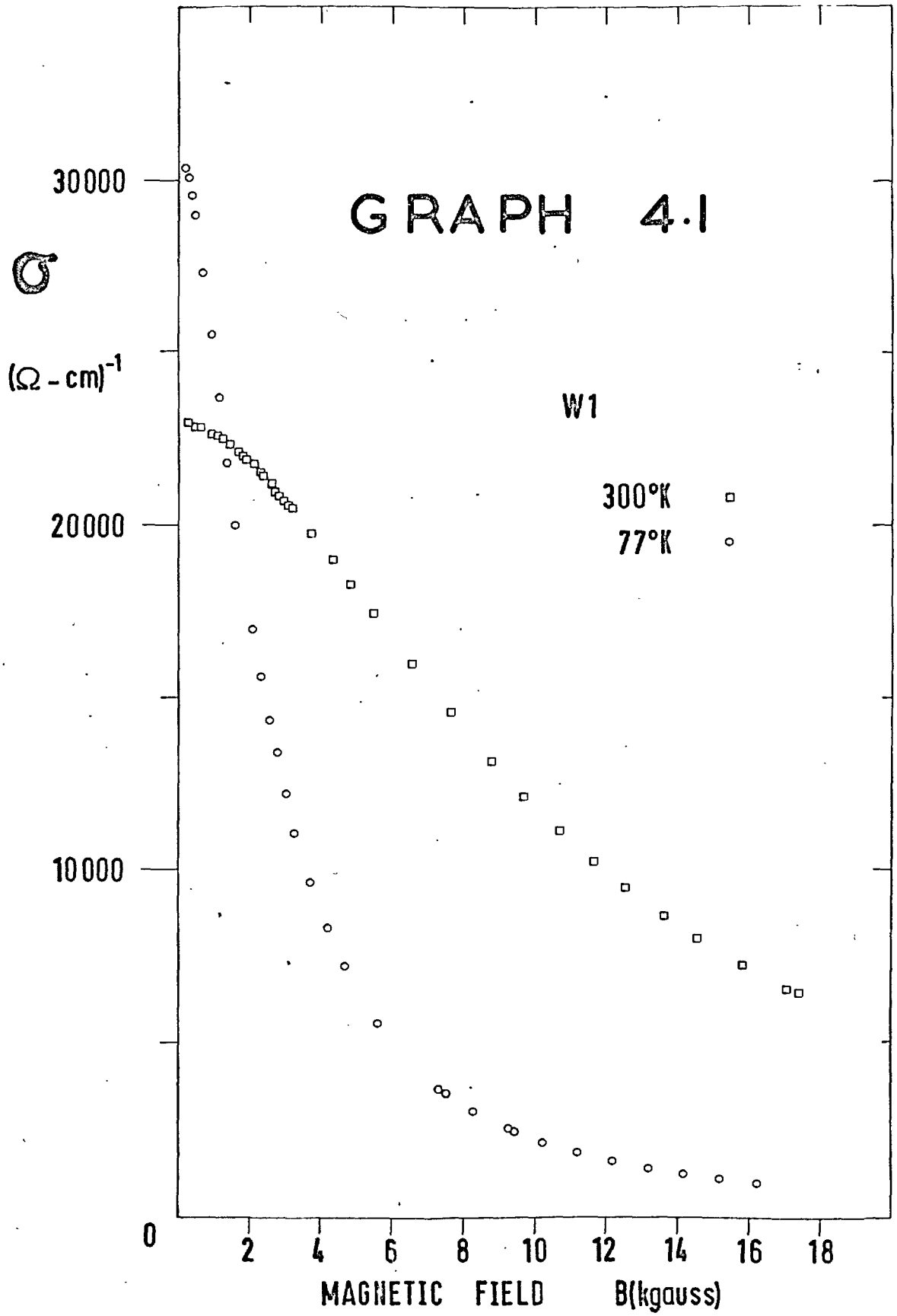
GRAPH 4.1
σ
(Ω - cm)⁻¹
30000
20000
10000
0
W1
300°K
77°K
2
4
6
8
10
12
14
16
18
MAGNETIC FIELD B(kgauss)

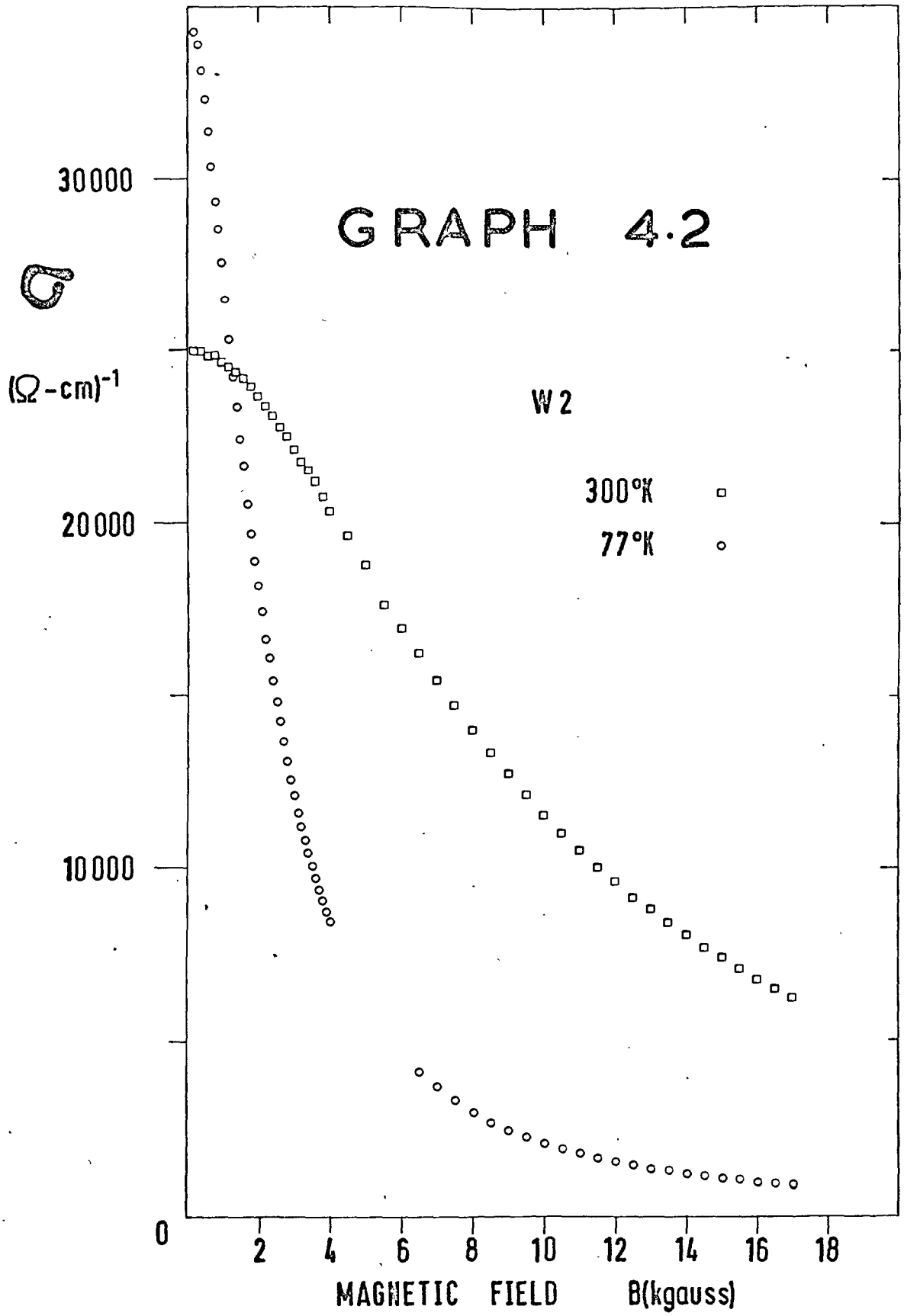
GRAPH 4.2
σ
(Ω-cm)⁻¹
W2
300°K
77°K
30000
20000
10000
0
2
4
6
8
10
12
14
16
18
MAGNETIC FIELD B(kgauss)

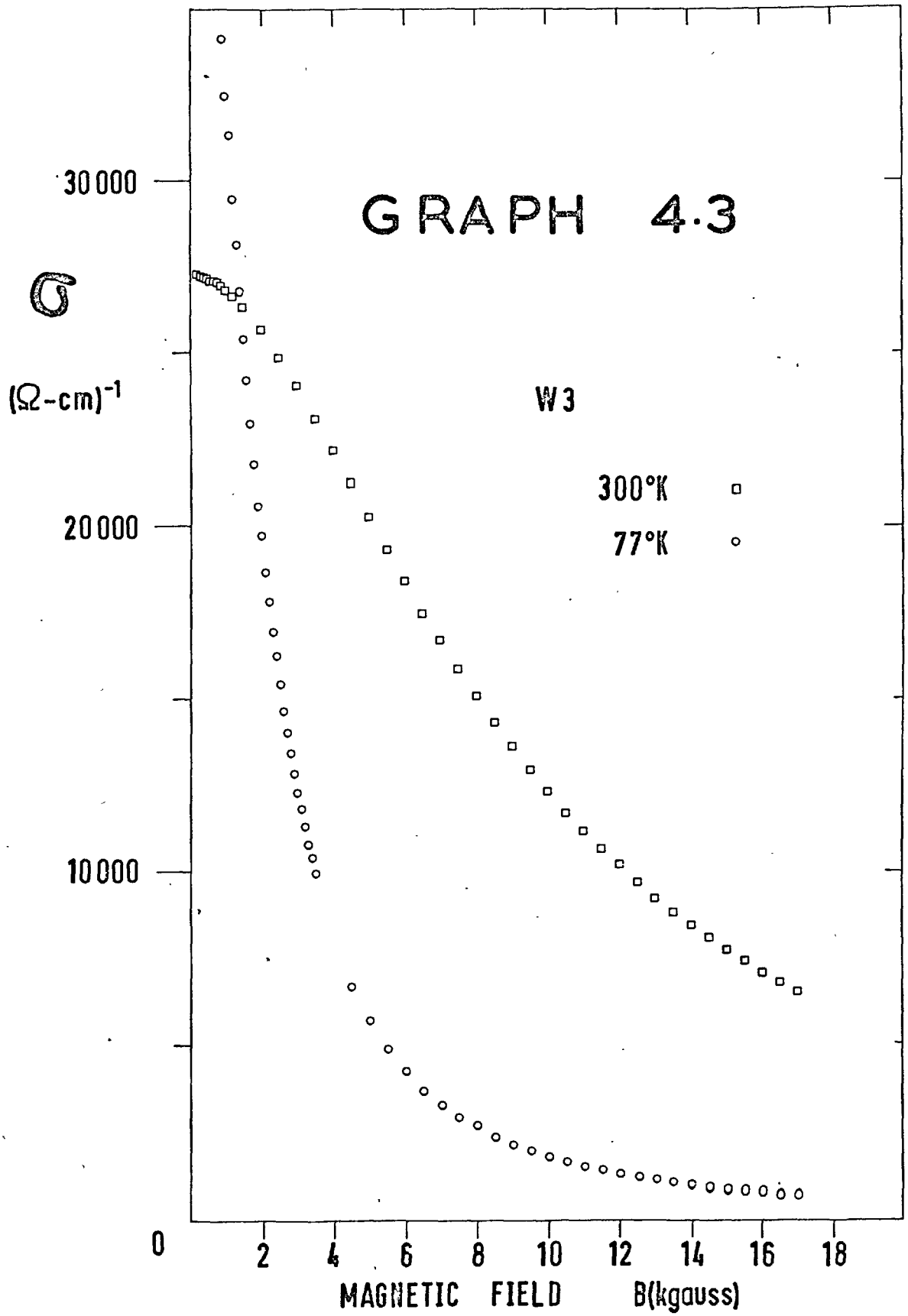
GRAPH 4.3
σ
(Ω-cm)⁻¹
30000
20000
10000
0
W3
300°K
77°K
2
4
6
8
10
12
14
16
18
MAGNETIC FIELD B(kgauss)

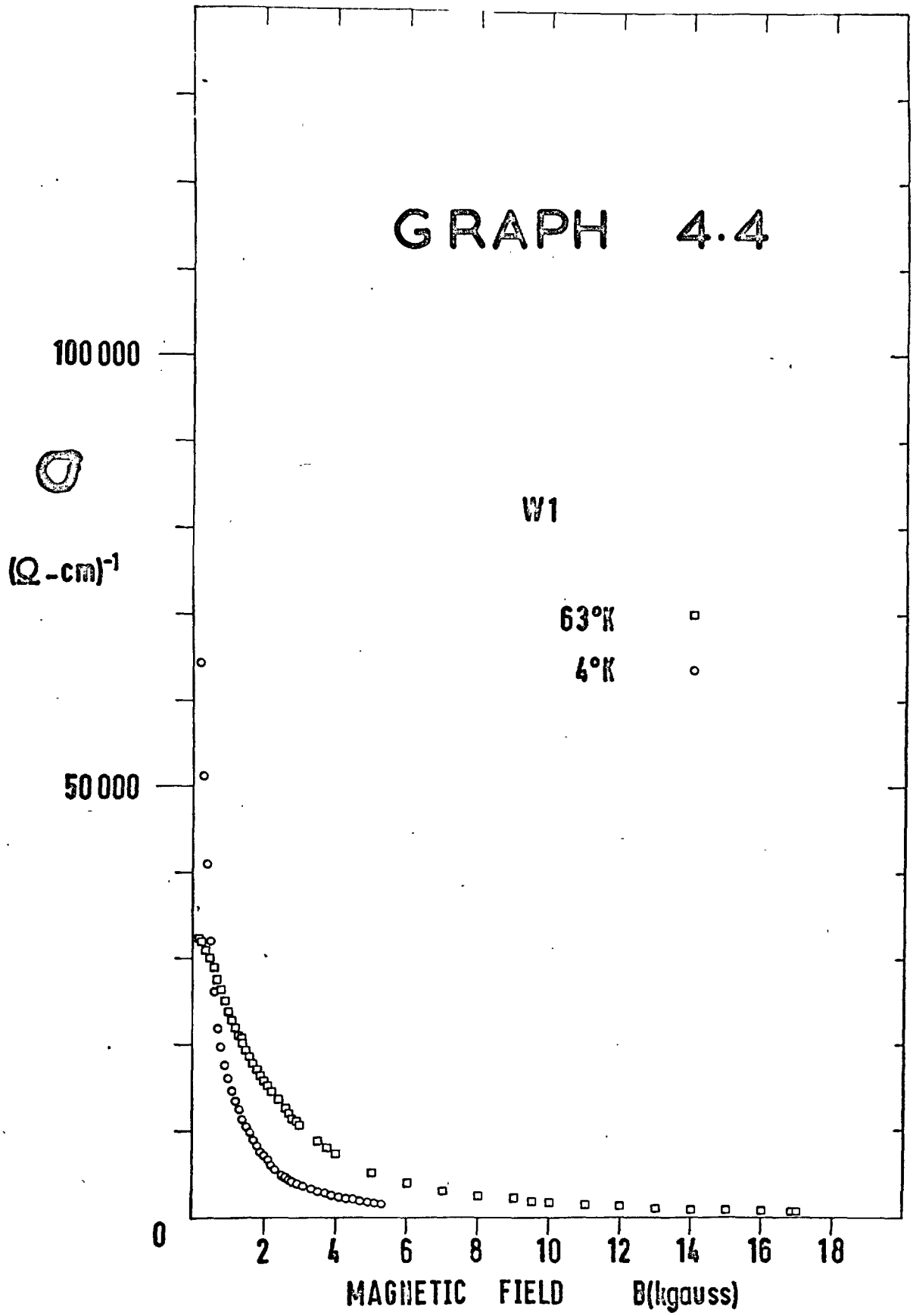
GRAPH 4.4
100 000
σ
(Ω-cm)⁻¹
W1
63°K
4°K
50 000
0
2
4
6
8
10
12
14
16
18
MAGNETIC FIELD B(kgauss)

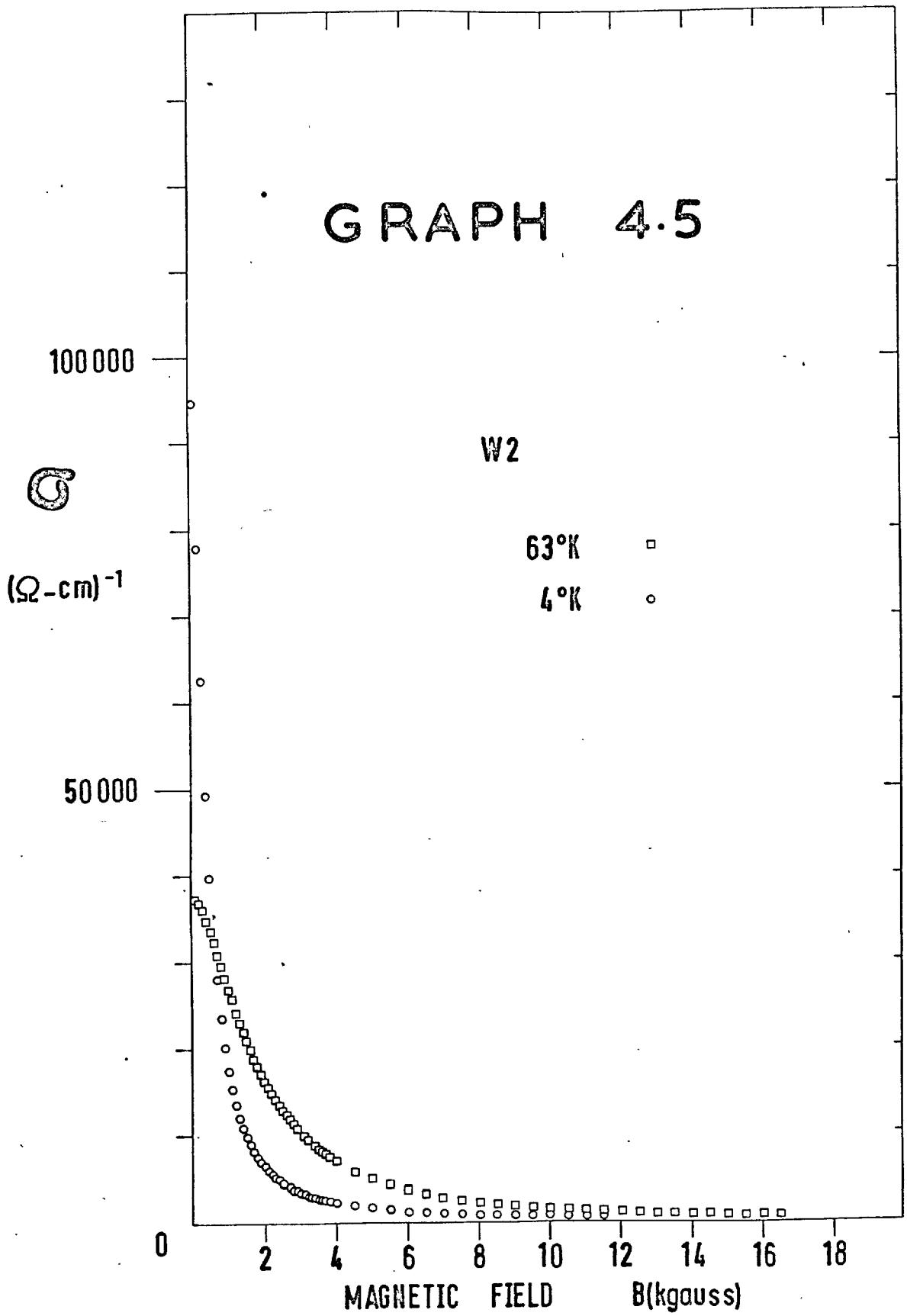
GRAPH 4.5
100000
50000
0
σ
(Ω-cm)⁻¹
W2
63°K
4°K
2
4
6
8
10
12
14
16
18
MAGNETIC FIELD B(kgauss)

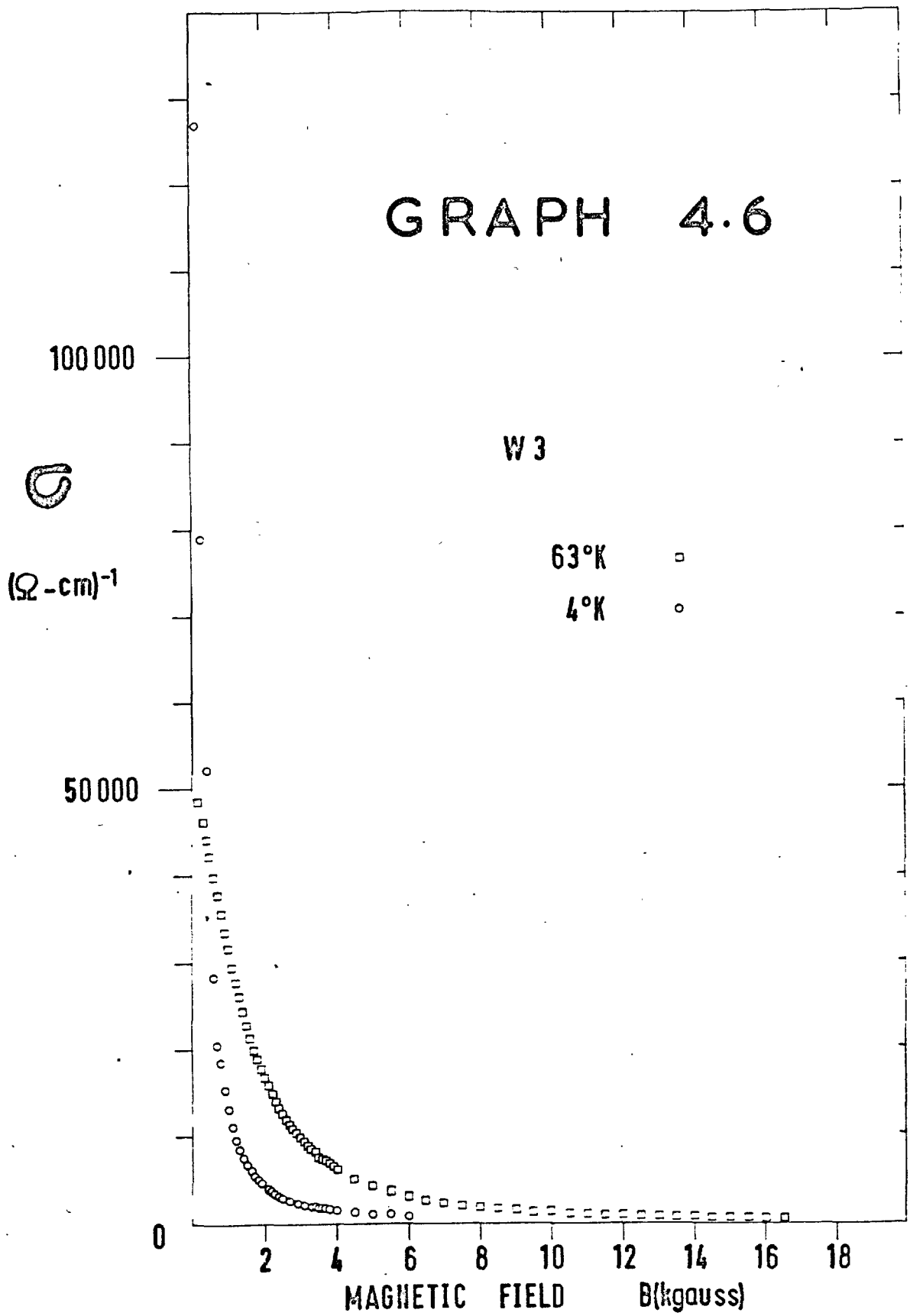
GRAPH 4.6
100 000
σ
(Ω-cm)⁻¹
50 000
0
W 3
63°K
4°K
2
4
6
8
10
12
14
16
18
MAGNETIC FIELD B(kgauss)

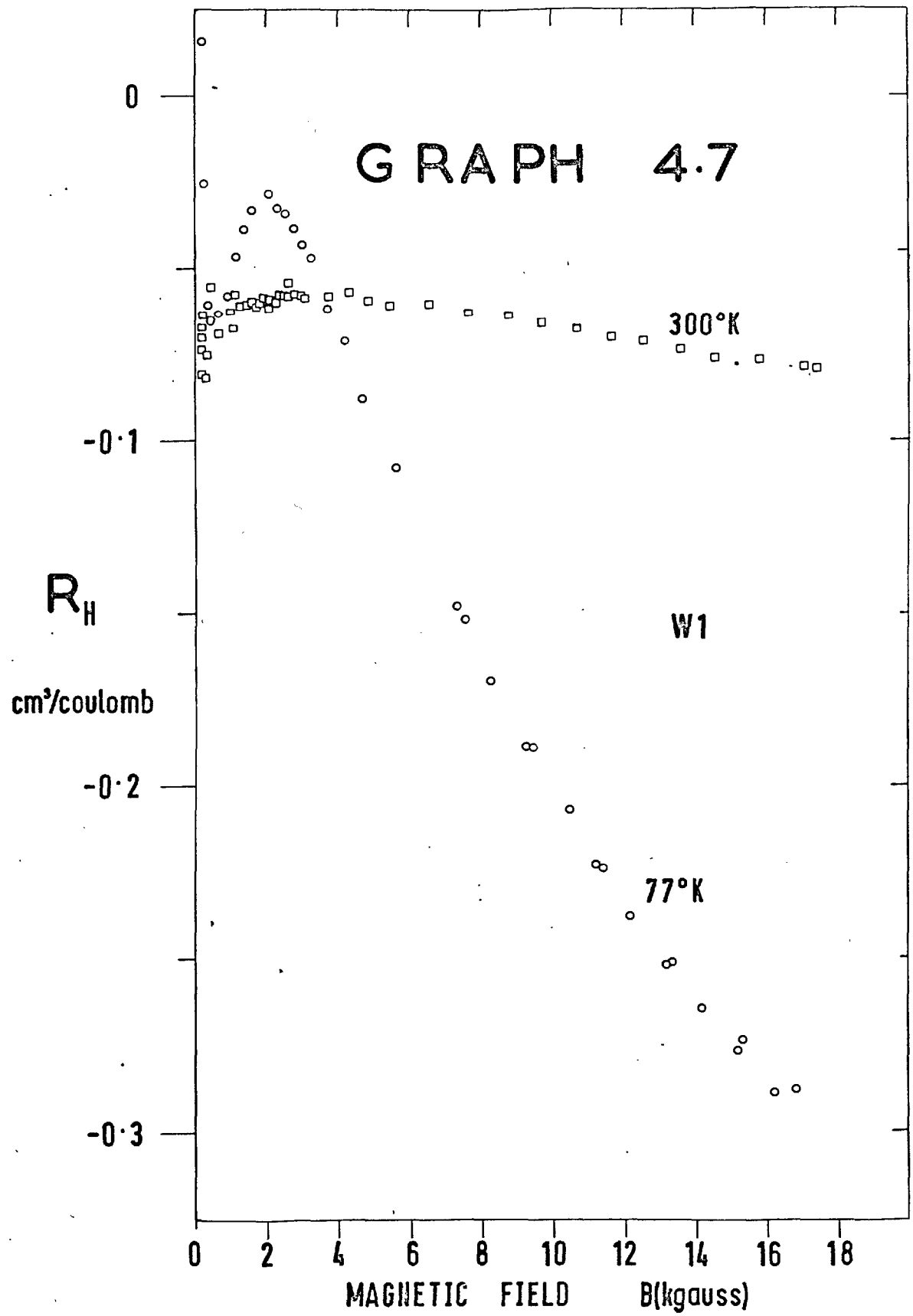
GRAPH 4.7
0
-0·1
-0·2
-0·3
R_H
cm³/coulomb
300°K
W1
77°K
0
2
4
6
8
10
12
14
16
18
MAGNETIC FIELD B(kgauss)

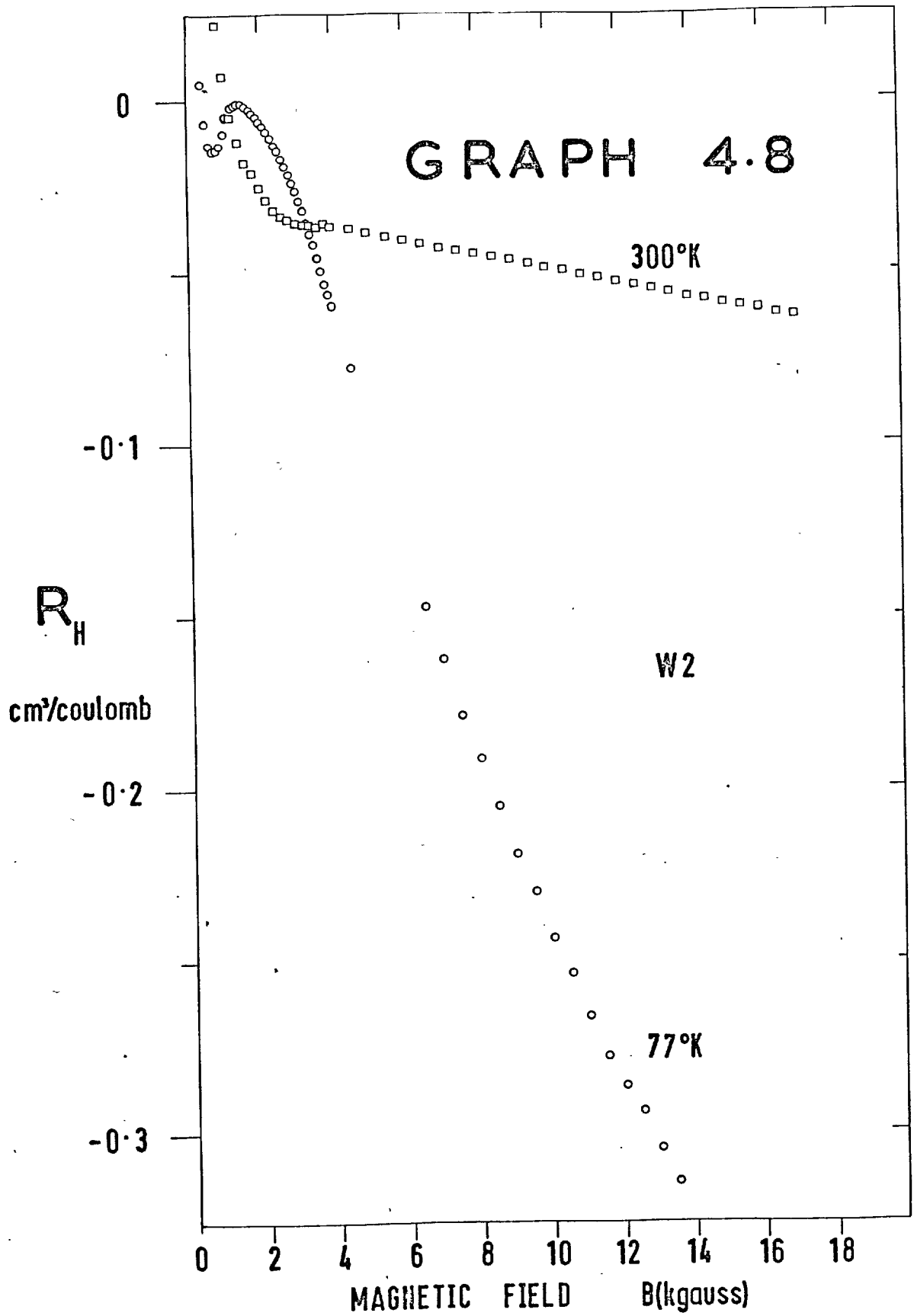
GRAPH 4.8
0
-0·1
-0·2
-0·3
R_H
cm³/coulomb
300°K
W2
77°K
0
2
4
6
8
10
12
14
16
18
MAGNETIC FIELD B(kgauss)

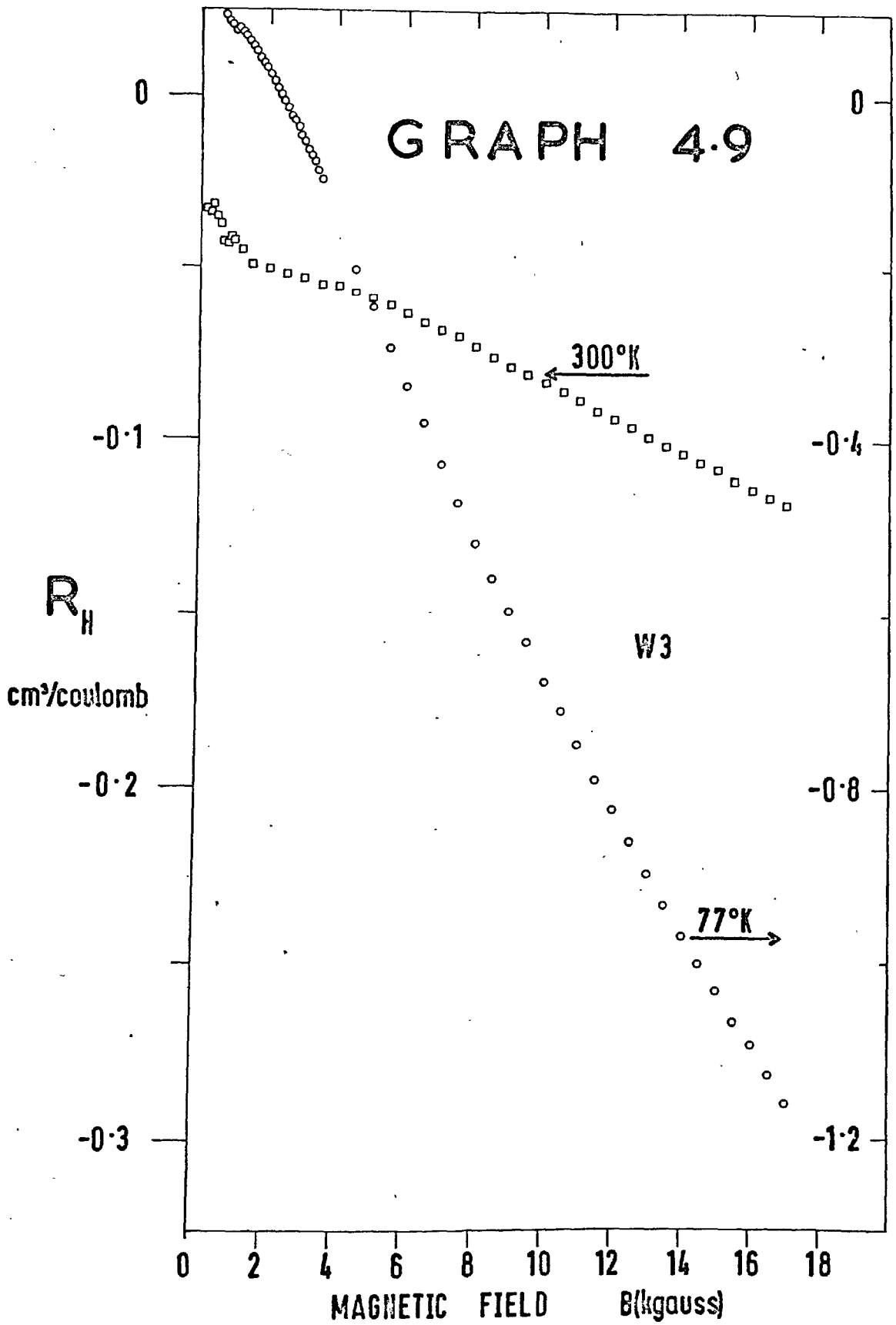
GRAPH 4.9
0
-0·1
-0·2
-0·3
0
-0·4
-0·8
-1·2
R_H
cm³/coulomb
300°K
77°K
W3
0
2
4
6
8
10
12
14
16
18
MAGNETIC FIELD B(kgauss)

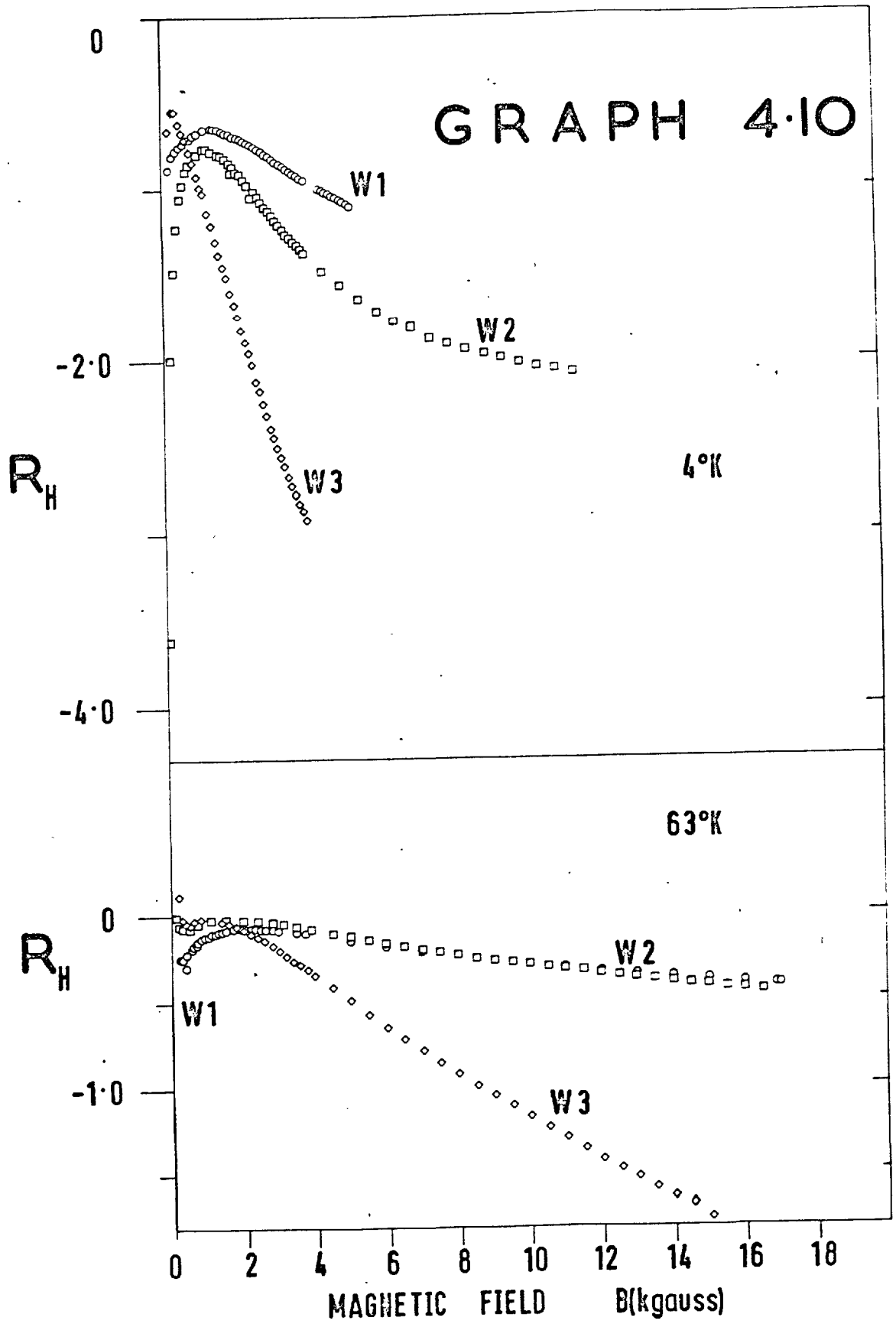
GRAPH 4·10
0
-2·0
-4·0
R_H
W1
W2
W3
4°K
63°K
0
-1·0
R_H
W1
W2
W3
0
2
4
6
8
10
12
14
16
18
MAGNETIC FIELD B(kgauss)

GRAPH 4.11

ILLUSTRATION OF CURVE-FITTING USING THREE AND FOUR LORENTZIANS

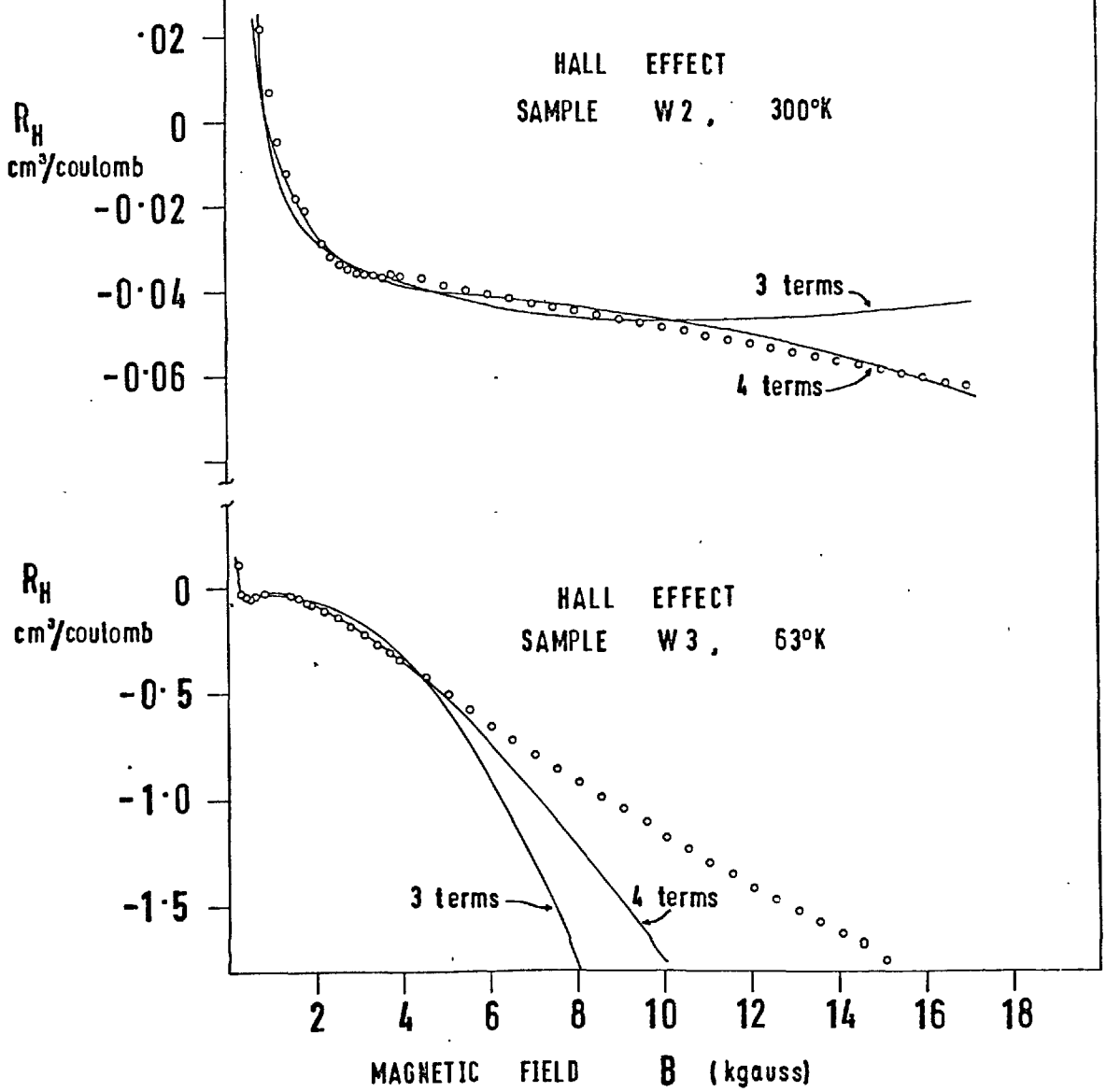

The Method of Least Squares.

Suppose measured quantities $y_1, y_2, \ldots y_n$ are related to the quantities x_{ij} by the equations $y_1 = x_{11}\ a_1 + x_{12}\ a_2 + \ldots + x_m a_m$

$$y_n = x_{n1}\ a_1 + \ldots + x_{nm} a_m$$

or, using matrix notation, $Y = XA$ where the a_j are the parameters which it is required to find. Since, in practice, $n > m$ there are more equations (n) than unknowns (m), and we must determine a criterion for defining the 'best' set of parameters a_i. The best set of a_i is usually taken to be that which minimises the sum of the squares of the residuals. That is, we want the a_i which make

$$\sum_{i=1}^{n} (y_i - x_{ij}a_j)^2$$

a minimum.

Differentiating:

$$\frac{\partial}{\partial a_K} \left[(y_1 - x_1 a_j)^2 + (y_z - x_{2j} a_j)^2 + \ldots \right] = 0$$

$$\text{ie} \quad [y_1 - x_{ij}a_j]\, x_{1K} + [y_2 - x_{2j}a_j] x_{2K} + \ldots = 0 \quad \text{for each } K(=1,2,\ldots m)$$

$$\text{ie} \quad \sum_i [Y-XA]_i x_{iK} = 0, \quad \sum_i \tilde{x}_{Ki}\ (Y-XA)_i = 0 \quad \text{for each K}$$

where $\tilde{x}$ is transpose of X

$$\text{ie} \quad [\tilde{x}\ (Y-XA)]_K = 0$$

We want to find A :

$$(\tilde{X}Y)_K = (\tilde{X}XA)_K \quad \text{for each K.}$$

$$\text{ie} \quad \tilde{X}Y = \tilde{X}XA$$

$$\text{and so} \quad A = (\frac{1}{\tilde{X}X})\tilde{X}Y$$

Thus the procedure for finding the fitting parameters a_i is first to set up the matrices X, Y then calculate the products $B = \tilde{X}Y$, $C = \tilde{X}X$. The matrix C is then inverted and post-multiplied by B. Stated in this way, the problem is seen to be ideally suited for computer solution espcially if FORTRAN language is used since this is well adapted to the handling of matrices. The Imperial College IBM 7090 computer was used for all the data-fitting calculations - they would have been impossibly time-consuming without its use. It should be noted that the method depends upon the first set of equations (the 'observational equations') being linear in the parameters a_i. In the present case this is only true for the parameters A_i and not for the H_i so, unless the Lorentzian functions can be linearised by Taylor expansion for instance, one is only able to use the above matrix method to find the best set of A_i for a given set of H_i. The best set of H_i will have to be found by another method, but at least the number of parameters to be varied has been reduced by a factor of two.

Methods Employed in Fitting the Data.

Two-term fits.

First attempts employed the method indicated above, viz. a set of H_i was decided upon and the corresponding 'best' set of A_i calculated by the matrix formulation of the method of least squares. Two terms were tried at first as it was known that graphite has two majority carriers, and it was hoped that the minority carriers would merely represent a small correction term. Values of H_1 and H_2 were selected in turn so that all pairs of values within prescribed limits on H_1 and H_2 were tried. For each pair the corresponding values of A_1, A_2 were calculated by least squares and the function (ΣR^2 termed the sum of the squares of residuals) evaluated. Finally the computer sorted the 30 sets of parameters giving the lowest values of ΣR^2 and printed them out for inspection. By plotting points representing these pairs of values of H_1, H_2 and labelling each point with its ΣR^2 value, it was possible to draw 'contour' lines of constant ΣR^2 value. From such a diagram the next area in the H_1 - H_2 plane for exploration was selected. In favourable cases it was possible to select the area containing the lowest value of ΣR^2 at the first attempt, in which case the contours took the form of closed loops and the position of the minimum could be estimated. An example of such a diagram is shown in Figure 4.1.

FIGURE 4·1

CONTOURS OF ΣR^2 PLOTTED TO GIVE AN ESTIMATION OF THE POSITION OF THE MINIMUM. THE ACCURATE MINIMUM IS SHOWN BY A CROSS.

$(W, \sigma_{xz}, 300^{\circ}K)$

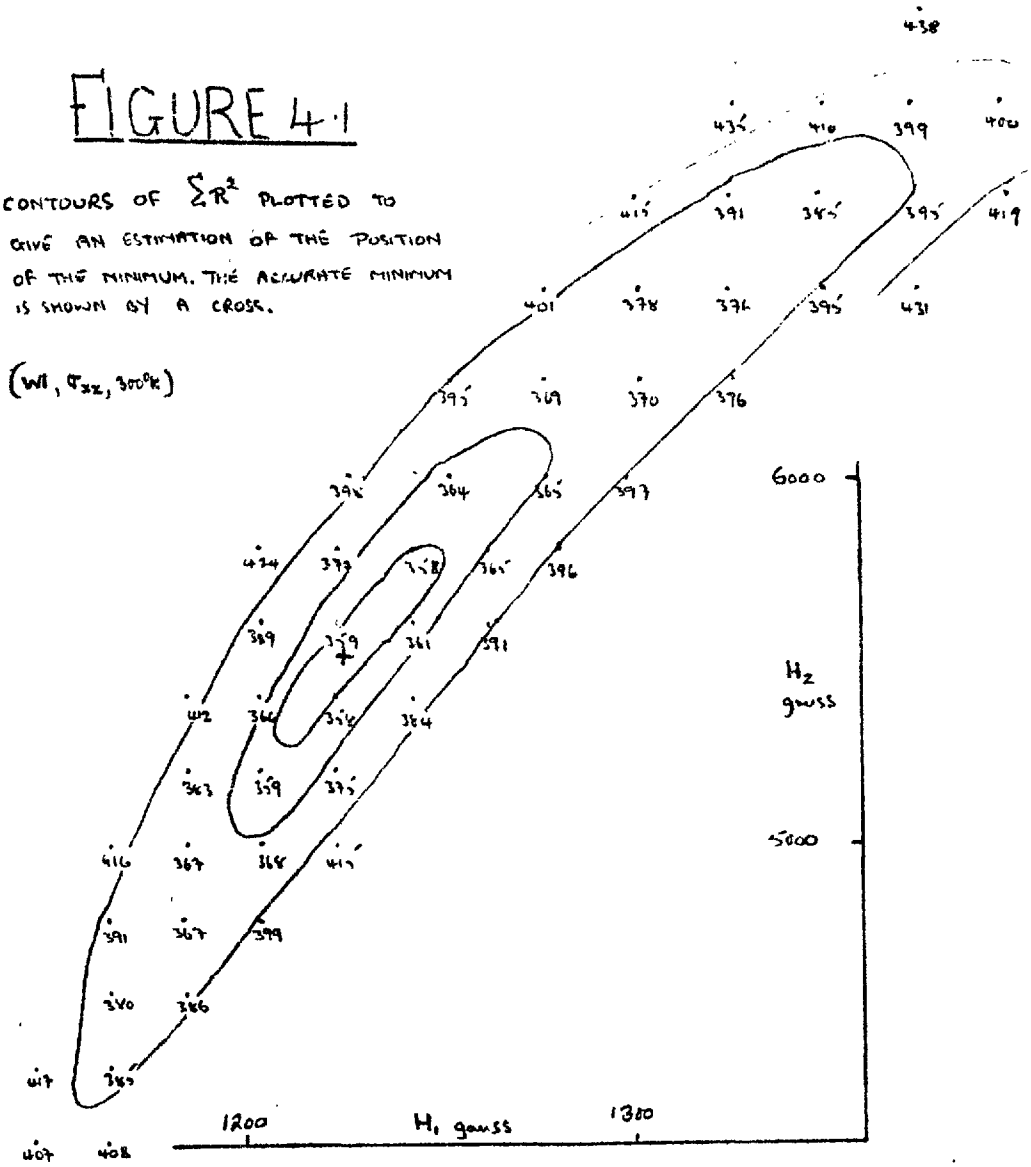

Unfortunately, the contours around the minimum were not simple circles or ellipses, but were shaped more like the longitudinal cross-section of a banana, so location of the minimum was not easy. A programme written to overcome this difficulty was based on a Taylor expansion of the Lorentzian expression about values of H_1, H_2 which were considered to be close to the true values at the minimum. This essentially linearised the observational equations in all the parameters H_1, H_2, A_1, A_2 and enabled one calculation by the matrix method to find approximations to the best values of all parameters. Of course, the method depended upon discarding higher order terms in the expansion and so it was necessary to repeat the calculation several times, changing H_1 H_2 to the latest values before each calculation in order to arrive at the best set of values. Five or so repetitions were usually sufficient to produce unchanging values of the parameters, but the calculation was only stable provided the distance between the starting point and the actual minimum in the H_1-H_2 plane was less than about 20% of the values of H_1,H_2. Stability also depended somewhat upon the direction in which the starting point lay from the minimum.

After two-term fits to the data of each sample at each measured temperature had been produced by the above methods it was decided to extend the fits to three terms.

Three-Term Fits.

With three terms to be fitted the problem became much more difficult. Although the linear parameters A_1, A_2, A_3 could still be found by the linear least squares method for a given set of H_1, H_2, H_3, it was extremely difficult to find the best set of the latter parameters since this involved drawing contour diagrams in three dimensions - or at least superimposing two-dimensional plots. Even with closed-loop contours in the two-term problem it was not easy to decide where the minimum lay within the elongated contours, but with the contours of the three-term problem one could wander along the resulting narrow, curving tunnel without much indication as to the proximity of the minimum. It soon became evident that a new approach was needed and it was decided to try a gradient-following method:

A computer programme was written to find a minimum of the function ΣR^2 by, in effect, moving in H_i space in such a direction that ΣR^2 was always decreased. The principle is best illustrated by considering the two-term problem where one has to find two parameters H_1, H_2. (Perhaps it should be stressed that in all the methods described for fitting data to Lorentzians the only problem was in finding the best set of H_i. The A_i were always calculated by the matrix formulation of the method of least squares described above). By plotting ΣR^2 against the two parameters H_1, H_2 in three dimensions one sees immediately that the problem is to find the lowest point of

the surface so defined. The computer programme was started at a point whose (H_1, H_2) co-ordinates were expected to be reasonably close to those of the minimum. It then proceeded to decide in which direction lay the steepest gradient down the surface by taking two side-steps parallel to the H_1, H_2 axes and noting the resulting changes in height; a simple calculation then gave the direction and values of the steepest down-gradient at this starting point. A step was then taken in this direction, this step being much longer than the two exploratory side "shuffles", and the whole process of shuffle-and-step was repeated until a particular step produced an increase in the 'height' of the surface (i.e. the value of ΣR^2) when it was deduced that a minimum had just been traversed. Going back to the start of this last step, (Δ) the programme then proceeded to take a series of steps (each from the same position) and in the same direction as the step (Δ), with the condition that each was half the length of the preceding step until one of them finally landed on the slope at a lower point than the commencement of step Δ. The usual process of shuffle-and-step was then resumed or the programme terminated itself according to criteria built into the programme concerning the accuracy with which the position of the minimum was desired. Of course, for a three-term fit the surface is plotted in four-dimensional space, but this makes little difference to the algebraic expressions for the gradient at any point - the programme could operate in either of these modes as required.

A further point embodied in the hill-descending programme was that an initial two-term fit was performed using only high-field data in the belief that the violent excursions of the data at low fields were caused by Lorentzians with low characteristic fields (H_i) and so would not unduly influence the main terms at high fields. The object in performing this two-term fit was to obtain a better estimate of the position of the minimum for three terms to save time on the three-term hill-descending. This was always desirable because the hill-descending programme was not very refined and tended to take a long time in reaching the minimum, especially if it were started on the side of a valley, when it would proceed to zig-zag across the valley, making only slow progress along the length. In summary, then, this method involved sorting the data into high and low-field then making a two-term hill-descent with the high-field data only and finally, after a rough scan with changing H_3 values, a three term hill-descent down a new hill defined by all the data.

An extension to more terms soon became desirable, if only to check the effect of an extra term on the goodness of fit and, besides, the simple method of proceeding step by step downhill was time-consuming. A more satisfactory way of reaching the minimum would be to try to predict its position from the local curvature and move each time to the predicted position. M.D. Powell has written several sub-routines for minimising any function of several variables and one of

these (VA01A; see Computer Journal 7, 303, 1964) was employed on a programme for fitting data to up to five Lorentzians. This proved to be extremely reliable and reasonably fast in operation though there is another subroutine (VA02A) which might prove faster in this application since it is specially designed to minimise a function composed of the sum of the squares of quantities, however, VA01A started working smoothly before VA02A and it was felt that the fault-finding time necessary to make the latter work was not available.

Programme to fit data to five or less Lorentzians.

We now describe in outline the fitting programme employing VA01A. A little knowledge of the FORTRAN computing language is assumed here but the essential points are that variables being manipulated must be given names of up to six letters (e.g. DATA, ESCALE, TEXT, etc.), that orders or 'statements' are obeyed sequentially in general; starting with the first and moving through to the last which is usually STOP, and that 'subroutines' are self-contained programmes which may be 'called' into operation by the main programme. Once a subroutine has been called, it performs its calculations until it reaches a statement within itself returning control to the main programme. The main programme, in effect, ties the separate subroutines together and may call a given subroutine as many times as necessary. Indeed one reason for writing a subroutine is to avoid having to write whole blocks of statements again and again.

The purpose of our main programme is to provide subroutine VA04A with a suitable set of input numbers and to accept the output from it. In addition, experimental data must be read in and the final set of fitting parameters printed out at the end. The essential input to VA04A is the array X(I) of parameters which it has to vary in order to minimise the function ΣR^2. Here $X(1) \equiv H_1$, $X(2) \equiv H_2$, ... in previous notation. VA04A returns execution to the main programme when it has found the minimum, in which case the array X will contain the set of best parameters H_1, H_2, and a variable, F, equal to the latest value of the function ΣR^2. Now, VA04A is a subroutine for minimising a general function so our function (which is $\Sigma\,(\text{Resid})^2$) must be explicitly stated. In fact, we must provide our own subroutine called CALCFX to calculate the function $F = \Sigma R^2$ each time it is required; the latest values of H_1, H_2, .. are fed in and the corresponding value of ΣR^2 must come out. So far no mention has been made of the linear parameters A_i. As in previous fitting programmes, these are found for each set of H_i's by the matrix method described above. In fact CALCFX itself calls on a subroutine LSTSQR which takes the latest values of $H_1, H_2, \ldots$ and sets up the matrices necessary to perform the least squares calculation. A final subroutine MATRIX is employed to calculate $(\frac{1}{\tilde{X}X})(\tilde{X}Y)$ and so find the coefficients A_i. Once the best A_i are known for the given set of H_i, the function is calculated by LSTSQR and returned, via CALCFX, to VA04A for examination. VA04A

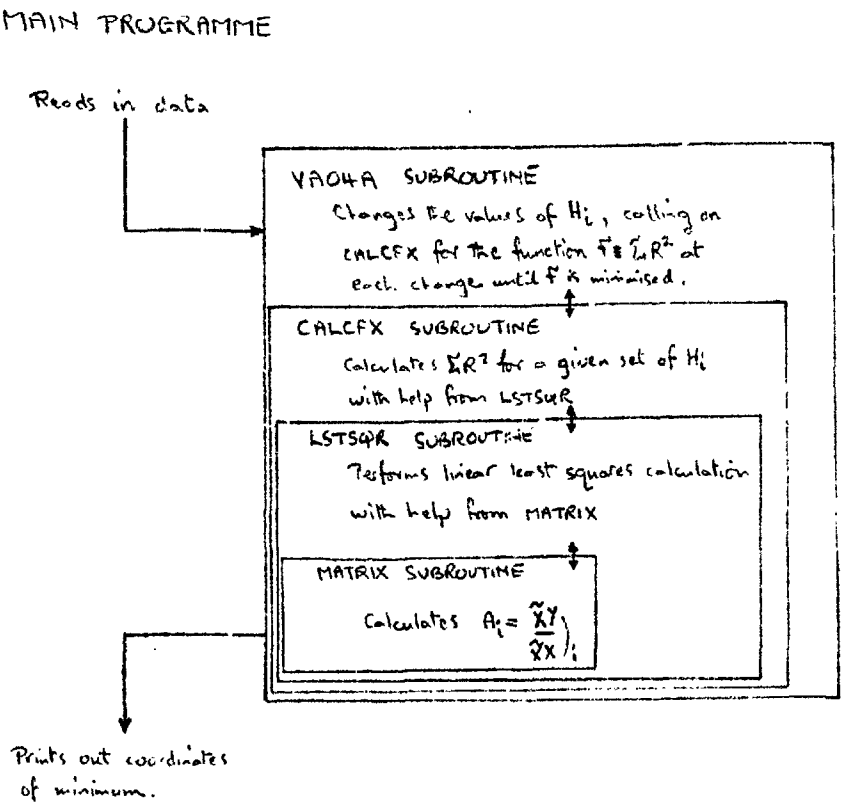

FIGURE 4·2

BLOCK DIAGRAM OF COMPUTER PROGRAMME FOR FITTING DATA TO THE SUM OF UP TO FIVE LORENTZIANS.

calls for many (possibly over 300 on occasions) such calculations of ΣR^2 to be made with slightly different values of H_i before deciding on a change in one of the H_i. In operation, changes are made cyclically in the list H_1, H_2, ... and so on until a minimum is reached. It then only remains to print out the latest values of H_i, A_i and ΣR^2, as shown in the block diagram below Figure 4.2. A photograph of the actual programme statements is included in Appendix 4.

Whilst very good fits were obtained for σ_{xx} by this method, it was found that better fits could be obtained for σ_{xy}/H by weighting the high-field data; the violent excursions in the data at low fields tended to make the sum of the squares of the residuals insensitive to the high field data points. More representative fits were obtained by making several copies of the high field data cards and including them with the data (the IBM 7090 accepts instructions and data coded on to punched cards).

4.2 Oscillatory Data

At temperatures below about $5^{\circ}K$ and for magnetic fields greater than a few kilogauss oscillations in the Hall effect and magneto-resistance (were observed) as the field was swept slowly upwards. These consequences of the quantisation of energy levels are reported here. We first describe how the oscillatory part of the data was separated from the monotonically varying background, since

theories of these quantum effects do not include the background terms quantitatively at the present time.

4.2.1. Separation of Oscillatory Effects from the Background.

An example of the charts obtained at low temperatures is shown below. It can be seen that there is a strong background to the oscillations in the form of a fairly simple curve which might possibly be fitted to a polynomial expression. However, the difficulties attending such an attempt especially when beats were present made it attractive to use a simpler method of fitting the midline by eye: Tangents were drawn between the adjacent maximum excursions of the curve as shown, and points were constructed by taking mean Y-values from these straight-line segments. Finally a smooth curve was drawn to follow these points as closely as possible.

Between 110 and 140 lines were then drawn on the chart parallel to the Y-axis at intervals of 1 mm. along the X (field)-axis. The lengths of these lines between the chart trace and the midline were found by taking them off with dividers and pricking on to graph paper. In this way, a plot of the oscillatory function was built up as measurements were noted down. The fact that this plotted curve appeared to oscillate equally above and below the axis indicated that a satisfactory midline had been used. The figure (4.3) illustrates the necessity of associating a sign, + or -, with each measurement according as the trace lies above or below the

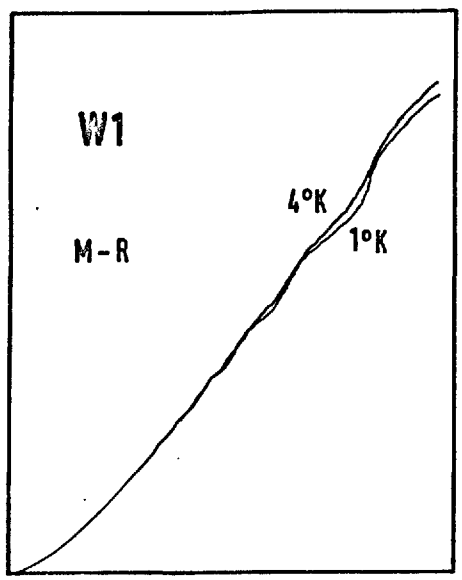

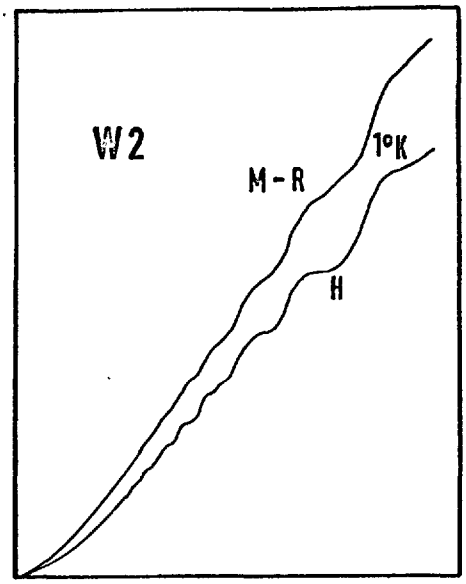

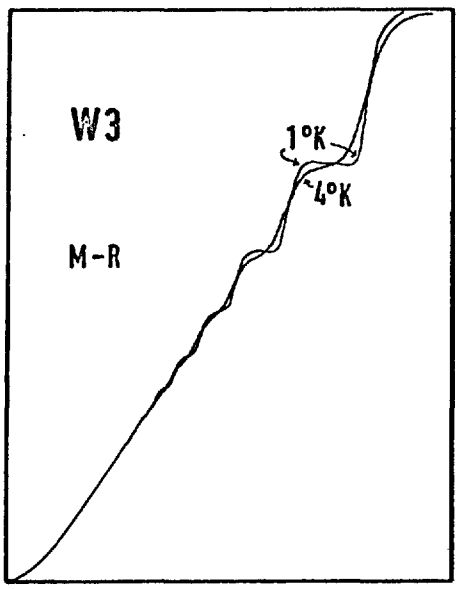

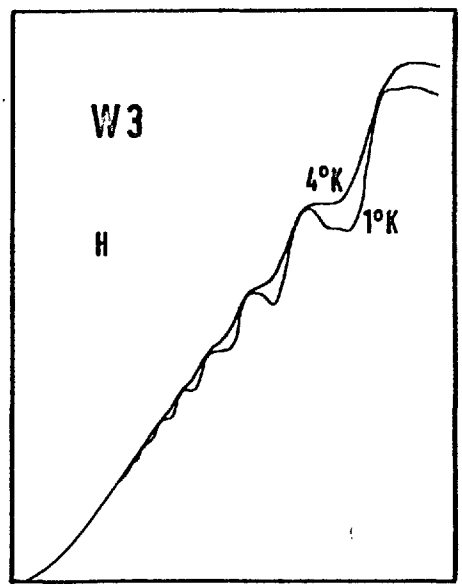

FIGURE 4·3

Showing effect of temperature on Hall (H) and magnetoresistance (M-R) for different samples.

midline respective. By applying the chart calibration constants, found as described earlier (Section 4.1.1), it was possible to convert chart distances into magnetic-field values and sample (voltage/current). These pairs of values were then recorded on punched cards for later detailed analysis, described in Section 4.2.3. Most charts were not treated in such detail, but were merely examined for the field values at which the trace crossed the midline. Resulting "Nodal Plots" are presented below in Section 4.2.2.

Figure 4.3 shows tracings of the chart recordings obtained at helium temperatures. The horizontal axis for each trace represents a magnetic field change from zero to nearly 18kG and is the same to within 2% for all curves whilst the vertical axis is proportional to the sample voltage arising from the Hall effect (H) or magnetoresistance (M-R).

Superposition of the two M-R curves for sample W1 shows clearly how the oscillatory magnetoresistance changes with temperature. The oscillations deepen in the negative direction with a lowering of temperature, but the positive peaks and background are essentially unaltered. Sample W2 is used to illustrate the greater detail which is present in the Hall effect oscillations compared with magnetoresistance oscillations taken at the same temperature. It can be seen that the amplitude of the oscillatory part is a

greater fraction of the background in the former case. This is not all, however, for the W3 curves bring out very clearly the increased structure visible in the Hall effect oscillations. The effect of a lowered temperature is much more dramatic in the case of this sample.

Data for three curves from which the background has been removed are included in appendix 3. One of these, the Hall effect at 1.2°K for sample W3, was intensively analysed in the manner reported in Section 4.2.3. The results of this analysis appear in Section 5.2.

4.2.2. Nodal Plots.

Suppose one attached integer labels to corresponding points of successive oscillations of a single-period function f(x). Then a plot of integer against x would yield a straight line whose slope gives the frequency of f(x). Such a procedure is not valid in general for a function containing more than one periodic element. It is interesting, however, in the absence of sufficient data to make the periodogram technique of astronomy (Whittaker and Robinson, 1956, p.344) worthwhile to plot the midline-crossing points ("nodes", labelled by integers) against reciprocal magnetic field. We do not at first sight expect much information from such Nodal Plots since the oscillatory effects in graphite have contributions from two majority carriers with distinct periods. However, the plots (shown for W1, W2, W3 in Graphs 4.12, 4.13, 4.14 respectively) turn out to be well represented by straight-line segments.

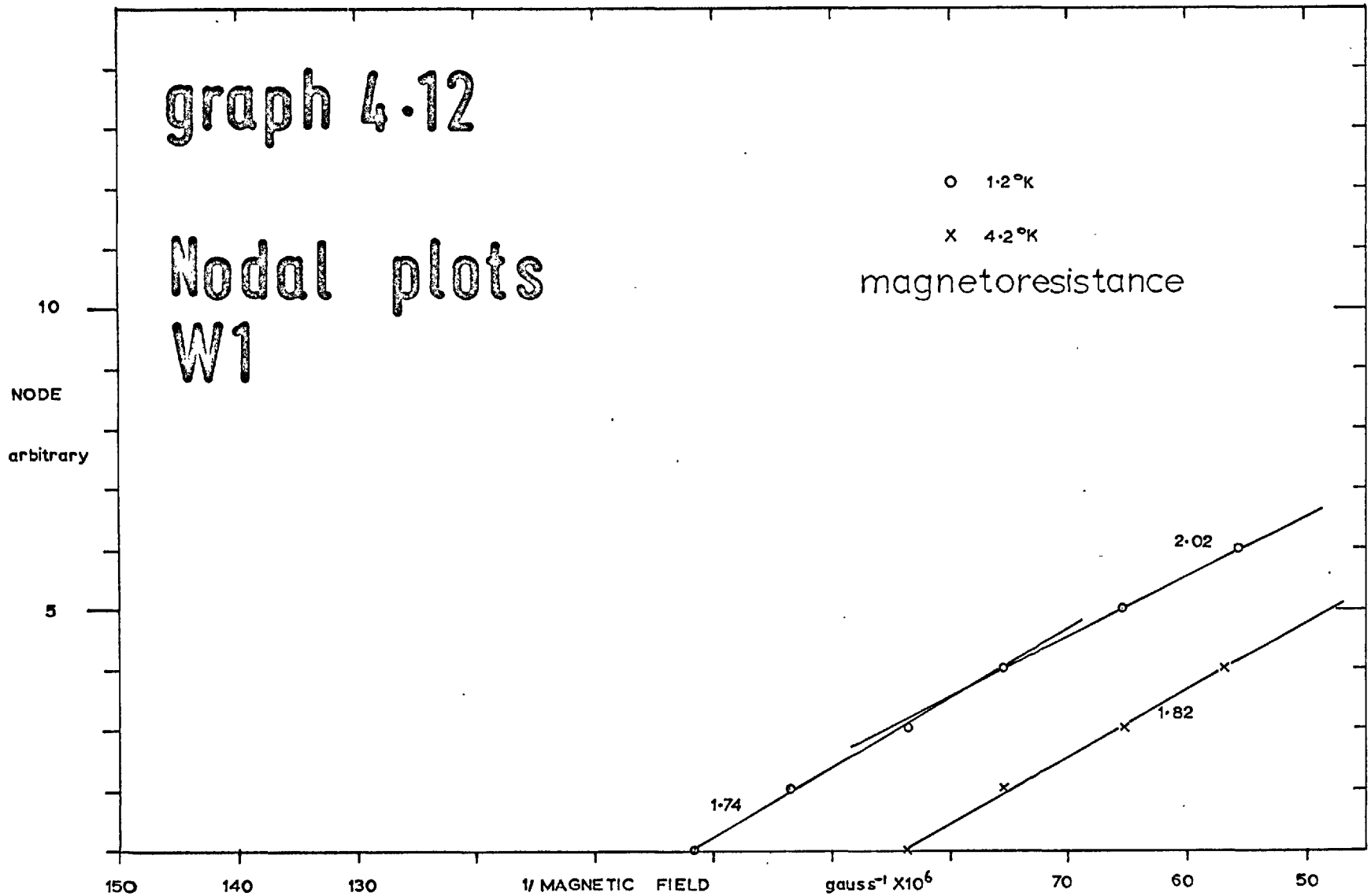
graph 4.12
Nodal plots
W1
o 1·2°K
x 4·2°K
magnetoresistance
10
NODE
arbitrary
5
2·02
1·74
1·82
150
140
130
1/ MAGNETIC FIELD
gauss⁻¹ X10⁶
70
60
50

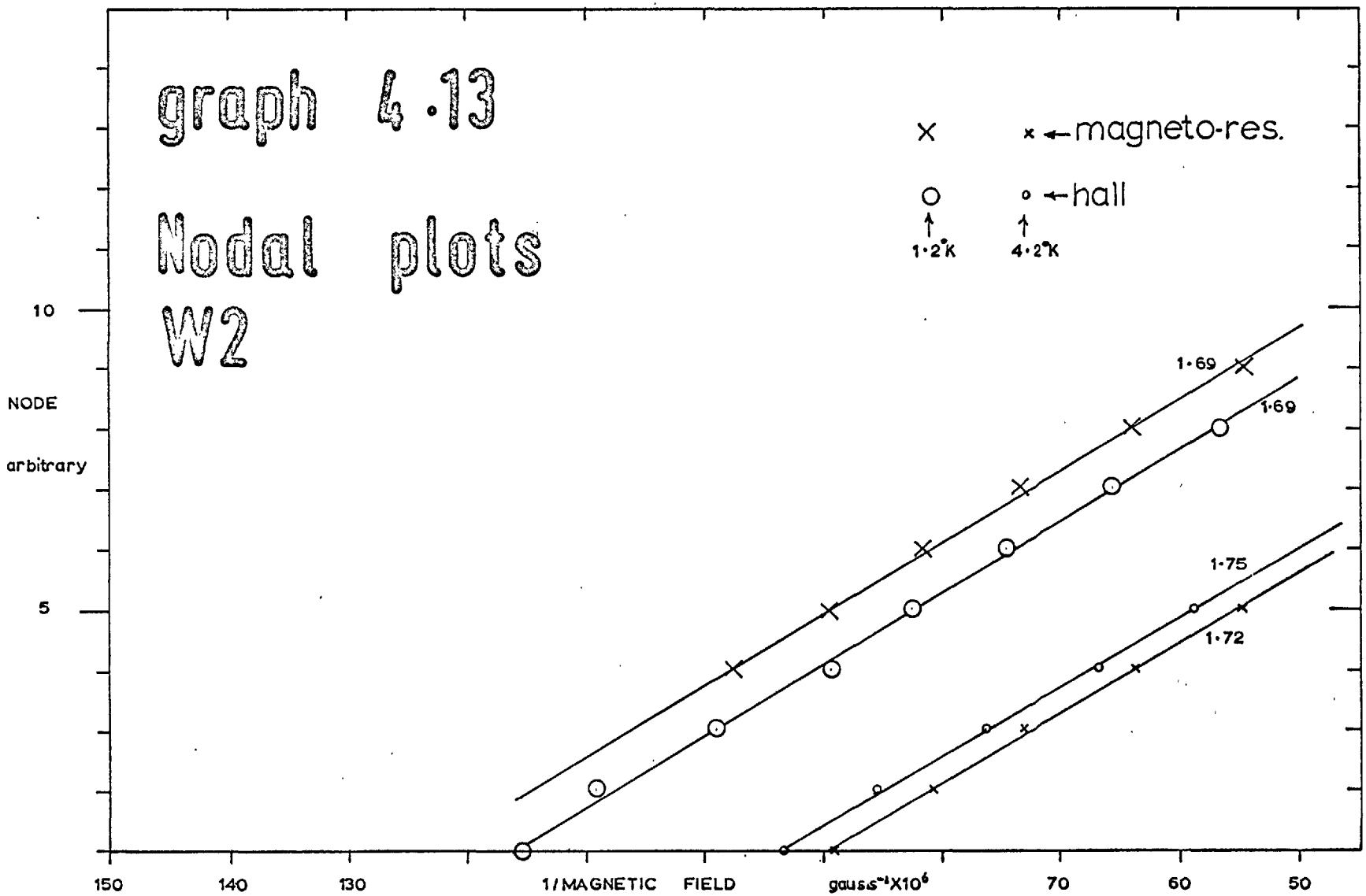
graph 4.13
Nodal plots
W2
× ← magneto-res.
o ← hall
1·2°K
4·2°K
10
NODE
arbitrary
5
1·69
1·69
1·75
1·72
150
140
130
1/MAGNETIC FIELD
gauss⁻¹X10⁶
70
60
50

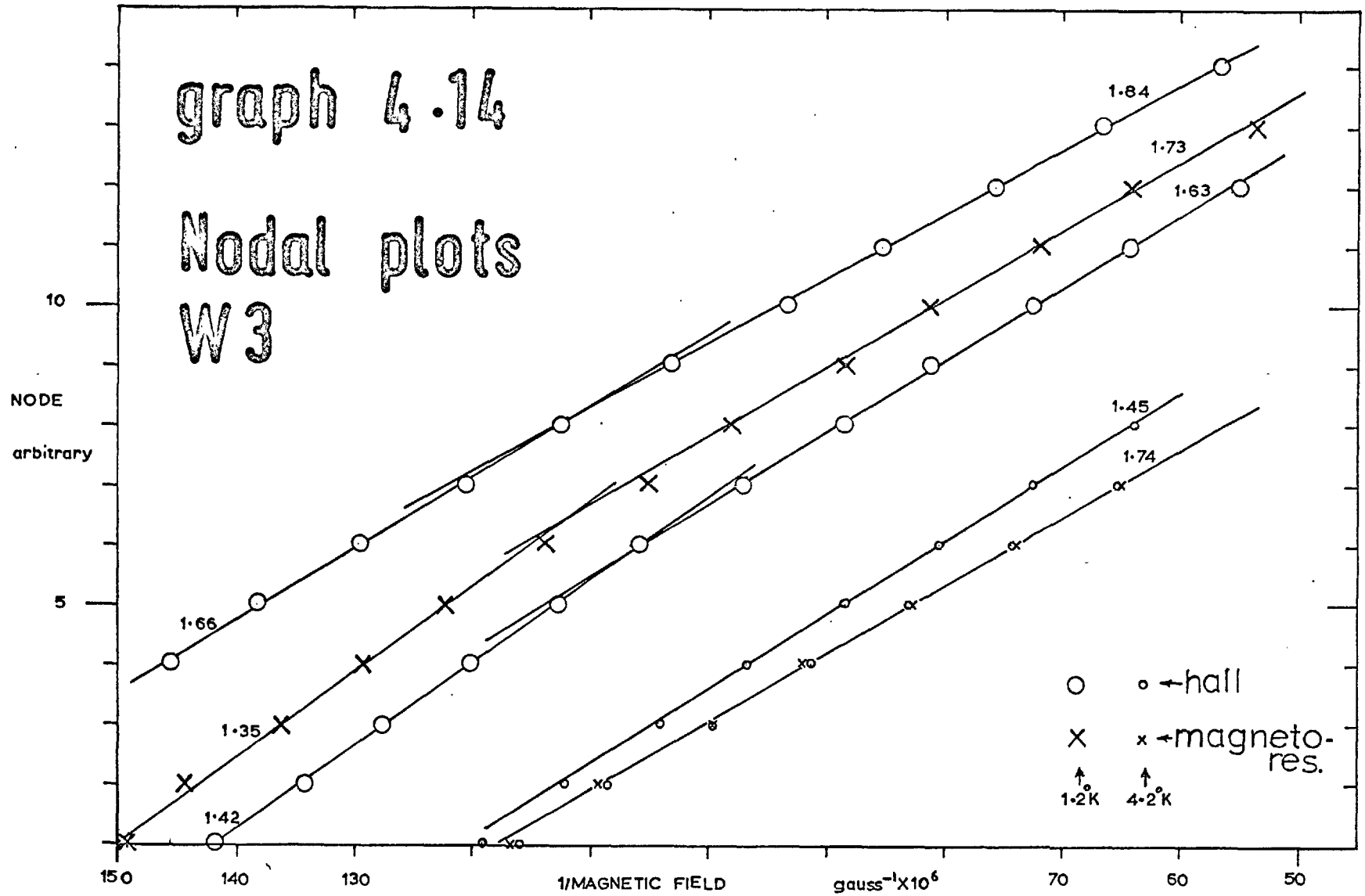
graph 4.14
Nodal plots
W 3
NODE
arbitrary
10
5
1·84
1·73
1·63
1·66
1·35
1·42
1·45
1·74
o ← hall
x ← magneto-res.
1·2°K
4·2°K
150
140
130
1/MAGNETIC FIELD
gauss⁻¹X10⁶
70
60
50

We attribute this to a rapid decline in the amplitude due to one carrier with decreasing magnetic field; at low fields only one carrier is contributing whereas at high fields both contribute. It should be pointed out that the slopes quoted on each curve (in units of 10^{-5} gauss^{-1}) could be in error by as much as $\pm$ 0.1 x 10^{-5} gauss^{-1} because it depends critically on the number of points chosen to be represented by the straight line.

At 1^{o}K the mean behaviour of W3 is to move from a slope of 1.38 to 1.73 with increasing magnetic field. W2 has a constant slope of 1.69 whilst W1 moves from 1.74 to 2.02 x 10^{-5} gauss^{-1}. Since high fields must yield some sort of weighted mean of the separate periods one concludes that the more lightly damped carrier has an oscillation period around 1.4 x 10^{-5} gauss^{-1} for W3 and this becomes mixed at higher fields with a period somewhat higher than 1.7 x 10^{-5} gauss^{-1}.

The single straight lines for W3 at 4.2^{o}K most likely mean the observed behaviour is due to both carriers; the slope of two of these curves (1.74) bears this out but the third 4.2^{o}K curve has a much lower slope. W2 yields single straight lines at both 4.2 and 1^{o}K and moreover they have practically the same slope. This sample, like W1, showed no remarkable increase in structure when the temperature was lowered to 1^{o}K.

4.2.3 Fitting Oscillatory Data to the Landau Expression

It was described earlier (Section 2.3) how we expect the oscillatory data to follow the generalized Landau expression:

$$G = H^n \sum_{K\ (\text{harmonics})} W(K) \quad \frac{(KU)}{\sinh(KU)} \quad e^{-KU\frac{\Delta T}{T}} \quad \cos\left(\frac{2\pi K}{PH} + \phi(k)\right)$$ ~~the other carriers~~

where $U = \frac{2\pi^2 KTm^*C}{\hbar e} \quad \frac{1}{H} = \frac{A}{H}$, say $(A \text{ and } \underset{\Delta T}{U}, P, \phi, n)$ can differ for the other carriers.

We attempted to fit our data to this expression by iteration. Powell's VA04A subroutine was again employed to minimise a function defined as the sume of the squares of the differences between calculated and experimental values, but the main programme was complicated by provisions for choosing the number of carriers to be fitted and the number of harmonics of each to be included. In addition, it was decided to hold various parameters (PERIOD, POWER, A, DTBT) constant when desired in order to have some control over the direction in which the minimum was approached and to prevent physically unrealistic swings during the initial stages. It should be borne in mind that for two carriers, with two terms each, a total of 16 parameters are being varied. This represents a major problem in data fitting and some control over the process was thought essential, even though it considerably complicated the computer programme.

It is proposed to describe the fitting programme in outline, indicating the function of each subroutine in sufficient detail to enable an understanding to be gained of the FORTRAN listing (see photograph in appendix 4) if this is desired.

Once more, the main task was to supply subroutine VA04A with a list X(I) of independent variables to be changed in order to obtain a minimum in the function defined in the subroutine CALCFX to be the sum of the squares of residuals. The MAIN programme first reads the number of carriers, and harmonics of each one it is desired to fit and a set of starting values for all the parameters: P ≡ PERIOD, n ≡ POWER, A, $\frac{\Delta T}{T}$ ≡ DTBT, ψ ≡ PSI. In addition, a matrix NHOLD(I,J) must be filled with 1's or 0's depending on which of the parameters PERIOD, POWER, A, DTBT it is desired to hold constant during this fitting attempt. For instance, if NHOLD(3,1)=1 and NHOLD(1,1),(2,1),(4.1) = 0 then A for carrier 1 will be held constant and PERIOD, POWER, DTBT for carrier 1 will be allowed to vary. Similarly, NHOLD(i,2) where i = 1,2,3,4, defines which parameters for carrier 2 are to be allowed to vary.

This facility introduces complications in the programme in the form of two subroutines ADJINL and ADJUST, which are necessary to fill the matrix X(I) with only those parameters which are to be varied during the run. In effect, ADJINL is a shunting yard, filling the siding X with only those trucks marked "to be fitted", and with

NHOLD controlling the switching of points. Once ADJINL has filled X with the appropriate parameters (these always include W,PSI for all harmonics of each carrier) then VA04A is called upon to take control.

VA04A periodically calls upon CALCFX to supply it with the value of the function $\Sigma(\text{Residuals})^2$, giving CALCFX the latest values of the fitting parameters in X(I). Before CALCFX can do this, however, it must change the values of PERIOD, POWER, A, etc. to the latest values in X, leaving unchanged the values of parameters not contained in X. To do this, CALCFX calls upon ADJUST which employs the array NHOLD as a translation key in unravelling X(I) and presents the latest values of all parameters to CALCFX. CALCFX next calls upon CALC to evaluate the value of the Landau expression G, given these parameters and the data points one at a time. As each value of G comes back from CALC, CALCFX subtracts from it the corresponding experimental value, squares this difference, and adds it to the current value of ΣR^2. When all data points have been used CALCFX returns the final value of ΣR^2 to VA04A. This process is repeated each time VA04A calls for a new value of ΣR^2, which might happen several hundred times before it decides upon a new approximation to the best set of parameters (one 'iteration'). We see then, that ADJINL is called upon once only to perform the initial filling of X(I), while ADJUST is required each time VA04A calls upon CALCFX.

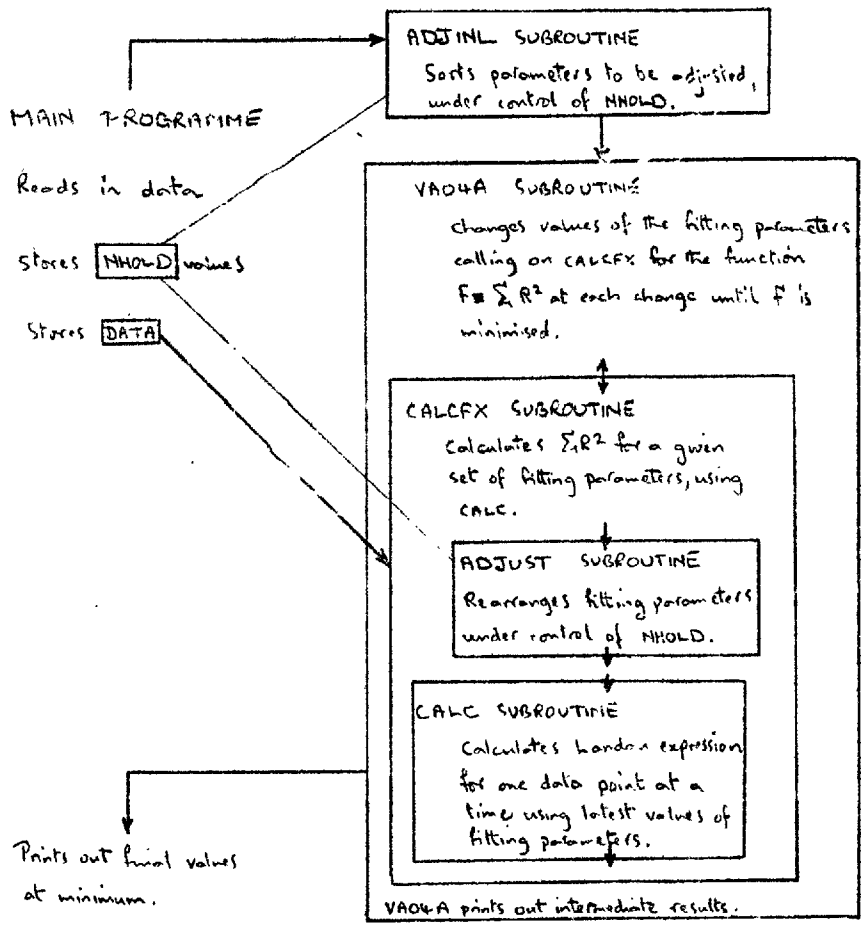

FIGURE 4.4

BLOCK DIAGRAM OF COMPUTER PROGRAMME FOR FITTING DATA TO THE GENERALISED LANDAU EXPRESSION. ("FRIER")

Usually the programme was terminated automatically, having exceeded the five or ten minutes running time it was allowed. The print out from VA04A was then examined to assess progress made in reducing ΣR^2 and the latest values were punched on to cards for the programme to be restarted, possibly with changes made in NHOLD (i,j). On occasions, however, probably under fairly restrictive conditions of NHOLD, VA04A found a minimum in ΣR^2 and returned control to the main programme, which then printed out the complete list of parameters in easily readable form under appropriate headings. The fitting process was finally completed when this form of termination of the programme occurred under the conditions NHOLD(i,j)=0 for all i,j. A block diagram is shown below in Figure 4.4.

4.3 Resistance Variation with Temperature.

We briefly present here the variation of resistivity with temperature for the three samples W1,W2,W3. Graph 4.15 shows that the curves run parallel to each other at temperatures above $80^{\circ}K$ and indeed would coincide if each were normalized by its room temperature value. The much greater resistance ratio $\rho 295/\rho 4.2$ for W3 should be noted; it is some four or five times the ratios for W2 and W1. This indicates a greater perfection in texture for sample W3 and probably explains the much greater amplitude of oscillatory effects observed with this material.

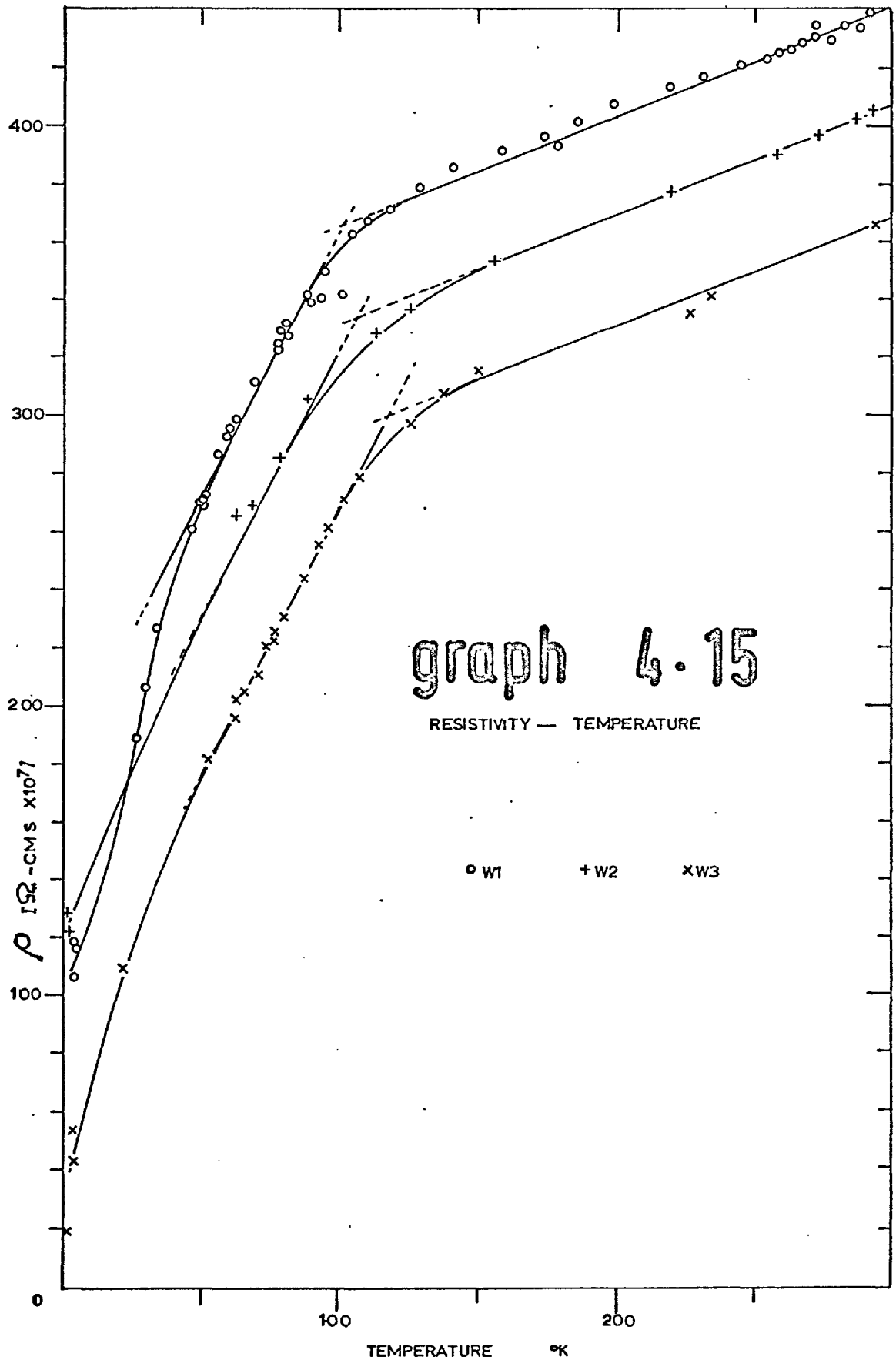
graph 4.15
RESISTIVITY — TEMPERATURE
o W1
+ W2
× W3
ρ [Ω-CM s X10⁷]
TEMPERATURE °K
0
100
200
300
400
100
200

APPENDIX 3A

c- AXIS RESISTIVITY

For the sake of completeness we present here some results and comments on c-axis conduction, that is, with current normal to the basal planes.

The technique of sample preparation was described in chapter 3, p90. Graph A3 shows the temperature-resistivity plot for one sample of hot-pressed annealed pyrolytic graphite (HJCT 61/2/A(62)) the dimensions of which were 0.065 x0.749 x 0.378 cms. Absolute values could be in error by as much as 10% because of (a) the error in the thickness measurement ± 4%, (b) possible correction of 5% or so from the effect of non-uniform current flow near the electrodes (mentioned on p90).

We have made use of c-axis results in the Discussion, p165, and shall now briefly present a few comments on this subject.

Spain et al (1967) found that ρ_c was insensitive to sample perfection (as judged, for instance, by basal plane resistivity) and concluded that the behaviour shown for a range of their hot-pressed and annealed material must be close to that of ideal graphite. Graph A3 agrees closely with their results for such material.

It has been conclusively argued that shorting of the c-axis resistivity by misaligned basal planes does not contribute significantly to measured c-axis effects. The

two main arguments are based on (a) basal plane and c-axis resistivity have opposite temperature coefficients above 60°K; compare graphs A3 and 4.15, and (b) neutron irradiation increases basal plane but decreases c-axis resistivity.

As the temperature is decreased from 300°K the c-axis resistivity rises because of the decrease in carrier concentration; it is thought that the mean free path in this region is limited to a few interlayer spacings. A constant mean free path at high temperatures is consistent with a conductivity pressure coefficient (Yeoman and Young, 1969) which closely follows the known (Anderson et al, 1967) carrier concentration pressure coeffient.

Below 50 - 60°K the scattering is dominated by the LA c-axis phonons which have the low Debye temperature of 185°K and couple strongly to charge carriers because of the sensitivity of band parameters such as γ_2 to interlayer spacing.

At the lowest temperatures we find ρ_c becomes constant with the mobility presumably dominated by some form of static obstacle scattering. We have seen some evidence for a minimum in the resistivity curve at around 4.5°K but the region appears to be structure-dependent and changes on thermal cycling.

The description of c-axis conduction in terms of a band model is not yet satisfactory, particularly at higher temperatures.

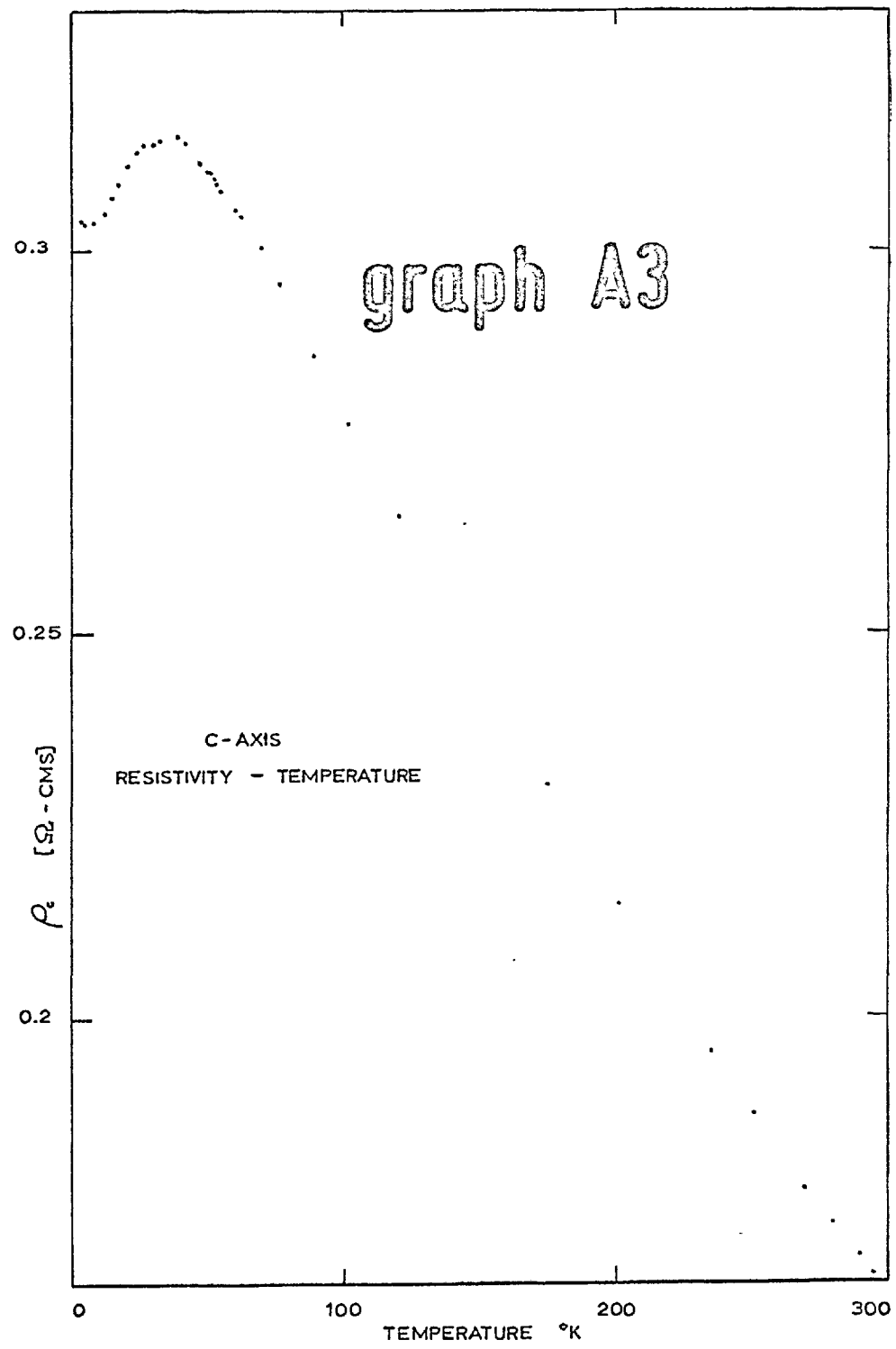
graph A3
0.3
0.25
0.2
C-AXIS
RESISTIVITY - TEMPERATURE
ρ_c [Ω-CMS]
0
100
200
300
TEMPERATURE °K

CHAPTER 5

DERIVED RESULTS

We now present the tensor components σ_{xx} and σ_{xy} derived as described in Section 4.1.3. This is followed by a derivation of hole and electron mobilities and densities. Section 5.2 is devoted to the Landau expression for Hall effect oscillations in W3 and its interpretation.

5.1 Non-Oscillatory.

5.1.1 Derived Conductivity Tensor Components.

It has been described elsewhere (Section 4.1.3) how the Hall coefficient and conductivity curves were fitted to the sum of up to four Lorentzians in the form

$$\sigma_{xx} = \Sigma \frac{A_i}{1 + \left(\frac{H}{H_i}\right)^2}$$

where A_i and H_i are the fitting parameters. Sections 2.4 show how this representation of the data can be used to separate out the effects of electrons and holes and derive partial conductivities for these two types of carrier. These, in turn, lead to values for electron and hole densities and mobilities. We present here the results of such an analysis, performed by a computer programme which accepted the fitting parameters for σ_{xx} and $\sigma_{xy/H}$ and then derived

densitities and mobilities for each type of carrier. In addition, tables of conductivity σ and Hall coefficient R with corresponding magnetic field values were printed out for comparison with experimental curves, and total and partial conductivity tensor components

$$\sigma_{xx},\ \sigma_{xx}^{P},\ \sigma_{xx}^{n},\ \sigma_{xy},\ \sigma_{xy}^{P},\ \sigma_{xy}^{n}$$

were tabulated against magnetic field. Appendix 3 contains these results for the four standard temperatures for W1,W2,W3. Table 5.1 of Section 5.1.3. lists the carrier mobilities and densities.

Referring to Graphs 5.1 and 5.2, we see that the σ_{xx} curves have the appearance of being single Lorentzians. However, any attempt to fit them to a single term yields disappointing results. The appearance is due to the simple fact that a sum of Lorentzians has the same form as a single Lorentzian at both high and low values of the argument (magnetic field). The constants of these equivalent single terms are different at the two extremes, however. In practice, it was found that up to four terms were required to achieve a satisfactory fit. In all graphs presented in this section the data points are discrete symbols whilst the solid curve is the final result of the fitting process; it has been regenerated from the fitting parameters (up to eight in number) which best describe that data.

The σ_{xx} component presents little trouble, as the agreement between data and fitted curves in Graphs 5.1, 5.2 shows. The graphs are all arranged to facilitate comparison between samples.

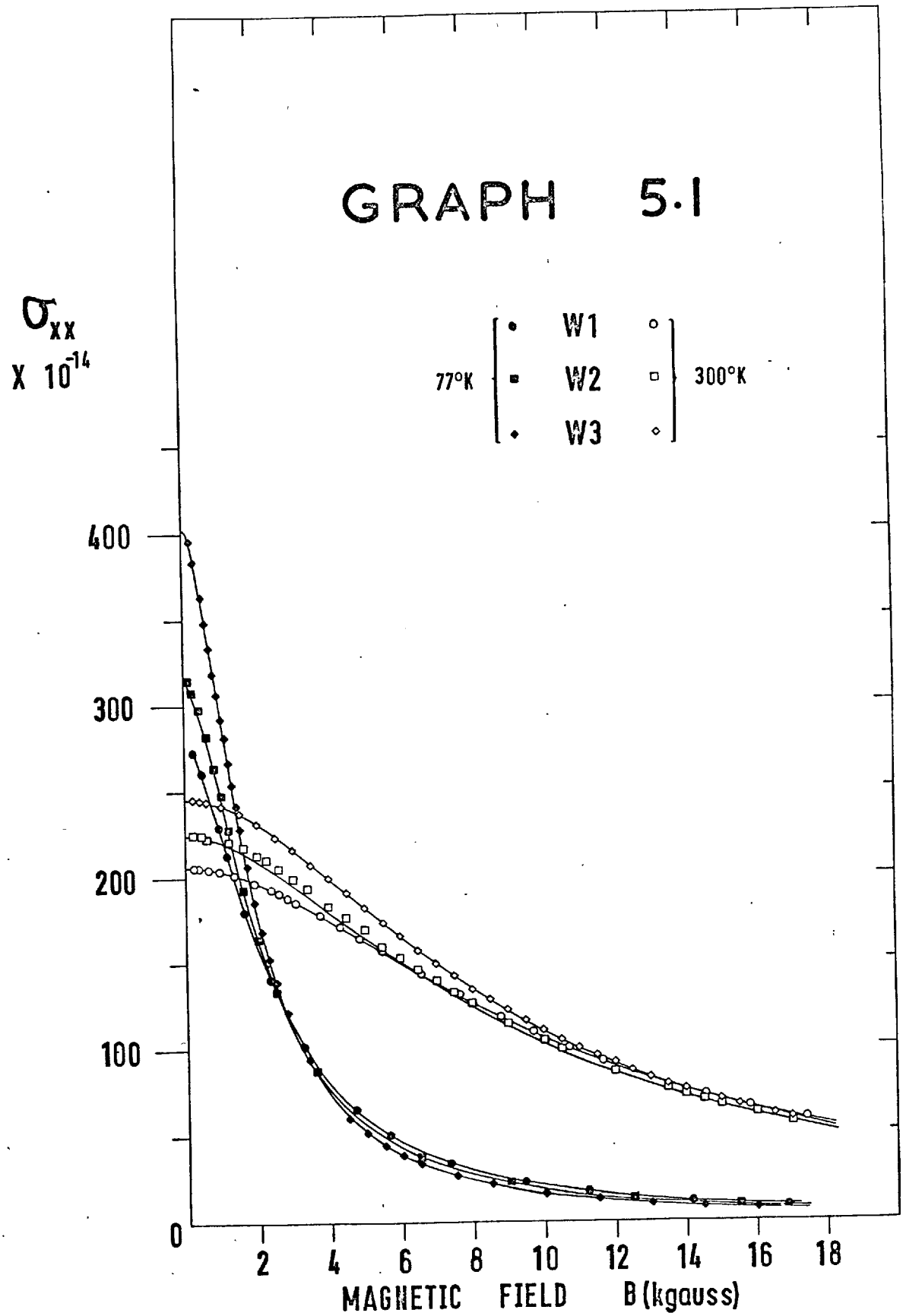
GRAPH 5.1
σ_{xx}
X 10^{-14}
77°K
W1
W2
W3
300°K
400
300
200
100
0
2
4
6
8
10
12
14
16
18
MAGNETIC FIELD B (kgauss)

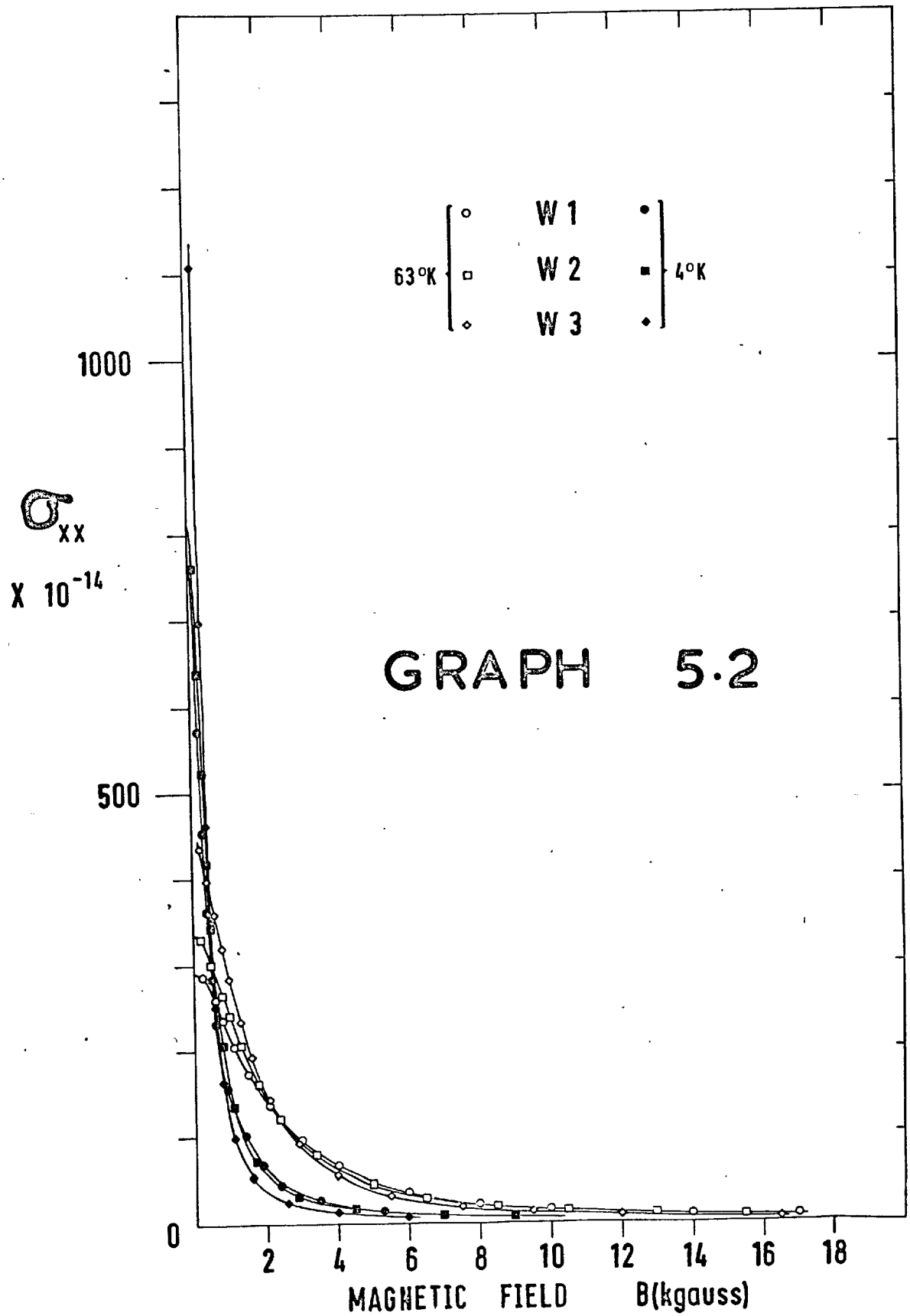
63°K
W 1
W 2
W 3
4°K
1000
500
0
σ_{xx}
X 10^{-14}
GRAPH 5.2
2
4
6
8
10
12
14
16
18
MAGNETIC FIELD B(kgauss)

Fitting σ_{xy} data proved more difficult as Graphs 5.3 to 5.6 demonstrate. Nevertheless, reasonable fits were achieved with the exception of curves having violent oscillations at low field. At $77^{o}K$ there is a striking contrast between the excellent fit for W3 which shows no anomalous low field behaviour and those for W2 and W1. Both of the latter execute marked oscillations below 5kG. and we see that the fitted curves tend to smooth out such extremes. It is evident that more forceful application of the art of weighting the data points could have improved the fit in situations like this.

Except at $4^{o}K$ all σ_{xy} curves move towards positive values at very low fields and in some cases actually cross the zero line. This behaviour is not visible at $4^{o}K$ presumably because it has moved to much lower fields.

5.1.2 Average mobility and numbers, following Soule.

For later comparison, we present here the result of applying a two-band model to conductivity and Hall data, as employed by Soule (1958) in his analysis of single crystal data.

Using the expression $\rho = \sigma_{xx}/(\sigma_{xx}^2 + \sigma_{xy}^2)$ and the representation of the tensor components below (c.f. Section 2.2.1).

$$\sigma_{xx} = \sum_{\text{carriers}} \sigma_{oi}/(1+H^2/H_{si}^2) \qquad \sigma_{xy} = \sum_{\text{carriers}} (n_i e_i CH/H_{si}^2)/(1+H^2/H_{si}^2)$$

Soule derived an expression for the magnetoresistance

$$\Delta\rho/\rho_o \equiv (\rho(H)-\rho(0))/\rho(0).$$

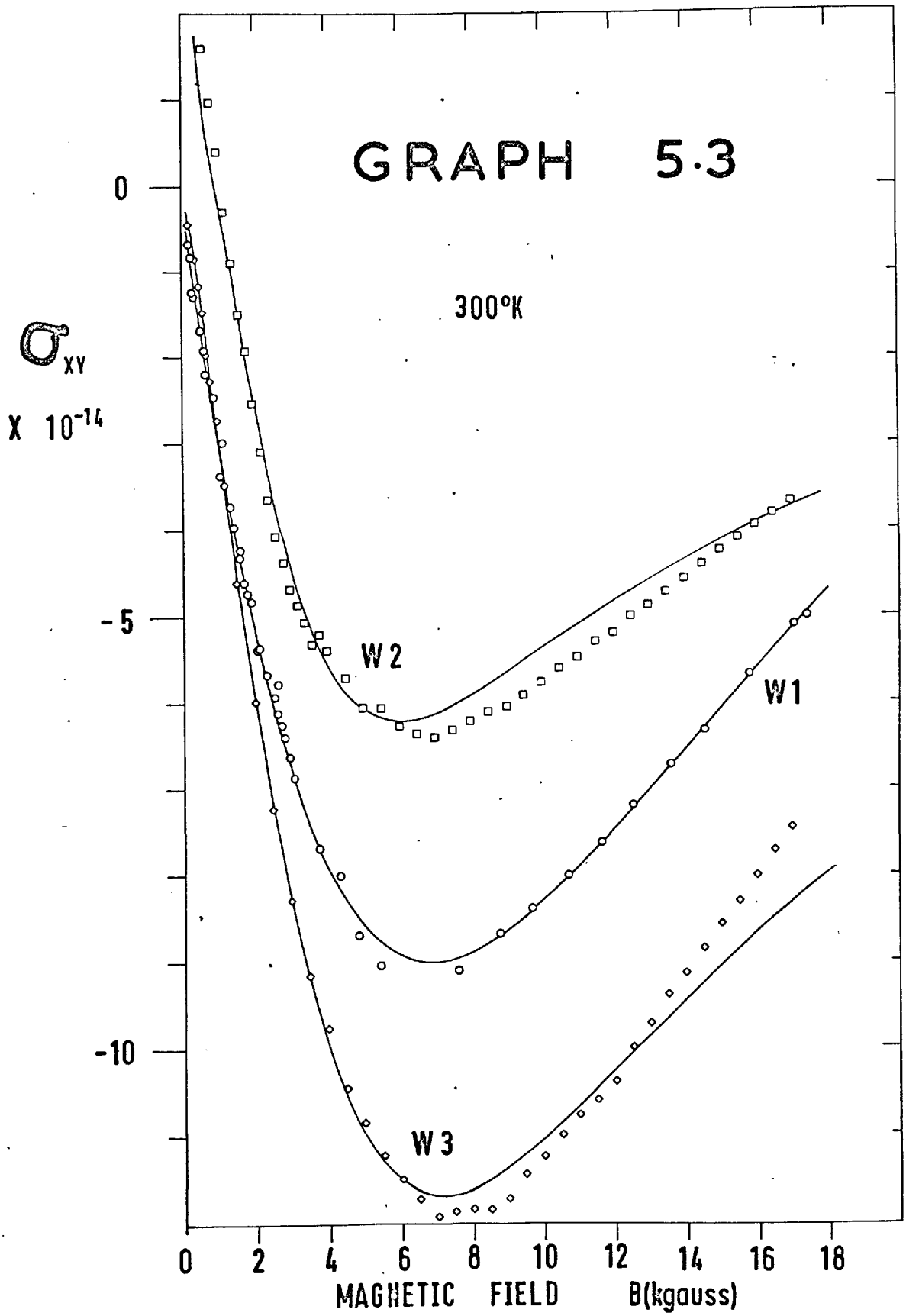
GRAPH 5.3
300°K
σ_{xy}
X 10^{-14}
0
-5
-10
W 2
W 1
W 3
0
2
4
6
8
10
12
14
16
18
MAGNETIC FIELD B(kgauss)

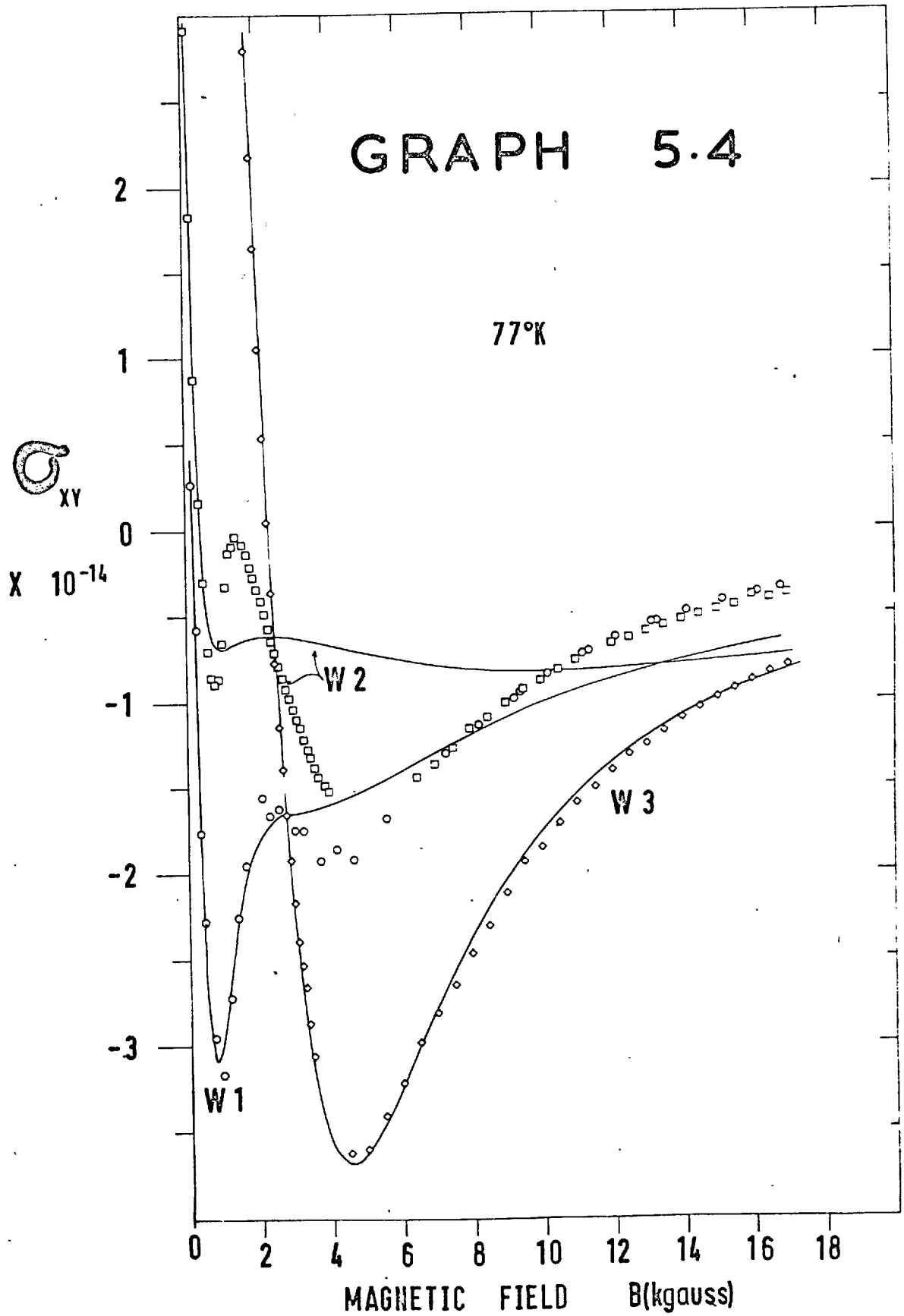
GRAPH 5.4
77°K
σ_{xy}
X 10^{-14}
2
1
0
-1
-2
-3
W 1
W 2
W 3
0
2
4
6
8
10
12
14
16
18
MAGNETIC FIELD B(kgauss)

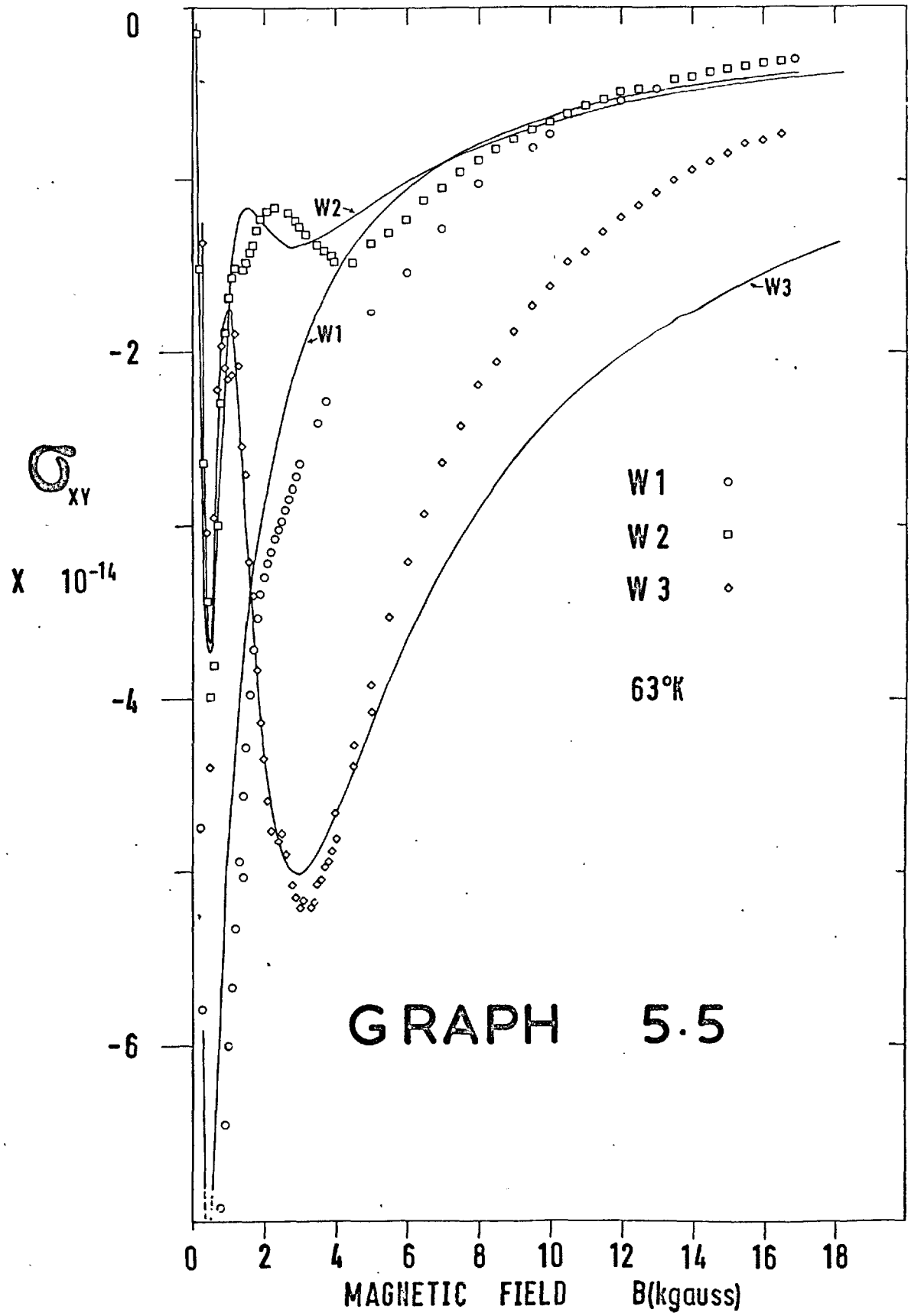
0
-2
-4
-6
σ_{xy}
X 10^{-14}
W2
W1
W3
W 1
W 2
W 3
63°K
GRAPH 5.5
0
2
4
6
8
10
12
14
16
18
MAGNETIC FIELD B(kgauss)

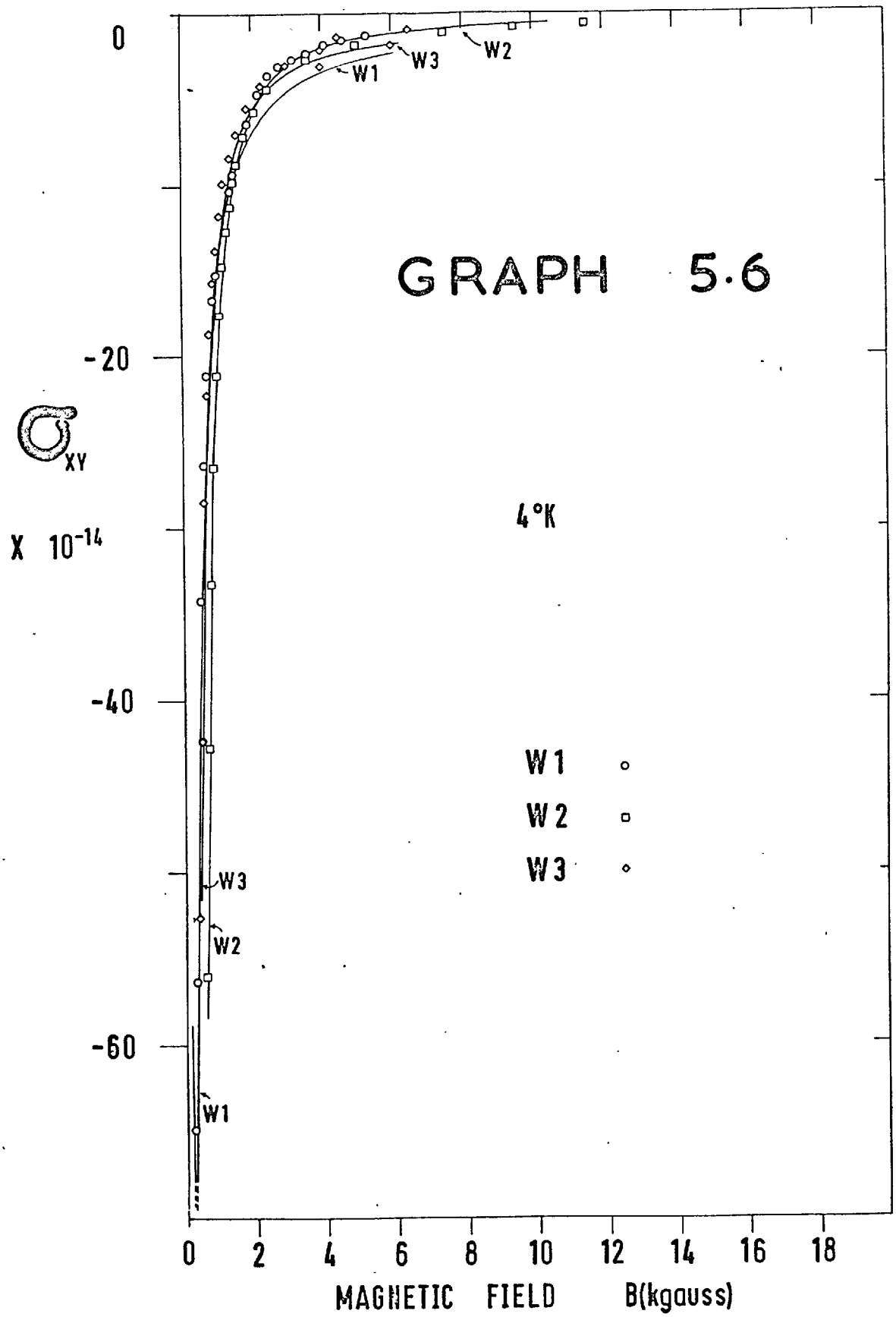
GRAPH 5.6
0
-20
-40
-60
σ_{XY}
X 10^{-14}
4°K
W1
W2
W3
W1 ○
W2 □
W3 ◇
0
2
4
6
8
10
12
14
16
18
MAGNETIC FIELD B(kgauss)

Using $\sigma_{oi} = n_i e_i \mu_i$ and $H_{si} \equiv \frac{Cm_i^*}{e\tau_i} \equiv \frac{C}{\mu_i'}$ where μ_i' is an average mobility (assumed equal to the conductivity mobility) an expression for the low field magnetoresistance is obtained:

$$\frac{\Delta\rho}{\rho_o H^2} = \frac{ab}{C^2}\left[\frac{1+b}{a+b}\right]^2 \mu_h^2$$

where $a = \frac{n_h}{n_e}$, the ratio of carrier densities

$b = \frac{\mu_e}{\mu_h}$ the ratio of carrier mobilities.

This reduces further to $\frac{\Delta\rho}{\rho_o H^2} \simeq \frac{b}{C^2}\mu_h^2 = \frac{1}{C^2}\mu_e\mu_h = \frac{1}{C^2}(\bar{\mu})^2$ if $a \simeq 1$, which is a good approximation at the higher temperatures.

Graph 5.8 was calculated from conductivities at zero field and at 3kgauss, using

$$\frac{\Delta\rho}{\rho_o} = \left(\frac{-\Delta\sigma}{\sigma_o}\right)/\left(1+\frac{\Delta\sigma}{\sigma_o}\right) \quad \text{and} \quad \bar{\mu} = \left(\frac{\Delta\rho}{\rho_o H^2}\right)^{\frac{1}{2}} \times 10^8 \quad (cm^2 volt^{-1} sec^{-1})$$

Magnetic field values have been corrected by -4% because of a late discovery of a calibration error relating to our Norma fluxmeter. Tables of results in the appendices and graphs do not embody this correction, but it has been applied to all final derived values, in particular Table 5.1 and graphs arising from this.

Included in Graph 5.8 is the slope of Soule's EP-14 (-1.2) for comparison with samples W1,W2,W3 which give slopes of -0.94, -0.98, -1.09 respectively.

A rough determination of the total carrier density, $n_e + n_h$ can be made from the above mean mobility and zero field resistivity, for $n_e+n_h = 1/e\rho_o\bar{\mu}$ ($e = 1.602 \times 10^{-19}$ coulombs, ρ_o is in ohm-cm). Graph 5.9 presents the result of this calculation and shows that W1,W2 yield practically coincident straight lines against temperature down to about 60°K whilst W3 has a slightly higher concentration. The analysis breaks down at lower temperatures as boundary and impurity scattering take over.

5.1.3. Carrier densities and mobilities.

This section contains the final stage of the magnetoconductivity tensor analysis. Expressions were derived in Section 2.4.2 for carrier mobilities and densities in terms of the parameters used to fit σ_{xx}, σ_{xy} data to Lorentzians as detailed in Section 4.1.3. A computer programme was written to perform the summations of equations 2.4.2 (11 to 15) and print out tables of mobilities and densities which are here presented as Table 5.1.

The -4.0% magnetic field correction mentioned earlier (5.1.2) has been applied and thus is embodied in graphs based on the table.

Table 5.1 is in three sections corresponding to the three samples W1, W2, W3. The six columns are as follows: Column 1; the sample temperature in degrees Kelvin. Column 2 is a code giving the conditions under which the data were fitted to Lorentzians; W means the points were weighted in an effort to improve the fit, U means the data were

DENSTIES AND AVERAGE MOBILITIES. SAMPLE W1
N TERMS WEIGHTED =NW
N TERMS UNWEIGHTED =NU

TEMP.		MOBILITY*10-4 HOLES	MOBILITY*10-4 ELECTRONS	NUMBER*10-18 HOLES	NUMBER*10-18 ELECTRONS
295.0	3U	0.90155	0.96987	7.25807	7.98818
295.0	3W	0.04517	-0.03137	192.95218	-177.70593
295.0	4U	0.03165	-0.00952	350.96486	-335.75671
295.0	4W	0.03424	-0.01293	307.42439	-292.21623
88.0	3U	1.70446	1.79080	-102.10783	107.31364
88.0	3W	3.83725	3.83675	0.00000	0.00000
88.0	4U	-4.55935	-4.95373	111.20354	-106.01037
88.0	4W	2.35049	2.35179	0.00000	0.00000
77.0	3U	3.93215	3.97473	2.40397	2.43490
77.0	3W	3.95352	3.95363	2.37906	2.45981
77.0	4U	3.96799	3.93794	2.38893	2.47668
77.0	4W	3.95869	3.94687	2.39633	2.46928
63.0	3U	3.06967	3.27026	3.21047	3.28602
63.0	3W	0.00000	0.00000	3.21275	3.28375
63.0	4U	2.60988	2.77278	3.70786	3.74830
63.0	4W	2.73068	2.65263	3.73994	3.71622
15.0	3U	0.00000	0.00000	4.25579	1.75090
15.0	3W	0.00000	0.00000	3.24809	0.75859
15.0	4U	0.00000	0.00000	-2.40828	5.77645
15.0	4W	0.00000	0.00000	0.00000	0.00000
4.5	3U	17.91965	22.47239	1.26742	1.34091
4.5	3W	17.82480	22.53929	1.26095	1.34738
4.5	4U	13.80276	31.35004	1.82466	0.76742
4.5	4W	17.59695	21.07825	1.54899	1.04308

DENSTIES AND AVERAGE MOBILITIES. SAMPLE W2
N TERMS WEIGHTED =NW
N TERMS UNWEIGHTED =NU

TEMP.		MOBILITY*10-4 HOLES	MOBILITY*10-4 ELECTRONS	NUMBER*10-18 HOLES	NUMBER*10-18 ELECTRONS
291.0	3U	1.04452	1.09858	7.31810	7.20997
291.0	3W	1.08430	1.05922	7.02708	7.50099
291.0	4U	1.08283	1.06750	7.01050	7.46108
291.0	4W	1.08345	1.06694	6.99806	7.47353
77.0	3U	13.93430	-4.96730	2.42180	2.40048
77.0	3W	10.73934	-1.70812	2.41489	2.40739
77.0	4U	0.00000	0.00000	4.52909	4.73069
77.0	4W	0.00000	0.00000	4.57375	4.68603
63.0	3U	5.86269	5.01280	1.90685	2.36665
63.0	3W	5.44456	5.37105	2.09830	2.21378
63.0	4U	5.32927	5.38337	2.15498	2.19944
63.0	4W	9.96581	10.76914	29.35896	-25.00299
47.5	3U	6.34459	7.55588	1.92618	1.90479
47.5	3W	-28.01369	42.31794	1.87227	1.89416
47.5	4U	-1.04187	6.91015	6.62482	6.73242
47.5	4W	-39.65044	51.84171	1.89584	1.96297
4.5	3U	0.00000	0.00000	1.44075	1.51068
4.5	3W	0.00000	0.00000	1.44077	1.51067
4.5	4U	0.00000	0.00000	1.45518	1.49188
4.5	4W	0.00000	0.00000	1.46379	1.48326
1.0	3U	0.00000	0.00000	0.00000	0.00000
1.0	3W	0.00000	0.00000	0.00000	0.00000
1.0	4U	0.00000	0.00000	0.00000	0.00000
1.0	4W	0.00000	0.00000	0.00000	0.00000

DENSTIES AND AVERAGE MOBILITIES, SAMPLE W3
N TERMS WEIGHTED =NW
N TERMS UNWEIGHTED =NU

TEMP.		MOBILITY*10-4 HOLES	MOBILITY*10-4 ELECTRONS	NUMBER*10-18 HOLES	NUMBER*10-18 ELECTRONS
293.0	3U	1.08731	1.12930	7.13264	8.20793
293.0	3W	1.08513	1.13132	7.15618	8.18439
293.0	4U	1.08723	1.13087	7.12834	8.19381
293.0	4W	0.04793	-0.03267	217.32399	-202.00241
77.5	3U	6.08992	5.05112	2.41405	2.62113
77.5	3W	6.09286	5.04892	2.41280	2.62238
77.5	4U	5.77998	5.03741	2.55420	2.62477
63.2	3U	11.02604	4.58333	2.00546	2.33811
63.2	3W	11.20319	4.36984	2.02652	2.31705
63.2	4U	0.00000	0.00000	4.07277	4.23760
63.2	4W	0.00000	0.00000	4.07509	4.23528
54.0	3U	9.19685	9.29372	1.87581	2.02360
54.0	3W	9.13873	9.34843	1.88386	2.01556
54.0	4U	9.57668	9.49395	1.78968	1.98912
54.0	4W	9.55334	9.51499	1.78788	1.99092
4.2	3U	1.06628	88.44487	1.71281	1.75974
4.2	3W	1.06880	88.48973	1.71376	1.75879
4.2	4U	26.35945	40.78255	2.50907	2.30271
4.2	4W	26.52297	39.82773	2.37465	2.43712
1.5	3U	23.69151	5.43289	2.71874	2.78293
1.5	3W	23.81568	5.37372	2.70936	2.79230
1.5	4U	0.00000	0.00000	-65.15516	74.81471
1.5	4W	0.00000	0.00000	4.76858	4.89097

unweighted. The number preceeding U or W gives the number of Lorentzian terms employed to fit the data and hence used to generate the rest of that row of the table. Columns 3 and 4 give the carrier mobilities in units of $10^4 cm^2/volt\text{-}sec$ and the final two columns 5 and 6 give carrier densities in units of $10^{18}/cm^3$. All zero entries in the table are to be ignored as they represent large numbers which are physically unrealistic and have been set to zero to avoid an untidy appearnace. Negative entries once more result from unrealistic fits.

Graph 5.10 presents the mean carrier mobility as a function of temperature in the same way as Graph 5.8 which was based on simpler calculations. We see that the two approaches yield essentially the same results at high temperature, but Graph 5.10 indicates a decreasing slope at lower temperatures.

Carrier densities in Table 5.1 are a little higher (Graphs 5.11) than the values given by the simpler treatment (Graph 5.9) but the temperature dependence is essentially unaltered.

The mobility ratio μ_e/μ_h is extremely dependent on the data-fitting process but the expected shape (Spain et al, 1967) is obtained in Graph 5.12.

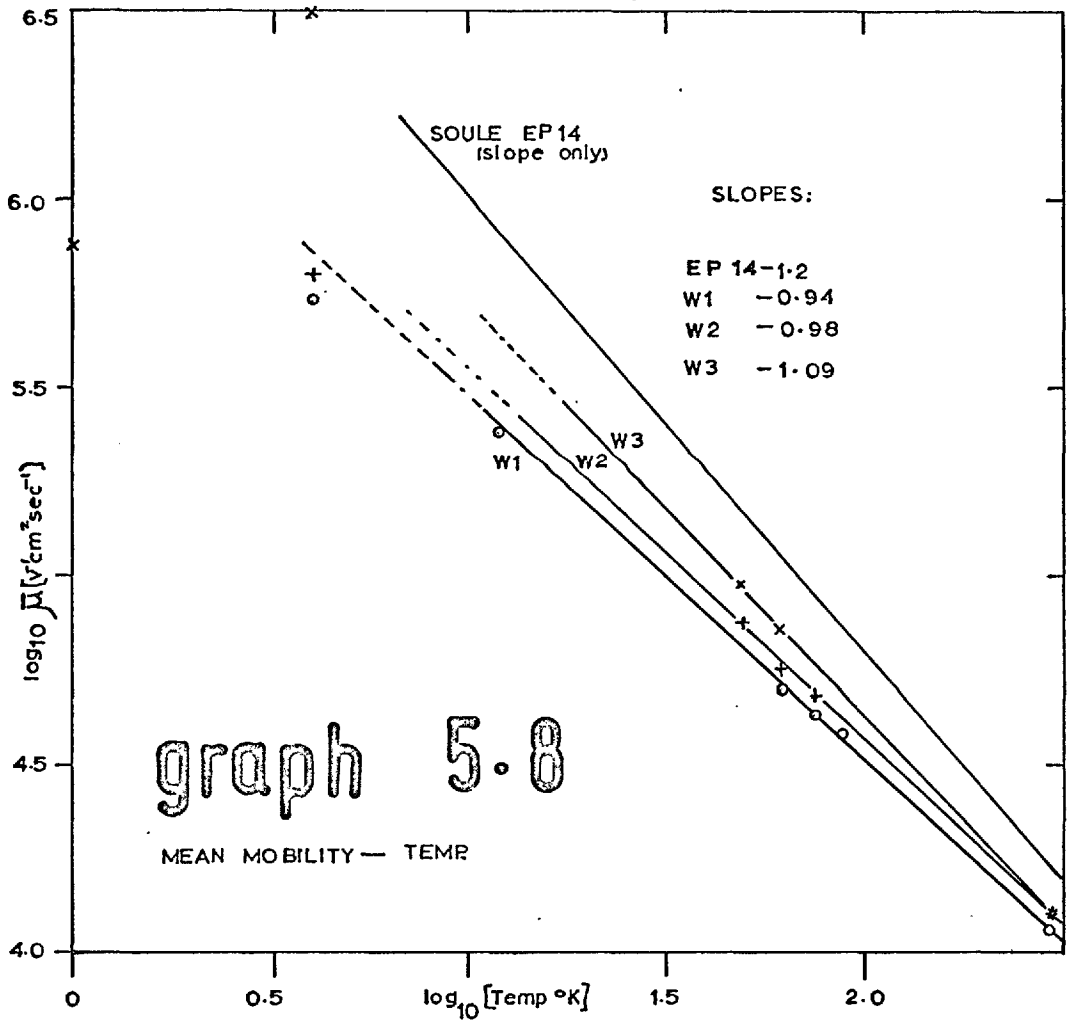
SOULE EP14
(slope only)
SLOPES:
EP 14-1·2
W1 −0·94
W2 −0·98
W3 −1·09
W1
W2
W3
graph 5.8
MEAN MOBILITY — TEMP
log10 μ [v²cm²sec⁻¹]
log10 [Temp °K]
6.5
6.0
5.5
4.5
4.0
0
0.5
1.5
2.0

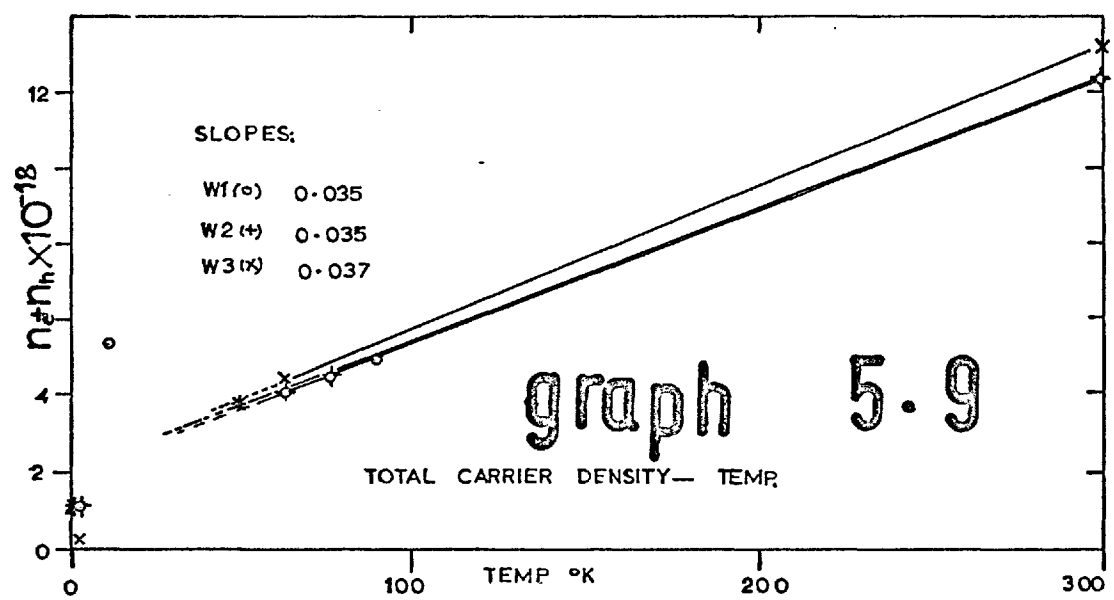
SLOPES:
W1 (o) 0·035
W2 (+) 0·035
W3 (x) 0·037
graph 5.9
TOTAL CARRIER DENSITY — TEMP
n+nh X10⁻¹⁸
TEMP °K
12
4
2
0
0
100
200
300

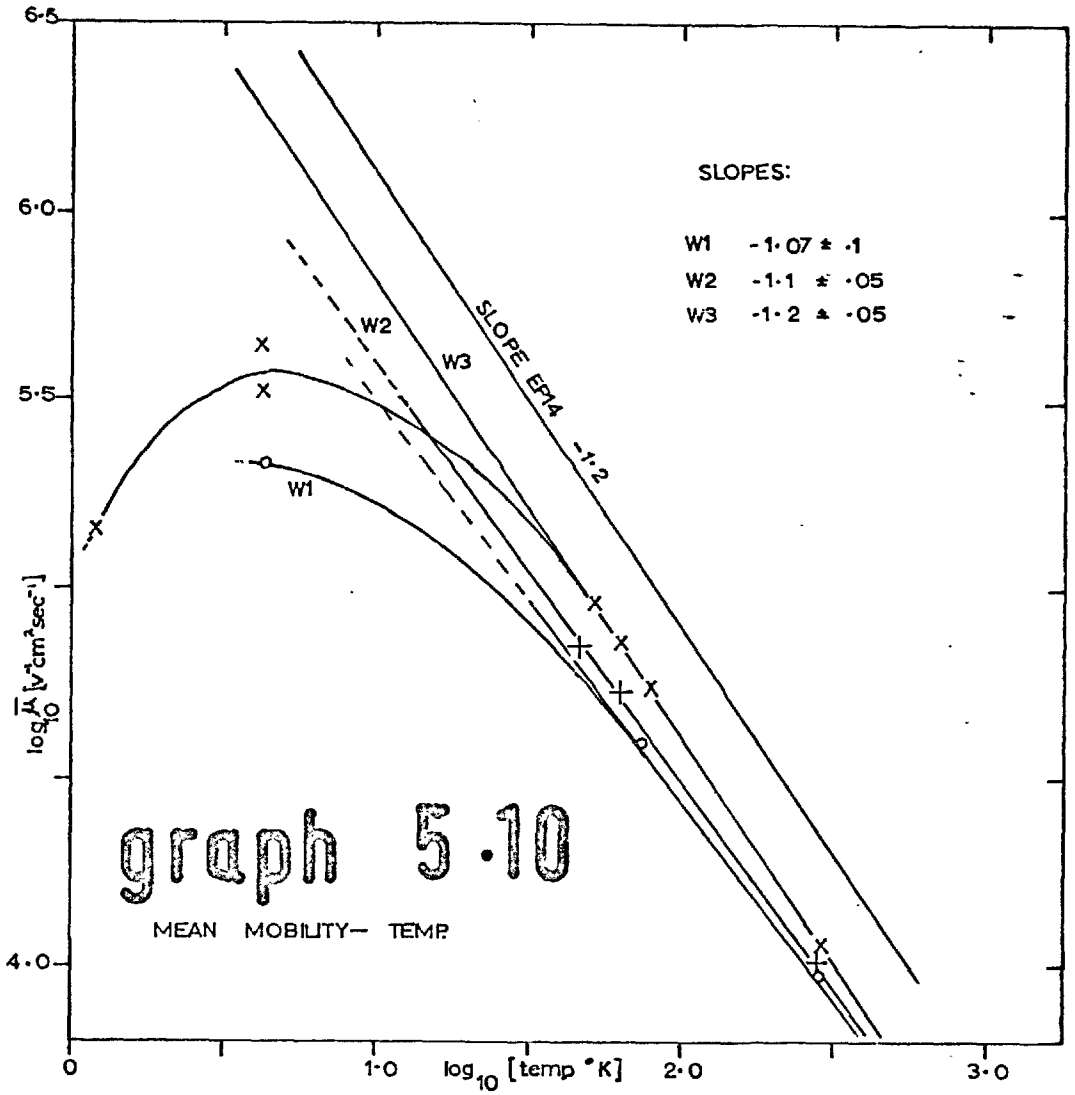
SLOPES:
W1 -1·07 ± ·1
W2 -1·1 ± ·05
W3 -1·2 ± ·05
W2
W3
SLOPE EP14 -1·2
W1
graph 5·10
MEAN MOBILITY— TEMP.
6·5
6·0
5·5
4·0
0
1·0
log10 [temp °K]
2·0
3·0
log10 μ̄ [v²cm²sec⁻¹]

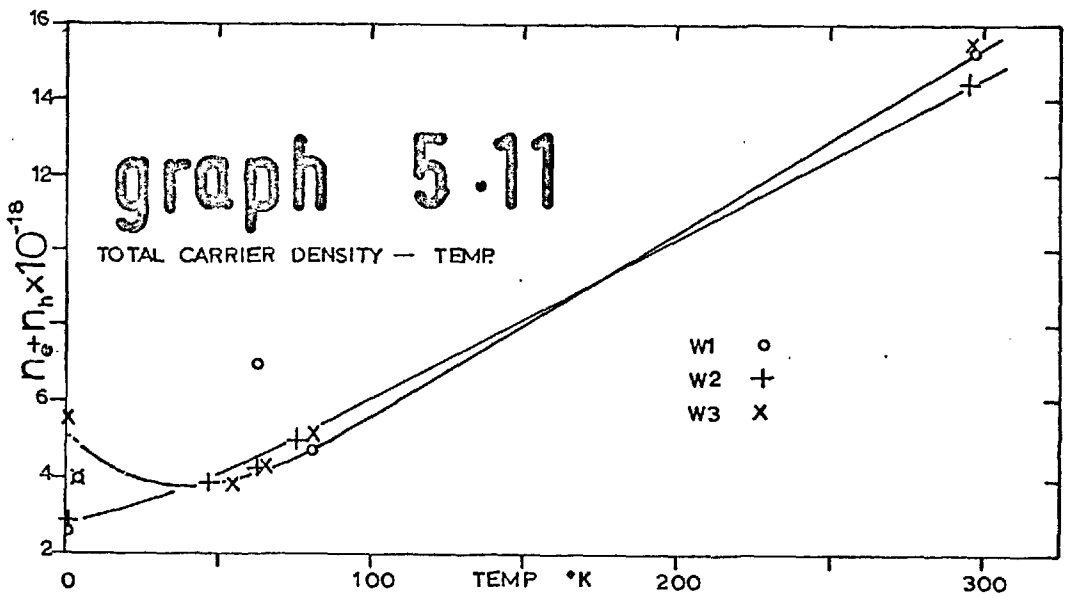
graph 5·11
TOTAL CARRIER DENSITY — TEMP.
W1 o
W2 +
W3 X
16
14
12
6
4
2
0
100
TEMP °K
200
300
ne+nh×10⁻¹⁸

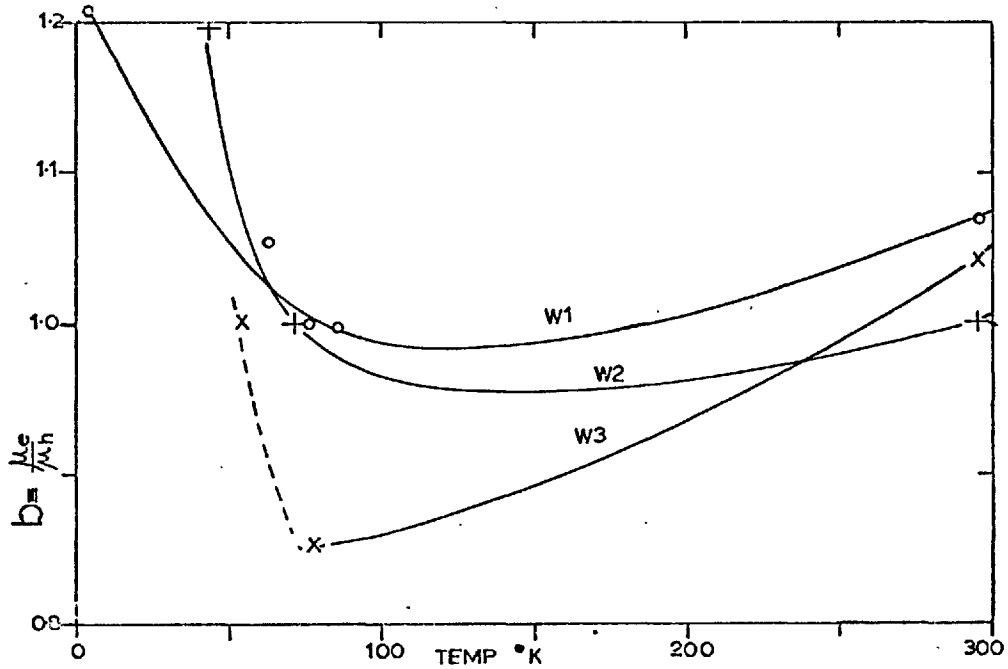

graph 5.12

MOBILITY RATIO — TEMPERATURE

5.2 Oscillatory derived results.

5.2.1 Result of the Landau fitting.

In Graph 5.7 is shown the analysis of the oscillatory part of the Hall effect in W3 at 1.2°K. The circles are data points, obtained by eliminating the monotonic background from a chart recording as detailed in Section 4.2.1. The generalized Landau fitting programme (FRIER, Section 4.2.3) chose the 'best' set of sixteen fitting parameters to generate the continuous line superimposed on the data points. This curve, labelled "total", is composed of contributions from both holes and electrons each of which, in turn, are split into fundamental and 1st harmonic terms.

The function describing the electron term is (Section 2.5)

$$G_e = H^n\left\{W_1 \frac{U}{\sinh U} e^{-U\frac{\Delta T}{T}} \cos\left(\frac{2\pi}{PH} - \phi_1\right) + W_2 \frac{2U}{\sinh 2U} e^{-2U\frac{\Delta T}{T}} \cos\left(\frac{4\pi}{PH} - \phi_2\right)\right\}$$

where $U = \frac{2\pi^2 KTm^* c}{\hbar e} \times \frac{1}{H} \equiv \frac{A}{H}$, say

Thus, n, W_1, W_2, A, $\frac{\Delta T}{T}$, P, ϕ_1, ϕ_2 are adjustable parameters. A similar expression[5] holds for the hole term.

We report here the result of allowing FRIER to run until it was very close to the best fit as defined in Section 4.2.3. Under restrictions such as holding A, $\frac{\Delta T}{T}$, etc. constant the run did terminate itself (that is, it satisfied convergence criteria specifying

approximately 1% accuracy of parameters) but under conditions where all sixteen parameters were allowed to change during the fitting process it had a little way still to go. We believe, however, that values of P, $\frac{\Delta T}{T}$ and n listed below are realistically close to their final values; errors were estimated by comparing an earlier run (where the sum of the squares of the residuals, ΣR^2, was 20.41) with the final run ($\Sigma R^2 = 17.3$).

Electrons

n	Period	A	$\Delta T/T$	W	ϕ
0.5005	1.77×10^{-5}	5303	5.034	0.1346	3.301
				-0.1406	17.90
± 0.5%	± 2%	± 20%	± 1%	± 50%	± 5%

Holes

n	Period	A	$\Delta T/T$	W	ϕ
0.4995	1.48×10^{-5}	9654	2.509	0.0188	-0.496
				0.1032	-2.245
± 0.5%	± 10%	± 50%	± 20%	± 200%	± 100%

We see that the electron parameters are much more closely defined than those of the holes. A glance at Graph 5.7 will show that it is indeed the electron behaviour which dominates with the hole terms supplying detail and, of more importance, perturbing the zero-crossing points.

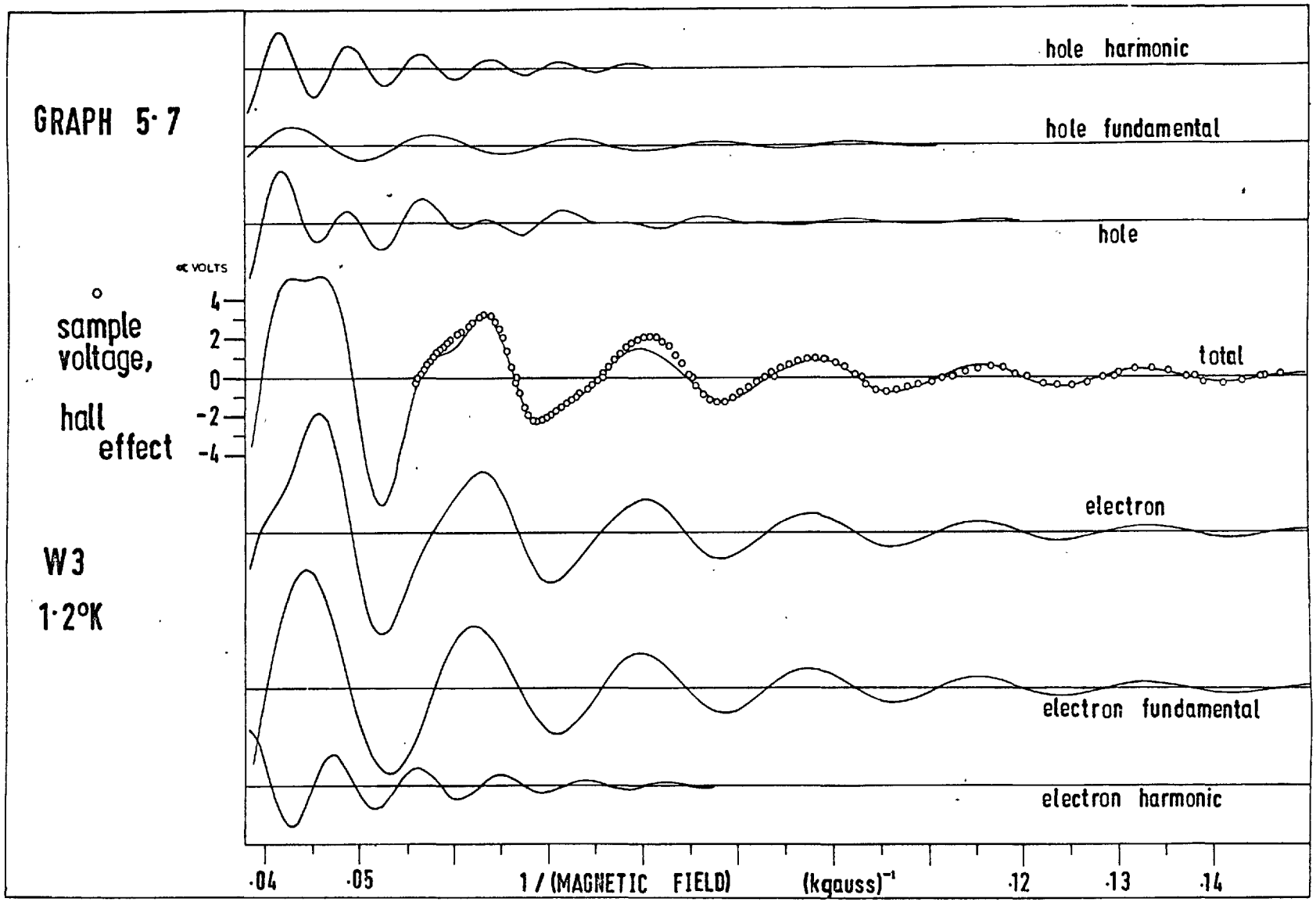
GRAPH 5·7
sample
voltage,
hall
effect
W3
1·2°K
μ VOLTS
4
2
0
-2
-4
hole harmonic
hole fundamental
hole
total
electron
electron fundamental
electron harmonic
·04
·05
1 / (MAGNETIC FIELD) (kgauss)⁻¹
·12
·13
·14

5.2.2. Effective masses, collision damping, periods.

Recalling the definition of the parameter A from Section 4.2.3 and 2.5. ;

$$A \equiv \frac{2\pi^2 KTm^* C}{\hbar e}$$

we can derive estimates for the effective masses. Calculation gives m^*/m_o = 0.036, 0.065 for the electrons and holes respectively. These are to be compared with the values 0.030, 0.060 respectively found by Soule (1958) and 0.039, 0.057 respectively by Soule, McClure and Smith (1964) for single crystal graphite.

The factors $\Delta T/T$ yield values for the so-called Dingle temperatures; the effective increase in temperature due to collisions. We calculate ΔT = 6.0, 3.0 for electrons and holes respectively.

Our corrected periods for pyrolytic graphite are 1.84×10^{-5} and 1.54×10^{-5} gauss^{-1} for electrons and holes respectively. The electron period is much lower than values found in single crystal graphite (2.01, 1.57; Soule and 2.07, 1.51; Soule, McClure and Smith), though the hole period is in satisfactory agreement. Later, unpublished, work by J.D. Cooper has suggested that the present electron period is uncharacteristically low even for pyrolytic graphite, for which he reports periods in the region of $2.1 \times 10^{-5} G^{-1}$. The reason for the discrepancy is not known at present. Other features of the present analysis are fully confirmed, however.

5.2.3. Estimation of γ_2 and E_F

The oscillation periods were used to calculate γ_2 and E_F given the well-established values of γ_o, γ_1 and Δ ($\gamma_4=\gamma_3=\gamma_5=0.0$) and the oscillation periods P_e, P_h.

It is difficult to obtain analytic expressions for γ_2 and E_F from the equations in Sections 2.1.3., 2.1.4, so a double iteration technique was used; assuming a value of K_z for the point M of figure 2.4 γ_2 and F_F were calculated and recalculated, in order, from starting values until a consistent pair of values was obtained. These were then used to obtain a better estimate of the position of M. The whole process was repeated until a consistent set of three values was obtained. In practice, convergence was extremely rapid and was checked by calculating P_e and P_h from the final set of band parameters for comparison with the values supplied.

Using our corrected periods; $P_e = 1.84\text{x}10^{-5}$, $P_h = 1.54\text{x}10^{-5}$ gauss^{-1} and $\gamma_o = 2.88$, $\gamma_1 = 0.395$, $\gamma_4 = \gamma_3 = \gamma_5 = 0.0$, we obtained for various values of Δ the values of γ_2 and E_F shown below:

Δ	γ_2	E_F
-0.006	0.0162	0.0227
-0.01	0.0162	0.0225
-0.02	0.016	0.0221
-0.05	0.0156	0.0209

An extension to this computer programme accepted the complete set of band parameters and by perturbing these by $\pm$ 10% produced estimates of the partial differential coefficients of the oscillation periods $\frac{\partial P}{\partial b}$ where b is a band parameter. It was found that for all the combinations above $\frac{\partial P}{\partial \gamma_2}$, $\frac{\partial P}{\partial E_F}$ were one or two orders of magnitude greater than the others. Their values were (for $\Delta = 0.006$):

$$\frac{\partial P_e}{\partial \gamma_2} = -0.53 \times 10^{-3} \qquad \frac{\partial P_e}{\partial E_F} = 0.12 \times 10^{-2}$$

$$\frac{\partial P_h}{\partial \gamma_2} = 0.35 \times 10^{-2} \qquad \frac{\partial P_h}{\partial E_F} = 0.17 \times 10^{-2}$$

The largest of the other differential coefficients was $\frac{\partial P_e}{\partial \Delta} = -0.46 \times 10^{-4}$.

Finally, we mention that using Anderson et al's values $\gamma_o = 2.85$, $\gamma_1 = 0.30$, $\Delta = 0.006$, $P_e = 2.088\ 10^{-5}$, $P_h = 1.502\ 10^{-5}$, we obtained $\gamma_2 = 0.0194$ and $E_F = 0.0256$ which compare well with their quoted values of 0.02 and 0.26 respectively. Once more, their periods were more sensitive to γ_2 and E_F than to other parameters by one or two orders of magnitude.

CHAPTER 6.

DISCUSSION AND CONCLUSIONS.

6.1 Classical Results

For the first time for pyrolytic graphite (PG) the present work provides a complete set of parameters whereby the zero field conductivity can be related to the electronic band structure in the sense that relaxation times and carrier densities are defined as a function of temperature. There is essentially nothing in the present analysis to identify physical restrictions on the mean free paths; one cannot discern the origins of scattering from these results alone. However, at the lowest temperatures it is reasonable to assume that carrier-phonon scattering is absent, the relaxation times being determined in the main by crystalline imperfections, whereas at high temperatures one supposes that scattering originating in thermal effects outweighs static obstacle scattering. At intermediate temperatures a mixed scattering régime evidently occurs.

In the past (cf Young 1968) the specific scattering mechanisms invoked have been high-angle scattering at basal plane crystallite boundaries and stacking faults for the lowest temperatures, with electron-acoustic phonon interactions at high temperatures in the spirit of the theoretical work of Sugihara and Sato (1963), Ono and Sugihara (1966) and McClure and Smith (1961). An apparently self-consistent account of both basal plane and c-axis conduction could

be obtained by considering out-of-plane vibrations associated with a deformation potential of ~ 18 eV and in-plane vibrations with a deformation potential of ~ 5 eV, with various assumptions involving the rôle of the trigonal warping parameter γ_3. For present purposes a less sophisticated model is required. Thus we note that a mean mobility $\bar{\mu} = (\mu_e \mu_h)^{\frac{1}{2}}$ can be defined and that for the best single crystals (Soule's EP11) its temperature dependence can be represented between 4.2 and 295°K as $\alpha T^{-1.24}$. Following Klein (1962) and Hooker (1963), Spain et al (1967) assumed a dependence

$$(\bar{\mu})^{-1} = \frac{\bar{m}^* \bar{v}}{\text{ex10}^7} \left(\frac{1}{\lambda'} + \frac{1}{\lambda} \text{ carrier-phonon} \right)$$

to explain why $\bar{\mu}$ for PG always falls below Soule's limiting relationship particularly at low temperatures. λ' represents the effects of static obstacle scattering which, it was held, dominates the basal plane resistivity at the lowest temperatures. As the temperature is increased, interaction with the longitudinal acoustic c-axis mode (θ_D = 185°K, Dolling and Brockhouse 1962), which couples strongly to the charge carriers via γ_2, dominates c-axis resistivity up to 60°K and basal plane resistivity up to 170°K, above which the c-axis mean free-path is limited to ~ 3Å, leading to a decreasing resistivity with increasing temperatures. The basal plane resistivity continues to increase, whereby acoustic in-plane modes with high characteristic temperatures are invoked.

However, Yeoman and Young have recently indicated (May 1969) that the source of charge carrier scattering has hitherto been completely misrepresented. They have measured the pressure coefficient of conductivity at temperatures in the range room to 4.2°K using pressures up to ~ 400 bar and find that conductivity always increases on application of pressure but the increase is always less than that expected from the known (Anderson et al 1967) pressure coefficient of carrier density, $\frac{d \ln n}{dP} \simeq 37.5 \times 10^{-6} \text{bar}^{-1}$. Thus, they write for the pressure coefficient of conductivity

$$\frac{d \ln \sigma}{dP} = \text{constant} + \frac{d \ln n}{dP} + \frac{d}{dP} \ln \Lambda$$

The mean free path Λ is given by $\frac{1}{\Lambda} = \sum_i \frac{1}{\Lambda_i}$ where i stands for all possible scattering mechanisms. Now, carrier-obstacle and carrier-charged acceptor scattering are expected to be pressure independent provided non-parabolicity is disregarded and carrier-phonon scattering would lead to the opposite pressure dependence, for increase in pressure would raise the characteristic temperature leading to a greater mean free path. One is left with carrier-carrier scattering of which Yeoman and Young only consider electron (e) - hole (h) interactions: e-e and h-h collisions would only affect conductivity via a randomisation of carrier energies which would be reflected by energy-dependent relaxation times were the electron and hole masses single-valued. The known range of electron masses in graphite

will, it is true allow light electrons to be scattered by heavier carriers leading to the well-known anomalous low-field behaviour in the Hall effect (see Section 6.3), but not much change in the zero-field conductivity will thereby result since the partial conductivity of light electrons is only a few percent of the whole.

In the c-axis direction the fixed mean free path at high temperatures leads to a pressure dependence of conductivity which is nearly independent of temperature and close to that of the carrier density. The basal plane pressure coefficient, however, falls rapidly as the temperature is increased from $4^{o}K$, the carrier density change being almost completely compensated at room temperature. Yeoman and Young attribute this temperature dependence to e-h scattering which will increase in importance in the same way as does the carrier density. Neutron irradiation doses which are small enough not to affect the Fermi level as judged by electron and hole periods, nevertheless increased the pressure coefficient $\frac{d}{dP} \ln\sigma$ towards $\frac{d}{dP} \ln n$ because the e-h scattering can be no longer dominate in the presence of charged traps, even at room temperature.

For electron-hole scattering, $\frac{1}{\lambda_{e-h}}$ is approximately proportional to carrier density and thus to temperature, accounting for the observed mobility-temperature relationship. A corresponding relationship has been found to apply to $\frac{\partial \ln}{\partial P}\sigma$ by Young and Howell. It may be written $[\frac{\partial \ln n}{\partial P} \cdot \frac{\partial P}{\partial \ln \sigma} - 1] = \frac{\lambda'}{const} \times T$.

We accordingly conclude with Yeoman and Young that carrier-carrier scattering is of the foremost importance in graphite. In good PG samples at all temperatures $\bar{\mu} \sim T^{-1}$; in bad PG it is $\sim T^{-1}$ at high temperatures becoming independent of temperature at low temperatures. Typically $\lambda'(PG) = 17000\text{Å}$. Good and bad single crystals show the same behaviour as PG except that here the exponent is closer to -1.2. In graphites which have not been irradiated there is an element of carrier-carrier scattering even at $0^{\circ}K$ which reduces $\frac{\partial \ln \sigma}{\partial P}$ by some 20% of $\frac{\partial \ln n}{\partial P}$. At this temperature, carrier-carrier scattering is only made completely unimportant by the introduction of at least 10^{12} charged traps per cm^3. It is reasonable to assume that any fixed mean free path, however introduced, will make carrier-carrier scattering less important.

The experimental work which led to these conclusions became available after the bulk of this thesis was written. Accordingly, the analysis of low temperature data is put into a completely new perspective but the data itself exists, where it did not before, ready for analysis in the light of the latest interpretation.

6.2 Oscillatory Results.

With the oscillatory phenomena the key point is the question:- "Can one replicate single crystal properties if one makes a mosaic well-oriented pyrolytic graphite or are the band parameters of single crystal and pyrolytic graphite intrinsically different?"

It was argued that if one could observe oscillations at all the analysis of these would highlight any differences. At the start of this investigation no such oscillations had been observed, though they are now commonplace. One single crystal (ЭР14) had given a hole period of 1.5×10^{-5} gauss^{-1} and an electron period of $2.07 \times 10^{-5} g^{-1}$. It was evident that the Dingle temperature for the electrons was higher than that for the holes, but no quantitative analysis for these had ever been attempted. Our aim was to determine both periods and Dingle temperatures for PG to answer the question whether PG is the same sort of material as single crystal graphite or whether the high basal dislocation content and mosaic structure measurably affects the band parameters.

The best sample, W3, at $1^{\circ}K$ produced a sufficient number of oscillations for analysis though with only about 1/5th of the single crystal amplitudes. There is evidence of structure in the oscillatory pattern indicating that both electron and hole effects were being observed. The analysis described in the text (Section 5.2.2) leads to a hole period of $1.52 \times 10^{-5} g^{-1}$, in general agreement with that found in other work, but the electron period is somewhat less than is found elsewhere. The Dingle temperatures bear the correct relationship to the effective masses of the carriers involved. Later work by J.D. Cooper at Imperial College on other pyrolytic graphites suggests that the periods might be higher (1.63, $2.15 \times 10^{-5} g^{-1}$ respectively), but the

Dingle temperatures are wholly confirmed. Accordingly the present results are used to compute values of γ_2 and the Fermi energy, E_f, which are not well determined by the magnetoreflection experiments of Dresselhauss and Mavroides (1964).

We conclude that apart from uncertainty in the electron period the electronic structure of pyrolytic graphite is essentially comparable to that of single crystal graphite, the differences lying partly in scattering introduced by the microcrystalline nature of the former. At the lowest temperatures in single crystal graphite the mean free paths and thus the Dingle temperatures, are determined in the main by carrier–carrier scattering, whereas in PG high-angle scattering events at grain boundaries are necessarily dominant. We therefore suppose that for our better graphites (W3) the Dingle temperatures will be smaller than for the less perfect materials (W1, W2) not merely because λ' is larger but also because low angle scattering on other carriers will play a part.

6.3 The low-field Hall coefficient

One outstanding problem is the sign of the Hall coefficient below 2kG. Spain et al (1967) using a range of PG always found a negative zero-field Hall coefficient at 77°K with a positive slope against magnetic field, indicating that the light electrons are exerting their proper Hall effect with a mean free path limited by static obstacle scattering. Soule, with good single crystal material

observed a positive zero-field Hall coefficient at 77°K with a negative initial slope which he took to indicate the presence of minority holes. Now, it is true that in the electronic band structure of graphite as known there is a pocket for minority holes contained by the band E_2 below Δ near to the hexagonal zone faces at H. This pocket might just be accessible by thermal spread of the electron energy distribution (~ kT) above 77°K, but Soule continues to observe this hole-like behaviour even at 4°K. Spain, with his more imperfect material consistently observed a negative Hall coefficient at 4°K in agreement with Sugihara's calculations (1966), but the present work shows clearly a tendency to more positive low field values for samples W1, W2, W3 in that order of increasing perfection. We conclude that Soule's attribution of the zero-field Hall coefficient to minority holes is incorrect. Following McLean and Paige (1960), Sugihara (1966) attributes a positive Hall coefficient (for the best material) to drag on light electrons by carrier-carrier interactions. Evidently, only when λ is controlled by carrier-carrier scattering can such a drag effect be of importance. Yeoman and Young confirmed that this is so in the best material. The effect can be suppressed by increasing the static obstacle scattering, permitting the light electrons to contribute their normal negative Hall coefficient. Pre-irradiation with light doses of fast neutrons has shown that this is so.

REFERENCES

Anderson, O'Sullivan and Schirber, Phys. Rev. 164, No. 3, 1038, 1967.

Bacon, 1958, A.E.R.E. Report M/R 2707

Berman, Brock, Huntley, Cryogenics, 4, 233, 1964

Berman, Huntley, Cryogenics, 3, 1963

Bernal, 1924, Proc. Roy. Soc., A106, 749

Birss, 'Symmetry and Magnetism', North-Holland, 1964

Blackman, Saunders, Ubbelohde, Proc. Roy. Soc., A264, 19, 1961

Bloch, Z.Physik, 52, 555, 1928

Blount, Solid State Physics, 13, p. 305, 1962.

Boyle, Nozieres, Phys. Rev., 111, 782, 1958

B.S.W. Bouckaert, Smoluchowski, Wigner, Phys. Rev., 50, 58, 1936

Callaway, "Energy Band Theory", Academic Press, 1964.

Carter, Ph.D thesis Cornell University, 1953

Carter, Krumhansl, J.Chem.Phys. 21, 2238, 1953

Chambers, Proc. Phys. Soc. A65, 458 and 903, 1952 also A238, 344, 1958

Corbato, Proc. 3rd. Carbon Conf. Pergamon Press p173, 1956

Coulson, Taylor, Proc. Phys. Soc. A65, 815, 1952

Dawson, Follet, Proc. Roy. Soc. A253, 390, 1959

Dingle, Proc. Roy. Soc., A211, 517, 1952

Dresselhaus, Dresselhaus, Phys. Rev., 140A, 401, 1965

Dresselhaus, Mavroides, IBM Journal Res. and Devel. 8, 262, 1964

Franklin, Acta Cryst., 4, 253, 1951

Galt, Yager, Dail, Phys. Rev., 103, 1586, 1956

Haering, Mrowski, Prog. in Semicond., 273, 1960

Haering, Wallace, J. Phys. Chem. Solids 3, 253, 1957.

Herring, J.Appl.Phys. 31, 1939, 1960

Hennig, Science, 147, 733, 1965

Hooker, Ubbelohde, Young, Proc. Roy. Soc., A276 83, 1963

also " A284, 17, 1965

Hove, Phys. Rev., 100, 645, 1955

Ichikawa, Phys. Rev., 109, 653, 1958

Inoue, J.Phys.Soc. Japan, 17, 808, 1962

Jenkins, Turnbull, Williamson, J. Nucl. Mater., 7, 215, 1969

Johnston, Proc. Roy. Soc., A227, 349, 1955 also A237, 48, 1956

Jones, "Theory of Brillouin Zones" North-Holland 1960.

Jones, Zener, Proc. Roy. Soc., A144, 101, 1934

Juretschke, Appl. Phys. Letters, 12, 213, 1968

Kao, Katz J. PHYS. CHEM. SOLIDS 6, 223, 1958

Kanter, Phys. Rev., 107, 655, 1957

Klein, Rev. Mod. Phys., 34, 56, 1962

Landau, Appendix D. Shoenberg, Proc. Roy. Soc. A170, 341, 1939.

Lewis, Solid State Physics, 7, p.353, 1958.

Lifshitz, note added in proof of Shoenberg, Prog. in Low Temp. Phys. 2, 226, 1957

Lifshitz, Azbel, Kaganov, Soviet Phys., JETP 4, 41, 1957

Lomer, Proc. Roy. Soc. A227, 330, 1955

McClure, Phys. Rev., 104, 666, 1956; 108, 612, 1957; 112, 715, 1958; 119, 606, 1960 also IBM J. Res. and Dev., 8, 258, 1964

McClure, Smith, Proc. 5th Carbon Conf. 2, 3, 1961, Pergamon

McClure, Yafet, Proc. 5th Carbon Conf. 1, 22, 1962, Pergamon

Moore, Ubbelohde, Young, Proc. Roy. Soc., A280, 153, 1964

Nozieres, Phys. Rev., 109, 1510, 1958

Ono, Sugihara, J. Phys. Soc. Japan, 21, 861, 1966 also 24, 818, 1968

Onsager, Phil. Mag., 43, 1006, 1952

Pippard, "Dynamics of Conduction Electrons", Blackie and Son, 1965

Powell , Computer Journal, 7, 303, 1964.

Putley, "The Hall Effect and Related Phenomena", Butterworths, 1960

Roscoe, Thomas, Carbon, 4, 383, 1966

Rose-Innes , "Low Temperature Techniques" English Univ. Press, 1964.

Roth, Argyres, "Semicond. and Semimetals", Vol. 1, p159, 1966 Academic Press

Schiff, "Quantum Mechanics", 1955, McGraw Hill

Shoenberg, Trans. Roy. Soc. A245, 1, 1952

Shubnikov-de Haas, Commun. Phys. Lab. Univ. Leiden, No. 207a, 1930

Slater , "Quantum Theory of Molecules and Solids" McGraw-Hill 1963-65.

Slonczewski, Ph.D. thesis, Rutgers University, unpubl., 1955

Slonczewski, Weiss, Phys. Rev., 99, 636A, 1955 also 109, 272, 1958

Sondheimer, Proc. Roy. Soc. A203, 75, 1950

Soule, Phys. Rev., 112, 698 and 708, 1958

Soule, McClure, Smith, Phys. Rev., 134, A453, 1964

Spain, Ubbelohde, Young, Phil. Trans. Roy. Soc., A262, 345, 1967

Sugihara, J. Phys. Soc. Japan, 21, supplement VIII-2, 1966

Sugihara, Sato, J. Phys. Soc. Japan, 18, 332, 1963

Swanson, Phys. Rev., 98, 1534, 1955 also 99, 1799, 1955

Wallace, Phys. Rev., 71, 622, 1947 also 72, 258, 1947

Whittaker, Robinson, p344

Yeoman, Young, J. Physics, part C (Solid State Physics) in press, 1969.

Young, Carbon, 6, 135, 1968

Young, Howell, Imperial College, 1969, unpubl.

Wilson, "Theory of Metals" 2nd ed. Cambr. Univ. Press, 1953

Ziman, "Principles of the Theory of Solids" 1965.

Ehrenberg "Electric Conduction in Semiconductors and Metals" Oxf. Univ. press, 1958.

APPENDIX 1

Wave Mechanics of Conduction Electrons

In using the Pippard-type geometrical approach to visualise electron processes we are applying a model which, at first sight, is extremely unlikely. One would suspect the presence of many pitfalls in an unwary application of the model and we accordingly propose to outline the main quantum-mechanical arguments leading to a justification for our sometimes regarding electrons in a lattice as discrete particles obeying classical laws of motion.

The quantum-mechanical treatment is mainly due to Bloch, 1928 whose work was based on Schrodinger's early work. Born's theory of lattice vibrations is also of great importance in this field and an excellent accounts are given by Blount and Lewis 1962, 1958 respectively.

We start with Schrodinger's time-dependent wave equation

$$(H + \frac{\hbar}{i} \frac{\partial}{\partial t}) \Phi = 0 \qquad (1)$$

For an electron in a magnetic field $\underline{H}$ described by a vector potential $\underline{A}$ and an electric field $\underline{E}$ described by a scalar potential V, we have the hamiltonian

$$H = - \frac{\hbar^2}{2m} \nabla^2 + \frac{ie\hbar}{mc} \underline{A} \cdot \nabla + \frac{ie\hbar}{2mc} \nabla \cdot \underline{A} + \frac{e^2}{2mc^2} A^2 + \phi \qquad (2)$$

where curl $\underline{A} \equiv \nabla \wedge \underline{A} = \underline{H}$,

and, by Maxwell's laws, $\underline{\varepsilon} = -\nabla V - \frac{1}{C}\frac{\partial \underline{A}}{\partial t}$ (3)

ϕ is the potential energy of the electron, = eV. (See Schiff 1955, equation 23.24).

Now, by identifying $\Phi^* \Phi$ as the time-averaged density of matter and in particular for charged matter, $\Phi^* \Phi = \frac{\rho}{e}$ (where ρ is the charge density and e is the electronic charge), we can relate $\frac{\partial \rho}{\partial t}(\Phi^* \Phi)$ to current flow $\underline{I}$ through the conservation equation $-\frac{\partial \rho}{\partial t} = \nabla . \underline{I}$.

Thus $$\frac{\partial}{\partial t}(\Phi^* \Phi) = \frac{\partial}{\partial t}\left(\frac{\rho}{e}\right) = -\frac{1}{e}\ \nabla . \underline{I}$$

$\frac{\partial}{\partial t}(\Phi^* \Phi)$ can be obtained from the Schrödinger equation (1) and the hamiltonian (2) to give a relation between current $\underline{I}$ and the quantities in the hamiltonian. Finally, identifying $\int \underline{I} d\tau$ with $e\underline{v}$, where $\underline{v}$ is the velocity of a wave packet described by Φ, we have

$$\underline{v} = \frac{\hbar}{im}\int d\tau\ \Phi^* \nabla \Phi - \frac{e}{mc}\int d\tau\ \underline{A}\ \Phi^* \Phi \qquad (4)$$

In the absence of a magnetic field, the Shrodinger equation simplifies to

$$i\hbar\ \frac{\partial \Phi}{\partial t} = \left(-\frac{\hbar^2}{2m}\nabla^2 + \phi\right)\Phi \qquad (5)$$

and if Φ is zero at infinity or periodic boundary conditions are applied then Φ can be split into time dependent and time independent parts

$$\Phi = \psi \, e^{-iEt/\hbar} \tag{6}$$

is a solution of (5) where ψ does not depend on time and satisfies the time independent Schrodinger equation

$$\left(\frac{\hbar^2}{2m} \nabla^2 + E - \phi\right) \psi = 0 \tag{7}$$

The application of Born-Karman boundary conditions then leads to discrete eigenfunctions ψ_n and eigenvalues E_n, distinguished by the set of quantum numbers, n.

Linear combinations of solutions of type (6) can be constructed to describe any type of charge distribution. In general

$$\Phi = \sum_n C_n \, \psi_{ne}^{-iEnt/\hbar} \tag{8}$$

where, by normalisation, $\Sigma |C_n|^2 = 1$.

Now let us assume we have the solutions to the above problem for a potential ϕ_o and we apply small electric and magnetic fields. Thus, we require solutions of

$$i\hbar \frac{\partial \Phi}{\partial t} = \left(- \frac{\hbar^2}{2m} \nabla^2 + \phi_o + H^1 \right) \Phi \tag{9}$$

$$H' = \frac{ie\hbar}{mc}\,\underline{A}.\nabla + \frac{ie\hbar}{2mc}\,\nabla.\underline{A} + \frac{e^2}{2mc^2}A^2 + eV \qquad (9A)$$

Then, for a small enough perturbation, the new solutions will still have the form (8), but the coefficients C_n will be time dependent.

The $C_n(t)$ satisfy

$$\dot{C}_{n'} = (i\hbar)^{-1} \sum_n C_n H'_{n'n} e^{i(E_{n'} - E_n)t/\hbar} \qquad (10)$$

where the matrix element $H'_{nn'} = \int \psi^*_{n'} H' \psi_n \, d\tau$

(H' can be simplified for small H; $H' = \frac{ie\hbar}{mc}\,\underline{A}.\nabla + eV$) (10A)

Motion in a periodic potential

Bloch's theorem states that solutions of (7), when ϕ is periodic, are of the form

$$\psi_k = C\, e^{i\underline{k}.\underline{r}}\, U_k(\underline{r})$$

where $U_k(\underline{r})$ has the same periodicity as the lattice. Substituting into the Schrodinger equation, (7), gives

$$\nabla^2 U + 2i\underline{k}.\nabla U + \frac{2m}{\hbar^2}\left(E - \phi - \frac{\hbar^2 k^2}{2m}\right)U = 0 \qquad (11)$$

Solving this equation for a given value of $\underline{k}$ leads to a discrete set of eigenfunctions, $U_{\underline{k}',n}(\underline{r})$ and eigenvalues $E_{\underline{k}',n}$ characterised by para-

meters $\underline{k}$ and n.

However, as things stand, we have some ambiguity in the wave function ψ, for we can add to $\underline{k}$ some vector $\underline{k}'$ leaving ψ unchanged

$$\psi = e^{i\underline{k}\cdot\underline{r}}\, U_{\underline{k}}(\underline{r}) = e^{i(\underline{k}+\underline{k}')\cdot\underline{r}}\,(e^{-i\underline{k}'\cdot\underline{r}}\, U_k(\underline{r}))$$

This expression for ψ is still a solution of (7) provided $e^{-i\underline{k}'\cdot\underline{r}}\, U_k(r)$ has the required periodicity. If $\underline{R}$ is a lattice translation vector then we must have $e^{-i\underline{k}'\cdot\underline{r}}\, U_k(\underline{r}) = e^{-i\underline{k}'\cdot(\underline{r}+\underline{R})} U_k(\underline{r}+\underline{R})$ i.e. $e^{-i\underline{k}'\cdot\underline{R}} = 1$, as $U_k(\underline{r})$ is periodic.

For a cubic lattice of primitive translation a the components of $\underline{k}$ have to satisfy $k_x\, a = 2\pi$ x integer, etc. Thus we can change the components of vector $\underline{k}$ by integral multiples of $\frac{2\pi}{a}$ without affecting ψ, provided the phase of the periodic function $U_k(r)$ is changed at the same time.

In general, it is possible to make the $\underline{k}$ vector describing any state lie within the first Brillouin zone ($-\frac{\pi}{a} < k_i < \frac{\pi}{a}$ for a cubic lattice). The resulting vector is called the "reduced wave vector".

By substituting $\psi_k = c e^{i\underline{k}\cdot\underline{r}}\, U_k(r)$ into the Schrodinger equation (7) and imposing Born-Karman periodic boundary conditions $\psi_k\,(\underline{r} + N\underline{R} = \psi_k\,(\underline{r})$ where N is an integer, we find that $\underline{k}$ can only take values such that $\underline{k}.N\underline{R} = 2\pi n$ where n is an integer and $\underline{R}$ is a translation vector of the lattice. For a cubic lattice, this means that compon-

ents of adjacent $\underline{k}$ vectors are separated by $\frac{2\pi}{aN}$. This is a very small quantity compared with the width of the Brillouin Zone and we can usually regard $\underline{k}$ as being continuous.

The sets of eigenfunctions $\psi_{\underline{k},n}$ for different values of the quantum number n usually have widely separated sets of eigenvalues $E_{\underline{k},n}$. Almost all conduction processes involve much smaller energies than these gaps and n will not usually change for these processes. At most, we are concerned with a few such n values, corresponding to the "valence" and "conduction" bands and we shall omit the band index in what follows.

Velocity of electron packets

Let us construct a wave packet from Bloch states with wave vectors $\underline{l}$ localised near $\underline{l} = \underline{k}$:

$$\Phi_{\underline{k}} = \sum_{\underline{l}} C_{\underline{l}} \psi_{\underline{l}} e^{-iE_{\underline{l}}t/\hbar} \tag{12}$$

By 4 and 12 the velocity of the packet is

$$\underline{V}_{\underline{k}} = \frac{\hbar}{im} \int \left(\sum_{\underline{l}} C^*_{\underline{l}} \psi^*_{\underline{l}} e^{iE_{\underline{l}}t/\hbar} \nabla \sum_{\underline{l}} C_{\underline{l}} \psi_{\underline{l}} e^{-iE_{\underline{l}}t/\hbar}\right) d\tau - \frac{e}{mc} \int \underline{A} \Phi^*_{\underline{k}} \Phi_{\underline{k}} \, d\tau$$

This can be reduced to

$$\underline{V}_{\underline{k}} = \frac{\hbar}{im} \sum_{\underline{l}} |C_{\underline{l}}|^2 \int_{\underline{l}} \psi^*_{\underline{l}} \nabla\psi_{\underline{l}} \, d\tau - \frac{e}{mc} \int_{\underline{l}} \underline{A} \Phi^*_{\underline{k}} \Phi_{\underline{k}} \, d\tau$$

Now, if $\Phi_{\underline{l}}$ is localised near $\underline{l} = \underline{k}$ and also $\Sigma |C_{\underline{l}}|^2 = 1$ by normalisation of ψ then

$$\underline{V}_{\underline{k}} = \frac{\hbar}{im} \int_1 \psi^*_{\underline{k}} \nabla\psi_{\underline{k}} \, d\tau - \frac{e}{mc} \int_1 \underline{A}\, \Phi^*_{\underline{k}} \Phi_{\underline{k}} \, d\tau \qquad (13)$$

which relates the velocity of a wave packet to the wave vector of the eigenfunction which contributes most strongly to the wave packet. $\underline{k}$ is the "representative wave vector". The shape of the wave packet enters through the second term.

Now we must digress to point out that the magnetic field $\underline{H}$ is still described by a vector potential $\underline{A}$ when this latter is changed by addition of the gradiant of any scalar field, f.

For $\nabla \wedge (\underline{A} + \nabla f) = \nabla \wedge \underline{A} + \nabla \wedge \nabla f = \nabla \wedge \underline{A} = \underline{H}$

(since curl (grad f) $\equiv$ 0).

But this "gauge transformation" changes the potential V.

Thus, for constant magnetic field $\underline{H}$ and electric field ϵ we have $\underline{A} = \frac{1}{2} \underline{H} \wedge \underline{r} + \nabla f$ and $V = -\underline{\epsilon}.\underline{r} - \frac{1}{c} \frac{\partial f}{\partial t}$ (from(3)).

Thus, (13) can be reduced to a single term if we add $\nabla f = -\frac{1}{2} \underline{H} \wedge \bar{\underline{r}}$ to $\frac{1}{2} \underline{H} \wedge \underline{r}$, where $\bar{\underline{r}} = \int \Phi^*_{\underline{k}}\, \underline{r}\, \Phi_{\underline{k}} \, d\tau$, for the second term is easily shown to be zero.

Then $$\underline{V}_{\underline{k}} = \frac{\hbar}{im} \int \psi_{\underline{k}} \nabla\psi_{\underline{k}} \, d\tau \qquad (14)$$

This simpler expression is thus valid provided we use a vector potential whose mean value is zero. This is known as the "Jones-Zener condition".

Now the $\psi_{\underline{k}}$ have the Bloch form, and satisfy $\frac{\hbar^2}{2m} \nabla^2 \psi_{\underline{k}} + (E_{\underline{k}} - \phi)\psi_{\underline{k}} = 0$ where ϕ is the periodic potential. By operating with $\frac{\partial}{\partial k_x}$, multiplying

by $\psi^*_{\underline{k}}$ and integrating, we find $\hbar\dot{x}_{\underline{k}} = \frac{\partial}{\partial k_x} E_{\underline{k}}$. Thus, combining similar equations for the other components, we have for the velocity of the wave packet:

$$\hbar \underline{V}_{\underline{k}} = \nabla_k E_{\underline{k}} \tag{15}$$

Acceleration of the electron

Taking $\underline{V}_{\underline{k}}$ formally as a function of $\underline{k}$ and $\underline{r}$ we have

$$\frac{d}{dt} \underline{V}_{\underline{k}\,x} \equiv \dot{\underline{V}}_{\underline{k}\,x} = \left(\frac{\partial \dot{x}}{\partial k_x} \dot{k}_x + \frac{\partial \dot{x}}{\partial k_y} \dot{k}_y + \frac{\partial \dot{x}}{\partial k_z} \dot{k}_z\right) + \left(\frac{\partial \dot{x}}{\partial x} \dot{x} + \frac{\partial \dot{x}}{\partial y} \dot{y} + \frac{\partial \dot{x}}{\partial z} \dot{z}\right)$$

or
$$\dot{\underline{V}}_{\underline{k}} = \hbar \underline{\underline{T}}\, \dot{\underline{k}} + \hbar \underline{\underline{T}}' \underline{V}_{\underline{k}} \tag{16}$$

where the tensors have elements:

$$T_{ij} = \frac{1}{\hbar} \frac{\partial V_{ki}}{\partial k_j} = \frac{1}{\hbar^2} \frac{\partial^2 E_k}{\partial k_i \partial k_j}$$

$$T'_{ij} = \frac{1}{\hbar^2} \frac{\partial^2 E_k}{\partial k_i \partial x_j} \tag{17}$$

Rigorous justification for letting the eigenvalues $E_{\underline{k}}$ vary with position in this way is not easy. It is as if the conductor were made of adjoining pieces, each having slightly different sets of eigenvalues.

We must find an expression for $\dot{\underline{k}}$. From (10) we have

$$\dot{c}(1) = \frac{1}{(i\hbar)} \Sigma\, c(1)\, H'_{1'1} \exp(i(E_{1'} - E_1)\frac{t}{\hbar}) \qquad (18)$$

Now, using the vector potential satisfying the Jones-Zener condition,

$$\frac{\partial f}{\partial t} = -\tfrac{1}{2}(\underline{H} \Lambda \frac{\partial \bar{r}}{\partial t}).\underline{r} = -\tfrac{1}{2}(\underline{H} \Lambda \underline{V}_k).\underline{r}$$

Hence the new potential $V = -\underline{E}.\underline{r} - \frac{e}{2c}(\underline{V}_k \Lambda \underline{H}).\underline{r}$ (19)

So, using (18), (10A), (19) and $\underline{A} = \frac{1}{2}\underline{H} \Lambda (\underline{r} - \bar{r})$ we have for small values of $\underline{H}$, t and $(E_{1'} - E_1)$:

$$\dot{c}(1') = \Sigma\, c(1) \int \psi^*_{1'} \left(\frac{ie\hbar}{2mc} \underline{H} \Lambda (\underline{r} - \bar{r}) \nabla - \frac{e}{2c}(\underline{V}_k \Lambda \underline{H}).\underline{r} - e\underline{\varepsilon}.\underline{r}\right)\psi_1 d\tau$$

This must be evaluated for the Bloch waves $\psi_1 = ce^{i\underline{l}.\underline{r}}U_1(\underline{r})$. After some involved calculation we find (Ehrenberg, P.99)

$$\dot{c}_{1'} = -\left(\frac{e}{\hbar}\underline{\varepsilon} + \frac{e}{2c\hbar}(\underline{V}_{1'} + \underline{V}_k) \Lambda \underline{H}\right) \nabla_k c_{1'} - \frac{ie}{2c\hbar} c_{1'} \underline{H} \Lambda \bar{\underline{r}}\, v_{1'}$$

For the representative vector, $\underline{1'} = \underline{k}$, this can be written

$$\frac{\partial}{\partial t}|c_{\underline{k}}|^2 = -\frac{e}{\hbar}(\underline{\varepsilon} + \frac{1}{c}\underline{V}_{\underline{k}} \Lambda \underline{H}).\nabla_k |c_k|^2$$

which is satisfied by

$$|c_k|^2 = \text{function of } (\hbar \underline{k} - e\underline{\epsilon}t - \frac{e}{c}\underline{\bar{r}} \Lambda \underline{H}).$$

For $\underline{k}$ to continue to denote the representative wave vector as the wave packet moves, $\underline{k}$ must change with time to keep the argument constant. Thus the rate of change of the representative wave vector of the wave packet, $\dot{\underline{k}}$, is given by

$$\hbar \dot{\underline{k}} = e\underline{\epsilon} + \frac{e}{c} \underline{V}_k \Lambda \underline{H} \tag{20}$$

But the RHS is the Lorentz force F acting on a particle with charge e. Thus, $\hbar\underline{k}$ changes under the force F just as does $m\underline{V}$ for a charged particle outside the lattice.

Equation (16) now reduces to

$$\dot{\underline{V}}_k = \hbar \underline{\underline{T}} \dot{\underline{k}} + \hbar \underline{\underline{T}}' \underline{V}_k = \underline{\underline{T}} \underline{F} + \hbar \underline{\underline{T}}' \underline{U}_k$$

For a homogeneous material, $\underline{\underline{T}}' = \underline{\underline{0}}$ and

$$\dot{\underline{V}}_k = \underline{\underline{T}} \underline{F} \tag{21}$$

Comparing this with Newton's relation $\dot{\underline{V}} = \frac{1}{m} \underline{F}$ we see that $\underline{\underline{T}}^{-1}$ is analogous to a mass tensor. This discovery is subject to the approxi-

mations we have made, viz. that the material is homogeneous and that the field H is small enough to neglect A^2 in(9A), leading to (10A). Jones and Zener have given the condition for the validity of neglecting A^2 as $(eH/2mc)t \ll 1$, where τ is the time over which $\hbar\underline{k} - e\underline{\varepsilon}t - \frac{e}{c}\underline{r} \wedge \underline{H}$ = constant is valid, essentially the relaxation time. For graphite, taking $m = 0.02\ m_o$, $t = 5 \times 10^{-13}$ secs, this gives $H \ll 250$ kgauss.

A further condition is that the carriers can be described by Bloch waves taken from single bands i.e. no band degeneracy is allowed or the effective mass approximation will break down. Of course, our picture suffers from the fundamental drawbacks of the independent-particle model; correlation effects are entirely neglected. "Electrons" and "holes" strictly exist, respectively, well above and below, the Fermi energy. Close to the Fermi energy neither particle is well-defined and there exists the possibility of strongly correlated states. However, for a semimetal like graphite we put our faith in the low density of carriers compared with the density of available states and hope that correlation effects are reasonably small.

APPENDIX 2.

Application of the Jones-Zener Expansion to Graphite

The object of this appendix is to reduce the Jones-Zener solution of the Boltzmann equation to a form where comparison can be made between Jones-Zener terms and terms in the phenomenological expansion of the magneto-conductivity tensor, $\sigma_{ij}(\underline{H})$. These tensor components are then reduced to fairly simple integrals over the Fermi surface which enable one to relate the low field magnetoconductivity tensor directly to the Slonczewski-Weiss band parameters.

We recall the solution of the Boltzmann equation $f = f_o - \phi\frac{\partial f_o}{\partial E}$ where ϕ is given by $\frac{1}{\tau}\phi + \frac{e}{\hbar}\,\underline{\varepsilon} \cdot \nabla_K E + \underline{H} \cdot \underline{\Omega}\,\phi = 0$ and $\underline{\Omega} = \frac{e}{C\hbar^2}\,\nabla_K E \wedge \nabla_K$ This can be solved for ϕ to any order by iteration; for instance, the zeroth order solution is $\phi_o = -\frac{\tau e}{\hbar}\,\underline{\varepsilon} \cdot \nabla_K E$. Substituting back, one obtains higher order solutions. Jones and Zener first obtained the series solution in 1934:-

$$\phi = -\frac{e}{\hbar}[\tau\underline{\varepsilon} \cdot \nabla_K E - \tau\,\underline{H} \cdot \underline{\Omega}\,(\tau\underline{\varepsilon} \cdot \nabla_K E) + \tau\underline{H} \cdot \underline{\Omega}\,(\tau\underline{H} \cdot \underline{\Omega}\,(\tau\underline{\varepsilon} \cdot \nabla_K E)) \ldots]$$

- where e is positive for electrons.

Now, bearing in mind the definition of $\underline{J}$, e, and ϕ, particularly in respect of their signs, one can write the current density $\underline{J}$ in terms of the above expansion :

$$\underline{J} = \frac{e}{4\pi^3} \int \underline{V}\,\phi\,\frac{\partial f_o}{\partial E}\,dV_K$$

Hence $J_i = -\frac{e^2}{4\pi^3}\int\frac{\partial f_o}{\partial \tau}\,\nu_i[\tau\underline{\varepsilon}.\underline{V} - \tau\underline{H}.\,\underline{\Omega}(\tau\underline{\varepsilon}.\underline{V}) + \tau\underline{H}.\,\underline{\Omega}(\tau\underline{H}.\,\underline{\Omega}(\tau\underline{\varepsilon}.\underline{V}))]dV_K$

- where we have used $\underline{V} = \frac{1}{\hbar}\nabla_K E \qquad = (\nu_1, \nu_2, \nu_3)$

It is easily shown that any function of energy alone commutes with the operator $\underline{\Omega}$; $\underline{\Omega}\, f(E(K)) = f(E(K))\,\underline{\Omega}$ so one may bring out the electric field components from within $\underline{\Omega}$:

$$J_i = -\frac{e^2}{4\pi^3}\int\frac{\partial f_o}{\partial E}\,\nu_i[\tau\varepsilon_j\nu_j - \tau\varepsilon_j\underline{H}.\,\underline{\Omega}(\tau\nu_j) + \varepsilon_j\tau\underline{H}.\,\underline{\Omega}(\tau\underline{H}.\,\underline{\Omega}(\tau\nu_j))]dV_K$$

The conductivity tensor follows immediately

$$\sigma_{ij}(H) = -\frac{e^2}{4\pi^3}\int\frac{\partial f_o}{\partial E}\,\nu_i[\tau\nu_j - \tau\underline{H}.\,\underline{\Omega}(\tau\nu_j) + \tau\underline{H}.\,\underline{\Omega}(\tau H.\,\underline{\Omega}(\tau\nu_j))]dV_K$$

Comparing this with phenomenological expansion

$$\sigma_{ij}(\underline{H}) = \sigma_{ij} + \sigma_{Kij}H_K + \sigma_{Klij}H_K H_l + \cdots$$

where $\sigma_{ij} = \sigma_{ij}(0)$, $\sigma_{Kij} = \left.\frac{\partial\sigma_{ij}(\underline{H})}{\partial H_K}\right)_{\underline{H}=0}$, $\sigma_{Klij} = \frac{1}{2}\left.\frac{\partial^2\sigma_{ij}(\underline{H})}{\partial H_K\partial H_l}\right)_{\underline{H}=0}$

one can identify the coefficients in the two expansions :-

$$\sigma_{ij} = -\frac{e^2}{4\pi^3}\int\frac{\partial f_o}{\partial E}\,\nu_i\tau\nu_j\,dV_K$$

$$\sigma_{Kij} = +\frac{e^2}{4\pi^3}\frac{\partial}{\partial H_K}\int\frac{\partial f_o}{\partial E}\,\nu_i\tau\,\underline{H}.\,\underline{\Omega}(\tau\nu_j)dV_K = \frac{e^2}{4\pi^3}\int\frac{\partial f_o}{\partial E}\,\nu_i\tau\,\Omega_K(\tau\nu_j)dV_K$$

$$\sigma_{Klij} = -\frac{e^2}{4\pi^3}\,\frac{1}{2}\,\frac{\partial^2}{\partial H_K \partial H_l}\int\frac{\partial f_o}{\partial E}\,\nu_i[\tau\underline{H}\cdot\underline{\Omega}(\tau\underline{H}\cdot\underline{\Omega}(\tau\nu_j))]dV_K$$

One can remove the product of the $\underline{\Omega}$ - operator from the last expression by using $\Omega(AB) = A\underline{\Omega}B + B\underline{\Omega}A$ with $A \equiv (\tau\nu_i)$, $B \equiv (\tau\underline{H}\cdot\underline{\Omega}(\tau\nu_j))$. Then

$$\sigma_{Klij} = -\frac{e^2}{4\pi^3}\,\frac{1}{2}\,\frac{\partial^2}{\partial H_K \partial H_l}\int\frac{\partial f_o}{\partial E}\,(\underline{H}\cdot\underline{\Omega}(\tau\nu_i(\tau\underline{H}\cdot\underline{\Omega}(\tau\nu_j))-\tau\underline{H}\cdot\underline{\Omega}(\tau\nu_j)\underline{H}\cdot\underline{\Omega}(\tau\nu_i))dV_K$$

We now show that the first integral is zero: Operate on any scalar field A with $(\underline{H}\cdot\underline{\nabla}_K\wedge\underline{V})$. By writing the scalar triple product in determinantal form it can be seen that this operation results in

$$(\underline{H}\cdot\underline{\nabla}_K\wedge\underline{V})A = -(\underline{H}\cdot\underline{V}\wedge\underline{\nabla}_K)A + A(\underline{H}\cdot\underline{\nabla}_K\wedge\underline{V})$$

However, the last expression is zero, for its terms cancel in pairs. Taking the pair associated with the H_x component as an example, we see

$$AH_x\left(\frac{\partial\nu_3}{\partial K_2} - \frac{\partial\nu_2}{\partial K_3}\right) = 0$$

since $\nu_i = \frac{1}{\hbar}\frac{\partial E}{\partial K_i}$, $i = 1, 2, 3$. Thus, we are left with

$$(\underline{H}\cdot\underline{\Omega})A = -(\underline{H}\cdot\underline{\nabla}_K\wedge\underline{V})A = -(\underline{\nabla}_K\cdot\underline{V}\wedge\underline{H})A = \mathrm{div}_K(-A(\underline{V}\wedge\underline{H}))$$

- which means that any scalar field can be transformed into the divergence of a vector field by application of the operator $(\underline{H}\cdot\underline{\Omega})$.

The above integral has thus been transformed into the integral over volume of the divergence of a vector field

$$[-\frac{\partial f_o}{\partial E}\, \tau\nu_i\, \tau\underline{H}\cdot\underline{\Omega}(\tau\nu_j)(\underline{V}\wedge\underline{H})].$$

By Gauss' theorem, this can be written as a surface integral of the vector field which immediately reduces to zero because $E(\underline{K})$ has the same values on opposite faces of the Brillouin zone.

One is left with:

$$\sigma_{Klij} = \tfrac{1}{2}\,\frac{e^2}{4\pi^3}\,\frac{\partial^2}{\partial H_K \partial H_l}\int\frac{\partial f_o}{\partial E}\,\tau\underline{H}\cdot\underline{\Omega}(\tau\nu_i)\underline{H}\cdot\underline{\Omega}(\tau\nu_j)dV_K$$

i.e.

$$\sigma_{Klij} = \frac{e^2}{8\pi^3}\int\frac{\partial f_o}{\partial E}\,\tau[\,\Omega_K(\tau\nu_j)\,\Omega_l(\tau\nu_i)+\Omega_l(\tau\nu_j)\Omega_K(\tau\nu_i)]dV_K$$

To go further, we look for simplifications resulting from the symmetry of the graphite crystal and impose the condition that the magnetic field vector lie parallel to the c-axis, $\underline{H} \equiv (0,0,H)$. It was shown in section 2.2.1. that the only tensor elements contributing to $\sigma_{ij}(\underline{H})$ with the magnetic field along the z-axis are

σ_{11}, $\sigma_{22}=\sigma_{11}$, σ_{33}, σ_{312}, $\sigma_{321}=-\sigma_{312}$, σ_{3311}, $\sigma_{3322}=\sigma_{3311}$, σ_{3333},

so one can work with K = 3, l = 3 from now on.

Taking σ_{3ij} first, one requires an expression for Ω_3. By expanding $\frac{e}{c\hbar}\,\underline{V}\wedge\nabla_K$ one obtains

$$\sigma_{3ij} = \frac{e^2}{4\pi^3}\,\frac{e}{c\hbar}\int\frac{\partial f_o}{\partial E}\,\nu_i\tau(\nu_1\frac{\partial}{\partial K_2} - \nu_2\,\frac{\partial}{\partial K_1})(\tau\nu_j)dV_K$$

The reduction of σ_{Klij} to σ_{33ij} follows simply:

$$\sigma_{33ij} = \frac{e^2}{4\pi^3} \int \frac{\partial f_o}{\partial E} \tau \Omega_3(\tau v_i) \Omega_3(\tau v_j) dV_K$$

$$= \frac{e^2}{4\pi^3} \left(\frac{e}{C\hbar} \right)^2 \int \frac{\partial f_o}{\partial E} \tau \left(v_1 \frac{\partial}{\partial K_2} - v_2 \frac{\partial}{\partial K_1} \right) (\tau v_i) \left(v_1 \frac{\partial}{\partial K_2} - v_2 \frac{\partial}{\partial K_1} \right) (\tau v_j) dV_K$$

Now, since the energy-band structure of graphite is not known over the whole Brillouin zone, we must introduce an approximation here to change the volume integral to an integral over the Fermi surface.

Using the well-known expansion for an integral $I(EF) = \int_o^\infty \frac{\partial f_o}{\partial E} f_o(E) dE$ where $G(E)$ is a known function of energy; $I(EF) = G(EF) - G(0) + \frac{(\pi kT)^2}{6} \frac{\partial^2 G}{\partial E^2} \cdots\cdots,$

one can verify, by integrating by parts, the following relation for any function $g(E)$ of energy:

$$- \int_o^\infty g(E) \frac{\partial f_o}{\partial E} dE = g(EF) + \frac{(\pi kT)^2}{6} \left(\frac{\partial^2 g}{\partial E^2} \right)_{EF} \cdots\cdot$$

We use the lowest order approximation, obtaining:

$$\sigma_{ij} = \frac{e^2}{4\pi^3} \int_{E=Ef} \nu_i \tau \nu_j \frac{dS}{|\nabla_K E|}$$

- since $dV_K = \left| \frac{dE dS}{\nabla_K E} \right|$ where dS is an element of Fermi surface area.

$$\sigma_{3ij} = \frac{-e^3}{4\pi^3 c\hbar} \int \nu_i \tau \left(\nu_1 \frac{\partial}{\partial K_2} - \nu_2 \frac{\partial}{\partial K_1}\right) \tau \nu_j \frac{dS}{|\nabla_K E|}$$

$$\sigma_{33ij} = \frac{-e^4}{4\pi^3 c^2 \hbar^2} \int \tau \left(\nu_1 \frac{\partial}{\partial K_2} - \nu_2 \frac{\partial}{\partial K_1}\right)(\tau\nu_i)\left(\nu_1 \frac{\partial}{\partial K_2} - \nu_2 \frac{\partial}{\partial K_1}\right)$$

$$(\tau\nu_j) \frac{dS}{|\nabla_K E|}$$

Our task is now to perform these integrations over the Fermi surface of graphite, and so relate the band parameters to the low-field conductivity tensor. To do this, we recognise that one can - not obtain an analytic expession for the Fermi surface from the secular equation of Sloncewski-Weiss's band model for $\gamma_3 \neq 0$. We accordingly assume $\gamma_3 = 0$ throughout and make great use of the resulting circular symmetry about the K_z-axis.

In view of the circular symmetry, let us transform to the cylindrical co-ordinates K, α, K_z as defined in section 2.1.3 . In what follows we make use of the relations

$$\frac{\partial}{\partial K_1} = \cos\alpha \frac{\partial}{\partial K} - \frac{\sin\alpha}{K} \frac{\partial}{\partial \alpha}, \quad \frac{\partial}{\partial K_2} = \sin\alpha \frac{\partial}{\partial K} + \frac{\cos\alpha}{K} \frac{\partial}{\partial \alpha}$$

and the resulting expressions for the Fermi velocities:

$$\nu_i = \frac{1}{\hbar} \frac{\partial E}{\partial K_i} \; ; \; \begin{pmatrix} \nu_1 \\ \nu_2 \end{pmatrix} = \frac{1}{\hbar}\left(\frac{\partial E}{\partial K}\right)\begin{pmatrix} \cos\alpha \\ \sin\alpha \end{pmatrix}$$

The expression $(v_1 \frac{\partial}{\partial K_2} - v_2 \frac{\partial}{\partial K_1})(\tau v_j)$ reduces as follows:

$$\frac{1}{\hbar}\left[\cos\alpha\left(\frac{\partial E}{\partial K}\right)\left(\sin\alpha\frac{\partial}{\partial K} + \frac{\cos\alpha}{K}\frac{\partial}{\partial\alpha}\right) - \sin\alpha\left(\frac{\partial E}{\partial K}\right)\left(\cos\alpha\frac{\partial}{\partial K} - \frac{\sin\alpha}{K}\frac{\partial}{\partial\alpha}\right)\right]$$

$$\left(\tau\frac{1}{\hbar}\frac{\partial E}{\partial K}\right)\begin{pmatrix}\cos\alpha\\ \sin\alpha\end{pmatrix} = \frac{\tau}{\hbar^2 K}\left(\frac{\partial E}{\partial K}\right)^2\begin{pmatrix}-\sin\alpha\\ \cos\alpha\end{pmatrix}$$

where one takes the $(-\sin\alpha)$ if $j = 1$ and $(\cos\alpha)$ if $j = 2$. In deriving this, we have used the key fact that $\frac{\partial E}{\partial\alpha} = 0$ for our band model with $\gamma_3 = 0$. An additional assumption is that τ is constant on an orbit round the Fermi surface in a plane perpendicular to the c-axis; $\tau = \tau(E, K_z)$.

The element of surface area is given by

$$dS = K d\alpha dK_z \left(1 + \left(\frac{dK}{dK_z}\right)^2\right)^{\frac{1}{2}}.$$

Because of the circular symmetry, one may integrate with respect to α immediately.

For $i, j = 1, 2$:-

$$\int_0^{2\pi} v_i \tau v_j d\alpha = \int_0^{2\pi} \left(\frac{1}{\hbar}\frac{\partial E}{\partial K}\right)^2 \tau \begin{pmatrix}\cos\alpha\\ \sin\alpha\end{pmatrix}\begin{pmatrix}\cos\alpha\\ \sin\alpha\end{pmatrix} d\alpha = \tau\left(\frac{1}{\hbar}\frac{\partial E}{\partial K}\right)^2 \begin{pmatrix}\pi & 0\\ 0 & \pi\end{pmatrix}$$

which shows that $\sigma_{21} = \sigma_{12} = 0$, $\sigma_{11} = \sigma_{22}$ as we have already seen from other symmetry considerations, in Section 2.2.1.

$$\int_0^{2\pi} \tau v_i \left(v_1 \frac{\partial}{\partial K_2} - v_2 \frac{\partial}{\partial K_1}\right)(\tau v_j)\,d\alpha = \int_0^{2\pi} \frac{\tau^2}{K\hbar^2} \left(\frac{\partial E}{\partial K}\right)^2 \left(\frac{1}{\hbar} \frac{\partial E}{\partial K}\right) \begin{pmatrix}\cos\alpha \\ \sin\alpha\end{pmatrix} \begin{pmatrix}-\sin\alpha \\ \cos\alpha\end{pmatrix} d\alpha$$

$$= \frac{\tau^2}{K\hbar^3} \left(\frac{\partial E}{\partial K}\right)^3 \begin{pmatrix}0 & \pi \\ -\pi & 0\end{pmatrix}$$

showing $\sigma_{311} = \sigma_{322} = 0$, $\sigma_{312} = -\sigma_{321}$

$$\int_0^{2\pi} \tau \left(v_1 \frac{\partial}{\partial K_2} - v_2 \frac{\partial}{\partial K_1}\right)(\tau v_i)\left(v_1 \frac{\partial}{\partial K_2} - v_2 \frac{\partial}{\partial K_1}\right)(\tau v_j)\,d\alpha$$

$$= \int_0^{2\pi} \frac{\tau^2}{\hbar^2 K} \left(\frac{\partial E}{\partial K}\right)^2 \begin{pmatrix}-\sin\alpha \\ \cos\alpha\end{pmatrix} - \frac{\tau}{\hbar^2 K} \left(\frac{\partial E}{\partial K}\right)^2 \begin{pmatrix}-\sin\alpha \\ \cos\alpha\end{pmatrix} d\alpha$$

$$= \frac{\tau^3}{(\hbar^2 K)^2} \left(\frac{\partial E}{\partial K}\right)^4 \begin{pmatrix}\pi & 0 \\ 0 & \pi\end{pmatrix}$$

showing $\sigma_{3311} = \sigma_{3322}$, $\sigma_{3312} = \sigma_{3321} = 0$.

For i,j = 3 we see that for σ_{33}

$$\int_0^{2\pi} v_3 \tau v_3 \,d\alpha = \frac{\tau}{\hbar^2} \left(\frac{\partial E}{\partial K_z}\right)^2 2\pi$$

Since $\tau v_3 = \frac{\tau}{\hbar} \frac{\partial E}{\partial K_z}$ has no K or α dependence we see that our assumption of $\gamma_3 = 0$ has imposed $\sigma_{3333} = 0$, whereas it is not necessarily zero from the symmetry of the crystal structure. One

deduces that a K or α - dependence of $\frac{\partial E}{\partial K_z}$ is essential to explain c-axis magneto-resistance or conductivity, both of which are proportional to σ_{3333}.

Before collecting our results, we present another simplification which leads to considerable reduction in the computational difficulties ahead.

We note simply that, since the integrations are being taken over the Fermi surface whose energy is, by definition, constant, the following relation must hold :

$$dE = \frac{\partial E}{\partial K} dK + \frac{\partial E}{\partial K_z} dK_z = 0$$

$$(\frac{\partial E}{\partial \alpha} = 0 \text{ since } \gamma_3 = 0)$$

This leads to

$$\frac{dK}{dK_z} = - \frac{\partial E}{\partial K_z} / \frac{\partial E}{\partial K}$$

Now, the integrals all contain a factor $\frac{[1+(\frac{dK}{dK_z})^2]^{\frac{1}{2}}}{|\nabla_K E|}$ and it is this which we simplify by realizing that

$$|\nabla_K E| = \sqrt{(\frac{\partial E}{\partial K})^2 + (\frac{\partial E}{\partial K_z})^2}$$

and using the above result;

$$\frac{\left[1+\left(\frac{dK}{dK_z}\right)^2\right]^{\frac{1}{2}}}{|\nabla_K E|} = \frac{1}{\left(\frac{\partial E}{\partial K}\right)}$$

The integrals may now be collected, in preparation for the final integration over K_z.

$$\sigma_{ij} = \begin{pmatrix} \pi & 0 \\ 0 & \pi \end{pmatrix} \frac{e^2}{4\pi^3 \hbar^2} \int \tau \left(\frac{\partial E}{\partial K}\right) K \, dK_z$$

$$\sigma_{31j} = \begin{pmatrix} 0 & \pi \\ -\pi & 0 \end{pmatrix} \frac{-e^3}{4\pi^3 c \hbar^4} \int \tau^2 \left(\frac{\partial E}{\partial K}\right)^2 dK_z$$

$$\sigma_{33ij} = \begin{pmatrix} \pi & 0 \\ 0 & \pi \end{pmatrix} \frac{-e^4}{4\pi^3 c^2 \hbar^6} \int \tau^3 \left(\frac{\partial E}{\partial K}\right)^3 \frac{1}{K} \, dK_z$$

To proceed further we must find the functions $K(K_z)$, $\frac{\partial E}{\partial K}(K_z)$ and assume some K_z-dependence for $\tau(K_z)$, but these expressions represent a remarkable simplification of the original Jones-Zener expressions.

APPENDIX 3

DATA.

The following tables of data are in three sections. First there is raw data on the variation of conductivity and Hall coefficient with magnetic field at stated temperatures for each of the three samples. This makes up the bulk of Appendix 3.

After this comes a short section detailing the results of fitting the raw data to Lorentzians. The solid curves of the graphs in Chapter 5 were plotted from the total conductivities σ_{xx}, σ_{xy} listed here. However, the tables also contain partial conductivities e.g. σ_{xy}^{n}, σ_{xy}^{P} from which the contribution of negative (n) and positive (P) carriers can be ascertained. Gaussian units are used. Magnetic field values are in gauss.

The last section presents raw data on the oscillations observed on W3 in three experiments at $1.2^{\circ}K$, two on the Hall effect and one on the magnetoresistance oscillations. The columns are magnetic field B (gauss), reciprocal field $^{1}/B$ ($gauss^{-1} \times 10^{6}$), and sample voltage V, arbitrary units. One of these experiments was subjected to the detailed analysis of Section 5.2.

Errors.

Errors were introduced mainly in the chart reading process. Chart calibration, involving measurement of chart distances (<1%), sample current (<0.1%) and sample voltages (1% for low field Hall voltage at $1^{\circ}K$, though greater for values of magnetic field giving near-zero Hall coefficient) introduced a slightly smaller error. Total errors from these sources to be expected at $1^{\circ}K$ vary from 10% at 200 gauss for magnetoresistance and 30% for Hall effect. This quickly drops to 3% for both effects at 2000 gauss and 2% or less above 4000 gauss. At $300^{\circ}K$ errors are similar in magnitude for both effects, being about 10% at 200 gauss and less than 2% above 5000 gauss.

The magnetic field values must be corrected by the factor 0.960 because of a late-discovered calibration error in our fluxmeter. Final derived values in Chapter 5, in particular Table 5.1 embody this -4% correction. Calibration of the Hall probe was accomplished to within 2%. It should be remembered that the magnetic field appears explicitly in the definition of Hall coefficient.

W1 295°K		
B gauss	$-R_H$ (cm^3/C)	σ $(\Omega\text{-cm})^{-1} \times 10^{-3}$
647	.06365	22.8
1093	.067529	22.56
1602	.05993	22.17
2128	.05969	21.71
2644	.05447	21.15
3758	.05841	19.75
4335	.05696	18.99
4860	.05983	18.25
5470	.06069	17.42
6560	.06064	15.95
7640	.06284	14.55
8790	.06398	13.13
9705	.06587	12.11
10710	.06789	11.10
11660	.07014	10.22
12550	.07168	9.47
13620	.07394	8.65
14550	.07616	8.00
15830	.07695	7.23

W1 295°K		
B gauss	$-R_H$ (cm^3/C)	σ $(\Omega\text{-cm})^{-1} \times 10^{-3}$
17080	.07919	6.51
17420	.07876	6.40
205	.07031	22.819
205	.07408	22.936
214	.06736	22.918
218	.08176	22.914
229	.06294	22.827
273	.06529	22.897
319	.0823	22.883
365	.07546	22.859
456	.05416	22.764
548	.06611	22.831
683	.06916	22.772
914	.05886	22.575
1003	.06281	22.595
1139	.0576	22.526
1253	.06111	22.449
1364	.06133	22.283
1459	.06087	22.288

W1 295°K		
B gauss	$-R_H$ (cm^3/C)	σ $(\Omega\text{-cm})^{-1}$ x10^{-3}
1595	.06132	22.168
1713	.06161	22.052
1822	.06039	21.905
1916	.05877	21.851
2056	.06197	21.715
2278	.06017	21.453
2374	.05828	21.380
2516	.05831	21.219
2630	.05823	21.090
2736	.05805	20.936
2836	.05784	20.852
2976	.05804	20.676
3090	.05885	20.525

W1 88°K		
B gauss	$-R_H$ (cm^3/C)	σ $(\Omega\text{-cm})^{-1} \times 10^{-3}$
3480	.0465	11.759
4436	.0637	8.831
5395	.0825	6.847
6360	.1012	5.3916
7330	.1197	4.3203
8300	.137	3.5679
9280	.1525	2.9792
10260	.1666	2.521
11245	.1792	2.1453
12240	.191	1.8612
13225	.2015	1.6350
14220	.2117	1.4385
15225	.2213	1.2719
16225	.2297	1.1325
16230	.2298	1.1314
221	.282	28.661
410	.1775	28.163
598	.133	27.062

W1 88°K		
B gauss	$-R_H$ (cm^3/C)	σ $(\Omega\text{-cm})^{-1} \times 10^{-3}$
786	.1055	26.044
974	.0837	25.036
1163	.0707	23.867
1352	.061	22.432
1537	.0536	21.350
1541	.0535	21.252
1731	.0482	20.274
1920	.0442	19.004
2110	.0416	17.948
2298	.0403	16.887
2445	.0402	15.838
2680	.0412	14.913
2682	.0412	14.870
2908	.0425	14.0495
3059	.0437	13.261
3251	.0452	12.445
3421	.0468	11.766
3632	.0492	11.094

W1 88°K		
B gauss	$-R_H$ (cm^3/C)	σ $(\Omega\text{-cm})^{-1} \times 10^{-3}$
3832	.0517	10.494
4208	.0562	9.377
4780	.0632	7.967

W1 77°K		
B gauss	$-R_H$ (cm^3/C)	σ $(\Omega\text{-cm})^{-1} \times 10^{-3}$
-	-	31.020
206	-0.0156	30.328
278	0.02546	30.043
370	0.06087	29.516
463	0.06532	28.947
695	0.06342	27.311
926	0.05865	25.471
1158	0.0469	23.627
1391	0.03807	21.748
1624	0.03344	19.9896
1857	0.03289	18.422
2092	0.02888	16.948
2324	0.03295	15.570
2558	0.03446	14.331
2790	0.03852	13.367
3022	0.04344	12.178
3260	0.04737	11.244
3730	0.06193	9.6309
4200	0.07155	8.3080
4670	0.08833	7.2106
5615	0.10796	5.5612
7515	0.1517	3.5422

W1 77°K		
B gauss	$-R_H$ (cm^3/C)	σ $(\Omega\text{-cm})^{-1} \times 10^{-3}$
9435	0.1891	2.4349
11370	0.2238	1.7732
13320	0.25112	1.3486
15290	0.27381	1.0613
16790	0.28802	0.9030
610	-	28.0097
1551	-	20.986
2498	0.03	14.714
3446	0.0502	10.477
4400	0.0737	7.758
5355	0.0975	5.8986
6315	0.1233	4.601
8250	0.1697	3.0116
9225	0.189	2.5141
10200	0.207	2.114
11185	0.223	1.8041
13160	0.252	1.3588
14150	0.2648	1.1975
15150	0.277	1.0622
7300	0.1485	3.6675
12140	0.2377	1.5634
16180	0.289	0.94761

W1 63°K		
B gauss	$-R_H$ (cm^3/C)	σ $(\Omega\text{-cm})^{-1} \times 10^{-3}$
-	-	33.100
204	0.2495	32.222
372	0.2975	30.947
699	0.1703	27.761
1400	0.09358	20.685
2808	0.0834	11.335
3750	0.1082	7.9227
9520	0.2772	1.8549
16885	0.4128	0.6951
250	0.254	31.88
400	0.219	30.85
500	0.1945	30.0
600	0.1718	28.88
700	0.154	27.5
800	0.140	26.24
900	0.1278	25.0
1000	0.1189	23.75
1100	0.111	22.73
1200	0.104	21.8

W1 63°K		
B gauss	$-R_H$ (cm^3/C)	σ $(\Omega\text{-cm})^{-1} \times 10^{-3}$
1300	0.0972	20.86
1400	0.0905	20.02
1500	0.0855	19.28
1600	0.0808	18.51
1700	0.0768	17.8
1800	0.0748	17.1
1900	0.074	16.4
2000	0.074	15.74
2100	0.0744	15.13
2200	0.0753	14.55
2300	0.0759	14.0
2400	0.0772	13.48
2500	0.0788	12.96
2600	0.0803	12.44
2700	0.082	11.97
2800	0.0838	11.5
2900	0.0856	11.04
3000	0.0875	10.6
4000	0.1262	7.25

W1 63°K		
B gauss	$-R_H$ (cm^3/C)	σ $(\Omega\text{-cm})^{-1} \times 10^{-3}$
5000	0.1517	5.095
6000	0.1839	3.94
7000	0.2128	3.10
8000	0.239	2.44
9000	0.2643	2.28
10000	0.2879	1.685
11000	0.3098	1.422

W1 63°K		
B gauss	$-R_H$ (cm^3/C)	σ $(\Omega\text{-cm})^{-1} \times 10^{-3}$
12000	0.3304	1.23
13000	0.35	1.075
14000	0.368	0.94
15000	0.3852	0.84
16000	0.4008	0.755
17000	0.415	0.698
3500	0.1002	8.75

W1 15°K		
B gauss	$-R_H$ (cm^3/C)	σ $(\Omega\text{-cm})^{-1} \times 10^{-3}$
220	2.75	144.46
350	1.8	104.0
400	1.61	83.0
500	1.36	67.0
600	1.19	48.0
700	1.05	38.0
800	0.94	32.0
900	0.86	27.0
1000	0.79	23.2
1100	0.74	20.0
1200	0.70	17.4
1300	0.665	15.4
1400	0.64	14.0
1500	0.6181	12.8
1600	0.62	11.7
1700	0.623	10.7
1800	0.626	9.9
1900	0.629	9.1

W1 15°K		
B gauss	$-R_H$ (cm^3/C)	σ $(\Omega\text{-cm})^{-1} \times 10^{-3}$
2000	0.632	8.45
2100	0.636	7.8
2200	0.640	7.28
2300	0.645	6.76
2400	0.650	6.26
2500	0.656	5.82
2600	0.662	5.44
2700	0.670	5.12
2800	0.677	4.84
2900	0.685	4.58
3000	0.694	4.32
3500	0.740	3.42
4000	0.789	2.78
4500	0.8335	2.27
5000	0.879	1.92
5500	0.925	1.64
6000	0.970	1.44
6500	1.0115	1.27

W1 15°K		
B gauss	$-R_H$ (cm^3/C)	σ $(\Omega\text{-cm})^{-1} \times 10^{-3}$
7000	1.053	1.14
7500	1.08	1.052
8000	1.113	0.944
8500	1.142	0.860
9000	1.168	0.794
9500	1.1895	0.733
10000	1.208	0.682
10500	1.224	0.638
11000	1.239	0.601
11500	1.2515	0.568

W1 15°K		
B gauss	$-R_H$ (cm^3/C)	σ $(\Omega\text{-cm})^{-1} \times 10^{-3}$
12000	1.264	0.538
12500	1.275	0.510
13000	1.285	0.485
13500	1.295	0.467
14000	1.3055	0.438
14500	1.315	0.417
15000	1.323	0.399
15500	1.331	0.382
16000	1.34	0.366
16500	1.349	0.352
17000	1.357	0.340

W1 4.5°K		
B gauss	$-R_H$ (cm^3/C)	σ $(\Omega\text{-cm})^{-1}\times10^{-3}$
200	0.882	64.4
300	0.81	51.2
400	0.778	40.9
500	0.754	32.0
600	0.733	26.0
700	0.715	21.8
800	0.699	19.56
900	0.683	17.5
1000	0.67	16.0
1100	0.66	14.6
1200	0.651	13.43
1300	0.644	12.4
1400	0.6415	11.38
1500	0.643	10.44
1600	0.65	9.8
1700	0.658	8.83
1800	0.667	8.15
1900	0.6765	7.5
2000	0.6865	7.0

W1 4.5°K		
B gauss	$-R_H$ (cm^3/C)	σ $(\Omega\text{-cm})^{-1}\times10^{-3}$
2100	0.697	6.58
2200	0.702	5.88
2300	0.717	5.4
2400	0.728	5.0
2500	0.739	4.70
2600	0.751	4.45
2700	0.765	4.22
2800	0.778	4.01
2900	0.792	3.83
3000	0.806	3.661
3100	0.820	3.518
3200	0.834	3.372
3300	0.849	3.24
3400	0.864	3.115
3500	0.878	2.99
3600	0.892	2.875
3700	0.905	2.76
3800	0.918	2.648
3900	0.935	2.542

W1 4.5°K		
B gauss	$-R_H$ (cm^3/C)	σ $(\Omega\text{-cm})^{-1} \times 10^{-3}$
4000	0.948	2.442
4100	0.912	2.35
4200	0.925	2,26
4300	0.936	2.18
4400	0.996	2.103
4500	1.005	2.035
4600	1.014	1.962

W1 4.5°K		
B gauss	$-R_H$ (cm^3/C)	σ $(\Omega\text{-cm})^{-1} \times 10^{-3}$
4700	1.023	1.90
4800	1.032	1.84
4900	1.043	1.78
5000	1.053	1.725
5100	1.069	1.68
5200	1.081	1.63
5300	1.095	1.583

W2 291°K		
B gauss	$-R_H$ (cm^3/C)	σ $(\Omega\text{-cm})^{-1} \times 10^{-3}$
0	-	25.006
100	-	-
200	- 0.2472	24.967
300	-	-
400	- 0.0978	24.928
500	-	-
600	- 0.0482	24.791
700	-	-
800	- 0.0218	24.791
900	-	-
1000	- 0.00715	24.637
1100	-	-
1200	+ 0.00472	24.485
1300	-	-
1400	+ 0.01229	24.316
1500	-	-
1600	0.01796	24.168
1700	-	-
1800	0.02095	23.931
1900	-	-

W2 291°K		
B gauss	$-R_H$ (cm^3/C)	σ $(\Omega\text{-cm})^{-1} \times 10^{-3}$
2000	0.02526	23.628
2100	-	-
2200	0.02879	23.249
2300	-	-
2400	0.03176	23.060
2500	-	-
2600	0.03373	22.746
2700	-	-
2800	0.03453	22.440
2900	-	-
3000	0.03564	22.081
3100	-	-
3200	0.03582	21.733
3300	-	-
3400	0.03597	21.483
3500	-	-
3600	0.03682	21.153
3700	-	-
3800	0.03556	20.724
3900	-	-

W2 291°K		
B gauss	$-R_H$ (cm^3/C)	σ $(\Omega\text{-cm})^{-1} \times 10^{-3}$
4000	0.03634	20.339
4500	0.03686	19.597
5000	0.0383	18.773
5500	0.03948	17.635
6000	0.04046	16.965
6500	0.04149	16.202
7000	0.04274	15.445
7500	0.04348	14.693
8000	0.04445	13.962
8500	0.04530	13.312
9000	0.04649	12.699
9500	0.04741	12.107

W2 291°K		
B gauss	$-R_H$ (cm^3/C)	σ $(\Omega\text{-cm})^{-1} \times 10^{-3}$
10000	0.04863	11.501
10500	0.04936	10.983
11000	0.05061	10.482
11500	0.05165	9.987
12000	0.05270	9.582
12500	0.05377	9.119
13000	0.05475	8.752
13500	0.05587	8.373
14000	0.05691	8.011
14500	0.05783	7.67
15000	0.05909	7.314
15500	0.05989	7.029
16000	0.06084	6.741
16500	0.06210	6.464
17000	0.06290	6.205

W2 77°K		
B gauss	$-R_H$ (cm^3/C)	σ $(\Omega\text{-cm})^{-1} \times 10^{-3}$
0		35.547
100	-0.264	34.998
200	-0.087	34.205
300	-0.0283	33.840
400	-0.00422	33.098
500	+0.00648	32.257
600	0.01321	31.363
700	0.01483	30.314
800	0.01451	29.305
900	0.01318	28.489
1000	0.00965	27.524
1100	0.00475	26.468
1200	0.00190	25.286
1300	0.001375	24.205
1400	0.000573	23.332
1500	0.000687	22.393
1600	0.001269	21.410
1700	0.002206	20.510
1800	0.003448	19.658

W2 77°K		
B gauss	$-R_H$ (cm^3/C)	σ $(\Omega\text{-cm})^{-1} \times 10^{-3}$
1900	0.004559	18.885
2000	0.005805	18.160
2150	0.007167	17.422
2200	0.008853	16.645
2300	0.01071	16.079
2400	0.01262	15.422
2500	0.01447	14.789
2600	0.01675	14.232
2700	0.01904	13.650
2800	0.02152	13.076
2900	0.02391	12.528
3000	0.02640	12.093
3100	0.02909	11.670
3200	0.03202	11.177
3300	0.03553	10.778
3400	0.03881	10.403
3500	0.04192	10.021
3600	0.04580	9.688
3700	0.04961	9.345

W2 77°K		
B gauss	$-R_H$ (cm^3/C)	σ $(\Omega\text{-cm})^{-1} \times 10^{-3}$
3800	0.05322	9.036
3900	0.05615	8.723
4000	0.05940	8.444
4500	0.07780	–
7000	0.1623	3.672
7500	0.1788	3.258
8000	0.1913	2.907
8500	0.2052	2.642
9000	0.2192	2.391
9500	0.2301	2.184
10000	0.2435	2.010
10500	0.2538	1.853
11000	0.2651	1.711
11500	0.2783	1.578
12000	0.2869	1.475
12500	0.2941	1.391
13000	0.3051	1.299
13500	0.3147	1.220

W2 77°K		
B gauss	$-R_H$ (cm^3/C)	σ $(\Omega\text{-cm})^{-1} \times 10^{-3}$
14000	0.3264	1.139
14500	0.3362	1.074
15000	0.3449	1.009
15500	0.3545	0.9557
16000	0.3388	0.9032
16500	0.3736	0.8647
17000	0.3820	0.8118

W2 63°K		
B gauss	$-R_H$ (cm^3/C)	σ $(\Omega\text{-cm})^{-1} \times 10^{-3}$
4000	0.0823	7.028
4500	0.1102	5.776
5000	0.1255	4.931
5500	0.1447	4.280
6000	0.1673	3.698
6500	0.1855	3.205
7000	0.2029	2.8618
7500	0.2191	2.551
8000	0.2339	2.293
8500	0.2506	2.077
9000	0.2658	1.891
9500	0.2772	1.728
10000	0.2931	1.587
10500	0.3050	1.462
11000	0.3174	1.349
11500	0.3288	1.258
12000	0.3450	1.164
12500	0.3565	1.088
13000	0.3704	1.017

W2 63°K		
B gauss	$-R_H$ (cm^3/C)	σ $(\Omega\text{-cm})^{-1} \times 10^{-3}$
13500	0.3826	0.954
14000	0.3952	0.8982
14500	0.4076	0.8462
15000	0.4191	0.7987
15500	0.4321	0.7546
16000	0.4427	0.7150
16500	0.4546	0.6793
0		37.348
100	0.01214	37.086
200	0.06274	36.657
300	0.07578	35.991
400	0.07943	34.692
500	0.07933	33.447
600	0.06802	32.224
700	0.0502	30.785
800	0.03685	29.441
900	0.02961	28.085
1000	0.02611	26.735
1100	0.02422	25.633

W2 63°K		
B gauss	$-R_H$ (cm^3/C)	σ $(\Omega\text{-cm})^{-1} \times 10^{-3}$
1200	0.02412	24.113
1300	0.02486	22.944
1400	0.02510	21.959
1500	0.02532	20.833
1600	0.02551	19.695
1700	0.02567	18.762
1800	0.02519	17.814
1900	0.02507	16.974
2000	0.02607	16.169
2100	0.02673	15.355
2200	0.02809	14.626
2300	0.02883	13.993
2400	0.03069	13.351
2500	0.03241	12.729
2600	0.03464	12.158
2700	0.03650	11.619
2800	0.03925	11.102
2900	0.04238	10.623

W2 63°K		
B gauss	$-R_H$ (cm^3/C)	σ $(\Omega\text{-cm})^{-1} \times 10^{-3}$
3000	0.04567	10.182
3100	0.04968	9.744
3200	0.05256	9.342
3300	0.05438	8.980
3400	0.05978	8.633
3500	0.06405	8.272
3600	0.06793	7.971
3700	0.07222	7.672
3800	0.07627	7.395
3900	0.08069	7.141
4000	0.08660	6.887
4500	0.1084	5.762

W2 47.5°K		
B gauss	$-R_H$ (cm^3/C)	σ $(\Omega\text{-cm})^{-1} \times 10^{-3}$
0	-	45.168
100	0.1727	43.856
200	0.05768	42.053
300	0.1172	40.341
400	0.1262	37.838
500	0.1198	35.631
600	0.1078	33.307
700	0.09733	31.55
800	0.09276	29.414
900	0.08920	27.814
1000	0.08567	25.695
1100	0.08218	24.26
1200	0.07870	22.633
1300	0.07524	21.069
1400	0.07228	19.707
1500	0.07286	18.510
1600	0.07505	17.299
1700	0.08056	16.277
1800	0.08507	15.259

W2 47.5°K		
B gauss	$-R_H$ (cm^3/C)	σ $(\Omega\text{-cm})^{-1} \times 10^{-3}$
1900	0.09054	14.322
2000	0.09613	13.499
2100	0.1028	12.709
2200	0.1095	12.006
2300	0.1144	11.292
2400	0.1209	10.734
2500	0.1255	10.212
2600	0.1279	9.617
2700	0.1312	9.154
2800	0.1344	8.659
2900	0.1400	8.281
3000	0.1466	7.884
3100	0.1530	7.514
3200	0.1612	7.169
3300	0.1674	6.816
3400	0.1736	6.523
3500	0.1736	6.2615
3600	0.1868	6.0019
3700	0.1914	5.7474

W2 47.5°K		
B gauss	$-R_H$ (cm^3/C)	σ $(\Omega\text{-cm})^{-1} \times 10^{-3}$
3800	0.1981	5.5366
3900	0.2058	5.2971
4000	0.2140	5.1011
4500	0.2414	4.2408
5000	0.2941	3.596
5500	0.3161	3.130
6000	0.3424	2.679
6500	0.3646	2.330
7000	0.6714	2.071
7500	0.4107	1.856
8000	0.4441	1.670
8500	0.4644	1.496
9000	0.4913	1.375
9500	0.5119	1.257
10000	0.5368	1.1497
10500	0.5623	1.0637

W2 47.5°K		
B gauss	$-R_H$ (cm^3/C)	σ $(\Omega\text{-cm})^{-1} \times 10^{-3}$
11000	0.5856	0.98534
11500	0.6095	0.91642
12000	0.6275	0.8563
12500	0.6492	0.8029
13000	0.6704	0.7535
13500	0.6936	0.7060
14000	0.7093	0.6689
14500	0.7295	0.6323
15000	0.7493	0.6008
15500	0.7721	0.5696
16000	0.7872	0.5449
16500	0.8034	0.5185
17000	0.8218	0.4942
17500	0.8342	

W2 4.5°K		
B gauss	$-R_H$ (cm^3/C)	σ $(\Omega\text{-cm})^{-1} \times 10^{-3}$
1500	0.9566	9.223
2000	0.9060	6.397
2500	1.0448	4.564
3000	1.1374	3.315
3500	1.2708	2.744
4000	1.3708	2.2536
4500	1.4696	1.8885
5000	1.5583	1.6244
5500	1.6387	1.4289
6000	1.7067	1.2755
6500	1.7706	1.159
7000	1.805	1.0427
7500	1.8700	0.9508
8000	1.8973	0.8689
8500	1.9301	0.8151
9000	1.9586	0.7580
9500	1.9840	0.7117
10000	2.0096	0.6706
10500	2.0354	0.6315

W2 4.5°K		
B gauss	$-R_H$ (cm^3/C)	σ $(\Omega\text{-cm})^{-1} \times 10^{-3}$
11000	2.0477	0.5978
11500	2.0707	0.5675
0	-	100.342
100	3.609	94.651
200	1.99	77.907
300	1.475	62.541
400	1.2278	49.236
500	1.0497	39.685
600	0.9737	33.272
700	0.8982	27.937
800	0.8517	23.592
900	0.8230	20.171
1000	0.7967	17.355
1100	0.7819	15.237
1200	0.7662	13.47
1300	0.7701	11.983
1400	0.7768	10.796
1500	0.7821	9.715
1600	0.7960	8.827

W2 4.5°K		
B gauss	$-R_H$ (cm^3/C)	σ $(\Omega\text{-cm})^{-1} \times 10^{-3}$
1700	0.8083	8.015
1800	0.8211	7.403
1900	0.8447	6.783
2000	0.8658	6.3051
2100	0.8921	5.899
2200	0.9156	5.473
2300	0.9406	5.104
2400	0.9728	4.8086
2500	0.9906	4.486
2600	1.0155	4.2148
2700	1.0441	3.9839
2800	1.0733	3.7766
2900	1.1005	3.5715
3000	1.1234	3.3876

W2 4.5°K		
B gauss	$-R_H$ (cm^3/C)	σ $(\Omega\text{-cm})^{-1} \times 10^{-3}$
3100	1.152	3.2243
3200	1.1837	3.0875
3300	1.2088	2.9414
3400	1.2323	2.8085
3500	1.2609	2.6871
3600	1.2797	2.5758
3700	1.3036	2.4695
3800	1.3242	2.3787
3900	1.3475	2.2927
4000	1.3659	2.2020
4500	1.4691	1.8630

W2 1°K		
B gauss	$-R_H$ (cm^3/C)	σ $(\Omega\text{-cm})^{-1} \times 10^{-3}$
3500	1.2172	2.602
4000	1.3295	2.1688
4500	1.4489	1.8392
5000	1.554	1.5966
5500	1.6485	1.4018
6000	1.728	1.2314
6500	1.780	1.1212
0	-	113.469
100	-	82.789
200	1.845	67.464
300	1.266	52.015
400	1.056	44.409
500	0.9714	37.164
600	0.9860	30.875
700	0.9502	26.579
800	0.9242	22.205
900	0.8920	19.276
1000	0.8669	17.020
1100	0.8261	14.572

W2 1°K		
B gauss	$-R_H$ (cm^3/C)	σ $(\Omega\text{-cm})^{-1} \times 10^{-3}$
1200	0.8191	13.011
1300	0.8132	11.752
1400	0.8307	10.591
1500	0.8459	9.4398
1600	0.8559	8.5930
1700	0.8833	7.9211
1800	0.9047	7.2575
1900	0.9238	6.6488
2000	0.9411	6.1966
2100	0.9746	5.783
2200	0.9999	5.398
2300	1.0254	5.0259
2400	1.0532	4.6712
2500	1.0831	4.4322
2600	1.1107	4.1738
2700	1.1206	3.9262
2800	1.1447	3.7436
2900	1.1636	3.54444
3000	1.1848	3.3426

W2 1°K		
B gauss	$-R_H$ (cm^3/C)	σ $(\Omega\text{-cm})^{-1} \times 10^{-3}$
3100	1.2149	3.1765
3200	1.2398	3.040
3300	1.2535	2.8957
3400	1.2788	2.7596
3500	1.3027	2.6490
3600	1.3254	2.5407
3700	1.3410	2.4391
3800	1.3655	2.3540
3900	1.3943	2.2714
4000	1.3966	2.1974
4500	1.4954	1.8586

W3 293°K		
B gauss	$-R_H$ (cm^3/C)	σ $(\Omega\text{-cm})^{-1} \times 10^{-3}$
200	0.0333	27.2668
300	0.0345	27.2223
400	0.0320	27.1780
500	0.0354	27.1338
600	0.0377	27.0897
700	0.0428	27.0897
800	0.0436	27.0020
900	0.0415	26.9149
1000	0.0423	26.8284
1200	0.0454	26.6569
1500	0.0495	26.3205
2000	0.0506	25.6726
2500	0.0523	24.8320
3000	0.0534	24.0102
3500	0.0549	23.0484
4000	0.0554	22.1607
4500	0.0574	21.2302
5000	0.0590	20.2511
5500	0.0613	19.2911

W3 293°K		
B gauss	$-R_H$ (cm^3/C)	σ $(\Omega\text{-cm})^{-1} \times 10^{-3}$
6000	0.0635	18.3775
6500	0.0662	17.4547
7000	0.0685	16.6867
7500	0.0705	15.8618
8000	0.0731	15.0601
8500	0.0763	14.3109
9000	0.0789	13.6105
9500	0.0810	12.9353
10000	0.0835	12.3056
10500	0.0863	11.6852
11000	0.0887	11.1540
11500	0.0916	10.6418
12000	0.0940	10.1870
12500	0.0963	9.6788
13000	0.0990	9.2291
13500	0.1015	8.7915
14000	0.1040	8.4189
14500	0.1062	8.0610
15000	0.1081	7.7323

W3 293°K		
B gauss	$-R_H$ (cm^3/C)	σ $(\Omega\text{-cm})^{-1} \times 10^{-3}$
15500	0.1114	7.3767
16000	0.1139	7.0525
16500	0.1160	6.7555
17000	0.1183	6.4775

W3 77.5°K		
B gauss	$-R_H$ (cm^3/C)	σ $(\Omega\text{-cm})^{-1} \times 10^{-3}$
4500	0.2437	6.6547
5000	0.2953	5.6913
5500	0.3513	4.8812
6000	0.4000	4.2593
6500	0.4452	3.7048
7000	0.4929	3.2383
7500	0.5309	2.8886
8000	0.5879	2.6020
8500	0.6322	2.3422
9000	0.6786	2.1330
9500	0.7228	1.9299
10000	0.7702	1.7621
10500	0.8058	1.6172
11000	0.8566	1.4910
11500	0.8964	1.3802
12000	0.9350	1.2774
12500	0.9725	1.1930
13000	1.0168	1.1080
13500	1.0560	1.0343

W3 77.5°K		
B gauss	$-R_H$ (cm^3/C)	σ $(\Omega\text{-cm})^{-1} \times 10^{-3}$
14000	1.0979	0.9698
14500	1.1351	0.9116
15000	1.1731	0.8557
15500	1.2088	0.8071
16000	1.2453	0.7612
16500	1.2804	0.7202
17000	1.3135	0.6834
200	-0.0667	43.8892
300	-0.0355	42.8163
400	-0.0233	41.7945
500	-0.0267	40.3502
600	-0.0222	38.8941
700	-0.0210	37.3394
800	-0.0200	35.8124
900	-0.0148	34.2373
1000	-0.0066	32.4907
1100	-0.0060	30.9136
1200	-0.0078	29.6072
1300	-0.0051	28.0653

W3 77.4°K		
B gauss	$-R_H$ (cm^3/C)	σ $(\Omega\text{-cm})^{-1}x10^{-3}$
4500	0.2030	6.6521
5000	0.2478	5.6993
5500	0.2940	4.8634
6000	0.3395	4.2114
6500	0.3812	3.6792
7000	0.4290	3.2487
7500	0.4732	2.9013
8000	0.5198	2.5869
8500	0.5608	2.3340
9000	0.5973	2.1111
9500	0.6322	1.9086
10000	0.6783	1.7569
10500	0.7120	1.6100
11000	0.7512	1.4766
11500	0.7907	1.3667
12000	0.8242	1.2680
12500	0.8618	1.1756
13000	0.8981	1.1018
13500	0.9333	1.0278
14000	0.9690	0.9600

W3 77.4°K		
B gauss	$-R_H$ (cm^3/C)	σ $(\Omega\text{-cm})^{-1}x10^{-3}$
14500	1.0022	0.9006
15000	1.0332	0.8470
15500	1.0676	0.8004
16000	1.0940	0.7568
16500	1.1276	0.7142
17000	1.1599	0.6792
200	-0.3171	44.0033
300	-0.1989	42.6506
400	-0.1515	41.7179
500	-0.1240	40.3929
600	-0.1073	38.7519
700	-0.0940	37.0581
800	-0.0852	35.4238
900	-0.0809	34.0791
1000	-0.0747	32.4143
1100	-0.0769	31.2848
1200	-0.0728	29.5866
1300	-0.0676	28.1668
1400	-0.0621	26.8299
1500	-0.0564	25.3587

W3 77.4°K		
B gauss	$-R_H$ (cm^3/C)	σ $(\Omega\text{-cm})^{-1} \times 10^{-3}$
1600	-0.0496	24.1547
1700	-0.0423	22.9212
1800	-0.0365	21.7455
1900	-0.0302	20.5730
2000	-0.0235	19.7222
2100	-0.0159	18.6611
2200	-0.0085	17.7910
2300	-0.0008	16.9230
2400	0.0065	16.2042
2500	0.0145	15.4184
2600	0.0228	14.6489
2700	0.0293	14.0037
2800	0.0368	13.4129
2900	0.0451	12.8052
3000	0.0538	12.2403
3100	0.0623	11.7593
32000	0.0695	11.2729
3300	0.0775	10.7641
3400	0.0875	10.3692
3500	0.0990	9.9241

W3 63.2°K		
B gauss	$-R_H$ (cm^3/C)	σ $(\Omega\text{-cm})^{-1} \times 10^{-3}$
3500	0.2996	7.5794
4000	0.3592	6.0285
4500	0.4291	4.9803
5000	0.5062	4.1739
5500	0.5757	3.5429
6000	0.6513	3.0413
6500	0.7153	2.6641
7000	0.7852	2.3274
7500	0.8505	2.0745
8000	0.9165	1.8379
8500	0.9872	1.6657
9000	1.0461	1.5052
9500	1.1025	1.3657
10000	1.1744	1.2483
10500	1.2328	1.1393
11000	1.2955	1.0619
11500	1.3589	0.9737
12000	1.4214	0.9021
12500	1.4761	0.8417
13000	1.5279	0.7841

W3 63.2°K		
B gauss	$-R_H$ (cm^3/C)	σ $(\Omega\text{-cm})^{-1} \times 10^{-3}$
13500	1.5838	0.7318
14000	1.6381	0.6842
14500	1.7009	0.6424
15000	1.7501	0.6062
15500	1.7962	0.5694
16000	1.8525	0.5447
16500	1.9055	0.5153
200	-0.1162	48.4404
300	0.0239	46.0864
400	0.0433	44.1781
500	0.0549	42.2118
600	0.0345	39.8470
700	0.0247	37.7332
800	0.0216	35.5340
900	0.0230	33.5770
1000	0.0241	31.5887
1100	0.0249	29.4117
1200	0.0229	27.6940
1300	0.0263	26.0064
1400	0.0341	24.3727

W3 63.2°K		
B gauss	$-R_H$ (cm^3/C)	σ $(\Omega\text{-cm})^{-1} \times 10^{-3}$
1500	0.0386	22.8095
1600	0.0488	21.3811
1700	0.0559	19.9797
1800	0.0659	18.9590
1900	0.0767	17.7746
2000	0.0864	16.7294
2100	0.0967	15.8591
2200	0.1077	14.9691
2300	0.1162	14.0801
2400	0.1269	13.2908
2500	0.1353	12.5483
2600	0.1496	11.8514
2700	0.1591	11.2574
2800	0.1751	10.7471

W3 63.2°K		
B gauss	$-R_H$ (cm^3/C)	σ $(\Omega\text{-cm})^{-1} \times 10^{-3}$
2900	0.1900	10.2073
3000	0.2051	9.7192
3100	0.2181	9.2354
3200	0.2345	8.7976
3300	0.2489	8.4159
3400	0.2645	8.0205
3500	0.2752	7.6743
3600	0.2892	7.3568
3700	0.3033	7.0412
3800	0.3184	6.7623
3900	0.3336	6.4800
4000	0.3473	6.2293
4500	0.4190	5.1104
5000	0.4988	4.2887

W3 54°K		
B gauss	$-R_H$ (cm^3/C)	σ $(\Omega\text{-cm})^{-1} \times 10^{-3}$
3500	0.6920	5.4802
4000	0.8193	4.2490
4500	0.9514	3.4515
5000	1.0645	2.8558
5500	1.1942	2.4002
6000	1.3209	2.0571
6500	1.4195	1.7901
7000	1.5571	1.5620
7500	1.6764	1.3913
8000	1.7901	1.2448
8500	1.8948	1.1111
9000	1.9961	1.0063
9500	2.1181	0.9222
10000	2.2055	0.8489
10500	2.3130	0.7699
11000	2.4107	0.7142
11500	2.5225	0.6581
12000	2.5971	0.6119
12500	2.6866	0.5747

W3 54°K		
B gauss	$-R_H$ (cm^3/C)	σ $(\Omega\text{-cm})^{-1} \times 10^{-3}$
13000	2.7663	0.5374
200	0.0827	55.1862
300	0.1379	52.4828
400	0.1656	49.2650
500	0.1738	45.1158
600	0.1794	41.6112
700	0.2011	38.1535
800	0.1863	34.8444
900	0.1886	31.4363
1000	0.1904	28.8929
1100	0.1994	26.0796
1200	0.2001	23.9425
1300	0.2038	22.1292
1400	0.1981	20.3112
1500	0.2235	18.7146
1600	0.2303	17.1654
1700	0.2508	15.9316
1800	0.2668	14.8290
1900	0.2920	13.7212

W3 54°K		
B gauss	$-R_H$ (cm^3/C)	σ $(\Omega\text{-cm})^{-1} \times 10^{-3}$
2000	0.3125	12.7927
2100	0.3391	11.8933
2200	0.3594	11.0738
2300	0.3762	10.3934
2400	0.3933	9.7325
2500	0.4189	9.0988
2600	0.4331	8.6228
2700	0.4600	8.1319
2800	0.4849	7.6487
2900	0.5125	7.2349
3000	0.5382	6.8204
3100	0.5609	6.4508
3200	0.5873	6.1899
3300	0.6072	5.8732
3400	0.6295	5.5776
3500	0.6588	5.3104
3600	0.6831	5.0756
3700	0.7093	4.8314
3800	0.7299	4.6363
3900	0.7515	4.4317
4000	0.7700	4.2670
4500	0.8822	3.4737

W3 4.2°K		
B gauss	$-R_H$ (cm^3/C)	σ $(\Omega\text{-cm})^{-1} \times 10^{-3}$
3500	3.9411	1.7602
4000	4.3071	1.4627
4500	4.5667	1.2271
5000	4.7407	1.0569
5500	4.9854	0.9471
6000	5.1142	0.8424
200	0.6590	126.8895
300	0.5364	78.8938
400	0.5478	52.0479
500	0.6129	39.5022
600	0.6684	28.2968
700	0.7081	22.4756
800	0.7833	18.3428
900	0.8418	15.2873
1000	0.9177	13.0300
1100	0.9798	11.0794
1200	1.0195	9.5965
1300	1.1314	8.4950
1400	1.2065	7.4959

W3 4.2°K		
B gauss	$-R_H$ (cm^3/C)	$(\Omega\text{-cm})^{-1} \times 10^{-3}$
1500	1.2910	6.6680
1600	1.3741	6.0206
1700	1.4473	5.4358
1800	1.5044	4.9760
1900	1.5975	4.5515
2000	1.6632	4.1861
2100	1.7399	3.8948
2200	1.8196	3.6070
2300	1.8861	3.3441
2400	1.9469	3.1255
2500	2.0146	2.9262
2600	2.1107	2.7640
2700	2.1672	2.6011
2800	2.2406	2.4563
2900	2.3089	2.3315
3000	2.3823	2.2017
3100	2.4322	2.0971
3200	2.4926	2.0019
3300	2.5494	1.9055

W3 4.2°K		
B gauss	$-R_H$ (cm^3/C)	σ $(\Omega\text{-cm})^{-1} \times 10^{-3}$
3400	2.6028	1.8295
3500	2.6657	1.7540
3600	2.7170	1.6820
3700	2.7694	1.6134
3800	2.8191	1.5501
3900	2.8625	1.4956
4000	2.9146	1.4429

W3 1.5°K		
B gauss	$-R_H$ (cm^3/C)	σ $(\Omega\text{-cm})^{-1} \times 10^{-3}$
1500	1.9933	6.3412
2000	2.4426	3.9935
2500	2.8754	2.8528
3000	3.2987	2.1655
3500	3.6207	1.7229
4000	3.9132	1.4305
4500	4.1066	1.2119
200	-1.9790	101.2501
300	-1.1109	67.0239
400	-0.5875	47.1155
500	-0.3270	33.2772
600	-0.1236	26.5845
700	0.1238	21.5322
800	0.2870	17.5595
900	0.4338	14.7326
1000	0.6049	12.5557
1100	0.7773	10.7418
1200	0.8641	9.4982

W3 1.5°K		
B gauss	$-R_H$ (cm^3/C)	σ $(\Omega\text{-cm})^{-1} \times 10^{-3}$
1300	1.0288	8.3338
1400	1.1404	7.3097
1500	1.2610	6.5817
1600	1.3943	5.9408
1700	1.5015	5.3891
1800	1.6266	4.9007
1900	1.7385	4.5277
2000	1.8347	4.1487
2100	1.9601	3.8407
2200	2.0537	3.5752
2300	2.1742	3.3069
2400	2.2548	3.0920
2500	2.3433	2.9069
2600	2.4594	2.7301
2700	2.5635	2.5820
2800	2.6347	2.4391
2900	2.7164	2.3338
3000	2.8284	2.1818

W3 1.5°K		
B gauss	$-R_H$ (cm^3/C	σ $(\Omega\text{-cm})^{-1} \times 10^{-3}$
3100	2.8985	2.0862
3200	2.9755	1.9902
3300	3.0478	1.9012
3400	3.1368	1.8225

Derived Conductivity

$\times 10^{-14}$

W1

300°K

77°K

field	σ^n_{xx}	σ^P_{xx}	σ_{xx}	field	σ^n_{xy}	σ^P_{xy}	σ_{xy}
0.	52.4730	153.5929	205.9859	0.	-0.	0.	-0.
100.0	52.4297	153.5695	205.8992	100.0	-1.3358	0.9566	-0.3791
200.0	52.2259	153.5168	205.7428	200.0	-2.5727	1.8921	-0.6806
300.0	52.0928	154.4518	206.5446	300.0	-3.8042	2.8147	-0.9895
400.0	51.9411	153.3748	205.3159	400.0	-5.0147	3.7345	-1.2802
500.0	51.7698	154.2790	206.0488	500.0	-6.2126	4.6536	-1.5590
600.0	51.5765	153.1642	204.7407	600.0	-7.4013	5.5710	-1.8304
700.0	51.3591	153.0288	204.3879	700.0	-8.5814	6.4850	-2.0964
800.0	51.1165	152.8727	203.9892	800.0	-9.7571	7.3960	-2.3581
900.0	50.8484	152.6963	203.5446	900.0	-10.9127	8.2969	-2.6157
1000.0	50.5565	152.5000	203.0544	1000.0	-12.0619	9.1927	-2.8691
1100.0	50.2354	152.2843	202.5197	1100.0	-13.1986	10.0806	-3.1180
1200.0	49.8915	152.0499	201.9414	1200.0	-14.3217	10.9596	-3.3621
1300.0	49.5247	151.7972	201.3205	1300.0	-15.4303	11.8292	-3.6010
1400.0	49.1326	151.5270	200.6596	1400.0	-16.5234	12.6888	-3.8346
1500.0	48.7193	151.2398	199.9592	1500.0	-17.6004	13.5378	-4.0626
1600.0	48.2846	150.9363	199.2210	1600.0	-18.6605	14.3757	-4.2848
1700.0	47.8296	150.6171	198.4467	1700.0	-19.7032	15.2021	-4.5011
1800.0	47.3551	150.2829	197.6380	1800.0	-20.7278	16.0166	-4.7113
1900.0	46.8625	149.9343	196.7968	1900.0	-21.7342	16.8187	-4.9154
2000.0	46.3520	149.5719	195.9240	2000.0	-22.7217	17.6084	-5.1134
2100.0	45.8253	149.1965	195.0218	2100.0	-23.6903	18.3851	-5.3052
2200.0	45.2831	148.8086	194.0917	2200.0	-24.6398	19.1488	-5.4909
2300.0	44.7264	148.4089	193.1352	2300.0	-25.5698	19.8994	-5.6704
2400.0	44.1559	147.9979	192.1539	2400.0	-26.4805	20.6363	-5.8442
2500.0	43.5727	147.5764	191.1491	2500.0	-27.3717	21.3594	-6.0118
2600.0	42.9776	147.1445	190.1225	2600.0	-28.2434	22.0699	-6.1735
2700.0	42.3713	146.7029	189.0752	2700.0	-29.0957	22.7662	-6.3294
2800.0	41.7547	146.2521	188.0088	2800.0	-29.9286	23.4489	-6.4797
2900.0	41.1285	145.7929	186.9244	2900.0	-30.7423	24.1180	-6.6243
3000.0	40.4934	145.3259	185.8234	3000.0	-31.5368	24.7734	-6.7635
3100.0	39.8502	144.8566	184.7068	3100.0	-32.3124	25.4152	-6.8972
3200.0	39.1993	144.3765	183.5758	3200.0	-33.0691	26.0434	-7.0257
3300.0	38.5416	143.8900	182.4316	3300.0	-33.8073	26.6582	-7.1491
3400.0	37.8775	143.3977	181.2752	3400.0	-34.5269	27.2596	-7.2674
3500.0	37.2077	142.8998	180.1076	3500.0	-35.2284	27.8477	-7.3807
3600.0	36.5326	142.3968	178.9294	3600.0	-35.9119	28.4226	-7.4892
3700.0	35.8528	141.8892	177.7420	3700.0	-36.5775	28.9845	-7.5930
3800.0	35.1687	141.3773	176.5460	3800.0	-37.2257	29.5335	-7.6922
3900.0	34.4809	140.8614	175.3424	3900.0	-37.8565	30.0698	-7.7869
4000.0	33.7898	140.3420	174.1318	4000.0	-38.4702	30.5931	-7.8772
4500.0	30.2985	137.7018	167.9003	4500.0	-41.2915	33.0254	-8.2661
5000.0	26.7797	135.0159	161.7956	5000.0	-43.7229	35.1634	-8.5596
5500.0	23.2384	132.3139	155.5523	5500.0	-45.7952	37.0263	-8.7689
6000.0	19.6800	129.6204	149.3004	6000.0	-47.5381	38.6339	-8.9042
6500.0	16.1094	126.9555	143.0649	6500.0	-48.9805	40.0054	-8.9751
7000.0	12.5366	124.3357	137.4023	7000.0	-50.1503	41.1600	-8.9902
7500.0	8.9672	121.7746	131.6118	7500.0	-51.0740	42.1164	-8.9578
8000.0	5.4155	119.2830	125.9985	8000.0	-51.7771	42.8926	-8.8844
8500.0	1.8995	116.8690	120.5685	8500.0	-52.2833	43.5062	-8.7771
9000.0	-1.6244	114.5390	115.1634	9000.0	-52.6152	43.9738	-8.6414
9500.0	-5.1369	112.2970	110.1601	9500.0	-52.7933	44.3111	-8.4822
10000.0	-8.6342	110.1496	105.5154	10000.0	-52.8340	44.5330	-8.3048
10500.0	-12.0852	108.0859	101.0007	10500.0	-52.7635	44.6530	-8.1105
11000.0	-9.6748	106.1180	96.6432	11000.0	-52.5886	44.6837	-7.9049
11500.0	-11.7441	104.2408	92.4966	11500.0	-52.3267	44.6367	-7.6900
12000.0	-13.8988	102.4525	88.5538	12000.0	-51.9934	44.5223	-7.4681
12500.0	-15.9405	100.7508	84.8055	12500.0	-51.5911	44.3499	-7.2411
13000.0	-17.8758	99.1329	81.2567	13000.0	-51.1387	44.1280	-7.0107
13500.0	-19.7082	97.5957	77.8876	13500.0	-50.6422	43.8640	-6.7782
14000.0	-21.4410	96.1359	74.6949	14000.0	-50.1093	43.5646	-6.5447
14500.0	-23.0852	94.7500	71.6648	14500.0	-49.5468	43.2356	-6.3112
15000.0	-24.6391	93.4346	68.7955	15000.0	-48.9606	42.8822	-6.0785
15500.0	-26.1111	92.1866	66.0749	15500.0	-48.3559	42.5089	-5.8470
16000.0	-27.5043	91.0010	63.4967	16000.0	-47.7372	42.1198	-5.6173
16500.0	-28.8216	89.8760	61.0524	16500.0	-47.1082	41.7183	-5.3899
17000.0	-30.0655	88.8079	58.7345	17000.0	-46.4727	41.3073	-5.1649

field	σ^n_{xx}	σ^P_{xx}	σ_{xx}	field	σ^n_{xy}	σ^P_{xy}	σ_{xy}
0.	140.4003	136.5072	276.9076	0.	-0.	0.	-0.
100.0	140.3871	135.4281	275.8151	100.0	-6.3721	7.4202	1.0481
200.0	139.5625	133.3489	272.9119	200.0	-13.2192	13.5633	0.3441
300.0	137.6425	131.1503	268.7928	300.0	-19.8242	18.9328	-0.8914
400.0	134.9645	128.8302	263.7947	400.0	-25.8425	23.9371	-1.9054
500.0	131.8014	126.2848	258.0862	500.0	-31.2308	28.6642	-2.5666
600.0	128.3247	123.4728	251.7975	600.0	-36.0167	33.0887	-2.9280
700.0	124.6514	120.4154	245.0667	700.0	-40.2420	37.1681	-3.0739
800.0	120.8674	117.1612	238.0287	800.0	-43.9519	40.8731	-3.0788
900.0	117.0380	113.7667	230.8047	900.0	-47.1930	44.1941	-2.9989
1000.0	113.2122	110.2882	223.5004	1000.0	-50.0110	47.1377	-2.8733
1100.0	109.4264	106.7745	216.2009	1100.0	-52.4550	49.7223	-2.7267
1200.0	105.7065	103.2652	208.9722	1200.0	-54.5514	51.9726	-2.5788
1300.0	102.0721	99.7912	201.8633	1300.0	-56.3529	53.9165	-2.4364
1400.0	98.5341	96.3755	194.9096	1400.0	-57.8884	55.5826	-2.3064
1500.0	95.1065	93.0347	188.1352	1500.0	-59.1881	56.9985	-2.1896
1600.0	91.7954	89.7806	181.5760	1600.0	-60.2786	58.1899	-2.0887
1700.0	88.5807	86.6208	175.1815	1700.0	-61.1841	59.1805	-2.0021
1800.0	85.4565	83.5601	169.0166	1800.0	-61.9218	59.9916	-1.9302
1900.0	82.4615	80.6011	163.0631	1900.0	-62.5127	60.6425	-1.8702
2000.0	79.5753	77.7448	157.3202	2000.0	-62.9713	61.1501	-1.8213
2100.0	76.7945	74.9911	151.7856	2100.0	-63.3114	61.5299	-1.7815
2200.0	74.1170	72.3389	146.4559	2200.0	-63.5452	61.7955	-1.7503
2300.0	71.5401	69.7865	141.3266	2300.0	-63.6835	61.9590	-1.7245
2400.0	69.0611	67.3321	136.3931	2400.0	-63.7362	62.0316	-1.7046
2500.0	66.6771	64.9730	131.6501	2500.0	-63.7121	62.0229	-1.6892
2600.0	64.3852	62.7068	127.0921	2600.0	-63.6189	61.9419	-1.6770
2700.0	62.1828	60.5307	122.7135	2700.0	-63.4640	61.7966	-1.6674
2800.0	60.0666	58.4418	118.5085	2800.0	-63.2540	61.5940	-1.6600
2900.0	58.0340	56.4372	114.4712	2900.0	-62.9947	61.3408	-1.6552
3000.0	56.0819	54.5141	110.5960	3000.0	-62.6916	61.0428	-1.6488
3100.0	54.2077	52.6693	106.8770	3100.0	-62.3497	60.7053	-1.6444
3200.0	52.4084	50.9000	103.3084	3200.0	-61.9735	60.3332	-1.6407
3300.0	50.6813	49.2034	99.8846	3300.0	-61.5672	59.9308	-1.6364
3400.0	49.0236	47.5764	96.6000	3400.0	-61.1345	59.5021	-1.6324
3500.0	47.4327	46.0164	93.4492	3500.0	-60.6788	59.0507	-1.6281
3600.0	45.9060	44.5206	90.4266	3600.0	-60.2034	58.5798	-1.6236
3700.0	44.4408	43.0868	87.5272	3700.0	-59.7111	58.0924	-1.6187
3800.0	43.0347	41.7110	84.7457	3800.0	-59.2044	57.5910	-1.6134
3900.0	41.6852	40.3920	82.0772	3900.0	-58.6857	57.0780	-1.6077
4000.0	40.4901	39.1270	79.5172	4000.0	-58.1572	56.5557	-1.6015
4500.0	34.6510	33.5320	68.1831	4500.0	-55.4277	53.8637	-1.5640
5000.0	29.9578	28.9687	58.9265	5000.0	-52.6716	51.1543	-1.5173
5500.0	26.0991	25.2244	51.3235	5500.0	-49.9926	48.5279	-1.4646
6000.0	22.9060	22.1306	45.0365	6000.0	-47.4459	46.0367	-1.4092
6500.0	20.2447	19.5551	39.7998	6500.0	-45.0568	43.7037	-1.3531
7000.0	18.0104	17.3947	35.4051	7000.0	-42.8333	41.5395	-1.2937
7500.0	16.1407	15.5688	31.6896	7500.0	-40.7730	39.5288	-1.2442
8000.0	14.5110	14.0143	28.5254	8000.0	-38.8683	37.6754	-1.1929
8500.0	13.1304	12.6815	25.8119	8500.0	-37.1089	35.9646	-1.1443
9000.0	11.9483	11.5311	23.4794	9000.0	-35.4834	34.3851	-1.0983
9500.0	10.9026	10.5318	21.4344	9500.0	-33.9804	32.9255	-1.0549
10000.0	9.9974	9.6587	19.6561	10000.0	-32.5891	31.5748	-1.0143
10500.0	9.2020	8.8914	18.0933	10500.0	-31.2991	30.3231	-0.9760
11000.0	8.4992	8.2136	16.7128	11000.0	-30.1011	29.1610	-0.9401
11500.0	7.8754	7.6119	15.4872	11500.0	-28.9865	28.0801	-0.9064
12000.0	7.3190	7.0752	14.3942	12000.0	-27.9478	27.0730	-0.8748
12500.0	6.8206	6.5945	13.4151	12500.0	-26.9779	26.1328	-0.8451
13000.0	6.3724	6.1622	12.5346	13000.0	-26.0706	25.2535	-0.8171
13500.0	5.9678	5.7718	11.7396	13500.0	-25.2204	24.4297	-0.7906
14000.0	5.6012	5.4182	11.0194	14000.0	-24.4223	23.6565	-0.7658
14500.0	5.2680	5.0966	10.3646	14500.0	-23.6719	22.9295	-0.7424
15000.0	4.9642	4.8034	9.7676	15000.0	-22.9652	22.2449	-0.7203
15500.0	4.6863	4.5353	9.2215	15500.0	-22.2985	21.5991	-0.6994
16000.0	4.4314	4.2893	8.7207	16000.0	-21.6687	20.9891	-0.6796
16500.0	4.1971	4.0631	8.2602	16500.0	-21.0729	20.4121	-0.6608
17000.0	3.9812	3.8546	7.8357	17000.0	-20.5083	19.8654	-0.6429

σ^{n}_{xx}	σ^{T}_{xx}	σ_{xx}	field	σ^{n}_{xy}	σ^{T}_{xy}	σ_{xy}
140.4586	139.1164	288.9750	0.	-0.	0.	-0.
150.2985	138.6628	288.9613	100.0	-7.6519	6.8879	-0.7641
149.9863	137.9950	287.9813	200.0	-16.9203	13.4447	-3.4756
147.4505	137.0541	284.4046	300.0	-26.5335	20.5566	-5.9770
142.8054	134.8510	277.6566	400.0	-35.0633	28.0969	-6.9664
137.2240	131.1759	268.4000	500.0	-42.0856	35.1530	-6.9318
131.2365	126.5176	257.7541	600.0	-47.6644	41.1458	-6.5188
125.2361	121.4164	246.6524	700.0	-52.0149	45.9747	-6.0402
119.4446	116.2662	235.7105	800.0	-55.3839	49.7874	-5.5965
113.9623	111.2631	225.2254	900.0	-57.9980	52.7915	-5.2065
108.8389	106.4926	215.3315	1000.0	-60.0397	55.1736	-4.8661
104.0035	101.9769	205.9804	1100.0	-61.6464	57.0799	-4.5665
99.4894	97.7088	197.1982	1200.0	-62.9170	58.6169	-4.3001
95.2449	93.6695	188.9144	1300.0	-63.9208	59.8599	-4.0609
91.2602	89.8478	181.0780	1400.0	-64.7074	60.8622	-3.8457
87.4995	86.1962	173.6957	1500.0	-65.3120	61.6622	-3.6498
83.8951	82.7220	166.6171	1600.0	-65.7598	62.2886	-3.4712
80.4277	79.4076	159.8351	1700.0	-66.0705	62.7623	-3.3087
77.1693	76.2395	153.4088	1800.0	-66.2594	63.1008	-3.1586
74.0527	73.2093	147.2620	1900.0	-66.3395	63.3185	-3.0208
71.0807	70.3097	141.4903	2000.0	-66.3211	63.4274	-2.8937
68.2417	67.5343	135.7760	2100.0	-66.2145	63.4384	-2.7761
65.5291	64.8782	130.4073	2200.0	-66.0285	63.3614	-2.6671
62.9376	62.3355	125.2731	2300.0	-65.7711	63.2052	-2.5658
60.4612	59.9051	120.3663	2400.0	-65.4500	62.9785	-2.4715
58.0959	57.5798	115.6757	2500.0	-65.0720	62.6884	-2.3836
55.8369	55.3567	111.1941	2600.0	-64.6437	62.3424	-2.3013
53.6799	53.2321	106.9121	2700.0	-64.1713	61.9471	-2.2242
51.6208	51.2023	102.8231	2800.0	-63.6603	61.5084	-2.1519
49.6553	49.2634	98.9188	2900.0	-63.1160	61.0319	-2.0841
47.7797	47.4120	95.1917	3000.0	-62.5430	60.5230	-2.0201
45.9900	45.6443	91.6343	3100.0	-61.9459	59.9860	-1.9599
44.2824	43.9569	88.2393	3200.0	-61.3284	59.4254	-1.9030
42.6533	42.3462	84.9995	3300.0	-60.6942	58.8451	-1.8491
41.0990	40.8089	81.9079	3400.0	-60.0468	58.2485	-1.7983
39.6161	39.3416	78.9578	3500.0	-59.3887	57.6388	-1.7499
38.2013	37.9412	76.1426	3600.0	-58.7229	57.0188	-1.7041
36.8511	36.6044	73.4555	3700.0	-58.0516	56.3911	-1.6605
35.5626	35.3282	70.8908	3800.0	-57.3770	55.7579	-1.6191
34.3328	34.1098	68.4425	3900.0	-56.7008	55.1213	-1.5796
33.1586	32.9467	66.1049	4000.0	-56.0248	54.4829	-1.5420
28.0313	27.8653	55.8935	4500.0	-52.6923	51.3149	-1.3773
24.9327	24.7951	49.7279	5000.0	-49.5173	48.2733	-1.2439
20.6291	20.5149	41.1440	5500.0	-46.5575	45.4237	-1.1339
17.9618	17.8656	35.8274	6000.0	-43.8314	42.7900	-1.0415
15.7455	15.6543	31.4098	6500.0	-41.3366	40.3738	-0.9628
13.9015	13.8265	27.7440	7000.0	-39.0602	38.1650	-0.8952
12.4797	12.3177	24.8074	7500.0	-36.9847	36.1483	-0.8364
11.0921	11.0376	22.1298	8000.0	-35.0915	34.3068	-0.7848
9.9096	9.8503	19.9480	8500.0	-33.3623	32.6232	-0.7391
8.8431	8.8008	18.0831	9000.0	-31.7800	31.0816	-0.6984
8.2574	8.2346	16.4760	9500.0	-30.3293	29.6670	-0.6620
7.5590	7.5240	15.0829	10000.0	-28.9955	28.3663	-0.6292
6.9508	6.9184	13.8693	10500.0	-27.7669	27.1675	-0.5994
6.4162	6.4873	12.9035	11000.0	-26.6324	26.0600	-0.5723
5.9459	5.9194	11.8653	11500.0	-25.5827	25.0346	-0.5476
5.5295	5.5052	11.0347	12000.0	-24.6080	24.0831	-0.5249
5.1592	5.1368	10.2960	12500.0	-23.7022	23.1981	-0.5041
4.8286	4.8018	9.6304	13000.0	-22.8582	22.3734	-0.4847
4.5327	4.5129	9.0457	13500.0	-22.0701	21.6032	-0.4669
4.2655	4.2476	8.5131	14000.0	-21.3329	20.8826	-0.4503
4.0248	4.0083	8.0331	14500.0	-20.6419	20.2071	-0.4348
3.8067	3.7911	7.5978	15000.0	-19.9931	19.5727	-0.4204
3.6096	3.5940	7.2036	15500.0	-19.3829	18.9760	-0.4069
3.4281	3.4144	6.8425	16000.0	-18.8079	18.4137	-0.3942
3.2643	3.2504	6.5137	16500.0	-18.2654	17.8831	-0.3822
3.1123	3.1001	6.2124	17000.0	-17.7527	17.3817	-0.3711

Derived

Conductivity

$\times 10^{-14}$

W1

63°K

4°K

field	σ^{n}_{xx}	σ^{T}_{xx}	σ_{xx}	field	σ^{n}_{xy}	σ^{T}_{xy}	σ_{xy}
0.	439.6171	321.2521	760.8691	0.	-0.	0.	-0.
100.0	398.1652	303.7952	701.8604	100.0	-122.9160	70.4202	-52.4958
200.0	313.2258	261.0789	574.4047	200.0	-187.1051	119.7069	-67.9982
300.0	236.4739	213.0564	449.5303	300.0	-202.7061	142.5296	-60.1793
400.0	181.5309	172.3841	353.9150	400.0	-195.3550	147.3647	-47.9903
500.0	144.3045	141.5207	285.8252	500.0	-181.3973	145.5577	-36.8396
600.0	118.8021	118.7481	237.5502	600.0	-166.9554	136.5649	-30.3904
700.0	100.7342	101.1629	202.5371	700.0	-153.9310	128.9051	-25.0258
800.0	87.4205	88.9007	176.3213	800.0	-142.6925	121.5819	-21.1107
900.0	77.2245	78.9039	156.0284	900.0	-133.1071	114.9249	-18.1842
1000.0	69.1488	70.6727	139.8110	1000.0	-124.9231	108.9841	-15.9391
1100.0	62.5293	63.9644	126.4927	1100.0	-117.8767	103.7034	-14.1733
1200.0	56.9697	58.3053	115.2910	1200.0	-111.7905	98.9933	-12.7572
1300.0	52.2404	53.4428	105.6816	1300.0	-106.3638	94.7676	-11.5962
1400.0	48.1106	49.2019	97.3125	1400.0	-101.5766	90.9462	-10.6303
1500.0	44.4683	45.4585	89.9268	1500.0	-97.2774	87.4651	-9.8143
1600.0	41.2721	42.1220	83.3941	1600.0	-93.3812	84.2646	-9.1166
1700.0	38.3080	39.1261	77.4341	1700.0	-89.8205	81.3077	-8.5128
1800.0	35.6736	36.4197	72.0933	1800.0	-86.5434	78.5575	-7.9859
1900.0	33.2817	33.9939	67.2756	1900.0	-83.5081	75.9873	-7.5214
2000.0	31.1019	31.7213	62.8231	2000.0	-80.6834	73.5748	-7.1086
2100.0	29.1087	29.6838	58.7925	2100.0	-78.0415	71.3020	-6.7395
2200.0	27.2820	27.8122	55.0942	2200.0	-75.5622	69.1541	-6.4081
2300.0	25.6041	26.0941	51.6982	2300.0	-73.2265	67.1200	-6.1084
2400.0	24.0609	24.5148	48.5757	2400.0	-71.0258	65.1898	-5.8359
2500.0	22.6318	23.0605	45.6923	2500.0	-68.9419	63.3547	-5.5872
2600.0	21.3204	21.7190	43.0394	2600.0	-66.9668	61.6077	-5.3591
2700.0	20.1138	20.4806	40.5943	2700.0	-65.0926	59.9426	-5.1494
2800.0	18.9920	19.3344	38.3264	2800.0	-63.3096	58.3541	-4.9555
2900.0	17.9537	18.2738	36.2268	2900.0	-61.6132	56.8367	-4.7765
3000.0	16.9896	17.2907	34.2804	3000.0	-59.9963	55.3866	-4.6097
3100.0	16.0952	16.3782	32.4734	3100.0	-58.4544	53.9997	-4.4547
3200.0	15.2639	15.5305	30.7944	3200.0	-56.9818	52.6724	-4.3094
3300.0	14.4905	14.7420	29.2324	3300.0	-55.5749	51.4010	-4.1739
3400.0	13.7701	14.0077	27.7778	3400.0	-54.2291	50.1824	-4.0467
3500.0	13.0985	13.3234	26.4219	3500.0	-52.9408	49.0141	-3.9267
3600.0	12.4717	12.6848	25.1565	3600.0	-51.7074	47.8935	-3.8138
3700.0	11.8867	12.0881	23.9741	3700.0	-50.5250	46.8174	-3.7076
3800.0	11.3389	11.5301	22.8682	3800.0	-49.3911	45.7841	-3.6070
3900.0	10.8251	11.0079	21.8330	3900.0	-48.3036	44.7909	-3.5120
4000.0	10.3443	10.5183	20.8625	4000.0	-47.2582	43.8363	-3.4219
4500.0	8.3435	8.4870	16.8306	4500.0	-42.6048	39.5717	-3.0331
5000.0	6.8548	6.9675	13.8223	5000.0	-38.7400	36.0159	-2.7241
5500.0	5.7222	5.8158	11.5380	5500.0	-35.4066	33.0156	-2.4727
6000.0	4.8434	4.9222	9.7656	6000.0	-32.7215	30.4574	-2.2641
6500.0	4.1494	4.2168	8.3662	6500.0	-30.3918	28.2537	-2.0880
7000.0	3.5921	3.6508	7.2429	7000.0	-28.2756	26.3382	-1.9374
7500.0	3.1398	3.1905	6.3301	7500.0	-26.4063	24.6598	-1.8072
8000.0	2.7666	2.8112	5.5778	8000.0	-24.8713	23.1779	-1.6934
8500.0	2.4557	2.4953	4.9509	8500.0	-23.4537	21.8606	-1.5931
9000.0	2.1940	2.2294	4.4234	9000.0	-22.1869	20.6826	-1.5042
9500.0	1.9719	2.0036	3.9755	9500.0	-21.0479	19.6233	-1.4246
10000.0	1.7816	1.8103	3.5919	10000.0	-20.0198	18.6658	-1.3536
10500.0	1.6175	1.6436	3.2611	10500.0	-19.0847	17.7964	-1.2883
11000.0	1.4751	1.4988	2.9738	11000.0	-18.2329	17.0034	-1.2295
11500.0	1.3505	1.3722	2.7227	11500.0	-17.4534	16.2774	-1.1759
12000.0	1.2411	1.2610	2.5021	12000.0	-16.7372	15.6104	-1.1268
12500.0	1.1444	1.1627	2.3071	12500.0	-16.0770	14.9954	-1.0816
13000.0	1.0585	1.0755	2.1340	13000.0	-15.4666	14.4267	-1.0398
13500.0	0.9822	0.9977	1.9797	13500.0	-14.9006	13.8994	-1.0013
14000.0	0.9134	0.9281	1.8415	14000.0	-14.3743	13.4090	-0.9654
14500.0	0.8518	0.8654	1.7172	14500.0	-13.8838	12.9517	-0.9320
15000.0	0.7961	0.8089	1.6051	15000.0	-13.4254	12.5245	-0.9009
15500.0	0.7458	0.7578	1.5036	15500.0	-12.9962	12.1244	-0.8718
16000.0	0.7001	0.7113	1.4114	16000.0	-12.5935	11.7490	-0.8445
16500.0	0.6584	0.6690	1.3274	16500.0	-12.2148	11.3959	-0.8188
17000.0	0.6204	0.6303	1.2507	17000.0	-11.8582	11.0634	-0.7947

Derived Conductivity $\times 10^{-14}$

W2

300°K

77°K

field	σ^{n}_{xx}	σ^{P}_{xx}	σ_{xx}	field	σ^{n}_{xy}	σ^{P}_{xy}	σ_{xy}
0.	114.7930	109.1914	223.9844	0.	-0.	0.	0.
100.0	115.2734	108.4441	223.9375	100.0	-0.3303	2.4937	2.1634
200.0	116.1085	107.6884	223.7969	200.0	-1.4315	4.2104	2.7789
300.0	116.8127	106.9453	223.5625	300.0	-3.0413	5.4045	2.3632
400.0	116.7968	106.4776	223.2344	400.0	-4.7356	6.4979	1.7623
500.0	116.6900	106.1382	222.8281	500.0	-6.3570	7.6354	1.2784
600.0	116.5099	105.8104	222.3203	600.0	-7.8997	8.8247	0.9250
700.0	116.2734	105.4699	221.7344	700.0	-9.3840	10.0370	0.6529
800.0	115.9952	105.0751	221.0703	800.0	-10.8299	11.2496	0.4197
900.0	115.6814	104.6546	220.3359	900.0	-12.2481	12.4471	0.1991
1000.0	115.3304	104.2009	219.5313	1000.0	-13.6430	13.6207	-0.0223
1100.0	114.9397	103.7165	218.6563	1100.0	-15.0152	14.7650	-0.2502
1200.0	114.5152	103.2714	217.7266	1200.0	-16.3700	15.8860	-0.4840
1300.0	114.0515	102.6829	216.7344	1300.0	-17.6964	16.9677	-0.7287
1400.0	113.5517	102.1358	215.6875	1400.0	-19.0040	18.0275	-0.9765
1500.0	113.0194	101.5744	214.5938	1500.0	-20.2831	19.0559	-1.2272
1600.0	112.4586	101.0023	213.4609	1600.0	-21.5339	20.0554	-1.4785
1700.0	111.8657	100.4155	212.2813	1700.0	-22.7559	21.0274	-1.7285
1800.0	111.2490	99.8213	211.0703	1800.0	-23.9526	21.9771	-1.9755
1900.0	110.6089	99.2192	209.8281	1900.0	-25.1177	22.8998	-2.2180
2000.0	109.9421	98.6047	208.5469	2000.0	-26.2500	23.7951	-2.4549
2100.0	109.2493	97.9772	207.2266	2100.0	-27.3559	24.6706	-2.6853
2200.0	108.5467	97.3517	205.8984	2200.0	-28.4335	25.5251	-2.9084
2300.0	107.8271	96.7198	204.5469	2300.0	-29.4779	26.3542	-3.1237
2400.0	107.0931	96.0731	203.1563	2400.0	-30.4908	27.1599	-3.3309
2500.0	106.3449	95.4307	201.7656	2500.0	-31.4790	27.9493	-3.5297
2600.0	105.5712	94.7804	200.3516	2600.0	-32.4378	28.7179	-3.7199
2700.0	104.7944	94.1255	198.9219	2700.0	-33.3694	29.4695	-3.9014
2800.0	104.0128	93.4677	197.4805	2800.0	-34.2702	30.1959	-4.0743
2900.0	103.2209	92.8064	196.0273	2900.0	-35.1440	30.9054	-4.2386
3000.0	102.4171	92.1376	194.5547	3000.0	-35.9916	31.5972	-4.3944
3100.0	101.6115	91.4705	193.0820	3100.0	-36.8134	32.2716	-4.5418
3200.0	100.7985	90.7991	191.5977	3200.0	-37.6097	32.9287	-4.6810
3300.0	99.9805	90.1250	190.1055	3300.0	-38.3778	33.5655	-4.8122
3400.0	99.1575	89.4479	188.6055	3400.0	-39.1242	34.1885	-4.9357
3500.0	98.3419	88.7696	187.1016	3500.0	-39.8431	34.7915	-5.0516
3600.0	97.5038	88.0809	185.5938	3600.0	-40.5413	35.3811	-5.1601
3700.0	96.6735	87.4085	184.0820	3700.0	-41.2142	35.9526	-5.2615
3800.0	95.8430	86.7273	182.5703	3800.0	-41.8677	36.5114	-5.3562
3900.0	95.0067	86.0402	181.0469	3900.0	-42.4948	37.0505	-5.4444
4000.0	94.1746	85.3559	179.5313	4000.0	-43.1034	37.5774	-5.5261
4500.0	90.0394	81.9337	171.9531	4500.0	-45.8289	39.9803	-5.8486
5000.0	85.9158	78.5256	164.4414	5000.0	-48.0787	42.0292	-6.0494
5500.0	81.9061	75.1524	157.0586	5500.0	-49.9068	43.7516	-6.1552
6000.0	78.0190	71.8677	149.8867	6000.0	-51.3625	45.1742	-6.1883
6500.0	74.2734	68.6602	142.9336	6500.0	-52.4917	46.3247	-6.1670
7000.0	70.6850	65.5572	136.2422	7000.0	-53.3344	47.2286	-6.1058
7500.0	67.2582	62.5670	129.8252	7500.0	-53.9359	47.9201	-6.0159
8000.0	63.9989	59.6994	123.6982	8000.0	-54.3217	48.4157	-5.9060
8500.0	60.9058	56.9575	117.8633	8500.0	-54.5300	48.7414	-5.7886
9000.0	57.9768	54.3435	112.3203	9000.0	-54.5834	48.9327	-5.6508
9500.0	55.2065	51.8540	107.0605	9500.0	-54.5062	48.9019	-5.6142
10000.0	52.5897	49.4933	102.0830	10000.0	-54.3197	48.9441	-5.3756
10500.0	50.1194	47.2516	97.3711	10500.0	-54.0395	48.8024	-5.2371
11000.0	47.7888	45.1272	92.9160	11000.0	-53.6816	48.5816	-5.1000
11500.0	45.5904	43.1151	88.7056	11500.0	-53.2625	48.2970	-4.9655
12000.0	43.5169	41.2102	84.7271	12000.0	-52.7883	47.9541	-4.8342
12500.0	41.5610	39.4073	80.9683	12500.0	-52.2707	47.5641	-4.7066
13000.0	39.7160	37.7015	77.4175	13000.0	-51.7199	47.1368	-4.5831
13500.0	37.9757	36.0873	74.0625	13500.0	-51.1409	46.6771	-4.4638
14000.0	36.3351	34.5595	70.8947	14000.0	-50.5408	46.1921	-4.3487
14500.0	34.7797	33.1134	67.8931	14500.0	-49.9233	45.6864	-4.2368
15000.0	33.3142	31.7449	65.0591	15000.0	-49.2940	45.1626	-4.1314
15500.0	31.9286	30.4484	62.3770	15500.0	-48.6562	44.6272	-4.0290
16000.0	30.6188	29.2206	59.8394	16000.0	-48.0134	44.0829	-3.9305
16500.0	29.3796	28.0569	57.4365	16500.0	-47.3684	43.5324	-3.8360
17000.0	28.2066	26.9538	55.1604	17000.0	-46.7234	42.9782	-3.7452

field	σ^{n}_{xx}	σ^{P}_{xx}	σ_{xx}	field	σ^{n}_{xy}	σ^{P}_{xy}	σ_{xy}
0.	834.2500843	5.812508	810.1250	0.	-0.	0.	0.
100.0	158.0578	156.4306	314.4884	100.0	-3286.6964	3289.6011	2.9047
200.0	155.4368	152.6256	308.0624	200.0	-1654.7294	1656.5628	1.8335
300.0	153.1395	149.9407	303.0801	300.0	-1115.8608	1116.6625	0.8017
400.0	150.1077	147.0145	297.1223	400.0	-849.7423	849.8377	0.0954
500.0	146.4768	143.6285	290.1053	500.0	-692.2768	691.9722	-0.3047
600.0	142.4052	139.7993	282.2045	600.0	-588.7958	588.2810	-0.5147
700.0	138.0219	135.6189	273.6408	700.0	-515.8891	515.2694	-0.6197
800.0	133.4350	131.1938	264.6287	800.0	-461.8713	461.2027	-0.6687
900.0	128.7355	126.6218	255.3574	900.0	-420.2720	419.5840	-0.6880
1000.0	123.9984	121.9856	245.9839	1000.0	-387.2308	386.5389	-0.6918
1100.0	119.2828	117.3506	236.6334	1100.0	-360.3110	359.6231	-0.6879
1200.0	114.6342	112.7673	227.4015	1200.0	-337.9054	337.2250	-0.6803
1300.0	110.0862	108.2730	218.3592	1300.0	-318.9148	318.2434	-0.6714
1400.0	105.6629	103.9944	209.6572	1400.0	-302.5652	301.9028	-0.6625
1500.0	101.4805	99.8497	201.3302	1500.0	-288.2974	287.6433	-0.6540
1600.0	97.6496	95.9510	193.6006	1600.0	-275.6984	275.0518	-0.6465
1700.0	93.2760	91.6055	184.8815	1700.0	-264.4575	263.8174	-0.6401
1800.0	89.4628	87.8167	177.2795	1800.0	-254.3370	253.7022	-0.6347
1900.0	85.8094	84.1853	169.9947	1900.0	-245.1520	244.5215	-0.6305
2000.0	82.4149	80.8104	163.0253	2000.0	-236.7571	236.1299	-0.6272
2100.0	78.9760	77.3894	156.3654	2100.0	-229.0364	228.4116	-0.6248
2200.0	75.7890	74.2187	150.0077	2200.0	-221.8966	221.2733	-0.6233
2300.0	72.7492	71.1941	143.9433	2300.0	-215.2615	214.6389	-0.6226
2400.0	69.8517	68.3107	138.1624	2400.0	-209.0689	208.4463	-0.6226
2500.0	67.0912	65.5635	132.6546	2500.0	-203.2668	202.6436	-0.6232
2600.0	64.4621	62.9470	127.4092	2600.0	-197.8122	197.1878	-0.6244
2700.0	61.9591	60.4560	122.4151	2700.0	-192.6686	192.0425	-0.6261
2800.0	59.5769	58.0849	117.6618	2800.0	-187.8051	187.1768	-0.6282
2900.0	57.3086	55.8284	113.1370	2900.0	-183.1952	182.5645	-0.6307
3000.0	55.1503	53.6809	108.8313	3000.0	-178.8163	178.1827	-0.6336
3100.0	53.0963	51.6375	104.7338	3100.0	-174.6487	174.0119	-0.6368
3200.0	51.1414	49.6928	100.8342	3200.0	-170.6752	170.0350	-0.6402
3300.0	49.2804	47.8421	97.1226	3300.0	-166.8808	166.2369	-0.6439
3400.0	47.5089	46.0806	93.5895	3400.0	-163.2521	162.6044	-0.6478
3500.0	45.8220	44.4036	90.2256	3500.0	-159.7775	159.1257	-0.6518
3600.0	44.2155	42.8069	87.0224	3600.0	-156.4463	155.7903	-0.6560
3700.0	42.6850	41.2861	83.9712	3700.0	-153.2492	152.5889	-0.6603
3800.0	41.2267	39.8374	81.0641	3800.0	-150.1776	149.5129	-0.6647
3900.0	39.8366	38.4568	78.2934	3900.0	-147.2239	146.5548	-0.6692
4000.0	38.5111	37.1409	75.6520	4000.0	-144.3812	143.7075	-0.6737
4500.0	32.7386	31.4156	64.1541	4500.0	-131.6256	130.9288	-0.6968
5000.0	28.1364	26.9603	54.9967	5000.0	-120.8758	120.1563	-0.7195
5500.0	24.4273	23.1981	47.6254	5500.0	-111.6967	110.9560	-0.7407
6000.0	21.4046	20.2221	41.6267	6000.0	-103.7741	103.0142	-0.7599
6500.0	18.9142	17.7780	36.6922	6500.0	-96.8728	96.0961	-0.7767
7000.0	16.8406	15.7502	32.5908	7000.0	-90.8122	90.0212	-0.7910
7500.0	15.0969	14.0515	29.1484	7500.0	-85.4515	84.6487	-0.8027
8000.0	13.6169	12.6155	26.2324	8000.0	-80.6787	79.8667	-0.8120
8500.0	12.3498	11.3912	23.7410	8500.0	-76.4042	75.5853	-0.8189
9000.0	11.2563	10.4342	21.6905	9000.0	-72.5553	71.7316	-0.8236
9500.0	10.3057	9.6287	19.9344	9500.0	-69.0722	68.2458	-0.8264
10000.0	9.4737	8.8352	18.3089	10000.0	-65.9059	65.0787	-0.8273
10500.0	8.7409	8.1495	16.8904	10500.0	-63.0156	62.1890	-0.8265
11000.0	8.0919	7.5259	15.6178	11000.0	-60.3668	59.5425	-0.8243
11500.0	7.5141	6.7819	14.2960	11500.0	-57.9307	57.1099	-0.8208
12000.0	6.9971	6.2972	13.2943	12000.0	-55.6829	54.8667	-0.8162
12500.0	6.5325	5.8634	12.3958	12500.0	-53.6023	52.7916	-0.8107
13000.0	6.1132	5.4734	11.5866	13000.0	-51.6711	50.8668	-0.8043
13500.0	5.7335	5.1215	10.8551	13500.0	-49.8737	49.0764	-0.7972
14000.0	5.3884	4.8028	10.1913	14000.0	-48.1966	47.4070	-0.7896
14500.0	5.0738	4.5132	9.5870	14500.0	-46.6282	45.8468	-0.7814
15000.0	4.7860	4.2492	9.0357	15000.0	-45.1583	44.3854	-0.7729
15500.0	4.5220	4.0078	8.5298	15500.0	-43.7778	43.0138	-0.7640
16000.0	4.2793	3.7865	8.0658	16000.0	-42.4788	41.7239	-0.7549
16500.0	4.0556	3.5830	7.6387	16500.0	-41.2544	40.5088	-0.7456
17000.0	3.8490	3.3956	7.2445	17000.0	-40.0981	39.3620	-0.7362

field	σ^n_{xx}	σ^p_{xx}	σ_{xx}	field	σ^n_{xy}	σ^p_{xy}	σ_{xy}
0.	170.5856	165.2414	335.8330	0.	-0.	0.	0.
100.0	170.0520	164.1088	334.1608	100.0	-10.8388	10.6810	-0.1578
200.0	167.8065	161.5155	329.3220	200.0	-21.8104	20.3528	-1.4576
300.0	163.7275	158.0651	321.7925	300.0	-32.0062	29.2211	-2.7851
400.0	158.3756	153.8304	312.2060	400.0	-40.9103	37.3685	-3.5419
500.0	152.3027	148.9050	301.2077	500.0	-48.4363	44.7160	-3.7203
600.0	145.9088	143.4478	289.3564	600.0	-54.6919	51.1906	-3.5012
700.0	139.4476	137.6387	277.0863	700.0	-59.8513	56.7703	-3.0810
800.0	133.0661	131.6456	264.7117	800.0	-64.0904	61.4816	-2.6088
900.0	126.8424	125.6078	252.4503	900.0	-67.5595	65.3850	-2.1745
1000.0	120.8163	119.6326	240.4489	1000.0	-70.3785	68.5586	-1.8199
1100.0	115.0082	113.7972	228.8054	1100.0	-72.6418	71.0869	-1.5549
1200.0	109.4295	108.1541	217.5836	1200.0	-74.4243	73.0524	-1.3719
1300.0	104.0869	102.7371	206.8240	1300.0	-75.7881	74.5316	-1.2565
1400.0	98.9843	97.5657	196.5500	1400.0	-76.7861	75.5936	-1.1925
1500.0	94.1233	92.6497	186.7730	1500.0	-77.4648	76.2995	-1.1653
1600.0	89.5034	87.9913	177.4947	1600.0	-77.8657	76.7028	-1.1630
1700.0	85.1218	83.5875	168.7093	1700.0	-78.0263	76.8499	-1.1764
1800.0	80.9738	79.4336	160.4074	1800.0	-77.9801	76.7813	-1.1987
1900.0	77.0532	75.5196	152.5728	1900.0	-77.7572	76.5319	-1.2253
2000.0	73.3522	71.8361	145.1883	2000.0	-77.3845	76.1318	-1.2527
2100.0	69.8621	68.3726	138.2341	2100.0	-76.8859	75.6069	-1.2790
2200.0	66.5734	65.1158	131.6892	2200.0	-76.2822	74.9794	-1.3028
2300.0	63.4761	62.0558	125.5319	2300.0	-75.5919	74.2685	-1.3233
2400.0	60.5601	59.1804	119.7405	2400.0	-74.8309	73.4905	-1.3404
2500.0	57.8153	56.4783	114.2936	2500.0	-74.0131	72.6592	-1.3539
2600.0	55.2315	53.9386	109.1701	2600.0	-73.1505	71.7866	-1.3639
2700.0	52.7991	51.5506	104.3497	2700.0	-72.2532	70.8826	-1.3707
2800.0	50.5086	49.3045	99.8131	2800.0	-71.3301	69.9557	-1.3744
2900.0	48.3510	47.1908	95.5418	2900.0	-70.3886	69.0132	-1.3755
3000.0	46.3178	45.2005	91.5183	3000.0	-69.4351	68.0610	-1.3741
3100.0	44.4009	43.3254	87.7263	3100.0	-68.4748	67.1043	-1.3705
3200.0	42.5926	41.5578	84.1503	3200.0	-67.5123	66.1472	-1.3651
3300.0	40.8858	39.8902	80.7760	3300.0	-66.5513	65.1932	-1.3581
3400.0	39.2738	38.3161	77.5899	3400.0	-65.5950	64.2453	-1.3497
3500.0	37.7504	36.8296	74.5794	3500.0	-64.6459	63.3059	-1.3400
3600.0	36.3098	35.4252	71.7330	3600.0	-63.7063	62.3769	-1.3294
3700.0	34.9465	34.0983	69.0398	3700.0	-62.7778	61.4598	-1.3180
3800.0	33.6555	32.8343	66.4897	3800.0	-61.8618	60.5560	-1.3058
3900.0	32.4322	31.6414	64.0736	3900.0	-60.9595	59.6665	-1.2930
4000.0	31.2721	30.5105	61.7826	4000.0	-60.0717	58.7919	-1.2799
4500.0	26.2897	25.6551	51.9448	4500.0	-55.8689	54.6588	-1.2100
5000.0	22.3928	21.8586	44.2513	5000.0	-52.0732	50.9341	-1.1391
5500.0	19.2963	18.8415	38.1382	5500.0	-48.6695	47.5986	-1.0709
6000.0	16.8000	16.4098	33.2098	6000.0	-45.6234	44.6161	-1.0073
6500.0	14.7610	14.4227	29.1837	6500.0	-42.8955	41.9467	-0.9489
7000.0	13.0155	12.7199	25.8554	7000.0	-40.4472	39.5518	-0.8954
7500.0	11.6672	11.4068	23.0741	7500.0	-38.2435	37.3968	-0.8467
8000.0	10.4789	10.2479	20.7268	8000.0	-36.2534	35.4511	-0.8024
8500.0	9.4670	9.2604	18.7274	8500.0	-34.4500	33.6881	-0.7619
9000.0	8.5984	8.4134	17.0118	9000.0	-32.8102	32.0852	-0.7250
9500.0	7.8471	7.6802	15.5273	9500.0	-31.3139	30.6227	-0.6912
10000.0	7.1928	7.0414	14.2342	10000.0	-29.9442	29.2839	-0.6602
10500.0	6.6192	6.4814	13.1007	10500.0	-28.6863	28.0545	-0.6317
11000.0	6.1136	5.9876	12.1012	11000.0	-27.5275	26.9221	-0.6055
11500.0	5.6653	5.5497	11.2150	11500.0	-26.4571	25.8759	-0.5812
12000.0	5.2660	5.1595	10.4255	12000.0	-25.4655	24.9068	-0.5587
12500.0	4.9085	4.8102	9.7187	12500.0	-24.5446	24.0067	-0.5379
13000.0	4.5872	4.4961	9.0832	13000.0	-23.6872	23.1687	-0.5184
13500.0	4.2972	4.2125	8.5097	13500.0	-22.8870	22.3867	-0.5003
14000.0	4.0344	3.9556	7.9900	14000.0	-22.1387	21.6553	-0.4834
14500.0	3.7956	3.7220	7.5175	14500.0	-21.4373	20.9697	-0.4675
15000.0	3.5777	3.5089	7.0866	15000.0	-20.7787	20.3260	-0.4527
15500.0	3.3785	3.3135	6.6923	15500.0	-20.1590	19.7203	-0.4387
16000.0	3.1956	3.1350	6.3306	16000.0	-19.5750	19.1494	-0.4255
16500.0	3.0275	2.9704	5.9979	16500.0	-19.0236	18.6105	-0.4131
17000.0	2.8724	2.8186	5.6910	17000.0	-18.5023	18.1009	-0.4014

Derived

Conductivity

$\times 10^{-14}$

W2

63°K

4°K

field	σ^n_{xx}	σ^p_{xx}	σ_{xx}	field	σ^n_{xy}	σ^p_{xy}	σ_{xy}
0.	635.9877	559.1704	816.7177	0.	-0.	0.	-0.
100.0	445.7676	315.6714	761.4388	100.0	-226.5401	-33.8568	-260.3969
200.0	341.4893	299.1057	640.5951	200.0	-255.5767	57.2421	-198.3346
300.0	295.9867	247.6915	518.6783	300.0	-253.2598	109.1204	-144.1394
400.0	197.7898	222.2213	420.0112	400.0	-237.1281	136.3950	-101.7332
500.0	158.0944	186.3405	344.4439	500.0	-219.0235	145.9998	-73.0236
600.0	129.7065	156.8779	285.5843	600.0	-202.2506	148.1172	-54.1331
700.0	108.6630	134.0945	241.5565	700.0	-187.3245	145.8405	-41.4841
800.0	92.0258	113.9254	205.9522	800.0	-174.1026	141.3611	-32.7415
900.0	78.0071	98.3924	177.3995	900.0	-162.3494	135.8559	-26.4925
1000.0	68.5219	85.7048	154.2267	1000.0	-151.8562	129.9713	-21.8849
1100.0	59.9677	75.2561	135.2238	1100.0	-142.4528	124.0587	-18.3940
1200.0	52.9145	66.5801	119.4946	1200.0	-133.9993	118.3117	-15.6876
1400.0	47.0492	59.3191	106.3683	1400.0	-126.3775	112.8310	-13.5464
1400.0	42.1201	53.1927	95.3128	1400.0	-119.4868	107.6629	-11.8239
1500.0	37.9554	47.9884	85.9438	1500.0	-113.2405	102.8224	-10.4187
1600.0	34.4083	43.5355	77.9435	1600.0	-107.5631	98.3068	-9.2563
1700.0	31.4442	39.7094	71.0448	1700.0	-102.3889	94.1031	-8.2958
1800.0	28.7408	36.3775	65.1183	1800.0	-97.6606	90.1938	-7.4668
1900.0	26.4595	33.4810	59.9420	1900.0	-93.3284	86.5586	-6.7498
2000.0	24.4702	30.9472	55.4174	2000.0	-89.3488	83.1768	-6.1320
2100.0	22.7219	28.7055	51.4274	2100.0	-85.6839	80.0283	-5.6555
2200.0	21.1787	26.7252	47.9040	2200.0	-82.3004	77.0935	-5.2068
2300.0	19.8109	24.9648	44.7758	2300.0	-79.1691	74.3551	-4.8141
2400.0	18.5902	23.3902	41.9804	2400.0	-76.2648	71.7961	-4.4697
2500.0	17.4884	21.9794	39.4678	2500.0	-73.5650	69.4014	-4.1636
2600.0	16.5158	20.7070	37.2228	2600.0	-71.0498	67.1574	-3.8924
2700.0	15.6310	19.5576	35.1886	2700.0	-68.7019	65.0515	-3.6504
2800.0	14.8298	18.5149	33.3434	2800.0	-66.5059	63.0723	-3.4336
2900.0	14.0990	17.5657	31.6646	2900.0	-64.4480	61.2095	-3.2385
3000.0	13.4334	16.6989	30.1322	3000.0	-62.5161	59.4537	-3.0624
3100.0	12.8290	15.9060	28.7350	3100.0	-60.6994	57.7966	-2.9028
3200.0	12.2643	15.1795	27.4438	3200.0	-58.9881	56.2304	-2.7577
3300.0	11.7480	14.5047	26.2526	3300.0	-57.3736	54.7483	-2.6253
3400.0	11.2729	13.8841	25.1569	3400.0	-55.8481	53.3439	-2.5042
3500.0	10.8320	13.3095	24.1404	3500.0	-54.4045	52.0116	-2.3929
3600.0	10.4225	12.7750	23.1976	3600.0	-53.0367	50.7459	-2.2908
3700.0	10.0414	12.2748	22.3201	3700.0	-51.7389	49.5424	-2.1964
3800.0	9.6857	11.8060	21.5017	3800.0	-50.5058	48.3966	-2.1092
3900.0	9.3520	11.3634	20.7366	3900.0	-49.3329	47.3044	-2.0284
4000.0	9.0411	10.9488	20.0199	4000.0	-48.2157	46.2625	-1.9532
4500.0	7.7449	9.2804	17.0244	4500.0	-43.3437	41.6973	-1.6464
5000.0	6.7477	8.0110	14.7487	5000.0	-39.4083	37.9863	-1.4220
5500.0	5.9674	7.0001	12.9675	5500.0	-36.1608	34.9092	-1.2516
6000.0	5.3404	6.2021	11.5061	6000.0	-33.4322	32.3142	-1.1180
6500.0	4.7992	5.5375	10.3057	6500.0	-31.1045	30.0939	-1.0106
7000.0	4.3142	4.9802	9.2944	7000.0	-29.0929	28.1705	-0.9225
7500.0	3.9241	4.5063	8.4304	7500.0	-27.3351	26.4862	-0.8489
8000.0	3.5854	4.0985	7.6838	8000.0	-25.7842	24.9977	-0.7865
8500.0	3.2885	3.7441	7.0326	8500.0	-24.4044	23.6715	-0.7329
9000.0	3.0266	3.4347	6.4613	9000.0	-23.1678	22.4816	-0.6863
9500.0	2.7940	3.1600	5.9540	9500.0	-22.0527	21.4072	-0.6455
10000.0	2.5844	2.9177	5.5035	10000.0	-21.0413	20.4319	-0.6094
10500.0	2.4004	2.7008	5.1011	10500.0	-20.1194	19.5422	-0.5777
11000.0	2.2420	2.5089	4.7398	11000.0	-19.2753	18.7269	-0.5484
11500.0	2.0917	2.3377	4.4744	11500.0	-18.4993	17.9770	-0.5223
12000.0	1.9448	2.1754	4.1202	12000.0	-17.7834	17.2847	-0.4987
12500.0	1.8203	2.0431	3.8534	12500.0	-17.1207	16.6435	-0.4772
13000.0	1.7070	1.9018	3.6108	13000.0	-16.5054	16.0479	-0.4575
13500.0	1.6045	1.7841	3.3906	13500.0	-15.9325	15.4931	-0.4394
14000.0	1.5087	1.6786	3.1874	14000.0	-15.3978	14.9751	-0.4226
14500.0	1.4218	1.5804	3.0021	14500.0	-14.8976	14.4903	-0.4073
15000.0	1.3419	1.4901	2.8320	15000.0	-14.4285	14.0355	-0.3930
15500.0	1.2683	1.4071	2.6755	15500.0	-13.9878	13.6082	-0.3796
16000.0	1.2004	1.3307	2.5311	16000.0	-13.5729	13.2058	-0.3672
16500.0	1.1374	1.2602	2.3978	16500.0	-13.1817	12.8262	-0.3556
17000.0	1.0795	1.1950	2.2744	17000.0	-12.8122	12.4676	-0.3446

Derived Conductivity $\times 10^{-14}$

W3

300°K

77°K

field	σ^n_{xx}	σ^P_{xx}	σ_{xx}	field	σ^n_{xy}	σ^P_{xy}	σ_{xy}
0.	193.8678	211.1342	245.0020	0.	-0.	0.	-0.
100.0	193.4429	211.1211	244.9656	100.0	-1.5936	1.3392	-0.2443
200.0	194.7461	211.0711	244.8552	200.0	-3.1485	2.6959	-0.4527
300.0	194.2127	210.9946	244.6704	300.0	-4.7102	4.0528	-0.6574
400.0	193.6192	210.7922	244.4104	400.0	-6.2884	5.3881	-0.9005
500.0	193.4965	210.5985	244.0741	500.0	-7.8860	6.6946	-1.1895
600.0	193.4005	210.4572	244.6677	600.0	-9.4939	7.9833	-1.5106
700.0	193.1629	210.1005	244.1433	700.0	-11.1025	9.2539	-1.8486
800.0	192.7721	209.9177	243.5908	800.0	-12.7041	10.5116	-2.1925
900.0	192.4207	209.5071	241.9429	900.0	-14.2931	11.7570	-2.5361
1000.0	192.0411	209.1676	241.2087	1000.0	-15.8655	12.9894	-2.8761
1100.0	191.6059	208.7998	240.4045	1100.0	-17.4192	14.2074	-3.2109
1200.0	191.1773	208.4009	239.5281	1200.0	-18.9486	15.4092	-3.5395
1300.0	190.6982	207.9746	238.5829	1300.0	-20.4547	16.5930	-3.8614
1400.0	190.0509	207.5211	237.5721	1400.0	-21.9347	17.7575	-4.1772
1500.0	189.4580	207.0418	236.4988	1500.0	-23.3872	18.9013	-4.4860
1600.0	188.9417	206.5382	235.3659	1600.0	-24.8114	20.0244	-4.7880
1700.0	188.1744	206.0110	234.1763	1700.0	-26.2063	21.1251	-5.0833
1800.0	187.4882	205.4645	232.9327	1800.0	-27.5714	22.1998	-5.3716
1900.0	186.7744	204.8975	231.6378	1900.0	-28.9063	23.2532	-5.6531
2000.0	186.0375	204.3124	230.2939	2000.0	-30.2109	24.2831	-5.9276
2100.0	185.2768	203.7106	228.9033	2100.0	-31.4848	25.2896	-6.1952
2200.0	184.4947	203.0933	227.4680	2200.0	-32.7284	26.2726	-6.4558
2300.0	183.6928	202.4618	225.9901	2300.0	-33.9416	27.2323	-6.7093
2400.0	182.8730	201.8172	224.4708	2400.0	-35.1246	28.1688	-6.9558
2500.0	182.0361	201.1604	222.9125	2500.0	-36.2775	29.0825	-7.1951
2600.0	181.1837	200.4924	221.3161	2600.0	-37.4007	29.9735	-7.4273
2700.0	180.3170	199.8141	219.6831	2700.0	-38.4944	30.8421	-7.6523
2800.0	179.4370	199.1264	218.0143	2800.0	-39.5588	31.6885	-7.8703
2900.0	178.5449	198.4298	216.3107	2900.0	-40.5943	32.5132	-8.0811
3000.0	177.6417	197.7252	214.5729	3000.0	-41.6010	33.3162	-8.2848
3100.0	176.7283	197.0133	213.7996	3100.0	-42.5794	34.0980	-8.4814
3200.0	175.8058	196.2946	212.1004	3200.0	-43.5297	34.8587	-8.6710
3300.0	174.8749	195.5698	210.4447	3300.0	-44.4522	35.5986	-8.8536
3400.0	173.9366	194.8395	208.7761	3400.0	-45.3474	36.3181	-9.0293
3500.0	172.9916	194.1041	207.0957	3500.0	-46.2154	37.0173	-9.1981
3600.0	172.0408	193.3643	205.4051	3600.0	-47.0566	37.6964	-9.3602
3700.0	171.0850	192.6205	203.7055	3700.0	-47.8714	38.3559	-9.5155
3800.0	170.1248	191.8733	201.9981	3800.0	-48.6602	38.9959	-9.6643
3900.0	169.1609	191.1232	200.2841	3900.0	-49.4232	39.6166	-9.8065
4000.0	168.1942	190.3706	198.5647	4000.0	-50.1608	40.2184	-9.9424
4500.0	163.4398	186.5855	189.9244	4500.0	-53.4824	42.9525	-10.5298
5000.0	158.6998	182.8005	181.3004	5000.0	-56.7296	45.2537	-10.9759
5500.0	153.9781	179.0546	172.7957	5500.0	-58.4559	47.1583	-11.2976
6000.0	149.0971	175.3947	164.4918	6000.0	-60.2162	48.7039	-11.5123
6500.0	144.6142	171.8356	156.4496	6500.0	-61.5549	49.9283	-11.6366
7000.0	140.4119	168.4006	148.7124	7000.0	-62.5539	50.8682	-11.6857
7500.0	136.2050	165.1078	141.3078	7500.0	-63.2319	51.5546	-11.6733
8000.0	132.3012	161.9508	134.2519	8000.0	-63.6432	52.0319	-11.6114
8500.0	128.6025	158.9342	127.5508	8500.0	-63.8275	52.3175	-11.5100
9000.0	125.1074	156.0956	121.2031	9000.0	-63.8198	52.4419	-11.3778
9500.0	121.8107	153.3914	115.2021	9500.0	-63.6508	52.4288	-11.2220
10000.0	118.7056	150.8319	109.5374	10000.0	-63.3474	52.2988	-11.0485
10500.0	115.7834	148.4133	104.1961	10500.0	-62.9324	52.0702	-10.8622
11000.0	113.0363	146.1220	99.1633	11000.0	-62.4256	51.7587	-10.6669
11500.0	110.4537	143.9699	94.4236	11500.0	-61.8440	51.3781	-10.4659
12000.0	108.0265	141.9366	89.9611	12000.0	-61.2019	50.9402	-10.2618
12500.0	105.7494	140.0145	85.7600	12500.0	-60.5117	50.4552	-10.0565
13000.0	103.6015	138.2044	81.8047	13000.0	-59.7836	49.9320	-9.8516
13500.0	101.5854	136.4968	78.0802	13500.0	-59.0265	49.3781	-9.6484
14000.0	99.6894	134.8828	74.5722	14000.0	-58.2480	48.8000	-9.4480
14500.0	97.9054	133.3615	71.2669	14500.0	-57.4542	48.2033	-9.2509
15000.0	96.2259	131.9254	68.1513	15000.0	-56.6505	47.5927	-9.0577
15500.0	94.6449	130.5692	65.2133	15500.0	-55.8413	46.9724	-8.8689
16000.0	93.1534	129.2880	62.4414	16000.0	-55.0304	46.3457	-8.6847
16500.0	91.7478	128.0770	59.8248	16500.0	-54.2209	45.7156	-8.5054
17000.0	90.4214	126.9319	57.3535	17000.0	-53.4155	45.0846	-8.3309

field	σ^n_{xx}	σ^P_{xx}	σ_{xx}	field	σ^n_{xy}	σ^P_{xy}	σ_{xy}
0.	189.9114	213.0226	402.9340	0.	-0.	0.	0.
100.0	193.0687	207.6549	400.7236	100.0	-7.4192	18.5205	11.1013
200.0	193.4304	201.0564	394.4928	200.0	-19.7312	30.7460	11.0148
300.0	190.3081	194.8651	385.1747	300.0	-31.3959	41.3075	9.9116
400.0	185.4985	188.3018	373.7903	400.0	-41.5356	50.7774	9.2418
500.0	179.8144	181.3228	361.1427	500.0	-50.2644	59.1326	8.8682
600.0	173.6889	174.0775	347.7616	600.0	-57.7877	66.4080	8.6203
700.0	167.4260	166.6600	333.9860	700.0	-64.2810	72.6758	8.3948
800.0	160.8423	159.1908	320.0329	800.0	-69.8773	78.0135	8.1361
900.0	154.3260	151.7479	306.0739	900.0	-74.6742	82.4965	7.8183
1000.0	147.8384	144.4024	292.2408	1000.0	-78.7567	86.1897	7.4330
1100.0	141.4391	137.2140	278.6530	1100.0	-82.1859	89.1697	6.9838
1200.0	135.1476	130.2356	265.3832	1200.0	-85.0250	91.5008	6.4759
1300.0	129.0736	123.5062	252.5798	1300.0	-87.3311	93.2549	5.9238
1400.0	123.0876	117.0504	240.1380	1400.0	-89.1590	94.4980	5.3390
1500.0	117.2609	110.8941	228.1549	1500.0	-90.5605	95.2942	4.7337
1600.0	111.8586	105.0467	216.9053	1600.0	-91.5842	95.7036	4.1193
1700.0	106.5900	99.5128	206.1028	1700.0	-92.2758	95.7817	3.5058
1800.0	101.5597	94.2909	195.8506	1800.0	-92.6771	95.5788	2.9018
1900.0	96.7583	89.3750	186.1433	1900.0	-92.8260	95.1401	2.3141
2000.0	92.2134	84.7557	176.9691	2000.0	-92.7570	94.5053	1.7484
2100.0	87.9898	80.4213	168.4111	2100.0	-92.5007	93.7095	1.2088
2200.0	83.7910	76.3594	160.1494	2200.0	-92.0845	92.7830	0.6985
2300.0	79.9089	72.5525	152.4613	2300.0	-91.5325	91.7519	0.2194
2400.0	76.2346	68.9868	145.2214	2400.0	-90.8660	90.6338	-0.2272
2500.0	72.7589	65.6525	138.4114	2500.0	-90.1035	89.4628	-0.6409
2600.0	69.4721	62.5289	132.0010	2600.0	-89.2612	88.2395	-1.0217
2700.0	66.3645	59.5948	125.9594	2700.0	-88.3533	86.9830	-1.3703
2800.0	63.4267	56.8438	120.2705	2800.0	-87.3921	85.7047	-1.6874
2900.0	60.6493	54.2598	114.9091	2900.0	-86.3883	84.4139	-1.9744
3000.0	58.0223	51.8327	109.8550	3000.0	-85.3510	83.1184	-2.2325
3100.0	55.5401	49.5528	105.0929	3100.0	-84.2882	81.8249	-2.4633
3200.0	53.1913	47.3960	100.5874	3200.0	-83.2069	80.5385	-2.6684
3300.0	50.9692	45.3519	96.3211	3300.0	-82.1129	79.2635	-2.8494
3400.0	48.8663	43.4365	92.3028	3400.0	-81.0113	78.0034	-3.0079
3500.0	46.8751	41.6211	88.4962	3500.0	-79.9064	76.7609	-3.1456
3600.0	44.9895	40.2079	85.1974	3600.0	-78.8022	75.5381	-3.2640
3700.0	43.2030	38.6347	81.8427	3700.0	-77.7016	74.3368	-3.3648
3800.0	41.5096	37.1597	78.6694	3800.0	-76.6073	73.1581	-3.4493
3900.0	39.9030	35.7698	75.6457	3900.0	-75.5218	72.0028	-3.5189
4000.0	38.3807	34.4402	72.8208	4000.0	-74.4468	70.8717	-3.5751
4500.0	31.8400	28.8059	60.6468	4500.0	-69.2775	65.5838	-3.6937
5000.0	26.7441	24.4460	51.1901	5000.0	-64.5193	60.9911	-3.6282
5500.0	22.7254	21.0056	43.7310	5500.0	-60.2014	56.7385	-3.4630
6000.0	19.5180	18.2455	37.7635	6000.0	-56.3098	53.0591	-3.2507
6500.0	16.9281	15.9985	32.9266	6500.0	-52.8116	49.7887	-3.0229
7000.0	14.8138	14.1454	28.9592	7000.0	-49.6674	46.8700	-2.7973
7500.0	13.0697	12.5997	25.6694	7500.0	-46.8374	44.2541	-2.5834
8000.0	11.6168	11.2975	22.9143	8000.0	-44.2847	41.8993	-2.3854
8500.0	10.3955	10.1905	20.5861	8500.0	-41.9756	39.7707	-2.2049
9000.0	9.3603	9.2419	18.6021	9000.0	-39.8807	37.8390	-2.0417
9500.0	8.4758	8.4220	16.8997	9500.0	-37.9741	36.0793	-1.8948
10000.0	7.7146	7.7111	15.4258	10000.0	-36.2336	34.4705	-1.7630
10500.0	7.0552	7.0888	14.1440	10500.0	-34.6397	32.9949	-1.6448
11000.0	6.4802	6.5415	13.0217	11000.0	-33.1757	31.6371	-1.5386
11500.0	5.9760	6.0578	12.0338	11500.0	-31.8272	30.3840	-1.4432
12000.0	5.5314	5.6282	11.1596	12000.0	-30.5816	29.2244	-1.3572
12500.0	5.1374	5.2440	10.3813	12500.0	-29.4281	28.1485	-1.2796
13000.0	4.7886	4.9015	9.6880	13000.0	-28.3571	27.1477	-1.2094
13500.0	4.4778	4.5925	9.0654	13500.0	-27.3605	26.2147	-1.1457
14000.0	4.1911	4.3136	8.5047	14000.0	-26.4309	25.3431	-1.0878
14500.0	3.9371	4.0610	7.9980	14500.0	-25.5619	24.5270	-1.0350
15000.0	3.7072	3.8313	7.5385	15000.0	-24.7481	23.7614	-0.9866
15500.0	3.4985	3.6219	7.1204	15500.0	-23.9843	23.0420	-0.9423
16000.0	3.3084	3.4304	6.7388	16000.0	-23.2662	22.3646	-0.9016
16500.0	3.1347	3.2548	6.3895	16500.0	-22.5899	21.7258	-0.8641
17000.0	2.9754	3.0934	6.0688	17000.0	-21.9519	21.1225	-0.8294

field	σ^n_{xx}	σ^p_{xx}	σ_{xx}
0.	17126.000068	11.933685	437.9375
100.0	258.0658	259.1859	495.2517
200.0	227.3699	207.9005	435.2704
300.0	215.0161	199.5677	414.5838
400.0	204.3620	192.3762	396.7382
500.0	193.9362	184.3784	378.3146
600.0	183.6315	175.4968	359.1283
700.0	173.5214	166.0312	339.5726
800.0	163.6908	156.4014	320.0922
900.0	154.2096	146.8415	301.0511
1000.0	145.1296	137.5789	282.7086
1100.0	136.4858	128.7449	265.2307
1200.0	128.2987	120.4117	248.7103
1300.0	120.5765	112.6103	233.1868
1400.0	113.3181	105.3444	218.6625
1500.0	106.5148	98.6004	205.1152
1600.0	100.1525	92.3545	192.5070
1700.0	94.2131	86.5776	180.7907
1800.0	88.6760	81.2383	169.9144
1900.0	83.5192	76.3047	159.8238
2000.0	78.7196	71.7495	150.4692
2100.0	74.2545	67.5511	141.7856
2200.0	70.1013	63.6334	133.7347
2300.0	66.2382	60.0262	126.2644
2400.0	62.6443	56.6854	119.3297
2500.0	59.2997	53.5889	112.8886
2600.0	56.1857	50.7162	106.9020
2700.0	53.2851	48.0487	101.4337
2800.0	50.5813	45.5693	96.1506
2900.0	48.0595	43.2624	91.3219
3000.0	45.7055	41.1140	86.8196
3100.0	43.5066	39.1111	82.6177
3200.0	41.4508	37.2419	78.6927
3300.0	39.5272	35.4957	75.0229
3400.0	37.7257	33.8628	71.5886
3500.0	36.0372	32.3343	68.3715
3600.0	34.4531	30.9020	65.3551
3700.0	32.9657	29.5585	62.5242
3800.0	31.5678	28.2972	59.8650
3900.0	30.2529	27.1118	57.3647
4000.0	29.0150	25.9967	55.0117
4500.0	23.8017	21.3097	45.1114
5000.0	19.8492	17.7652	37.6144
5500.0	16.7941	15.0300	31.8242
6000.0	14.3909	12.8811	27.2720
6500.0	12.4705	11.1653	23.6358
7000.0	10.9140	9.7706	20.6846
7500.0	9.6363	8.6334	18.2717
8000.0	8.5755	7.6890	16.2644
8500.0	7.6855	6.8953	14.5808
9000.0	6.9320	6.2233	13.1553
9500.0	6.2885	5.6496	11.9381
10000.0	5.7347	5.1559	10.8906
10500.0	5.2547	4.7279	9.9827
11000.0	4.8360	4.3546	9.1906
11500.0	4.4685	4.0270	8.4955
12000.0	4.1442	3.7378	7.8820
12500.0	3.8565	3.4812	7.3378
13000.0	3.6001	3.2525	6.8527
13500.0	3.3706	3.0477	6.4183
14000.0	3.1642	2.8636	6.0278
14500.0	2.9779	2.6973	5.6752
15000.0	2.8092	2.5467	5.3558
15500.0	2.6558	2.4097	5.0654
16000.0	2.5159	2.2847	4.8006
16500.0	2.3879	2.1704	4.5583
[illegible]	[illegible]	2.0654	4.3359

field	σ^n_{xy}	σ^p_{xy}	σ_{xy}
0.	-0.	0.	-0.
100.0	-2870.4947	2893.0378	22.5431
200.0	-1461.2544	1466.1516	4.8972
300.0	-1000.4007	999.1157	-1.2850
400.0	-774.9034	771.4864	-3.4170
500.0	-642.3520	638.6659	-3.6862
600.0	-555.4945	552.2777	-3.2168
700.0	-494.2242	491.6241	-2.6002
800.0	-448.5813	446.4756	-2.1057
900.0	-413.6984	411.2769	-1.8214
1000.0	-384.9451	382.8007	-1.7445
1100.0	-360.9050	359.0703	-1.8347
1200.0	-340.8638	338.8211	-2.0427
1300.0	-323.5354	321.2121	-2.3232
1400.0	-308.3044	305.6646	-2.6398
1500.0	-294.7332	291.7676	-2.9656
1600.0	-282.5035	279.2214	-3.2820
1700.0	-271.3788	267.8014	-3.5774
1800.0	-261.1807	257.3357	-3.8450
1900.0	-251.7715	247.6899	-4.0816
2000.0	-243.0436	238.7571	-4.2866
2100.0	-234.9113	230.4506	-4.4607
2200.0	-227.3052	222.6995	-4.6057
2300.0	-220.1685	215.4444	-4.7240
2400.0	-213.4537	208.6355	-4.8182
2500.0	-207.1209	202.2302	-4.8907
2600.0	-201.1361	196.1919	-4.9441
2700.0	-195.4696	190.4888	-4.9808
2800.0	-190.0960	185.0931	-5.0029
2900.0	-184.9925	179.9801	-5.0123
3000.0	-180.1391	175.1282	-5.0109
3100.0	-175.5179	170.5177	-5.0001
3200.0	-171.1129	166.1314	-4.9814
3300.0	-166.9095	161.9535	-4.9560
3400.0	-162.8945	157.9696	-4.9249
3500.0	-159.0560	154.1670	-4.8890
3600.0	-155.3829	150.5338	-4.8491
3700.0	-151.8653	147.0592	-4.8060
3800.0	-148.4937	143.7335	-4.7603
3900.0	-145.2598	140.5475	-4.7124
4000.0	-142.1556	137.4928	-4.6628
4500.0	-128.3420	123.9408	-4.4012
5000.0	-116.8684	112.7313	-4.1370
5500.0	-107.2060	103.3211	-3.8849
6000.0	-98.9705	95.3198	-3.6507
6500.0	-91.8763	88.4474	-3.4360
7000.0	-85.7076	82.4673	-3.2403
7500.0	-80.2984	77.2360	-3.0624
8000.0	-75.5195	72.6189	-2.9006
8500.0	-71.2690	68.5156	-2.7534
9000.0	-67.4652	64.8460	-2.6191
9500.0	-64.0423	61.5459	-2.4964
10000.0	-60.9467	58.5678	-2.3839
10500.0	-58.1343	55.8537	-2.2806
11000.0	-55.5682	53.3828	-2.1854
11500.0	-53.2179	51.1265	-2.0975
12000.0	-51.0576	49.0416	-2.0161
12500.0	-49.0653	47.1248	-1.9405
13000.0	-47.2224	45.3521	-1.8702
13500.0	-45.5127	43.7080	-1.8047
14000.0	-43.9225	42.1790	-1.7435
14500.0	-42.4397	40.7535	-1.6862
15000.0	-41.0539	39.4215	-1.6324
15500.0	-39.7559	38.1740	-1.5819
16000.0	-38.5378	37.0034	-1.5344
16500.0	-37.3922	35.9027	-1.4896
17000.0	-36.3131	34.8659	-1.4473

Derived

Conductivity

$\times 10^{-14}$

W3

63°K

4°K

field	σ^n_{xx}	σ^p_{xx}	σ_{xx}
0.	1407.7364	896.6426	2304.3790
100.0	989.2017	813.1587	1802.3603
200.0	539.2325	570.4444	1109.6769
300.0	328.8829	366.8780	695.7609
400.0	221.9602	247.5821	469.5423
500.0	159.6421	178.6260	338.2681
600.0	120.3472	135.8338	256.1810
700.0	94.1631	107.3271	201.4902
800.0	75.9093	87.2617	163.1711
900.0	62.6896	72.5401	135.2297
1000.0	52.8021	61.3874	114.1895
1100.0	45.2032	52.7185	97.9216
1200.0	39.2263	45.8365	85.0628
1300.0	34.4320	40.2748	74.7067
1400.0	30.5208	35.7111	66.2318
1500.0	27.2881	31.9168	59.1999
1600.0	24.5693	28.7255	53.2948
1700.0	22.2692	26.0143	48.2835
1800.0	20.3109	23.6903	43.9912
1900.0	18.6024	21.6820	40.2844
2000.0	17.1253	19.9344	37.0597
2100.0	15.8323	18.4037	34.2360
2200.0	14.6934	17.0552	31.7486
2300.0	13.6848	15.8610	29.5458
2400.0	12.7873	14.7982	27.5854
2500.0	11.9848	13.8482	25.8330
2600.0	11.2644	12.9956	24.2600
2700.0	10.6152	12.2275	22.8427
2800.0	10.0280	11.5341	21.5612
2900.0	9.4953	10.9033	20.3986
3000.0	9.0104	10.3304	19.3408
3100.0	8.5679	9.8076	18.3755
3200.0	8.1629	9.3294	17.4923
3300.0	7.7913	8.8908	16.6821
3400.0	7.4496	8.4876	15.9372
3500.0	7.1347	8.1161	15.2508
3600.0	6.8438	7.7731	14.6169
3700.0	6.5745	7.4558	14.0303
3800.0	6.3248	7.1617	13.4865
3900.0	6.0929	6.8885	12.9814
4000.0	5.8771	6.6344	12.5115
4500.0	4.9939	5.5956	10.5895
5000.0	4.3505	4.8398	9.1903
5500.0	3.8677	4.2731	8.1408
6000.0	3.4961	3.8315	7.3276
6500.0	3.2041	3.4955	6.6996
7000.0	2.9704	3.2220	6.1924
7500.0	2.7804	2.9999	5.7803
8000.0	2.6238	2.8168	5.4406
8500.0	2.4931	2.6642	5.1572
9000.0	2.3827	2.5354	4.9182
9500.0	2.2886	2.4258	4.7144
10000.0	2.2077	2.3315	4.5392
10500.0	2.1374	2.2498	4.3872
11000.0	2.0760	2.1784	4.2544
11500.0	2.0219	2.1156	4.1375
12000.0	1.9739	2.0600	4.0339
12500.0	1.9310	2.0104	3.9415
13000.0	1.8926	1.9660	3.8585
13500.0	1.8578	1.9259	3.7837
14000.0	1.8263	1.8896	3.7158
14500.0	1.7974	1.8565	3.6539
15000.0	1.7710	1.8262	3.5972
15500.0	1.7467	1.7983	3.5450
16000.0	1.7241	1.7726	3.4968
16500.0	1.7032	1.7488	3.4519
17000.0	1.6836	1.7266	3.4102

field	σ^n_{xy}	σ^p_{xy}	σ_{xy}
0.	-0.	0.	-0.
100.0	-631.5782	302.6249	-328.9534
200.0	-653.2232	466.5583	-186.6650
300.0	-552.8333	462.4817	-90.3517
400.0	-467.2894	410.8105	-56.4789
500.0	-401.1442	359.5668	-41.5773
600.0	-349.6612	317.0927	-32.5685
700.0	-309.0164	282.7476	-26.2688
800.0	-276.4022	254.7635	-21.6387
900.0	-249.7995	231.6379	-18.1616
1000.0	-227.7605	212.2538	-15.5067
1100.0	-209.2388	195.7971	-13.4418
1200.0	-193.4755	181.6633	-11.8122
1300.0	-179.9059	169.4022	-10.5037
1400.0	-168.1078	158.6690	-9.4388
1500.0	-157.7577	149.1979	-8.5597
1600.0	-148.6053	140.7811	-7.8242
1700.0	-140.4545	133.2530	-7.2015
1800.0	-133.1492	126.4809	-6.6683
1900.0	-126.5648	120.3565	-6.2083
2000.0	-120.5994	114.7914	-5.8080
2100.0	-115.1688	109.7135	-5.4553
2200.0	-110.2049	105.0808	-5.1442
2300.0	-105.6495	100.7827	-4.8668
2400.0	-101.4542	96.8359	-4.6183
2500.0	-97.5778	93.1836	-4.3942
2600.0	-93.9853	89.7940	-4.1913
2700.0	-90.6468	86.6398	-4.0071
2800.0	-87.5362	83.6975	-3.8387
2900.0	-84.6307	80.9468	-3.6839
3000.0	-81.9109	78.3695	-3.5414
3100.0	-79.3598	75.9445	-3.4102
3200.0	-76.9620	73.6732	-3.2888
3300.0	-74.7039	71.5285	-3.1754
3400.0	-72.5742	69.5039	-3.0703
3500.0	-70.5620	67.5899	-2.9722
3600.0	-68.6577	65.7778	-2.8799
3700.0	-66.8530	64.0598	-2.7933
3800.0	-65.1407	62.4283	-2.7124
3900.0	-63.5133	60.8776	-2.6357
4000.0	-61.9650	59.4016	-2.5635
4500.0	-55.2304	52.9746	-2.2559
5000.0	-49.8145	47.7987	-2.0158
5500.0	-45.3656	43.5433	-1.8223
6000.0	-41.6474	39.9840	-1.6634
6500.0	-38.4944	36.9639	-1.5305
7000.0	-35.7872	34.3698	-1.4174
7500.0	-33.4383	32.1181	-1.3202
8000.0	-31.3810	30.1455	-1.2354
8500.0	-29.5647	28.4035	-1.1612
9000.0	-27.9496	26.8542	-1.0954
9500.0	-26.5042	25.4675	-1.0367
10000.0	-25.2032	24.2192	-0.9839
10500.0	-24.0261	23.0899	-0.9363
11000.0	-22.9563	22.0633	-0.8930
11500.0	-21.9799	21.1261	-0.8538
12000.0	-21.0851	20.2673	-0.8177
12500.0	-20.2622	19.4775	-0.7847
13000.0	-19.5031	18.7488	-0.7543
13500.0	-18.8005	18.0745	-0.7261
14000.0	-18.1486	17.4487	-0.6999
14500.0	-17.5420	16.8664	-0.6756
15000.0	-16.9762	16.3234	-0.6528
15500.0	-16.4474	15.8157	-0.6316
16000.0	-15.9520	15.3402	-0.6118
16500.0	-15.4869	14.8938	-0.5931
17000.0	-15.0496	14.4741	-0.5756

DATA - OSCILLATIONS.

B	1/B	V
5379.8	185.880	0.
5595.3	178.723	0.
5820.7	171.801	0.
6115.1	163.530	0.
6498.3	153.885	0.
6872.4	145.510	0.
7237.2	138.175	0.
7711.3	129.680	0.
8285.5	120.693	0.
8881.0	112.600	0.
9697.4	103.120	0.
10747.2	93.048	0.
11721.3	85.315	0.
13195.4	75.784	0.
14995.8	66.685	0.
17698.2	56.503	0.
5810.9	172.091	-0.143
6007.1	166.470	0.169
6203.5	161.200	-0.026
6400.0	156.250	-0.169
6596.7	151.590	0.130
6793.6	147.197	0.130
6892.1	145.094	0.
6990.6	143.048	-0.221
7089.2	141.059	-0.351
7187.9	139.127	-0.312
7286.5	137.239	0.
7385.2	135.405	0.299
7484.0	133.618	0.403
7582.8	131.877	0.390
7681.6	130.180	0.208
7780.5	128.526	-0.065
7879.5	126.912	-0.312
7978.4	125.338	-0.481
8077.4	123.802	-0.416
8176.5	122.302	-0.377
8275.6	120.837	-0.065
8374.7	119.407	0.156
8473.9	118.009	0.468
8573.2	116.643	0.520
8672.4	115.308	0.416
8771.7	114.003	0.260
8871.1	112.726	0.078
8970.5	111.477	-0.078
9069.9	110.254	-0.260
9169.4	109.058	-0.390
9269.0	107.887	-0.520
9368.5	106.740	-0.650
9468.2	105.617	-0.754
9567.8	104.517	-0.663
9667.5	103.439	-0.351
9767.3	102.383	0.169
9867.1	101.347	0.520
9966.9	100.332	0.728
10066.8	99.337	0.923
10166.7	98.360	0.988
10266.7	97.402	0.923
10366.7	96.463	0.832
10466.8	95.541	0.663
10566.9	94.635	0.481
10667.0	93.747	0.273
10767.2	92.875	0.
10867.4	92.018	-0.234
10967.7	91.177	-0.494
11068.0	90.350	-0.780
11168.4	89.538	-1.053
11268.8	88.740	-1.274
11369.3	87.956	-1.300
11469.8	87.185	-1.196
11570.4	86.428	-0.884
11670.9	85.683	-0.390
11771.6	84.950	0.104
11872.3	84.230	0.702
11973.0	83.521	1.170
12073.8	82.824	1.560
12174.6	82.138	1.807
12275.5	81.463	2.041
12376.4	80.799	2.080
12477.3	80.145	2.054
12578.3	79.502	1.963
12679.4	78.868	1.781
12780.5	78.244	1.547
12881.6	77.630	1.222
12982.8	77.025	0.923
13084.0	76.429	0.572
13185.3	75.842	0.247
13286.6	75.264	-0.130
13388.0	74.694	-0.364
13489.4	74.132	-0.598
13590.9	73.579	-0.780
13692.4	73.033	-0.975
13793.9	72.496	-1.157
13895.5	71.966	-1.326
13997.2	71.443	-1.521
14098.9	70.928	-1.716
14200.6	70.420	-1.924
14302.4	69.918	-2.093
14404.2	69.424	-2.210
14506.1	68.936	-2.249
14608.0	68.455	-2.223
14710.0	67.981	-1.937
14812.0	67.513	-1.560
14914.1	67.051	-0.793
15016.2	66.595	-0.286
15118.4	66.145	0.546
15220.6	65.701	1.378
15322.8	65.262	2.080
15425.1	64.829	2.496
15527.5	64.402	2.873
15629.9	63.980	3.172
15732.3	63.563	3.250
15834.8	63.152	3.224
15937.4	62.746	3.107
16039.9	62.344	2.951
16142.6	61.948	2.834
16245.3	61.556	2.652
16348.0	61.170	2.444
16450.8	60.787	2.353
16553.6	60.410	2.210
16656.5	60.037	2.067
16759.4	59.668	1.950
16862.4	59.304	1.781
16965.4	58.944	1.599
17068.5	58.588	1.456
17171.6	58.236	1.300
17274.7	57.888	1.040
17377.9	57.544	0.845
17481.2	57.204	0.650
17584.5	56.868	0.403
17687.9	56.536	0.195
17791.3	56.207	-0.039
17894.7	55.882	-0.260

(Fitted to Landau)

Hall | M-R

W3 1·2°K

B	1/B	V
6259.5	159.784	0.
6494.2	153.983	0.
6907.4	144.772	0.
7301.6	136.955	0.
7745.9	129.100	0.
8349.6	119.766	0.
9074.1	110.204	0.
9761.1	102.448	0.
10860.5	92.077	0.
11844.5	84.427	0.
13490.9	74.124	0.
15108.6	66.187	0.
18214.3	54.902	0.
7775.6	128.608	0.
7973.4	125.418	1.626
8270.3	120.914	-0.542
8567.7	116.717	-2.384
8815.8	113.433	0.
9064.2	110.324	4.335
9561.7	104.584	0.
9960.6	100.396	-4.335
8171.3	122.379	0.325
8369.4	119.483	-1.517
8567.7	116.717	-2.492
8766.2	114.075	-0.650
8964.8	111.547	3.251
9163.6	109.127	3.251
9362.6	106.808	2.059
9561.7	104.584	0.
9761.1	102.448	-2.709
9860.8	101.412	-3.359
9960.6	100.396	-4.660
10060.4	99.400	-4.443
10160.2	98.423	-2.709
10260.1	97.465	0.542
10360.1	96.524	3.359
10460.1	95.602	6.069
10560.1	94.696	6.502
10660.2	93.807	7.261
10760.3	92.936	6.502
10860.5	92.077	6.177
10960.7	91.235	4.877
11061.0	90.408	4.118
11161.3	89.595	2.167
11261.6	88.797	1.409
11362.0	88.012	-0.433
11462.5	87.241	-2.384
11562.9	86.483	-3.901
11663.5	85.738	-5.635
11764.1	85.005	-7.477
11864.7	84.284	-8.453
11965.3	83.575	-8.453
12066.0	82.877	-7.802
12166.8	82.191	-5.527
12267.6	81.516	-2.384
12368.4	80.851	1.517
12469.3	80.197	4.660
12570.3	79.553	8.453
12671.2	78.919	10.945
12772.3	78.295	13.004
12873.3	77.680	13.654
12974.5	77.074	13.979
13075.6	76.478	13.112
13176.8	75.891	12.787
13278.1	75.312	11.487
13379.4	74.742	9.970
13480.7	74.180	8.344
13582.1	73.626	6.502
13683.6	73.080	4.768
13785.1	72.542	3.251
13886.6	72.012	1.951
13988.2	71.489	0.
14089.8	70.973	-1.300
14191.5	70.465	-2.601
14293.2	69.963	-4.118
14395.0	69.469	-5.635
14496.8	68.981	-7.261
14598.6	68.500	-8.886
14700.5	68.025	-10.837
14802.5	67.556	-12.679
14904.5	67.094	-13.979
15006.5	66.638	-15.388
15108.6	66.187	-16.255
15210.8	65.743	-15.280
15313.9	65.304	-14.088
15415.2	64.871	-10.295
15517.5	64.444	-5.960
15619.8	64.021	0.
15722.2	63.604	6.394
15824.6	63.193	12.137
15927.1	62.786	17.122
16029.6	62.385	21.565
16132.1	61.988	22.865
16234.8	61.596	24.491
16337.4	61.209	25.033
16440.1	60.827	25.900
16542.9	60.449	25.683
16645.7	60.076	25.249
16748.5	59.707	24.708
16851.4	59.342	23.841
16954.4	58.982	23.191
17057.4	58.626	21.998
17160.4	58.274	21.565
17263.5	57.926	20.481
17366.7	57.582	19.506
17469.9	57.241	18.422
17573.1	56.905	16.905
17676.4	56.573	15.930
17779.7	56.244	14.196
17883.1	55.919	13.004
17986.6	55.597	11.487
18090.1	55.279	9.861
18193.6	54.964	8.453
18297.2	54.653	6.719
18400.8	54.345	5.418
18504.5	54.041	3.901
18608.2	53.740	2.276

DATA - OSCILLATIONS.

B	1/B	V
7184.6	139.186	-3.543
7283.2	137.302	-5.906
7381.9	135.466	-7.283
7480.6	133.679	-2.165
7579.4	131.937	4.331
7678.2	130.239	7.874
7777.0	128.584	7.874
7875.9	126.970	3.937
7974.8	125.395	-0.984
8073.8	123.858	-6.299
8172.8	122.357	-8.268
8271.8	120.892	-9.843
8370.9	119.461	-9.646
8470.1	118.063	-3.937
8569.3	116.696	0.984
8668.5	115.360	10.236
8767.8	114.054	11.417
8867.1	112.777	8.465
8966.4	111.527	5.118
9065.8	110.304	1.575
9165.3	109.108	-0.591
9264.7	107.936	-3.543
9364.3	106.789	-5.906
9463.8	105.665	-9.843
9563.5	104.565	-11.614
9663.1	103.486	-13.386
9762.8	102.429	-13.386
9862.6	101.393	-7.480
9962.4	100.378	3.346
10062.2	99.382	9.843
10162.1	98.405	16.142
10262.0	97.447	17.717
10362.0	96.507	17.717
10462.0	95.584	16.142
10562.0	94.679	14.173
10662.1	93.790	11.811
10762.3	92.917	7.874
10862.5	92.060	3.937
10962.7	91.218	-1.575
11063.0	90.391	-6.299
11163.3	89.579	-13.386
11263.7	88.781	-19.291
11364.1	87.996	-23.819
11464.6	87.225	-28.346
11565.1	86.467	-27.756
11665.6	85.722	-25.197
11766.2	84.989	-21.654
11866.8	84.268	-12.795
11967.5	83.559	-3.346
12068.3	82.862	12.008
12169.0	82.176	22.047
12269.8	81.501	28.937
12370.7	80.836	33.071
12471.6	80.182	35.827
12572.6	79.538	35.236

B	1/B	V
7125.5	140.342	0.
7974.8	125.395	0.
8559.3	116.831	0.
9145.4	109.345	0.
9962.4	100.378	0.
10962.7	91.218	0.
11997.7	83.349	0.
13371.7	74.785	0.
15295.3	65.379	0.
5906.3	169.310	-1.969
6004.4	166.545	-3.346
6102.5	163.867	0.
6200.7	161.273	3.543
6298.9	158.758	1.181
6397.1	156.320	-0.394
6495.4	153.955	-2.362
6593.7	151.659	-1.772
6692.1	149.430	-0.984
6790.5	147.264	3.937
6889.0	145.159	5.512
6987.5	143.113	4.134
7086.0	141.123	0.394

B	1/B	V
12673.6	78.904	34.843
12774.6	78.280	31.496
12875.7	77.666	28.346
12976.8	77.060	22.244
13078.0	76.464	17.126
13179.3	75.877	10.630
13280.5	75.298	3.937
13381.9	74.728	-5.315
13483.2	74.166	-10.433
13584.6	73.613	-16.142
13686.1	73.067	-19.685
13787.6	72.529	-23.228
13889.1	71.999	-26.575
13990.7	71.476	-29.134
14092.4	70.960	-32.480
14194.1	70.452	-35.433
14295.8	69.951	-38.976
14397.6	69.456	-42.323
14499.4	68.968	-45.276
14601.3	68.487	-47.047
14703.2	68.012	-47.244
14805.2	67.544	-45.276
14907.2	67.082	-39.764
15009.3	66.625	-31.299
15111.4	66.175	-21.260
15213.6	65.731	-8.465
15315.8	65.292	3.937
15418.0	64.859	22.638
15520.3	64.432	35.630
15622.7	64.010	43.701
15725.1	63.593	48.819
15827.5	63.181	53.543
15930.0	62.775	54.724
16032.5	62.373	54.134

W3

Hall 1·2°K

APPENDIX 4

COMPUTER PROGRAMMES.

Only the two most important programmes are listed here.

The Lorentzian fitting programme is in the form of a main programme followed by three subroutines.

The more complicated programme FRIER, for fitting data to the generalised Landau expression, is in the form of a fairly long main programme followed by four subroutines and, finally, M.D. Powell's long subroutine VA04A. This last subroutine is also essential to the working of the above Lorentzian fitting programme, of course.

Lorentzian fitting programme.

```
      0 DIMENSION DATAX(100),DATAY(100),X(5),E(5),W(40),
     1  TEXT(13)  , COEFFB(5)
      COMMON DATAX,DATAY,COEFFB,NDATA
      READ(5,100) NSETS
  100 FORMAT(I5)
      DO 99 NSET = 1, NSETS
      READ(5,110) (TEXT(I), I=1,13)
  110 FORMAT(13A6)
      READ(5,120) ICON, NDATA, JXXY, M, ESCALE
  120 FORMAT(I1,I4,I1,I4,F10.4 )
      IF(ICON.EQ.0)  ICON = 1
      DO 1 I=1,M
    1 READ(5,125) X(I), E(I)
  125 FORMAT(2F10.1)
      WRITE(6,115)  (TEXT(I),I=1,13)
  115 FORMAT(1H1,1X,13A6  ///)
      IF(JXXY) 11,11,12
   12 DO 2 I= 1, NDATA
      READ(5,130)  DATAX(I), DATAY(I)
  130 FORMAT(F10.4,10X,F10.4)
    2 DATAY(I)= DATAY(I)/DATAX(I)
      WRITE(6,140)
  140 FORMAT(1HO,9(2HXY,10X)  ///)
      GO TO 4
   11 DO 3 I= 1, NDATA
    3 READ(5,150) DATAX(I), DATAY(I)
  150 FORMAT(2F10.4)
      WRITE(6,145)
  145 FORMAT(1HO,9(2HXX,10X)  ///)
    4 CONTINUE
      MAXIT = 200
      N3N = 40
      IPRINT = 1
      EXTERNAL CALCFX
      CALL VA04A(X,E,M,F,ESCALE,IPRINT,ICON,MAXIT,CALCFX,W,N3N)
      WRITE(6,160)       (TEXT(I), I=1,13)
  160 FORMAT(1H1,1X, 13A6  ///)
      IF(JXXY) 13,13,14
   14 WRITE(6,170)
  170 FORMAT(1HO, 9(2HXY,10X)   ///)
      GO TO 15
   13 WRITE(6,180)
  180 FORMAT(1HO, 9(2HXX,10X)  ///)
   15 CONTINUE
      WRITE(6,190)
  190 FORMAT(1HO,13HFINAL VALUES- )
      DO 6 I=1, M
    6 WRITE(6,200) I, COEFFB(I),  I, X(I)

  200 FORMAT(1HO,2HB1,I2,2H)=,E12.5,13X,2HH(,I2,2H)=,E12.5  //)
      WRITE(6,210) F
  210 FORMAT(1HO,9X,15HSUM SQ RESIDS.= ,E20.8 ///30X,6(5H-----) )
      WRITE(6,220) NDATA, JXXY, M, ESCALE, MAXIT , ICON
 2200FORMAT(1HO,15HDATA INPUT WAS- /1HO,2X,5HNDATA,1X,4HJXXY,3X,
     1 6HNTERMS,3X,6HESCALE,3X,5HMAXIT /1HO,2X,I3,6X,I1,6X,I1,
     2 E10.3,1X,I5 / 1HO,5HICON= , I2 )
   99 CONTINUE
      STOP
      END
```

```
      SUBROUTINE CALCFX(M,X,F)
      DIMENSION X(5),DATAX(100),DATAY(100),COEFFB(5)
      COMMON DATAX,DATAY,COEFFB,NDATA
      CALL LSTSQR(DATAX,DATAY,NDATA,M,X,COEFFB,F)
      RETURN
      END
```

```
      SUBROUTINE LSTSQR(X,Y,N,M,H,B1,SUMR2)
     0 DIMENSION A(10,10),B(10),C(10,100),Y(100),X(100),
     1 RESID(100),H(5),B1(5)
      DOUBLE PRECISION A,B,C
C     SET UP C(I,J), WHERE OBS. EQU IS Y = (TRANSPOSEC)*B.
      DO 6 I= 1, M
      DO 7  J= 1, N
      C(I,J) = 0.0
    7 C(I,J) = 1.0/( (X(J)/H(I))*(X(J)/H(I)) +1.0 )
    6 CONTINUE
C     SET UP  A= C*(TRANSPOSEC)  AND B-DASH = C*Y.
      DO 8  I= 1,M
      DO 9 J= 1, M
      A(I,J) = 0.0
      B(I) = 0.0
      DO 10 K= 1, N
   10 A(I,J) = C(I,K) * C(J,K)  +  A(I,J)
    9 CONTINUE
      DO 11 K= 1,N
   11 B(I) = C(I,K) * Y(K)  + B(I)
    8 CONTINUE
      NUM = 10
C
      CALL MATRIX(A,B,M,NUM,DETER)
C
      SUMR2 = 0.0
      DO 12 I= 1,N
      RESID(I) = Y(I)
      DO 13 J= 1, M
   13 RESID(I) = RESID(I) - C(J,I)*B(J)
   12 SUMR2 = SUMR2 + RESID(I)*RESID(I)
      DO 14 I=1, 5
   14 B1(I) = B(I)
      RETURN
      END
```

Lorentzian fitting.

```
      SUBROUTINE MATRIX (A,B,N,M,DETER)
C
C     THIS DECK REPLACES  MATRX1
C
C     THIS SOLVES THE SET OF LINEAR EQUATIONS
C          A(1,1)X(1)+A(1,2)X(2) + . . . . . A(1,N)X(N) = B(1)
C        TO    A(N,1)X(1)+A(N,2)X(2) + . . . . . A(N,N)X(N) = B(N)
C
C     M IS THE DIMENSION OF BOTH A(M,M) AND B(M) AND MUST BE SET EQUAL
C     TO THAT OF THE MATRICES IN THE MAIN PROGRAMME.  M MUST BE GREATER
C     THAN OR EQUAL TO N.
C
C     AFTER COMPUTATION
C     A CONTAINS THE INVERSE OF THE ORIGINAL MATRIX.
C     B CONTAINS THE VALUES OF X(1) TO X(N) IN ORDER.
C     DETER  CONTAINS THE VALUE OF THE DETERMINANT OF A.
C
C     ENTRY LINEQN GIVES THE SOLUTIONS OF THE EQUATIONS AND THE
C     INVERSE OF A ONLY.
C
C     ENTRY DETERM GIVES THE VALUE OF THE DETERMINANT OF A AND ITS
C     INVERSE ONLY.
C
C     THE MAXIMUM NUMBER OF EQUATIONS IS 100.
C
      DIMENSION IPIVOT(100), INDEX(100,2)
      DIMENSION A(M,M),B(M)
      EQUIVALENCE (AMAX,T,SWAP)
      DOUBLE PRECISION A,B,AMAX,SWAP,PIVOT,T
C
C
      ENTRY LINEQN (A,B,N,M)
      IND   = 1
      GO TO 10
C
      ENTRY DETERM (A,N,M,DETER)
      IND   = 2
C
C     INITIALIZATION
C
      IF (N.LT.101) GO TO 10
      WRITE (6,5) N
    5 FORMAT (19H TOO MANY EQUATIONS, I6)
      STOP
C
   10 DETER  = 1.0
   15 DO 20 J= 1,N
   20 IPIVOT(J)=0
   30 DO 550 I=1,N
C
C     SEARCH FOR PIVOT ELEMENT
C
   40 AMAX =0.0
   45 DO 105 J=1,N
   50 IF (IPIVOT(J)-1) 60,105,60
   60 DO 100 K=1,N
   70 IF (IPIVOT(K)-1) 80,100,740
   80 IF (ABS(AMAX)-ABS(A(J,K))) 85,100,100
   85 IROW=J
   90 ICOLUM=K
   95 AMAX=A(J,K)
  100 CONTINUE
  105 CONTINUE
  110 IPIVOT(ICOLUM)=IPIVOT(ICOLUM)+1
C
C     INTERCHANGE ROWS TO PUT PIVOT ELEMENT ON DIAGONAL
C
  130 IF (IROW-ICOLUM) 140,260,140
  140 DETER  = -DETER
  150 DO 200 L=1,N
  160 SWAP =A(IROW,L)
  170 A(IROW,L)=A(ICOLUM,L)
  200 A(ICOLUM,L)=SWAP
      IF (IND  .EQ.2) GO TO 260
  220 SWAP=B(IROW)
  230 B(IROW)=B(ICOLUM)
  250 B(ICOLUM)=SWAP
  260 INDEX(I,1) = IROW
  270 INDEX(I,2) = ICOLUM
  310 PIVOT=A(ICOLUM,ICOLUM)
  320 DETER  = DETER *PIVOT
  330 A(ICOLUM,ICOLUM)=1.0
C
C     DIVIDE PIVOT ROW BY PIVOT ELEMENT
C
  340 DO 350 L=1,N
  350 A(ICOLUM,L)=A(ICOLUM,L)/PIVOT
      IF (IND  .EQ.2) GO TO 380
  370 B(ICOLUM)=B(ICOLUM)/PIVOT
C
C     REDUCE NON PIVOT ROWS
C
  380 DO 550 L1=1,N
  390 IF (L1-ICOLUM) 400,550,400
  400 T=A(L1,ICOLUM)
  420 A(L1,ICOLUM)=0.0
  430 DO 450 L=1,N
  450 A(L1,L) =A(L1,L)-A(ICOLUM,L)*T
      IF (IND  .EQ.2) GO TO 550
  500 B(L1)=B(L1)-B(ICOLUM)*T
  550 CONTINUE
C
C     INTERCHANGE COLUMNS
C
  600 DO 710 I=1,N
  610 L=N+1-I
  620 IF (INDEX(L,1)-INDEX(L,2)) 630,710,630
  630 JROW=INDEX(L,1)
  640 JCOLUM=INDEX(L,2)
  650 DO 705 K=1,N
  660 SWAP=A(K,JROW)
  670 A(K,JROW)=A(K,JCOLUM)
  700 A(K,JCOLUM)=SWAP
  705 CONTINUE
  710 CONTINUE
  740 RETURN
  750 END
```

```
      SUBROUTINE VA04A (X,E,N,F,ESCALE,IPRINT,ICON,MAXIT,CALCFX,W,N3N)
      REAL X(N),E(N)
      REAL W(N3N)
      ABSF(XYZ123)=ABS(XYZ123)
      IF(N3N-N*(N+3)) 8000,8002,8002
 8000 WRITE(6,8001)
 8001 FORMAT(26H DIMENSION OF W TOO SMALL )
      STOP
 8002 CONTINUE
      DUMAG=0.1*ESCALE
      SCER=0.05/ESCALE
      JJ=N*N+N
      JJJ=JJ+N
      K=N+1
      NFCC=1
      IND=1
      INN=1
      DO 1 I=1,N
      DO 2 J=1,N
      W(K)=0.
      IF(I-J)4,3,4
    3 W(K)=ABSF(E(I))
      W(I)=ESCALE
    4 K=K+1
    2 CONTINUE
    1 CONTINUE
      ITERC=1
      ISGRAD=2
      CALL CALCFX(N,X,F)
      FKEEP=ABSF(F)+ABSF(F)
    5 ITONE=1
      FP=F
      SUM=0.
      IXP=JJ
      DO 6 I=1,N
      IXP=IXP+1
      W(IXP)=X(I)
    6 CONTINUE
      IDIRN=N+1
      ILINE=1
    7 DMAX=W(ILINE)
      DACC=DMAX*SCER
      DMAG=AMIN1(.DMAG,0.1*DMAX)
      DMAG=AMAX1(DMAG,20.*DACC)
      DUMAX=10.*DMAG
      GO TO (70,70,71),ITONE
   70 DL=0.
      D=DMAG
      FPREV=F
      IS=5
      FA=F
      DA=DL
    8 DD=D-DL
      DL=0
   98 K=IDIRN
      DO 9 I=1,N
      X(I)=X(I)+DD*W(K)
      K=K+1
    9 CONTINUE
      CALL CALCFX(N,X,F)
      NFCC=NFCC+1
      GO TO (10,11,12,13,14,96),IS
   14 IF(F-FA)15,16,24
   16 IF(ABSF(D)-DMAX)17,17,18
   17 D=D+D
      GO TO 8
   18 WRITE(6,19)
   19 FORMAT(5X,44HVA04A MAXIMUM CHANGE DOES NOT ALTER FUNCTION)
      GO TO 20
   15 FB=F
      DB=D
      GO TO 21
   24 FB=FA
      DB=DA
      FA=F
      DA=D
   21 GO TO (83,23),ISGRAD
   23 D=DB+DB-DA
      IS=1
      GO TO 8
   83 D=0.5*(DA+DB-(FA-FB)/(DA-DB))
      IS=4
      IF((DA-D)*(D-DB))25,8,8
   25 IS=1
      IF(ABSF(D-DB)-DUMAX)8,8,26
   26 D=DB+SIGN(DUMAX,DB-DA)
      IS=1
      DUMAX=DUMAX+DUMAX
      DUMAG=DUMAG+DUMAG
      IF(DUMAX-DMAX)8,8,27
   27 DUMAX=DMAX
      GO TO 8
   13 IF(F-FA)28,23,23
   28 FC=FB
      DC=DB
   29 FB=F
      DB=D
      GO TO 30
   12 IF(F-FB)28,28,31
   31 FA=F
      DA=D
      GO TO 30
   11 IF(F-FB)32,10,10
   32 FA=FB
      DA=DB
      GO TO 29
   71 DL=1.
      DUMAX=5.
      FA=FP
      DA=-1.
      FB=FHOLD
      DB=0.
      D=1.
   10 FC=F
      DC=D
   30 A=(DB-DC)*(FA-FC)
      B=(DC-DA)*(FB-FC)
      IF((A+B)*(DA-DC))33,33,34
   33 FA=FB
      DA=DB
      FB=FC
      DB=DC
      GO TO 26
   34 D=0.5*(A*(DB+DC)+B*(DA+DC))/(A+B)
      DI=DB
      FI=FB
      IF(FB-FC)44,44,43
   43 DI=DC
      FI=FC
   44 GO TO (86,86,85),ITONE
   85 ITONE=2
      GO TO 45
   86 IF(ABSF(D-DI)-DACC) 41,41,93
   93 IF(ABSF(D-DI)-0.03*ABSF(D)) 41,41,45
   45 IF((DA-DC)*(DC-D)) 47,46,46
   46 FA=FB
      DA=DB
      FB=FC
      DB=DC
      GO TO 25
   47 IS=2
      IF((DB-D)*(D-DC)) 48,8,8
   48 IS=3
      GO TO 8
   41 F=FI
      D=DI-DL
      DD=SQRT(.(DC-DB)*(DC-DA)*(DA-DB)/(A+B))
      DO 49 I=1,N
      X(I)=X(I)+D*W(IDIRN)
      W(IDIRN)=DD*W(IDIRN)
      IDIRN=IDIRN+1
   49 CONTINUE
      W(ILINE)=W(ILINE)/DD
      ILINE=ILINE+1
      IF(IPRINT-1)51,50,51
   50 WRITE(6,52)                ITERC,NFCC,F,(X(I),I=1,N)
   52 FORMAT (/1X,9HITERATION,I5,I10,16H FUNCTION VALUES
     1 10X,3HF =,E21.8 /(5E24.8 ))
      GO TO(51,53),IPRINT
   51 GO TO (55,38),ITONE
```

VA04A

1

VA04A 2

```
      55 IF (FPREV-F-SUM) 94,95,95
      95 SUM=FPREV-F
         JIL=ILINE
      94 IF ((DIRN-JJ) 7,7,84
      84 GO TO (92,72),IND
      92 FHOLD=F
         IS=6
         IXP=JJ
         DO 59 I=1,N
         IXP=IXP+1
         W(IXP)=X(I)-W(IXP)
      59 CONTINUE
         DD=1.
         GO TO 58
      96 GO TO (112,87),IND
     112 IF (FP-F) 37,91,91
      91 D=2.*(FP+F-2.*FHOLD)/(FP-F)**2
         IF (D*(FP-FHOLD-SUM)**2-SUM) 87,37,37
      87 J=JIL*N+I
         IF (J-JJ) 60,60,61
      60 DO 62 I=J,JJ
         K=I-N
         W(K)=W(I)
      62 CONTINUE
         DO 97 I=JIL,N
         W(I-1)=W(I)
      97 CONTINUE
      61 IDIRN=IDIRN-N
         ITONE=3
         K=IDIRN
         IXP=JJ
         AAA=0.
         DO 65 I=1,N
         IXP=IXP+1
         W(K)=W(IXP)
         IF (AAA-ABSF(W(K)/E(I))) 66,67,67
      66 AAA=ABSF(W(K)/E(I))
      67 K=K+1
      65 CONTINUE
         DDMAG=1.
         W(N)=ESCALE/AAA
         ILINE=N
         GO TO 7
      37 IXP=JJ
         AAA=0.
         F=FHOLD
         DO 99 I=1,N
         IXP=IXP+1
         X(I)=X(I)-W(IXP)
         IF (AAA*ABSF(E(I))-ABSF(W(IXP))) 98,99,99
      98 AAA=ABSF(W(IXP)/E(I))
      99 CONTINUE
         GO TO 72
      38 AAA=AAA*(1.+DII
         GO TO (72,106),IND
      72 IF (IPRINT-2) 53,50,50
      53 GO TO (109,88),IND
     109 IF (AAA-0.1) 89,89,76
      89 GO TO (20,116),ICON
     116 IND=2
         GO TO (100,101),INN
     100 INN=2
         K=JJJ
         DO 102 I=1,N
         K=K+1
         W(K)=X(I)
         X(I)=X(I)+10.*E(I)
     102 CONTINUE
         FKEEP=F
         CALL CALCFX (N,X,F)
         NFCC=NFCC+1
         DDMAG=0.
         GO TO 108
      76 IF (F-FP) 35,78,78
      78 WRITE(6,80)
      80 FORMAT (5X,37HVA04A ACCURACY LIMITED BY ERRORS IN F)
         GO TO 20
      88 IND=1
      35 DDMAG=0.4*SQRT (FP-F)
         ISGRAD=1
     108 IIERC=IIERC+1
         IF (IIERC-MAXIT) 5,5,81
      81 WRITE(6,82) MAXIT
      82 FORMAT(15,30H ITERATIONS COMPLETED BY VA04A)
         IF (F-FKEEP) 20,20,110
     110 F=FKEEP
         DO 111 I=1,N
         JJJ=JJJ+1
         X(I)=W(JJJ)
     111 CONTINUE
         GO TO 20
     101 JIL=1
         FP=FKEEP
         IF (F-FKEEP) 105,78,104
     104 JIL=2
         FP=F
         F=FKEEP
     105 IXP=JJ
         DO 113 I=1,N
         IXP=IXP+1
         K=IXP+N
         GO TO (114,115),JIL
     114 W(IXP)=W(K)
         GO TO 113
     115 W(IXP)=X(I)
         X(I)=W(K)
     113 CONTINUE
         JIL=2
         GO TO 92
     106 IF (AAA-0.1) 20,20,107
      20 RETURN
     107 INN=1
         GO TO 35
         END
```

FRIER. Landau fitting programme.

```
C        DATA -
C
C     NSETS.    THEN FOR EACH SET -
C
C                          TEXT.
C                          ICON,NDATA,NCARRIERS,ESCALE,PERCENT ACC.Y.
C                          AND N-WEIGHT (=1 FOR WEIGHTING).
C           THEN FOR EACH CARRIER, TWO CARDS -
C                      1   NHRMCS,NHOLD,PERIOD,POWER,A,DTBT
C                      2   UP TO THREE PAIRS (AMPLITUDE,PHASE).
C
C
C                          FINALLY, FIELD-AND-SAMPLE-VOLTS,
C                          UP TO 200 CARDS.
C
C
C        NHOLD(4,2) MUST BE SET EQUAL TO  1  IN THE
C        APPROPRIATE PLACE TO KEEP-PERIOD,POWER,A,DTBT- CONST.
C        RESPECTIVELY.                 1     2  3  4
C
C
C
C
C
C
      DIMENSION TEXT(13),DATAX(200),DATAY(200),POWER(2),PERIOD(2),A(2),
     1 DTBT(2),W(3,2),PSI(3,2),E(20),X(20),NHRMCS(2),AVA(400),NHOLD(4,2)
C
C
      COMMON PERIOD,POWER,A,DTBT,W,PSI,NCARRS,NHRMCS,DATAX,DATAY,NDATA,
     1 NHOLD,CONST,SLOPE
C
C
C
      READ(5,100) NSETS
  100 FORMAT(I6)
C
      DO 99 NSET=1,NSETS
      READ(5,110) (TEXT(I), I=1,13)
  110 FORMAT(13A6)
C
      READ(5,120) ICON,NDATA,NCARRS,ESCALE,ACCUR,NWT
  120 FORMAT(I1, I4, I5, E10.2, F10.1, I5)
      IF(NDATA.LE.200) GO TO 98
      WRITE(6,97)
   97 FORMAT(1H1, 17HNDATA TOO LARGE.  ////)
      GO TO 99
   98 CONTINUE
      IF(ICON.EQ.0) ICON = 1
      IF(ACCUR.EQ.0.0) ACCUR = 1.0
C
      DO 1 I = 1, NCARRS
      READ(5,130) NHRMCS(I),(NHOLD(K,I),K=1,4),PERIOD(I),POWER(I),A(I),
     1 DTBT(I)
  130 FORMAT(    5I1,5X,E10.2,3F10.4)
      READ(5,131) (W(K,I),PSI(K,I),K=1,3)
  131 FORMAT(6F10.4)
    1 CONTINUE
C
      DO 2 I=1, NDATA
    2 READ(5,140) DATAX(I), DATAY(I)
  140 FORMAT(F10.4,10X,F10.4)
C
      0       CALL ADJINL(PERIOD,POWER,A,DTBT,W,PSI,NCARRS,NHRMCS,NHOLD,M,
     1 X)
C
   10 WRITE(6,150) (TEXT(I), I=1,13)
  150 FORMAT(1H1, 1X, 13A6////)
C
      WRITE(6,200) ICON,NDATA,ESCALE,NCARRS,ACCUR,(NHRMCS(I),I=1,NCARRS)
 200 FORMAT(                    12HDATA INPUT-//1HO,4HICON,2X,
     1 5HNDATA,9X,6HESCALE,4X,6HNCARRS,5X,5HACCUR,5X,6HNHRMCS/1H ,2X,
     2 I1,4X,I3,9X,E9.2,4X,I1,7X,F6.1,7X,11(I1 ,53X,11) )
      WRITE(6,172)  (NHOLD(K,1),K= 1,4)
  172 FORMAT(1HO, 9HCARRIER 1 /1HO,6HNHOLD=,4I1)
      NHRMC = NHRMCS(1)
      WRITE(6,171) POWER(1),PERIOD(1),A(1),DTBT(1),(W(K,1),PSI(K,1),K=1,
     1 NHRMC)
  171 FORMAT(1HO, 1X, 1HN, 5X, 6HPERIOD,18X,1HA,18X,4HDT/T,17X,9HAMPLITUDE,
     119X, 5HPHASE //1H ,F5.1,
     2                  E10.3,5X,2E20.5,5X,E20.5,5X,E20.5/
     3 (1H ,65X,E20.5,5X,E20.5)  )
      IF(NCARRS.EQ.1) GO TO 96
      WRITE(6,181)  (NHOLD(K,2), K=1,4)
  181 FORMAT(1HO, 9HCARRIER 2 / 1HO,6HNHOLD=,4I1)
      NHRMC = NHRMCS(2)
      WRITE(6,191) POWER(2),PERIOD(2),A(2),DTBT(2),(W(K,2),PSI(K,2),K=1,
     1 NHRMC)
  191 FORMAT(1HO, 1X, 1HN, 5X, 6HPERIOD,18X,1HA,18X,4HDT/T,17X,9HAMPLITUDE,
     119X, 5HPHASE //1H ,F5.1,
     2                  E10.3,5X,2E20.5,5X,E20.5,5X,E20.5/
     3 (1H ,65X,E20.5,5X,E20.5)  )
   96 CONTINUE
```

FRIER

```
      WRITE(6,182)
  182 FORMAT(1HO,25X,10(5H-----) ///)
C
      IF(NNT.NE.1)  GO TO   1022
      XMIN = 1.0E06
      XMAX = 0.0
      DO 1020 K= 1, NDATA
      X = DATAX(K)
      AX = ABS(X)
      XMAX = AMAX1(XMAX,AX)
      XMIN = AMIN1(XMIN,AX)
 1020 CONTINUE
      DENOM = XMIN - XMAX
      CONST1 = XMIN -100.0*XMAX
      CONST2 = 99.0*XMAX*XMIN
      CONST = CONST1/DENOM
      SLOPE = CONST2/DENOM
      GO TO 1021
 1022 CONST = 1.0
      SLOPE = 0.0
 1021 CONTINUE
C
      M= 0
      JIND = 0
      DO 15 I= 1, NCARRS
   15 M = M + NHRMCS(I)
      M = 4*NCARRS + 2*M
      DO 94 K = 1,NCARRS
      DO 95 I = 1,4
   95 IF(NHOLD(I,K).EQ.1) JIND = JIND+1
   94 CONTINUE
      M = M - JIND
C
      N3N = M*(M+3)
C
      DO 11 I= 1, M
      XXX = X(I)
   11 E(I) = ABS(XXX)*(ACCUR/100.0)
C
C
      IPRINT = 1
      MAXIT = 200
      EXTERNAL CALCFX
C
C
      CALL VA04A(X,E,M,F,ESCALE,IPRINT,ICON,MAXIT,CALCFX,NVA,N3N)
C
C
      WRITE(6,1601 ((EX(I), I=1,13)
 1601 FORMAT(1HI, 1X, 13A6//////
     1                  1HO,13HFINAL VALUES- ///1H ,9HCARRIER 1 //)
      NHRMC = NHRMCS(1)
      WRITE(6,1701 POWER(1),PER100(1),A(1),DTBT(1),(W(K,1),PSI(K,1),K=1,
     1 NHRMC)
 1700 FORMAT(1HO,1X,1HN,5X,6HPER100,18X,1HA,18X,4HDT/T,17X,9HAMPLITUDE,
     119X,5HPHASE //1H ,F5.1,
     2                    E10.3,5X,2E20.5,5X,E20.5,5X,E20.5/
     3 (1H ,65X,E20.5,5X,E20.5)  )
      IF(NCARRS.EQ.1) GO TO 13
      WRITE(6,180)
  180 FORMAT(1HO,9HCARRIER 2 //)
      NHRMC = NHRMCS(2)
      WRITE(6,190) POWER(2),PER100(2),A(2),DTBT(2),(W(K,2),PSI(K,2),K=1,
     1 NHRMC)
 1900 FORMAT(1HO,1X,1HN,5X,6HPER100,18X,1HA,18X,4HDT/T,17X,9HAMPLITUDE,
     119X,5HPHASE //1H ,F5.1,
     2                    E10.3,5X,2E20.5,5X,E20.5,5X,E20.5/
     3 (1H ,65X,E20.5,5X,E20.5)  )
   13 WRITE(6,195)  F
  195 FORMAT(1HO,15HSUM SQ RESIDS.=,E20.5)
C
   99 CONTINUE
C
      STOP
      END
```

```
      SUBROUTINE CALCFX(M,X,F)
C
C
      DIMENSION PER100(2),POWER(2),A(2),DTBT(2),W(3,2),PSI(3,2),
     1 NHRMCS(2),NHOLD(4,2),X(20),DATAX(200),DATAY(200)
C
      COMMON PER100,POWER,A,DTBT,W,PSI,NCARRS,NHRMCS,DATAX,DATAY,NDATA,
     1  NHOLD,CONST,SLOPE
C
      SUMR2 = 0.0
C
C
      CALL ADJUST(PER100,POWER,A,DTBT,W,PSI,NCARRS,NHRMCS,NHOLD,M,
     1 X)
C
C
      DO 1 NO= 1, NDATA
      FIELD = DATAX(NO)
C
C
      CALL CALC(PER100,POWER,A,DTBT,W,PSI,FIELD,F,NCARRS,NHRMCS)
C
C
      RESID = F - DATAY(NO)
      WT = SLOPE/DATAX(NO)  +CONST
    1 SUMR2 = SUMR2 + (RESID*RESID*(WT**M))
      F = SUMR2
      RETURN
      END
```

FRIER

```
C
      SUBROUTINE ADJINL(PERIOD,POWER,A,DTBT,W,PSI,NCARRS,NHRMCS,NHOLD,M,
     1 K)
C
C
C     INITIAL FILLING OF -X-
C
C
      DIMENSION PERIOD(2),POWER(2),A(2),DTBT(2),W(3,2),PSI(3,2),
     1 NHRMCS(2),NHOLD(4,2),X(20)
C
      I = 1
      DO 5 K = 1, NCARRS
      IF(NHOLD(1,K).EQ.1) GO TO 1
      X(I) = PERIOD(K)
      I = I +1
    1 IF(NHOLD(2,K).EQ.1) GO TO 2
      X(I) = POWER(K)
      I = I + 1
    2 IF(NHOLD(3,K).EQ.1) GO TO 3
      X(I) = A(K).
      I = I + 1
    3 IF(NHOLD(4,K).EQ.1) GO TO 4
      X(I) = DTBT(K)
      I = I + 1
    4 CONTINUE
      X(I) = W(1,K)
      I = I + 1
      X(I) = PSI(1,K)
      I = I + 1
      IF(NHRMCS(K).EQ.1) GO TO 5
      X(I) = W(2,K)
      I = I + 1
      X(I) = PSI(2,K)
      I = I + 1
      IF(NHRMCS(K).EQ.2) GO TO 5
      X(I) = W(3,K)
      I = I + 1
      X(I) = PSI(3,K)
      I = I + 1
    5 CONTINUE
C
      RETURN
      END
```

```
      SUBROUTINE ADJUST(PERIOD,POWER,A,DTBT,W,PSI,NCARRS,NHRMCS,NHOLD,M
     1 X)
C
C
      DIMENSION PERIOD(2),POWER(2),A(2),DTBT(2),W(3,2),PSI(3,2),
     1 NHRMCS(2),NHOLD(4,2),X(20)
C
      I = 1
      DO 5 K = 1, NCARRS
      IF(NHOLD(1,K).EQ.1) GO TO 1
      PERIOD(K) = X(I)
      I = I + 1
    1 IF(NHOLD(2,K).EQ.1) GO TO 2
      POWER(K) = X(I)
      I = I + 1
    2 IF(NHOLD(3,K).EQ.1) GO TO 3
      A(K) = X(I)
      I = I + 1
    3 IF(NHOLD(4,K).EQ.1) GO TO 4
      DTBT(K) = X(I)
      I = I + 1
    4 CONTINUE
      W(1,K) = X(I)
      I = I + 1
      PSI(1,K) = X(I)
      I = I + 1
      IF(NHRMCS(K).EQ.1) GO TO 5
      W(2,K) = X(I)
      I = I + 1
      PSI(2,K) = X(I)
      I = I + 1
      IF(NHRMCS(K).EQ.2) GO TO 5
      W(3,K) = X(I)
      I = I + 1
      PSI(3,K) = X(I)
      I = I + 1
    5 CONTINUE
C
      RETURN
      END
      SUBROUTINE CALC(PERIOD,POWER,A,DTBT,W,PSI,FIELD,F,NCARRS,NHRMCS)
C
C
C     CALCULATES FUNCTION GIVEN PARAMETERS AND FIELD.
C
C
      DIMENSION PERIOD(2),POWER(2),A(2),DTBT(2),W(3,2),PSI(3,2),U(2),
     1 NHRMCS(2)
C
      F= 0.0
C
      DO 1 I = 1, NCARRS
      U(I)= A(I)/FIELD
      ARGEX = U(I)*DTBT(I)
      ARGCO = 12.0*3.141593/(FIELD*PERIOD(I))
      NHRMC = NHRMCS(I)
      G = 0.0
C
      DO 2 K= 1, NHRMC
      ARGEXP = -1.0*ARGEX*FLOAT(K)
      ARGCOS = ARGCO*FLOAT(K)    -    PSI(K,I)
      UK = U(I)*FLOAT(K)
    2 G = W(K,I)*(UK/SINH(UK))*EXP(ARGEXP)*COS(ARGCOS)    + G
C
      ENN = POWER(I)
      G = G*(FIELD**ENN)
    1 F = F + G
C
      RETURN
      END
```